ANNUAL REPORT

2011

and list of publications

Bayerisches Forschungsinstitut
für Experimentelle Geochemie und Geophysik
Universität Bayreuth

Bayerisches Geoinstitut
Universität Bayreuth
D-95440 Bayreuth
Germany

Telephone: +49-(0)921-55-3700
Telefax: +49-(0)921-55-3769
e-mail: bayerisches.geoinstitut@uni-bayreuth.de
www: http://www.bgi.uni-bayreuth.de

Editorial compilation by: Stefan Keyssner and Petra Buchert
Section editors: Andreas Audétat, Tiziana Boffa Ballaran, Leonid Dubrovinsky,
Dan Frost, Florian Heidelbach, Tomoo Katsura, Hans Keppler,
Catherine McCammon, Nobuyoshi Miyajima, Dave Rubie,
Henri Samuel, Gerd Steinle-Neumann, Nicolas Walte

Staff and guests of the Bayerisches Geoinstitut in **July 2011**:

Die Mitarbeiter und Gäste des Bayerischen Geoinstituts im **Juli 2011**:

First row, from left (1. Reihe, v. links) Giacomo Pesce, Vojtěch Vlček, Dickson Ojwang, Valerio Cerantola, Li Zhang, Ruifang Huang, Stefan Keyssner

Second row, from left (2. Reihe, v. links) Elena Bykova, Tiziana Boffa Ballaran, Julia Huber, Antje Kathrin Vogel, Martha Pamato, Lydia Kison-Herzing, Martha Evonuk, Vincenzo Stagno, Tomoo Katsura, Hongzhan Fei

Third row, from left (3. Reihe, v. links) Sven Linhardt, Petra Buchert, Gleb Parakhonskiy, Nobuyoshi Miyajima, Yuan Li, Xiaozhi Yang, Kilian Pollok, Holger Kriegl, Dan Frost, Dave Rubie, Nico Walte, Davide Novella, Florian Heidelbach, Henri Samuel, Ahmed El Goresy, Ana Cernok, Julia Hopf

Fourth row, from left (4. Reihe, v. links) Anna Spivak, Dmytro Trots, Eran Greenberg, Huaiwei Ni, Ryosuke Sinmyo, Gerd Steinle-Neumann, Vladislav Aleksandrov, Detlef Krauße, Stefan Übelhack

Fifth row, from left (5. Reihe, v. links) Heinz Fischer, Hubert Schulze, Egor Zakharchenko, Hans Keppler, Clemens Prescher, Dennis Harries, Kurt Klasinski, Konstantin Glazyrin, Alexander Kurnosov, Yoichi Nakajima

Absent (Es fehlten) Andreas Audétat, Nico de Koker, Leonid Dubrovinsky, Nicole Fischer, Mattia Giannini, Gertrud Gollner, Scott King, Ilya Kupenko, Linda Lerchbaumer, Geeth Manthilake, Catherine McCammon, Mainak Mookherjee, Mezhoura Oussadou, Sergey Ovsyannikov, Asiye Shabestari, Svyatoslav Shcheka, Vincent Soustelle, Willem van Mierlo

Contents

Foreword

The Bayerisches Geoinstitut has a long tradition in developing new experimental methods in high-pressure research. Deformation experiments under high pressure are technically particularly challenging. At the same time, such experiments are essential for understanding the viscous flow properties of mantle rocks that control plate tectonics, volcanism and mountain building at the Earth's surface. In deformation experiments, both strain and stress must be measured continuously. Previously, this was only possible by using synchrotron radiation, with the precision of stress measurements being on the order of 200 MPa (2,000 bar). A new method for measuring stress at high pressure has now been developed at the Geoinstitut that does not rely on synchrotron radiation and can therefore be carried out "in house" without access to large facilities. The new method involves the use of a piezoelectric sensor consisting of a crystal of $GaPO_4$. A piezoelectric effect has been measured at high pressure for the first time in such experiments. In order to calculate stress from the measured electrical effect, the expected piezoelectric effect for $GaPO_4$ was determined through quantum mechanical ab-initio calculations. With this new method, applied stresses on the order of 2-3 MPa can be measured in high pressure experiments. In comparison to conventional synchrotron methods, this represents an improvement in sensitivity of two orders of magnitude. It is therefore to be expected that this new method will lead to a much improved understanding of flow processes in the Earth's mantle.

A very interesting discovery has been made at the Geoinstitut last year. Water-rich fluids are responsible for many material transport processes in the Earth's interior, leading, for example, to the formation of ore deposits. Under the reducing conditions that are typical for the deep mantle, water contains considerable concentrations of hydrogen (H_2). It has now been observed through high pressure experiments that in the upper mantle at pressures of 1-2 GPa (10,000-20,000 bar) and temperatures up to more than 1000 °C, water and hydrogen are not completely mutually soluble - instead a water-rich fluid phase coexists with almost pure hydrogen. This effect could have been very important during the early history of the Earth. Degassing of almost pure hydrogen from the mantle could have stabilized a reducing atmosphere for millions of years. Such a strongly-reduced atmosphere would have resulted in the formation of complex organic molecules that may have been the building blocks for the origin of life.

The formation of the Earth was determined by events that occurred during the early history of the solar system. The composition and thermal structure of the Earth as well as its differentiation into core, mantle and crust can only be understood by reconstructing processes that occurred 4.5 billion years ago. The Bayerisches Geoinstitut is well known for high-pressure studies of core formation and the development of early magma oceans. A particularly gratifying event in 2011 was the awarding of an ERC Advanced Grant to Dave Rubie to fund a five-year project entitled "The Accretion and Early Differentiation of the Earth and Terrestrial Planets" (ACCRETE). The aim of this project is to integrate astrophysical models of planet formation with geochemical models based on high-pressure experiments and the results of studies of meteorites. Following DEEP (Deep Earth Elastic Properties, Dan Frost) ACCRETE is the second ERC Advanced Grant to be awarded to the Geoinstitut.

As in previous years, and also on behalf of my colleagues, I would like to thank the *Free State of Bavaria* as represented by the *Bayerisches Staatsministerium für Wissenschaft, Forschung und Kunst, the administration of the University of Bayreuth* as well as the *Kommission für Geowissenschaftliche Hochdruckforschung* of the *Bavarian Academy of Sciences* for their continuing support and strong commitment to the Bayerisches Geoinstitut. We also gratefully acknowledge generous support from external funding agencies, in particular the *Alexander von Humboldt Foundation*, the *European Union*, and the *German Science Foundation,* which have also contributed greatly to the development and success of the Institute.

Bayreuth, March 2012 Hans Keppler

Vorwort

Das Bayerische Geoinstitut hat eine lange Tradition in der Entwicklung neuer experimenteller Methoden der Hochdruckforschung. Verformungsexperimente unter hohem Druck sind eine besondere technische Herausforderung. Gleichzeitig sind diese Experimente aber entscheidend für das Verständnis der Fließprozesse von Gesteinen im Erdmantel, die letztlich Plattentektonik, Vulkanismus und Gebirgsbildung an der Erdoberfläche antreiben. Bei Deformationsexperimenten muss sowohl die Verformung als auch der gerichtete Druck (Stress) kontinuierlich gemessen werden. Bisher ist dies nur durch Anwendung von Synchrotronstrahlung möglich; die erreichbare Genauigkeit liegt hier bei 200 MPa (2000 bar). Am Geoinstitut wurde nun eine neue Methode zur Messung von Stress unter hohem Druck entwickelt, die unabhängig ist von Synchrotronstrahlung und die damit „im Haus“ ohne Zugang zu Großforschungseinrichtungen ausgeführt werden kann. Hierzu wird ein piezoelektrischer Sensor auf Basis von $GaPO_4$ verwendet. Es konnte in diesen Experimenten erstmals ein piezoelektrischer Effekt unter hohem hydrostatischem Druck gemessen werden. Zur Umrechnung des elektrischen Signals in Stress wurde der unter Druck zu erwartende piezoelektrische Effekt in $GaPO_4$ durch quantenmechanische *ab initio*-Berechnungen bestimmt. Mit dieser neuen Methode können nun im Labor gerichtete Drücke in der Größenordnung von 2-3 MPa gemessen werden. Im Vergleich zu konventionellen Synchrotronmethoden ist dies eine Verbesserung der Empfindlichkeit um zwei Größenordnungen. Es ist daher zu erwarten, dass diese neue experimentelle Methode zu einem wesentlich verbesserten Verständnis der Fließprozesse im Erdmantel führen wird.

Eine sehr interessante Entdeckung wurde am Geoinstitut im vergangenen Jahr durch Zufall gemacht. Wasserhaltige Fluide sind verantwortlich für viele Stofftransportprozesse im Erdinneren, die beispielsweise auch zur Bildung von Erzlagerstätten führen. Unter reduzierenden Bedingungen, die für den tieferen Mantel typisch sind, enthält das Wasser erhebliche Mengen an Wasserstoff (H_2). In Hochdruckexperimenten konnte nun beobachtet werden, dass im oberen Mantel bei Drücken von 1-2 GPa (10.000-20.000 bar) und Temperaturen bis über 1000 °C Wasser und Wasserstoff nicht vollständig miteinander mischbar sind – eine wasserreiche Fluidphase koexistiert mit fast reinem Wasserstoff. Dieser Effekt könnte sehr wichtig gewesen sein in der Frühgeschichte der Erde. Entgasung von fast reinem Wasserstoff aus dem Erdmantel könnte hier eine reduzierende Erdatmosphäre über Millionen von Jahren stabilisiert haben. Eine stark reduzierende Atmosphäre begünstigt die Bildung komplexer organischer Moleküle, die möglicherweise Bausteine für die Entstehung des Lebens waren.

Die Entwicklung der Erde wurde entscheidend geprägt durch Ereignisse in der Frühgeschichte des Sonnensystems. Die Zusammensetzung und thermische Struktur unseres Planeten sowie seine Differentiation in Kern, Mantel und Kruste kann man nur verstehen, wenn man die Vorgänge vor 4,5 Milliarden Jahren sehr genau rekonstruieren kann. Das Bayerische Geoinstitut ist bekannt für Hochdruckuntersuchungen über die Entstehung des Erdkerns und die Entwicklung des frühen Magmenozeans. Ein besonders erfreuliches Ereignis in 2011 war daher die Genehmigung eines ERC *Advanced Grants* an Dave Rubie für seine Untersuchungen zur Akkretion und frühen Differentiation der Erde (ACCRETE). Das Ziel dieses Projektes ist die Integration von astrophysikalischen Modellen der Planetenentstehung mit geochemischen Daten aus Hochdruckexperimenten und aus Untersuchungen von Meteoriten. ACCRETE ist nach DEEP (*Deep Earth Elastic Properties*, Dan Frost) bereits das zweite ERC *Advanced Grant* am Geoinstitut.

Wie in den vorangegangenen Jahren möchte ich auch im Namen meiner Kollegen dem *Freistaat Bayern*, vertreten durch das *Bayerische Staatsministerium für Wissenschaft, Forschung und Kunst*, der *Hochschulleitung der Universität Bayreuth*, als auch der *Kommission für Geowissenschaftliche Hochdruckforschung* der *Bayerischen Akademie der Wissenschaften* danken für ihre fortwährende Unterstützung und ihre enge Verbundenheit mit dem Bayerischen Geoinstitut. Wir sind auch sehr dankbar für die großzügige Förderung durch externe Geldgeber, insbesondere durch die *Alexander von Humboldt-Stiftung*, die *Europäische Union* und die *Deutsche Forschungsgemeinschaft*, die ebenfalls wesentlich zur Entwicklung und zum Erfolg des Bayerischen Geoinstituts beigetragen haben.

Bayreuth, im März 2012 Hans Keppler

1. Advisory Board and Directorship

1.1 Advisory Board

The *Kommission für Geowissenschaftliche Hochdruckforschung der Bayerischen Akademie der Wissenschaften* advises on the organisation and scientific activities of the institute. Members of this board are:

Prof. Dr. G. BREY	Institut für Geowissenschaften der Johann Wolfgang Goethe-Universität, Frankfurt am Main
Prof. Dr. U. CHRISTENSEN	Max-Planck-Institut für Sonnensystemforschung, Katlenburg-Lindau
Prof. Dr. R. KNIEP	Institut für Chemische Physik fester Stoffe der Max-Planck-Gesellschaft, Dresden
Prof. Dr. H. PALME	Institut für Mineralogie und Geochemie der Universität zu Köln
Prof. Dr. M. RIEDERER (Chairman)	Julius-von-Sachs-Institut für Biowissenschaften, Würzburg
Prof. Dr. R. RUMMEL	Institut für Astronomische und Physikalische Geodäsie der TU München
Prof. Dr.-Ing. G. SACHS	Lehrstuhl für Flugmechanik und Flugregelung der TU München
Prof. Dr. E. SALJE, FRS, FRSA	Department of Earth Sciences, University of Cambridge
Prof. Dr. H. SOFFEL	Emeritus, Institut für Allgemeine und Angewandte Geophysik der Universität München

The Advisory Board held meetings in Bayreuth (15.04.2011) and in Munich (04.11.2011).

1.2 Leadership

Prof. Dr. Hans KEPPLER (Director)
Prof. Dr. Falko LANGENHORST (until 31.03.2011)
Prof. Dr. Tomoo KATSURA

2. Staff, Funding and Facilities

2.1 Staff

At the end of 2011 the following staff positions existed in the Institute:

Scientific staff *:	**12**
Technical staff:	**13**
Administrative staff:	**2**
Administrative officer:	**1**

* Including a tenure-track junior professorship in geodynamic modeling initially funded by *Stifterverband für die Deutsche Wissenschaft* for 6 years, started in 2007.

During 2011, 28 scientific (233 months) positions were funded by grants raised externally by staff members of the institute. In addition 10 long-term scientific positions (80 months) were funded by the resources of the BGI Visiting Scientists' Programme (see Sect. 8) which also supported short-term visits for discussing future projects or presenting research results (see Sect. 6). Positions for 5 Ph.D. students and 1 co-ordinator were funded under the BGI International Graduate School under the Elitenetzwerk Bayern "Structure, Reactivity and Properties of Oxide Materials" (see Sect. 4). 6 scientists (21 months) were supported by personal grants (stipends).

2.2 Funding

In 2011, the following financial resources were available from the Free State of Bavaria:

Visiting Scientists' Programme:	381.000 €
Consumables:	314.000 €
Investment Funding:	0 €

The total amount of national/international external funding (*"Drittmittel"*) used for ongoing research projects in 2011 was 2.920.000 € (Positions: 1.340.000 €; equipment, consumables and travel grants: 1.580.000 €).

	positions	**equipment, consum-ables, travel grants**	**total**
ENB	250.000 €	100.000 €	350.000 €
AvH	70.000 €	20.000 €	90.000 €
DFG	550.000 €	90.000 €	640.000 €
EU	210.000 €	50.000 €	260.000 €
BMBF	180.000 €	1.290.000 €	1.470.000 €
Stifterverband	50.000 €	10.000 €	60.000 €
Others	30.000 €	20.000 €	50.000 €
			2.920.000 €

(ENB = Int. Graduate School „Oxides“ in the Elite Network of Bavaria; AvH = Alexander von Humboldt Foundation; DFG = German Science Foundation; EU = European Union; BMBF = Federal Ministry of Education and Research; Stifterverband = Stifterverband für die Deutsche Wissenschaft; Others: DAAD, University of Bayreuth, Universitaet Bayern e.V., Industry

In the following list only the BGI part of the funding is listed in cases where joint projects involved other research institutions. Principal investigators and duration of the grants are listed in brackets. Total project funding refers to the funding over the entire duration of this project.

Funding institution	Project, Funding	Total Project Funding
BMBF	03G0718A (K. Pollok – 10.08 - 9.11) Nachwuchsgruppe "Microstructural Controls on Monosulfide Weathering" (MIMOS) Positions: 3 x E 13/2, each 36 months 241.086 € student assistent, (19,75h/month), 48 months 7.920 € Consumables and travel funding: 57.550 € Overhead: 6.915 € Total funding:	313.471 €
BMBF - DESY	05K10WC1 (L.S. Dubrovinsky – 7.10 - 6.13) "Verbundprojekt: Kernresonante Streutechniken: Entwicklung von Messplätzen zur Charakterisierung von Nanostrukturen, molekularen Schaltern, biologischen Mikroproben und Materie unter extremen Bedingungen mit kernresonanten Streutechniken. Teilprojekt 1" Total funding:	529.670 €
BMBF	05K10WC2 (H. Keppler – 7.10 - 6.13) "Aufbau einer Hochdruckpresse vom Multi-Anvil-Typ für TOF-Neutronenbeugung und Neutronen-Radiographie am FRM II" Total funding:	2.050.078 €
DAAD	(L.S. Dubrovinsky) "Studies of carbonates stability at extreme conditions"	3.000 €
DFG	AU 314/1-2 (A. Audétat – 7.11 - 6.12) "Fraktionierung von Schwefel, Kupfer und Gold in zweiphasigen Fluiden" Positions: E 13/2, 12 months 34.450 € Consumables and travel funding: 27.700 € Overhead: 6.800 €	68.950 €
DFG	Bo 2550/4-1 (T. Boffa Ballaran, F. Langenhorst – 2.10 - 1.12) "Crystal chemistry of hibonite as indicator for oxygen fugacities during solar nebula condensation" Positions: E 13/2, 24 months 68.900 € student assistant (57 h/month) 24 months 19.050 € Consumables and travel funding: 22.000 € Overhead: 19.400 €	129.350 €

DFG	Du 393/7-1 (L.S. Dubrovinsky, N.A. Dubrovinskaia – 6.09 - 5.12) "Elasticity of iron and iron-based alloys at conditions of the Earth's and planetary cores" Positions: student assistant (80 h/month), 36 months 23.760 € Consumables and travel funding 42.017 € Publication costs 1.500 € Overhead: 18.600 €	85.877 €
DFG	EV 166/1-1 (M. Evonuk – 11.10 - 10.13) "Core formation in Terrestrial planets via global Rayleigh-Taylor destabilization" 1 position: E 13, 36 months 206.700 € Consumables and travel funding: 6.727 € Publication costs 2.250 € Overhead: 37.100 €	252.777 €
DFG	FR 1555/5-1 (D.J. Frost, C.A. McCammon – 04.10 - 03.11) "Experimental investigation of the redox conditions at which carbonate minerals and melts transform to graphite or diamond in Earth's mantle" 1 position: E 13/2, 12 months 34.450 € Consumables and travel funding: 10.537 € Publication costs 500 € Overhead: 8.100 €	53.587 €
DFG	KE 501/8-1 (H. Keppler – 8.09 - 2.12) "Untersuchungen der Kristallisationskinetik und Gefüge-entwicklung von Basalten mit einer neuartigen Moissanit-Sichtzelle" 1 position: E 13, 24 months 137.800 € Consumables and travel funding: 27.690 € Publication costs 800 € Overhead: 32.200 €	198.490 €
DFG	KE 501/9-1 (H. Keppler – 2010 - 2013) "Noble gases in silicate perovskite: Solubility, dissolution mechanism and influence on the equation of state" 1 position: E 13, 36 months 206.700 € Consumables and travel funding: 15.000 € Overhead: 38.300 €	260.000 €
DFG	KO 3958/1-1 (N. de Koker, D.C. Rubie, D.J. Frost – 12.10. - 11.13) "Combining experimental and computational approaches to determine high P and T thermal conductivity of $CaGeO_3$ and $MgSiO_3$ perovskite" Positions: E 13, 20 months 114.835 € student assistant (57 h/month) 6 months 4.760 € Consumables and travel funding: 6.000 € Overhead: 22.000 €	147.595 €

DFG	KO 3958/2-1 (N. de Koker, G. Steinle-Neumann –2.11. - 1.14) "Thermal and electrical conductivity of iron at planetary core conditions from ab initio computations" Positions: E 13, 36 months 206.700 € student assistant (79 h/month) 12 months 7.965 € Consumables and travel funding: 9.000 € Publication costs: 2.250 € Overhead: 41.100 €	267.015 €
DFG	Mc 3/16-2 (C.A. McCammon, L.S. Dubrovinsky – 10.09 - 9.12) "High-pressure high-temperature ^{57}Fe Mössbauer spectroscopy in laser-heated diamond anvil cells: Applications for the mineralogy of Earth's lower mantle and core" Positions: student assistant (80 h/month), 36 months 23.760 € Equipment, consumables and travel funding: 30.000 € Overhead: 15.400 €	69.160 €
DFG	Mc 3/17-1 (C.A. McCammon, L.S. Dubrovinsky – 1.10 - 12.12) "Iron-bearing minerals in Earth's lower mantle and coremantle boundary: Development and application of a synchrotron Mössbauer source" Positions: student assistant flat rate 18.000 € Equipment, consumables and travel funding: 51.935 € Overhead: 14.000 €	83.935 €
DFG	OV 110/1-1 (S.V. Ovsyannikov – 07.11 - 06.13) "Structural and electronic properties of sesquioxides at high pressures and temperatures: new forms, new insights and new possible applications" Positions: E 13, 24 months 167.800 € Consumables and travel funding: 14.000 € Overhead: 26.500 €	208.300 €
DFG	RU 1323/2-1 (D.C. Rubie, D.J. Frost, H. Palme – 4.10 - 3.12) "Conditions, timescales and cosmochemical evolution during the early accretion of terrestrial planets" Positions: E 13/2, 24 months 68.900 € Consumables and travel funding: 16.750 € Overhead: 15.100 €	100.750 €
DFG	SA 2042/2-1 (H. Samuel – 10.10 - 9.13) "The effect of continental plates on convective stirring efficiency" Positions: E 13/2, 36 months 103.350 € student assistant (57 h/month) 12 months 9.525 € Consumables and travel funding: 9.464 € Overhead: 21.200 €	143.539 €

DFG	SA 2042/3-1 (H. Samuel – 10.11 - 9.14) "Convective mixing in magma chambers" Positions: ¾ E13, 36 months and funds for student assistants 142.500 € Consumables and travel funding: 7.000 € Publication costs: 2.250 € Overhead: 30.400 €	182.150 €
DFG	STE 1105/6-2 (G. Steinle-Neumann, H.-P. Bunge – 9.10 - 8.13) DFG SPP 1375 (SAMPLE) "Mineralogical and Dynamic Origin of the South African Superplume" Positions: ¾ E13, 36 months 155.025 € Consumables and travel funding: 7.200 €	162.225 €
DFG	STE 1105/8-1 (S. Gilder/LMU München, G. Steinle-Neumann, R. Egli and N. Petersen/LMU München – 2.11 - 1.14) DFG SPP 1488 (PlanetMag) "How pressure influences the magnetic properties of titanomagnetite and iron with implications for magnetic anomalies and core fields" Budget (G. Steinle-Neumann): Positions: ¾ E13, 36 months 155.025 € Travel funding: 9.250 €	BGI funding: 164.275 €
EU	Marie Curie Research Training Network "Crust to core: the fate of subducted material" (2.07 - 1.11) G. Steinle-Neumann (coordinator), G. Fiquet (Paris, France), A.I. Beccero (Sevilla, Spain), S. Buiter (Trondheim, Norway), O. Cadek (Prague, Czech Republic), D. Dobson (London, UK), D. Andrault (Clermont-Ferrand, France), P. Jochym (Krakow, Poland), S. Poli (Milan, Italy) and M.W. Schmidt (Zurich, Switzerland) Total funding: 3,3 Mio € BGI funding:	740.000 €
EU	European Research Council (ERC) Advanced Grant No. 227893 (D.J. Frost – 2.09 - 1.14) "Deep Earth elastic properties and a universal pressure scale DEEP" Positions, equipment, consumables and travel funding maximum EU contribution:	2.079.888 €
Stifter-verband	Stifterverband für die Deutsche Wissenschaft Junior-Professur Geodynamische Modellierung Positions: W1, 72 months 245.200 € Consumables and travel funding: 120.000 €	365.200 €
PROCOPE	Travel funding (C.A. McCammon, L.S. Dubrovinsky) "Multidisciplinary studies of structures in the deep mantle"	1.336 €

2.3 Laboratory and office facilities

The institute occupies an area of

ca. 1300 m^2	laboratory space
ca. 480 m^2	infrastructural areas (machine shops, computer facilities, seminar room, library)
ca. 460 m^2	office space

in a building which was completed in 1994.

2.4 Experimental and analytical equipment

The following major equipment is available at Bayerisches Geoinstitut:

I. High-pressure apparatus
- 6x800 tonne independently acting-anvil press (25 GPa, 3000 K)
- 5000 tonne multianvil press (25 GPa, 3000 K)
- 1200 tonne multianvil press (25 GPa, 3000 K)
- 1000 tonne multianvil press (25 GPa, 3000 K)
- 500 tonne multianvil press (20 GPa, 3000 K)
- 500 tonne press with a deformation DIA apparatus
- 4 piston-cylinder presses (4 GPa, 2100 K)
- Cold-seal vessels (700 MPa, 1100 K, H2O), TZM vessels (300 MPa, 1400 K, gas), rapid-quench device
- Internally-heated autoclave (1 GPa, 1600 K)
- High-pressure gas loading apparatus for DAC

II. Structural and chemical analysis
- 1 X-ray powder diffractometer
- 1 X-ray powder diffractometer with furnace and cryostat
- 2 automated single-crystal X-ray diffractometers
- High-brilliance X-ray system
- Single crystal X-ray diffraction with super-bright source
- 1 Mössbauer spectrometer (1.5 - 1300 K)
- 3 Mössbauer microspectrometers
- 2 FTIR spectrometers with IR microscope
- FEG transmission electron microscope, 200 kV analytical, with EDS and PEELS
- FEG scanning electron microscope with BSE detector, EDS, EBSD and CL
- 3 Micro-Raman spectrometers with ultraviolet and visible lasers
- Tandem-multipass Fabry-Perot interferometer for Brillouin scattering spectroscopy
- JEOL JXA-8200 electron microprobe; fully-automated with 14 crystals, 5 spectrometer configuration, EDX, capability for light elements
- 193 nm Excimer Laser-Ablation ICP-MS
- ICP-AES sequential spectrometer
- Water content determination by Karl-Fischer titration

GC/MS-MS for organic analyses
Confocal 3D surface measurement system

III. *In situ* determination of properties
Diamond anvil cells for powder and single crystal X-ray diffraction, Mössbauer, IR, Raman, optical spectroscopy and electrical resistivity measurements up to at least 100 GPa
Facility for in situ hydrothermal studies in DAC
Externally heated DACs for in situ studies at pressures to 100 GPa and 1200 K
1-atm furnaces to 1950 K, gas mixing to 1600 K, zirconia fO2 probes
1-atm high-temperature creep apparatus
Gigahertz ultrasonic interferometer with interface to resistance-heated diamond-anvil cells
Heating stage for fluid inclusion studies
Impedance/gain-phase analyser for electrical conduc-tivity studies
Apparatus for in situ measurements of thermal diffusivity at high P and T
Laser-heating facility for DAC
Portable laser heating system for DAC

IV. Computational facilities
9 node linux cluster (2x3.0 GHz Xeon Woodcrest Dual Core, 8 Gb memory), InfiniBand
8 node linux cluster (16x2.83 GHz Xeon 5440 Quad Core, 64 Gb memory), InfiniBand
RAID System (6 + 7 Tb storage)

The Geoinstitut is provided with well equipped machine shops, an electronic workshop and sample preparation laboratories. It has also access to the university computer centre.

Next page:
First observation of tight alternation of topotactic diopside and kaersutite lamellae in high-T mantle peridotite generated by a hydrous melt-peridotite interaction in the Balmuccia massif, Italy (Tarantino et al.; in this volume p. 158). (A) Optical micrograph of clinoamphibole lamellae (Amph, dark grey) in clinopyroxene (cpx, pale grey). The inset (B) is a dark-field TEM image, indicating misfit dislocations on the interface as white contrast. The inset (C) is a high resolution TEM image of a misfit dislocation between the two phases.

Nächste Seite:
Erstmalige Beobachtung von engständigen, topotaktischen Verwachsungen von Diopsid und Kaersutit-Lamellen, die durch die Reaktion von wasserhaltiger Schmelze mit Peridotit unter hohen Drücken und Temperaturen im Balmuccia-Massiv/Italien entstanden sind (Tarantino et al.; dieser Jahresbericht S. 158). (A) Dünnschliffaufnahme von Klinoamphibol-Lamellen (Amph, dunkelgrau) in Klinopyroxen (cpx, hellgrau). (B) TEM-Dunkelfeld-Aufnahme zeigt als weißen Kontrast an der Grenzfläche beider Phasen Versetzungen, die die Fehlpassung zwischen beiden Kristallstrukturen ausgleichen. (C) Hochaufgelöste TEM-Aufnahme einer Versetzung zwischen den beiden Phasen.

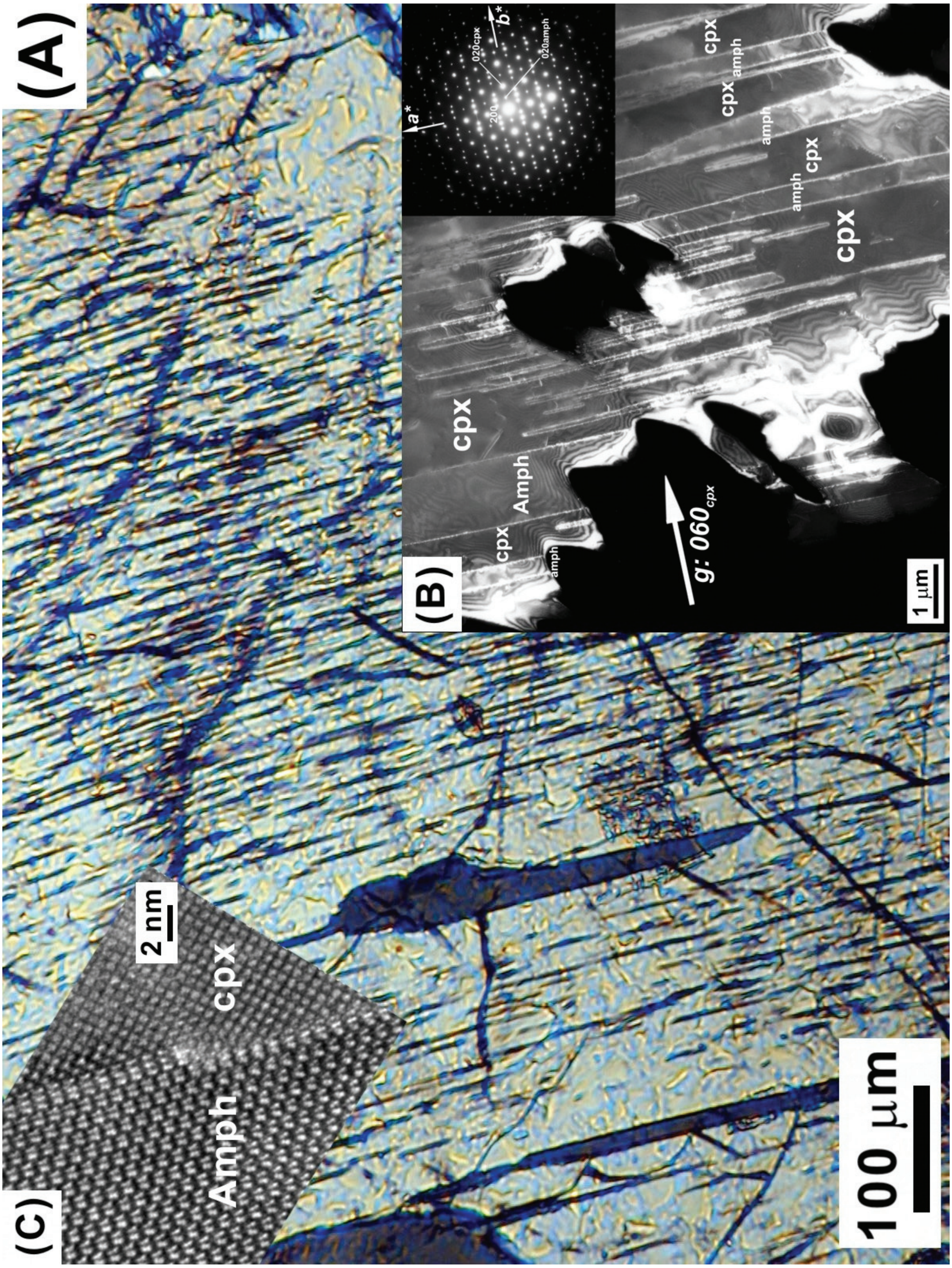
(A)
(B)
cpx
Amph
cpx
amph
g: 060cpx
1 µm
a*
b*
020cpx
200
020amph
cpx
cpxamph
amph
cpx
amph
cpx
(C)
Amph
cpx
2 nm
100 µm

3.1 Struktur und Dynamik der Erde und Planeten

Die Erde und andere planetare Körper sind durch verschiedene chemische und physikalische Prozesse ständigen Veränderungen unterworfen. Diese Prozesse laufen auf sehr unterschiedlichen Zeit- und Längenskalen ab; die planetare Entwicklung verläuft nicht-linear. Die ersten Jahrmillionen sind durch tiefgreifende Ereignisse wie Akkretion und Kernbildung geprägt. Im Vergleich dazu sind die folgenden Milliarden Jahre der Planetenentwicklung kontinuierlicher. Allerdings sind auch diese Vorgänge für die Entwicklung der Planeten wichtig, da sie über einen langen Zeitraum wirken. Das Verständnis der Abfolge dieser Vorgänge kann durch Forschung an physikalischen und thermodynamischen Eigenschaften von planetaren Materialien verbessert werden, indem deren Einfluss auf die Dynamik des Innern der Planeten untersucht wird.

Die ersten zwei Beiträge dieses Kapitels behandeln das früheste Stadium der Planetenentwicklung. Der Ablauf der Akkretion wird in einzelnen Schritten anhand eines Modells zur Kernbildung vorgestellt. Es wird gezeigt, dass die Zusammensetzungen von Erde und Meteoriten nicht übereinstimmt und dass unser Planet nicht aus einem homogenen Ausgangsmaterial entstanden sein kann. Daraus lässt sich ableiten, dass Meteoriten und Planeten in verschiedenen Regionen des Sonnensystems ihren Ursprung haben. Im zweiten Beitrag wird das Absinken tropfenförmiger Eisen-Massen durch den Magmaozean der jungen Erde hindurch numerisch simuliert: Berechnungen ergeben, dass ein Aufbrechen von Eisentropfen in cm-große Fragmente wahrscheinlich ist. Dadurch entstand ein thermodynamisches Gleichgewicht zwischen der Silkatschmelze des Mantels und dem Eisen, das den Erdkern bildet.

Die Kernbildung markiert einen wichtigen Wendepunkt in der Entwicklung erdähnlicher Planeten. Mantel und Kern bilden sich aus und entwickeln sich von nun an unabhängig voneinander. Nur an der Kern-Mantel-Grenze stehen die beiden Reservoire in Kontakt. Die folgenden Beiträge dieses Kapitels befassen sich mit Prozessen, die innerhalb des Mantels und des Kerns sowie an deren gemeinsamer Grenze stattfinden.

Das Eintauchen ozeanischer Platten in den Erdmantel in Subduktionszonen spielt in der thermischen und chemischen Entwicklung des Mantels eine große Rolle. Ein weiterer Beitrag modelliert die thermische Struktur einer abtauchenden Platte, unter Berücksichtigung realistischer physikalischer Eigenschaften des Plattenmaterials. In einem Modell mit variabler Wärmeleitfähigkeit für eine chemisch geschichtete Platte sind die Temperaturen innerhalb der Platte niedriger als in bisher angewandten Modellen mit konstanten Materialeigenschaften. Dies kann zu wichtigen Änderungen in der Eintauchrate absinkender Platten sowie der Temperatur im Erdmantel führen. Im Folgebeitrag werden aus dem entwickelten thermischen Modell Dichte und elastische Struktur der subduzierten Platte berechnet: im Vergleich zu einer einfacheren homogenen Platte führt der geschichtete Fall zu einer deutlich veränderten elastischen Struktur, sowohl bezüglich der Dichte als auch der seismischen Ausbreitungsgeschwindigkeiten.

Die seismische Wellenausbreitung im Erdmantel wird auch durch vorhandene Schmelzen beeinflusst; Zonen mit besonders niedrigen Geschwindigkeiten an der Kern-Mantel-Grenze gelten als Hinweis auf partielle Schmelzen in dieser Region. Deshalb sind Informationen über Schmelzbildung unter hohem Druck, wie sie im fünften Beitrag des Kapitels vorgestellt werden, von großer Bedeutung in der Geophysik. Hier wird die Schmelzbildung im MgO-$MgSiO_3$-System mit einer Hochdruck-Presse (Typ Multianvil) untersucht. Eine Extrapolation der gewonnenen Daten auf den Druck an der Kern-Mantel-Grenze zeigt, dass die Mantel-Temperatur in dieser Region unterhalb des Solidus liegt.

An der Kern-Mantel-Grenze ist möglicherweise auch die Post-Perowskit-Phase stabil, deren Einfluss auf Mantelströmungen im folgenden Beitrag untersucht wird. Eine mechanisch schwächere Post-Perowskit-Phase führt zu größerem Wärmefluss vom Kern zum Mantel, was wiederum zu einer verstärkten Konvektion und effizienterer Vermischung im Erdmantel führt.

Zusätzlich zur Rheologie von Post-Perowskit wird der Wärmefluss vom Erdkern zum Mantel von der Wärmeleitfähigkeit der Minerale im Erdmantel bestimmt. Im siebten Beitrag des Kapitels werden Messungen dieser Transporteigenschaft für Minerale des unteren Erdmantels vorgestellt. Es zeigt sich hierbei, dass die Zugabe von Eisen und Aluminium zu $MgSiO_3$-Perowskit und MgO selbst bei geringen Mengen zu einer starken Abnahme der thermischen Leitfähigkeit führt.

Thermische und elektrische Leitfähigkeiten spielen auch in planetaren Kernen, die hauptsächlich aus Metall bestehen, eine zentrale Rolle. Zwei Beiträge des Kapitels befassen sich mit verwandten Fragestellungen. Die elektrische und thermische Leitfähigkeit von flüssigem Aluminium sowie Eisen unter hohem Druck und hoher Temperatur werden in atomistischen Simulationen untersucht, zum einem um bisherige Näherungen aus der Geophysik zu testen, zum anderen um verlässliche Werte für den Erdkern zu bestimmen. Die neugewonnenen Werte zeigen, dass die Näherungen in bisherigen Extrapolationen, die auf experimentellen Messungen bei niedrigem Druck basieren, nicht zuverlässig sind. Die neu gewonnenen Daten führen zu wesentlich höherer Wärmeleitfähigkeit im Erdkern.

Konvektion in planetaren Kernen kann zur Bildung von globalen Magnetfeldern führen; Vortizität, d. h. lateral geschichtete Flüssigkeitsbewegung, spielt bei der Konvektion im Kern eine wichtige Rolle und kann durch vertikale Dichteunterschiede hervorgerufen werden. Es ist bekannt, dass Vortizität in planetaren Dynamos für die großen Gasplaneten eine zentrale Rolle spielt; für kleinere Planeten wurde sie bisher jedoch nicht untersucht, da Dichteunterschiede aufgrund von Selbst-Kompression hier relativ gering sind. Im letzten Beitrag des Kapitels wird die Bildung von Vortizität in solchen Planeten mit Hilfe dynamischer Simulationen untersucht. Die daraus gewonnenen Beziehungen weisen darauf hin, dass selbst in Kernen terrestrischer Planeten Vortizität eine wichtige Rolle spielt.

3.2 Geochemie und Kosmochemie

Chemische Fraktionierungsprozesse haben in fast allen metamorphen und magmatischen Gesteinen auf der Erde und aus dem Weltall stattgefunden. Bei ausreichend hohen Temperaturen verteilen sich Elemente zwischen verschiedenen Phasen, um sich einem Gleichgewichtszustand zu nähern. Wenn ein chemisches Gleichgewicht erreicht wurde, kann die Zusammensetzung der entstandenen Phasen Informationen über die Bildungsbedingungen dieses Gleichgewichtsereignisses liefern. Falls sich kein Gleichgewicht einstellen konnte, ist kinetische Information gespeichert. Beide Informationstypen liefern Daten über vorherrschende Temperaturen, Drücke, Sauerstofffugazitäten oder die Beteiligung bestimmter chemischer Spezies. In den meisten Fällen sind jedoch experimentelle Daten notwendig, um diese Zusammenhänge zu quantifizieren.

Die ersten drei in diesem Kapitel vorgestellten Forschungsarbeiten versuchen, die Bedingungen im kondensierenden Sonnennebel anhand der Elementverteilung in Mineralen von Meteoriten zu ergründen. Es werden Experimente vorgestellt, mit denen die Sauerstofffugazität aus dem Oxidationszustand von Titan in Mineralen bestimmt werden soll. Die anschließenden Beiträge beschreiben chemische und texturelle Beziehungen in primitiven Enstatit-Chondrit-Meteoriten. Aufgrund der verschiedenartigen Verteilungsmuster von Elementen der Seltenen Erden nimmt man an, dass in derartigen Meteoriten Material enthalten ist, das aus unterschiedlichen Regionen des Sonnennebels stammt; dagegen finden sich in einer weiteren Studie Hinweise auf eine Kondensationsabfolge, die nicht mit entsprechenden thermodynamischen Berechnungen übereinstimmt, was auf kinetischen Einflüssen beruhen könnte. Die darauffolgende experimentelle Studie soll dazu dienen, die Bedingungen zu definieren, bei denen sich bestimmte Elemente zur Zeit der Akkretion im Erdkern bzw. im Erdmantel anreicherten. Ein vielversprechender Ansatz ist die Untersuchung der Verteilung derjenigen Elementpaare, welche im Erdmantel in ähnlich großen relativen Anteilen auftreten. Diejenigen Bedingungen, die unzweifelhaft zu einer Fraktionierung dieser Elemente führen, wenn sich ein Gleichgewicht zwischen Kern und Mantel einstellt, können dann ausgeschlossen werden.

Der vierte und fünfte Beitrag befassen sich mit der Aufschmelzung des tiefen silikatischen Erdmantels, die wahrscheinlich schon bei der Akkretion der Erde auftrat und die immer noch entlang der Kern/Mantel-Grenze andauern mag. Die Untersuchungen zielen auf ein grundlegendes Verständnis des Einflusses von Druck und Temperatur auf den Solidus im Erdmantel. Indem man den Einfluss chemischer Zusammensetzungen auf die Schmelzbildung von einfachen auf komplexere Systeme überträgt, lassen sich thermodynamische Modelle ableiten, die auf alle Bedingungen im Erdmantel extrapoliert werden können. Die beiden nächsten Artikel widmen sich der Verteilung von Eisen und dessen Oxidationszustand im unteren Erdmantel. Einzelne Minerale des unteren Erdmantels lassen sich als seltene Einschlüsse in Diamanten finden. Aufgrund der experimentell gewonnenen Erkenntnisse zur Verteilung und des Oxidationszustands von Eisen als Funktion von Druck, Temperatur und

Sauerstofffugazität ermöglicht diese Art von Einschlüssen eine Abschätzung der im unteren Mantel herrschenden Bedingungen.

Sauerstofffugazitäten, diesmal allerdings im oberen Erdmantel, sind auch Thema der nächsten drei Artikel. In Mantel-Xenolithen lassen sich Sauerstofffugazitäten durch eine Untersuchung der Redox-Gleichgewichte in Mineralvergesellschaftungen bestimmen. Die thermodynamischen Eigenschaften dieser Gleichgewichte müssen kalibriert und überprüft werden. Daher werden Experimente zur Überprüfung derartiger Gleichgewichte an Granat-Peridotit-Gesteinen durchgeführt. Die Ergebnisse lassen den Schluss zu, dass die Basis der archaischen Lithosphäre nicht so reduziert ist wie bisher angenommen wurde. Eine andere Studie dient ersten Versuchen zur Bestimmung der Sauerstofffugazität in einem Eklogitkomplex. Die Resultate zeigen, dass die für eine Diamantbildung notwendige Reduzierung von kohlenstoffhaltigen Mineralen und Schmelzen in Eklogiten bei geringerer Sauerstofffugazität auftritt als in Peridotiten. Die Bestimmung von Sauerstofffugazität und Druckbedingungen bei der Entstehung von Eklogit-Xenolithen ist auch das Ziel der Untersuchungen, die im nächsten Beitrag beschrieben werden, wo eine experimentelle Kalibrierung der Verteilung von Spurenelementen zwischen verschiedenen Mineralphasen als Funktion der vorherrschenden Bedingungen im Mittelpunkt steht.

Der nächste Beitrag beschreibt das Budget und die Entwicklung des Stickstoffhaushalts der Erde. Erste Ergebnisse deuten an, dass die Stickstofflöslichkeit im Erdmantel stark von der Sauerstofffugazität abhängt und mit zunehmend reduzierenden Bedingungen steigt. Daher scheint die Evolution der Erdatmosphäre mit der fO_2-Entwicklung im oberen Erdmantel verknüpft gewesen zu sein; der reduzierte untere Mantel stellt möglicherweise ein großes Stickstoffreservoir dar.

Die Spurenelement-Signatur primitiver Basalte liefert wichtige Erkenntnisse über den Schmelzmechanismus und die Ursprungsregion dieser Magmen. Die Löslichkeiten von Wolfram und Molybdän in Fluiden des Erdmantels können im Vergleich mit Ergebnissen aus früheren Untersuchungen über die Uran- und Thorium-Löslichkeit dazu dienen, die Sauerstofffugazität und die Salinität von Mantelfluiden in der Schmelzregion von Subduktionszonen einzugrenzen.

Weitere Studien befassen sich mit Thermobarometrie, d. h. der Bestimmung des Drucks und der Temperatur, bei denen sich bestimmte Phasen im Gleichgewicht befinden. Die erste davon stellt eine kritische Bewertung des Titan-in-Quarz-Thermobarometers dar, das weithin für magmatische und metamorphe Gesteine und hydrothermale Mineralisationen angewendet wird. Während frühere Kalibrierungen offenbar fehlerhaft waren, stimmt die neue Kalibration relativ gut mit unabhängigen Abschätzungen an natürlichen Gesteinen überein. Weiterhin wird ein neues Sauerstoffbarometer für kieselsäurereiche magmatische Gesteine auf der Basis der Vanadiumverteilung zwischen Magnetit und Silikatschmelze vorgestellt.

Ein weiteres Projekt befasst sich mit dem Einfluss der Sauerstofffugazität auf die Wasserlöslichkeit in Plagioklas-Feldspat. Hier ist die Löslichkeit bei reduzierenden Bedingungen viel höher als bei oxidierenden Bedingungen. Die Ursache dieses Verhaltens konnte noch nicht gänzlich geklärt werden.

Die beiden letzten Beiträge dieses Kapitels behandeln hydrothermale Reaktionen und Verwitterungsprozesse. Es wird eine neuartige Methode zur Abschätzung von Löslichkeiten von Mischkristallen in wässerigen Lösungen bei erhöhten Drücken und Temperaturen präsentiert. Die Abschätzungen beruhen auf der Volumenveränderung die als Folge von Mineralverdrängungsreaktionen in hydrothermalen Experimenten auftritt. Die andere Studie zielt auf das Schicksal der toxischen Elemente Arsen und Chrom in Oberflächengewässern und Sedimenten ab. Hier wird die Absorption dieser Elemente in Partikeln aus Eisenverbindungen untersucht.

3.3 Mineralogie, Kristallchemie und Phasenübergänge

Die Hauptmasse des Erdinneren ist aus kristallinen Phasen aufgebaut; daher haben die Kristallstrukturen von Mineralen sowie ihre Veränderungen in Abhängigkeit von Druck, Temperatur und chemischer Zusammensetzung eine fundamentale Bedeutung für die Geowissenschaften. Am Bayerischen Geoinstitut wurde kürzlich ein Durchbruch erzielt, als es gelang, die Präzision von Röntgenbeugungsmessungen an Einkristallen mit der hohen Signalqualität von Synchrotronquellen der dritten Generation zu kombinieren. In diesem Kapitel wird über die ersten *in situ*-Beugungsuntersuchungen an α-FeOOH-Einkristallen, einschließlich ihrer Zustandsgleichung sowie über die Art des Strukturübergangs bei 4 GPa berichtet. Bei ähnlichen Untersuchungen an Cr_2O_3 konnte jedoch, im Gegensatz zu früheren Darstellungen, zumindest bis 70 GPa kein Phasenübergang identifiziert werden. Silikat-Perowskit steht als Hauptphase des unteren Erdmantels weiterhin im Fokus der Forschung; Einkristall-Untersuchungen in einer laserbeheizten Diamantstempelzelle ergaben eine geringe Kompression bis mindestens 80 GPa und widerlegen so Literaturangaben zu einem Übergang des zweiwertigen Eisens von „high spin“ nach „low spin“ im unteren Erdmantel. Diese Ergebnisse wurden mit einer innovativen Methode der Mössbauer-Spektroskopie in Verbindung mit Synchrotronstrahlung für ein breiteres Zusammensetzungsspektrum von Silikat-Perowskit bestätigt. Die Strukturbestimmung an Einkristallen wurde auch in Experimenten mit laserbeheizten Diamantstempelzellen an einem potentiellem Material des Erdkerns, Fe_7C_3, durchgeführt, wodurch eine genauere Bestimmung der Kristallstruktur und der Kompressibilität dieser Phase bei Erdkern-relevanten Drücken ermöglicht wurde.

Für weitere exakte Kenntnisse über das Erdinnere sind Bestimmungen des Verhaltens der Minerale unter hohen Druck- und Temperaturbedingungen allein nicht ausreichend; auch ein Verständnis der dort ablaufenden Prozesse ist erforderlich. An dieser Stelle wird über die potentielle Fähigkeit von Na-Majorit berichtet, Natrium in das tiefe Erdinnere zu transportieren. Diese Erkenntnisse beruhen auf Stabilitätsuntersuchungen des Minerals unter

Bedingungen des mittleren Erdmantels. Untersuchungen über die Löslichkeit von Aluminium und Silizium in Hochdruckmodifikationen der akzessorisch auftretenden TiO_2-Phase ergeben, dass diese Elemente möglicherweise als Indikator für Hochdruckbedingungen herangezogen werden können. Die Charakterisierung der Oberflächen-Reaktivität von Pyrrhotin ergab, dass in Abhängigkeit von den pH-Bedingungen und der kristallographischen Ausrichtung unterschiedliche Reaktionsraten zu erwarten sind. Eine Studie zur Verteilung der Kationen in Cr-Spinellen macht den Einfluss der Sauerstofffugazität deutlich und stellt Cr-Spinelle als potentielles Sauerstoffbarometer vor. Bei Synthesen von Silikat-Perowskit-Einkristallen wurde der starke Einfluss von Metall/Oxid-Reaktionen auf die Valenz des Eisens in diesen Mineralphasen erkannt.

An Mineralphasen lassen sich nicht nur die Vorgänge ablesen, die im Erdinneren ablaufen; sie speichern auch Hinweise auf extra-terrestrische Prozesse, wie zum Beispiel die, die im frühen solaren Nebel abliefen. Die Bedeutung von Gas/Feststoff-Reaktionen mit Stickstoff wird in einer Untersuchung der Sulphid- und Chromnitrit-Nanophasen in Chondriten vorgeführt. Abschließend liefert eine kristallographische Arbeit über ursprüngliche Metall-Nuggets des Murchison-Meteorits genauere Erkenntnisse zu Prozessen im frühen Solarnebel.

3.4 Physikalische Eigenschaften von Mineralen

Ein zentrales Forschungsziel des Bayerischen Geoinstituts ist stets, unser Wissen über die Eigenschaften von Mineralen und Materie unter den extremen Bedingungen des Erdinneren (Druck, Temperatur, chemische Zusammensetzung) zu vergrößern. Neue Erkenntnisse werden für einen Abgleich mit Messergebnissen aus der Seismik und für geophysikalische Modellierungen des aktuellen chemischen und thermischen Zustands des Erdinneren herangezogen. Informationen über Elastizität, elektrische Leitfähigkeit und magnetische Eigenschaften von Mineralen und Funktionsmaterialien lassen sich gewinnen, indem man einerseits Feststoffe mit bekannter Zusammensetzung und Struktur unter kontrollierten Laborbedingungen synthetisiert und charakterisiert, oder andererseits Computermodellierungen durchführt, mit denen sich häufig experimentelle Einschränkungen überwinden lassen.

Am Bayerischen Geoinstitut wurde unlängst ein neuartiges Analysesystem installiert, das simultane Bestimmungen von Schallgeschwindigkeit und Dichte an Einkristall-Proben bei hohen Drücken und Temperaturen ermöglicht (siehe Jahresbericht 2010). Bestimmungen des kompletten elastischen Tensors von Mineralen bei hohen Drücken sind nicht mehr nur auf kubische Systeme wie Pyrop beschränkt, sondern konnten auch für Minerale aus niedrigeren Symmetrieklassen, wie orthorhombischen $MgSiO_3$-Perowskit, durchgeführt werden. Die Werte aus den Tensor-Bestimmungen wurden mit Ergebnissen aus Ultraschall-Messungen bei Drücken bis 25 GPa und Temperaturen von 1200 K sowie mit präzisen Kompressibilitätswerten von $MgSiO_3$-Perowskit-Einkristallen mit unterschiedlichen Fe^{2+}-, Fe^{3+}- und Al-Anteilen bei Drücken bis 75 GPa kombiniert. Die gemeinsame Betrachtung dieser Daten ermöglicht es, das elastische Verhalten dieses Minerals unter den Bedingungen des unteren Erdmantels stark einzugrenzen.

Untersuchungen der elastischen Eigenschaften von Mineralen beschränkten sich jedoch nicht auf $MgSiO_3$-Perowskit. So wurden insbesondere Dichtefunktionalberechnungen angestellt, um einerseits den Einfluss der chemischen Zusammensetzung auf Stabilität und Elastizität von Fe- und Al-haltigem $MgSiO_3$-Post-Perowskit aufzuklären und um andererseits die seismische Signatur aluminiumführender Phasen in subduzierten Platten der Erdkruste genauer zu bestimmen. Mit Hilfe der Hochtemperatur-Pulverdiffraktometrie wurde die Wärmeausdehnung von Forsterit und Wadsleyit präzise quantifiziert. Die Entwicklung der Kristallstruktur von β-Realgar, einem seltenen Beispiel eines molekularen anorganischen Materials, wurde mit der Einkristall-Röntgendiffraktometrie bei hohem Druck untersucht.

Auch in Bezug auf die Tiefenabhängigkeit der elektrischen Leitfähigkeit konnten neue, wichtige Erkenntnisse erzielt werden. Die profilartige Darstellung der Leitfähigkeit als Funktion der Tiefe lässt Anomalien und Anisotropien in zahlreichen Regionen des ozeanischen und kontinentalen Erdmantels erkennen. Drei Beiträge dieses Kapitels widmen sich den elektrischen Leitfähigkeiten von Mineralen des Erdmantels; der erste beleuchtet Korngrößeneffekte auf die Leitfähigkeit in Klinopyroxen, wodurch eine Basis für die Extrapolation von Labordaten auf natürliche Systeme geschaffen wird. Zwei weitere Beiträge liefern genauere Kenntnisse zum Einfluss von Wasser auf die elektrische Leitfähigkeit von orientierten Olivin-Einkristallen und polykristallinem Wadsleyit.

Die beiden abschließenden Artikel des Kapitels präsentieren Anwendungen von Diamantstempelzellen in Kombination mit der Synchrotron-Mössbauer-Spektroskopie bzw. mit Laserheizung. Mit der ersten Methode wurde das magnetische Verhalten von Fe_7C_3 bis 72 GPa charakterisiert, die zweite ermöglichte die Bestimmung von Phasenstabilität und Schmelzeigenschaften von Kalzit bei bis zu 43 GPa und 3900 K.

3.5 Fluide, Schmelzen und ihre Wechselwirkung mit Mineralen

Fluide und Schmelze spielten eine entscheidende Rolle bei der chemischen Evolution unseres Planeten. Fluide in der Kruste und im oberen Mantel bestehen oft überwiegend aus Wasser. In einer reduzierenden Umgebung enthalten sie darüber hinaus erhebliche Anteile von Wasserstoff (H_2), von dem allgemein angenommen wird, dass er bei den hohen Temperaturen im oberen Mantel vollständig mit Wasser mischbar ist. Neue experimentelle Daten im ersten Beitrag dieses Kapitels zeigen, dass dies nicht der Fall ist. Wasser und Wasserstoff können im oberen Mantel als zwei separate Phasen auftreten. Diese Beobachtung hat wichtige Konsequenzen für die Entwicklung des Redoxzustandes unseres Planeten; sie könnte die schnelle Oxidation des Erdmantels unmittelbar nach der Kernbildung und die Stabilisierung einer reduzierenden frühen Erdatmosphäre erklären.

Aus subduzierten Platten freigesetztes Wasser führt zur Schmelzbildung in Subduktionszonen. Dagegen entstehen Schmelzen an mittelozeanischen Rücken primär aufgrund der adiabatischen Druckentlastung von aufsteigendem Mantelmaterial. Auch bei diesem Prozess spielen Spuren von Wasser jedoch eine wichtige Rolle. Die Auswirkungen kleiner Mengen von Wasser auf die Schmelzbildung im Mantel sind noch wenig verstanden. Zwei Beiträge in diesem Kapitel beschäftigen sich mit diesem Problem. Messungen der Mineral/Schmelze-Verteilungskoeffizienten von Wasser in einem peridotitischen System mit einer iterativen Sandwich-Technik zeigen, dass diese Koeffizienten im oberen Mantel nur wenig vom Druck abhängen. In einer komplementären Untersuchung wurde beobachtet, dass in den Systemen $MgSiO_3$-H_2O und Mg_2SiO_4-H_2O Wasser den Schmelzpunkt stärker herabsetzt als erwartet. Ein weiterer Beitrag in diesem Kapitel untersucht die Kristallisation von Diamant aus Silikat-Carbonat-Schmelzen in der Übergangszone des Mantels.

Chlor und Schwefel spielen eine wichtige Rolle bei der Bildung von Erzlagerstätten in vulkanisch-hydrothermalen Systemen. Die Freisetzung von Schwefel und Halogenen bei explosiven Vulkaneruptionen verändert darüber hinaus die chemische Zusammensetzung der Stratosphäre und kann zu globaler Abkühlung und einer Schädigung der Ozonschicht führen. Eine Raman-spektroskopische Untersuchung in diesem Kapitel zeigt, dass in magmatisch-hydrothermalen Fluiden nicht nur H_2S und SO_2, sondern auch H_2SO_4 stabil sein kann. Sechswertiger Schwefel kann damit bei einer explosiven Eruption direkt in die Stratosphäre injiziert werden. Die Adsorption von Schwefel und Chlor auf vulkanischen Aschen reduziert wahrscheinlich den Einfluss von Vulkaneruptionen auf das Klima. Einige vorläufige Daten zur Adsorption von HCl an rhyolitischen Aschen werden hier präsentiert. Interessanterweise scheint die Adsorption von HCl praktisch irreversible zu sein und dieser Prozess begrenzt daher den Einfluss von Vulkaneruptionen auf die stratosphärische Ozonschicht.

Ein sehr interessanter Beitrag in diesem Kapitel beschäftigt sich mit der Entstehung porphyrischer Kupferlagerstätten. Bisher wurde allgemein angenommen, dass in diesen Systemen Kupfer durch Komplexbildung mit Schwefelwasserstoff sehr stark in einer Gasphase angereichert wird, die im Gleichgewicht mit einer sehr konzentrierten Salzlösung steht. Es konnte nun gezeigt werden, dass die entsprechende Anreicherung von Kupfer in Gas-Einschlüssen in Quarz-Kristallen von natürlichen Erzlagerstätten wahrscheinlich ein Artefakt ist, das auf einer chemischen Veränderung dieser Einschlüsse nach der Bildung beruht. Bisher akzeptierte Modelle zur Entstehung porphyrischer Kupferlagerstätten werden daher revidiert werden müssen.

3.6 Rheologie und Metamorphose

Duktile Deformation und Metamorphose sind oft eng zusammenhängende Prozesse im tiefen Erdinneren. Sie sind beide zu einem großen Teil durch Festkörperdiffusion chemischer Spezies sowie die Präsenz von kristallinen Defekten wie Korn- und Phasengrenzen, Versetzungen und Fehlgitterstellen geprägt. Dadurch sind metamorphe Reaktionen und

Deformation oft miteinander verzahnte Prozesse, die sich gegenseitig induzieren und verstärken. Experimentelle Untersuchungen von Rheologie und Metamorphose zielen daher teilweise auf die Bestimmung ähnlicher mikrostruktureller und/oder chemischer Parameter unter hohen Drücken und Temperaturen. Als solche sind die Beiträge zu diesem Kapitel – obwohl sie einen relativ weiten Bereich von Materialien und (experimentellen oder natürlichen) p,T Bedingungen behandeln – durch den gemeinsamen Ansatz vereint, makroskopische Prozesse wie Deformation oder metamorphe Reaktion durch ihre mikroskopischen Mechanismen zu verstehen.

Die genaue Bestimmung von deviatorischen Spannungen, die eine Probe in einer Vielstempelpresse erfährt, ist wegen des Auftretens von Reibungsverlusten in der Festkörper-Probenzelle technisch immer noch nicht zufriedenstellend gelöst. In Pilotexperimenten hat sich aber jetzt die Verwendung von Piezokristallen als sehr vielversprechend herausgestellt, so dass Spannungsmessungen mit der Auflösung von wenigen MPa möglich werden. Mithilfe der neuen MAVO-Presse, bei der sechs unabhängig voneinander verfahrbare Stempel würfelförmig angeordnet sind, ist der Druckbereich für kontrollierte Deformationsexperimente signifikant erweitert worden. Durch die Verwendung sogenannter Komposit-Stempel, die aus dem eigentlichen Wolframcarbid-Stempel und einer Stahlfassung zusammengesetzt sind, können jetzt Experimente an Mineralen der Übergangszone des Mantels (z. B. Wadsleyit oder Ringwoodit) routinemäßig durchgeführt werden. Von besonderem Interesse sind dabei die Übergangstexturen, d. h. der Einfluss des Phasenübergangs auf das Verformungsverhalten und umgekehrt.

Mit der D-DIA Vielstempelpresse wurde das rheologische und mikrostrukturelle Verhalten von Gemischen aus Olivin, Orthopyroxen und Schmelze im oberen Erdmantel untersucht. Dabei wurde sowohl der starke Einfluss von Deformation auf die mikrostrukturelle Verteilung der Schmelze festgestellt als auch eine signifikante Änderung der Deformationstextur der festen Phasen durch Reaktion mit der Schmelze. Die Bestimmung von intrakristallinen Gleitsystemen in Hochdruckmineralphasen ist wichtig für das Verständnis der Rheologie dieser Phasen und ihrer Rolle bei der Ausbildung von anisotropen Gefügen durch Versetzungsgleiten. Die sogenannte Phase A kann potentiell Wasser in Subduktionszonen bis in den tiefen Erdmantel transportieren. Deformationsexperimente haben gezeigt, dass ihre Versetzungsstruktur bei plastischer Deformation relativ starke physikalische Gesteinsanisotropien erzeugt.

Die Schnelligkeit plastischer Verformung durch intrakristalline Prozesse oder der Fortschritt metamorpher Reaktionen wird in erster Näherung durch die Diffusionsrate der langsamsten chemischen Spezies bestimmt. Neue Daten deuten darauf hin, dass die Selbstdiffusion von Silizium in Olivin offenbar wesentlich schneller abläuft als bisher angenommen. Damit klärt sich auch der Widerspruch, der bisher zwischen gemessenen Diffusionsraten und solchen bestand, die aus Deformationsexperimenten abgleitet wurden. Experimentell unter hohen Drücken und Temperaturen gemessene Diffusionsraten der Elemente Ca, Mg und Fe in

Granaten mit majoritischer Zusammensetzung – wie sie für die hohen Drücke des tieferen Erdmantels erwartet wird – sind extrem niedrig. Sie können daher selbst auf der Zeitskala der Erdgeschichte kaum zur chemischen Homogenisierung des Erdmantels beitragen.

In Untersuchungen von natürlichen Proben wurden zwei Aspekte der Interaktion von Deformation und Diffusion näher analysiert. Die mylonitischen Gesteine des *Moresby Seamount Detachments* im westlichen Pazifik nahe Papua Neu Guinea sind durch ein komplexes Wechselspiel zwischen duktilen und bruchhaften Prozessen charakterisiert. Diffusionskriechen in Kombination mit Korngrenzgleitung des feinkörnigen mafischen Materials wurde immer wieder durch die bruchhafte Bildung von Kalzit- und Quarzadern unter hohen Fluiddrücken unterbrochen, die im Folgenden in die duktile mafische Matrix eingearbeitet wurden. In den Duniten des Balmuccia Massivs in den Südalpen führte die Reaktion mit Schmelzen aus benachbarten Gabbros zu engständigen Verwachsungen aus stöchiometrischem Kaersutit and Diopsid mit einer topotaktischen kristallographischen Orientierungsbeziehung. Inwieweit diese Verwachsungen primär sind oder sich erst später als Entmischungen bildeten, ist noch ungeklärt und wird gegenwärtig untersucht.

3.7 Materialwissenschaften

Hochdruckuntersuchungen in der Materialwissenschaft stützen sich auf dieselbe experimentelle Methodik und Verfahren für *in situ*-Untersuchungen unter extremen Bedingungen wie in der Mineralphysik und Petrologie. Das Bayerische Geoinstitut ermöglicht aufgrund seiner einzigartigen technischen Hochdruckausstattung und seiner *in situ*-Technologie anspruchsvolle und hochentwickelte Forschungsarbeiten über physikalische und chemische Eigenschaften von Materialien bei hohen Drücken. Es werden im Folgenden Untersuchungen an Feststoffen unterschiedlicher Kategorien (Elemente, Oxide, Carbide, Karbonate, Molybdate) vorgestellt.

Seit langem gilt Bor als zukunftsträchtiges Material für zahlreiche Anwendungen. Eine eindrucksvolle Kombination verschiedener Eigenschaften weist α-Bor auf – es ist ein Halbleiter mit direkter Bandlücke und hoher Härte, es ist thermisch und chemisch sehr resistent und ziemlich leicht. Aufgrund dieser Eigenschaften bietet sich α-B als ein Material erster Wahl für zahlreiche industrielle Halbleiteranwendungen an, besonders als aktives Element in Solarzellen mit einem hohen Wirkungsgrad bei der Umwandlung von Sonnenlicht in elektrische Energie. Bis heute scheiterte eine kommerzielle Forschung und die Entwicklung für potentielle Anwendungen von α-B an einer fehlenden Methode zur Synthese von Einkristallen. Das jetzt am Bayerischen Geoinstitut erarbeitete Phasendiagramm verdeutlicht, dass es sich bei α-B nicht nur um eine thermodynamisch über einen großen Druck- und Temperaturbereich stabile Phase handelt; das Material lässt sich auch in großem Maßstab produzieren und zwar unter Bedingungen, die der modernen Industrie leicht zugänglich sind (zum Beispiel ähnlich den Bedingungen zur Produktion synthetischer Diamanten).

Ein ikosaedrisches (zwanzigflächiges), quasi-molekulares Cluster aus 12 Boratomen (B_{12}) stellt den Baustein aller Allotrope sowohl des Bors als auch zahlreicher Bor-reicher Feststoffe dar. Die materialwissenschaftlich interessanten Eigenschaften von Bor-Polymorphen und Bor-reichen Verbindungen (sehr große chemische Beständigkeit mit hoher Härte und geringer Kompressibilität) gelten jedoch für molekulare Feststoffe als sehr ungewöhnlich. Zur Klärung dieses Phänomens ist eine genaue Analyse der Art der chemischen Bindungen zwischen Bor-Atomen erforderlich; in Bezug auf die Hochdruckmodifikation γ-B wurden diese Untersuchungen am Geoinstitut erfolgreich durchgeführt. Die topologische Analyse der Verteilung der Elektronendichte verdeutlicht, dass benachbarte B_{12}-Cluster durch einzigartige ein-Elektron-zwei-Zentren-Bindungen verbunden sind. Eine polar-kovalente zwei-Elektronen-drei-Zentren-Bindung zwischen einem Atompaar eines ikosahedrischen Clusters und einem Atom der B_2-Paare erklärt die beobachtete Ladungstrennung in γ-B.

BH_3NH_3 scheint aufgrund seines bemerkenswert hohen gravimetrischen und volumetrischen Wasserstoffgehalts ein vielversprechender Kandidat für die Speicherung von Wasserstoff zu sein. Untersuchungen von BH_3NH_3 bei hohen Drücken sind notwendig, um mehr Informationen über Stabilität und mögliche Bindungsänderungen zu erhalten sowie hinsichtlich der Synthese dichter Modifikationen mit einem noch höheren volumetrischen Wasserstoffgehalt. Mit Hilfe der Ramanspektroskopie ließen sich bei Drücken bis 64 GPa mindestens drei Phasenübergänge erkennen. Weiterhin konnte gezeigt werden, dass BH_3NH_3 bei Kompression unter Umgebungstemperaturen chemisch intakt bleibt und in der Lage ist, eine zweite harmonische Schwingung des Laserlichts bis mindestens 130 GPa zu erzeugen. Somit konnte bestätigt werden, dass BH_3NH_3 keine zentrosymmetrischen Strukturen im untersuchten Druckbereich annimmt, unabhängig von strukturellen Veränderungen.

Multiferroide Materialien stehen im Zentrum intensiver Untersuchungen in der Festkörper-Physik und -Chemie. Multiferroide verdeutlichen die Koppelung elektrischer und magnetischer Eigenschaften; sie haben eine große Bedeutung für die Entwicklung neuer elektronischer Bauteile, in denen Magnetismus durch ein elektrisches Feld beeinflusst wird. Kürzlich wurde eine neue Art von Multiferroiden entdeckt, in denen die Symmetrieanordnung geordneter magnetischer Momente die Inversionssymmetrie aufbricht und Ferro-Elektrizität erlaubt. Die $RbFe(MoO_4)_2$-Komponente stellt ein einzigartiges Beispiel derartiger Materialien dar, die multi-ferroische Phänomene in Kombination mit geometrisch frustriertem Magnetismus in einem dreieckigen Gitter zeigt. Hochdruck-Untersuchungen von $RbFe(MoO_4)_2$ zeigen ein komplexes Verhalten dieses Materials und deuten die Möglichkeit an, eine neue Modifikation unter höheren Drücken zu synthetisieren.

3.8 Methodische Entwicklungen

Neue Entwicklungen in experimenteller, analytischer und numerischer Methodik bilden das Rückgrat jeglicher wissenschaftlicher Forschung. Die Bedeutung dieser Neuentwicklungen kann nicht stark genug betont werden. Das Bayerische Geoinstitut weist auf diesem Gebiet eine lange Tradition mit höchsten Standards nach; zahlreiche Innovationen des Instituts wurden von Arbeitsgruppen weltweit übernommen. Entwurf, Anfertigung und Testen neuer experimenteller, analytischer und numerischer Methoden stellen eine zeitaufwendige Herausforderung dar und erfordern intensive technische Unterstützung, die am Bayerischen Geoinstitut vorhanden ist.

Das Berichtsjahr 2011 führt zu vielfältigen neuen Entwicklungen bei den Multianvil- und Diamantstempel-Pressen sowie bei numerischen Simulationen. Die Installation der Ende 2009 beschafften Multianvil-Presse (Typ: 6 Stempel) wurde 2011 abgeschlossen; die neue Apparatur wird jetzt speziell für wissenschaftliche Verformungsexperimente genutzt. Eine weitere ähnliche Großpresse wird 2012 am Forschungsreaktor München (FRM II) aufgebaut werden, um dort Neutronenbeugungs-Experimente bei hohen Drücken durchzuführen. Im Berichtsjahr wurde die Strahlführung des Neutronenstrahls untersucht, um die Strahlqualität für Beugungsmessungen und Bildgebung zu optimieren. Weitere technische Fortschritte wurden auf dem Gebiet der Schallgeschwindigkeitsmessungen an Mineralen des Erdmantels bei hohem Druck erreicht.

Auch beim Aufbau des institutseigenen Systems für Brillouin-Streuung für Experimente mit Diamantstempel-Zellen konnten weitere Erfolge erzielt werden. Das Aufheizen von Diamantstempel-Zellen wurde auch für optische Spektroskopiemessungen am BGI verbessert. Für den Messstand an der Europäischen Synchrotroneinrichtung in Grenoble (ESRF) wurde das Heizsystem und das dazugehörige Computerprogramm für Mössbauer-Experimente geschaffen.

Die Hauptentwicklungen auf dem Gebiet der geodynamischen Modellierung zielen auf eine Beschleunigung der Berechnungen durch eine Parallelisierung in der Zeit-Domäne. Andere Verbesserungen betreffen die exakte Simulation von Advektionsprozessen nach einem Modell, das auf der Wellengleichung beruht. Berechnungen von Konvektionsprozessen wurden mithilfe der Schur-Komplement-Methode verbessert.

3.1 Earth and Planetary Structure and Dynamics

The Earth and the other planetary bodies are constantly reshaped by a great variety of physical and chemical processes interacting at very different scales in space and time. As a consequence, planetary evolution is far from being linear. The first few millions of years of planetary evolution are punctuated by major events such as accretion processes and core formation. Compared to these dramatic events the following billions of years of planetary evolution appear much more steady. Nevertheless these subsequent changes remain important, as they occur over a significantly larger period of time. Understanding such a complex progression can be achieved through the study of the physical and thermodynamic properties of planetary material and by testing their dynamic influences.

The two opening contributions focus on the earliest stage of planetary evolution. One investigates the accretion conditions for the Earth using a model of multistage core formation. It is shown that the Earth cannot result from the accretion of homogeneous material. In addition, contrary to what is commonly assumed, the study concludes that the Earth cannot be accreted from material whose composition corresponds to that of the meteorite record. This implies that meteorites and planets are formed in distinct regions of the solar system. The second contribution investigates, by means of numerical modeling and analytical theory, the conditions for iron diapir breakup in silicate terrestrial magma oceans, a plausible core formation scenario. The results show that rapid fragmentation of iron diapirs down to centimeter-sized droplets is very likely, which suggests that metal-silicate equilibration of even large iron cores plunging into a silicate magma ocean is rapidly achieved.

The segregation of iron in terrestrial planets marks an important turn in planetary evolution as the resulting silicate mantle and iron cores evolve separately, only interacting at the core-mantle boundary. The following contributions aim to improve our understanding of the processes occurring within these major planetary envelopes as well as those acting along their common boundary.

Slab recycling plays a fundamental role in the Earth’s mantle’s thermo-chemical evolution. The third report investigates the thermal structure of a composite slab, using a kinematic model coupled to thermodynamic modeling of physical properties. Accounting for variable thermal diffusivity within a composite subducting slab generally yields lower temperatures. This may have a significant effect on slab dynamics and the thermal state of Earth’s mantle. Using the same kinematic and thermodynamic framework, the following contribution derives the elastic structure of down-going slabs. Compared to simplified homogeneous slabs, realistic composite slabs exhibit significantly different seismic signatures, with more pronounced variations in both density and seismic body wave speeds across the slab.

Seismic wave propagation within the Earth’s mantle may also be affected by the presence of melt. This has been proposed, for example, as a cause for the ultra low velocity zones in the lowermost mantle. A good understanding of melting relationships within the Earth’s mantle is therefore required to interpret such seismic observations. The next study presents the results of melting experiments in the $MgO-MgSiO_3$ system performed at high pressure in a multi-anvil press. Extrapolating these results to core-mantle boundary conditions suggests that temperatures in this region are below the Earth's mantle solidus.

The core-mantle boundary region is also the possible location for the presence of the post-perovskite phase. One contribution investigates the dynamical influence of changes in strength between the perovskite and post-perovskite phase that have been recently suggested. It is shown that the presence of weak post-perovskite enhances core-mantle heat flux, leading to an increase in both convective vigour and mantle stirring efficiency, possibly by several orders of magnitude.

In addition to the strength of post-perovskite, core-mantle heat flux is governed by the conductivity of mantle minerals. One contribution determines this transport property via a Debye extrapolation of low pressure values for deep mantle phases with different iron and aluminium content. The results suggest that both changes in composition and mineral phase proportions induced by temperature variations can result in significant changes in thermal conductivities.

Transport properties also play a fundamental role in the evolution of planetary cores composed mostly of metal. One report calculates the thermal and electric conductivity of compressed aluminum liquid using first-principles to test previous assumptions on their behavior and relation at high pressure. The results suggest that existing estimates of thermal conductivity in the Earth's core may be underestimated by up to a factor of three. The following contribution investigates the electrical resistivity and the thermal conductivity of liquid iron at high (P,T) conditions, using first-principles. The obtained new values of conductivity and resistivity are significantly different from accepted values obtained by extrapolation of experimental results to high pressure conditions.

Planetary core dynamics may result in the generation of a magnetic field. In this context, density variation due to compressibility in rotating fluid can induce vorticity. The later is an essential ingredient to the generation of a magnetic field in planetary cores. While this effect is known to be important in large bodies such as giant planets it has never been considered for Earth-sized planets for which density variations are much smaller. The closing contribution investigates dynamically this hypothesis using numerical simulations in the equatorial plane. The obtained scaling laws indicate that even small Earth-sized planets can fall in a regime where vorticity can be generated by density stratification.

a. *Composition of the Earth and the characteristics of early accreting material in the inner solar system (D.C. Rubie and D.J. Frost, in collaboration with H. Palme/Frankfurt)*

The composition of the Earth's mantle, as deduced form upper mantle rocks, is basically chondritic, but differs in detail from existing chondritic meteorite compositions.

As shown in Fig. 3.1-1 the Earth’s mantle is higher in Mg/Si and Al/Si than carbonaceous chondrites. Assuming 10 wt.% of a light element in the core together with the observed FeO content of the Earth’s mantle results in a Fe/Mg ratio of bulk Earth about 10 % above the CI-ratio. The extent of depletion of volatile elements in the Earth exceeds that of CV chondrites, but the depletion sequence follows a similar trend. Bulk Earth is thus compositionally different from any type of chondritic meteorite. However, a comparison of the composition of the bulk Earth with chondrite compositions requires the effects of (1) core formation, (2) heterogeneous accretion and (3) fractionation during accretion to be considered.

The early differentiation of the Earth involved the segregation of metal from silicate to form the mantle and core. We have formulated a model of multistage core formation that is based on a simplified accretion scenario. The Earth accretes through collisions with differentiated bodies that are approximately 0.1 × Earth’s mass at the time of impact. After each collision, the impactor’s core partially or completely equilibrates in a magma ocean before merging with the Earth’s proto-core. The resulting core composition in our model is: ~ 5 wt.% Ni, ~ 8 wt.% Si, ~ 2 wt.% S and ~ 0.5 wt.% O. With 8 % Si in the core the bulk Earth Mg/Si and Al/Si ratios would be within the range of CV-meteorites (Fig. 3.1-1).

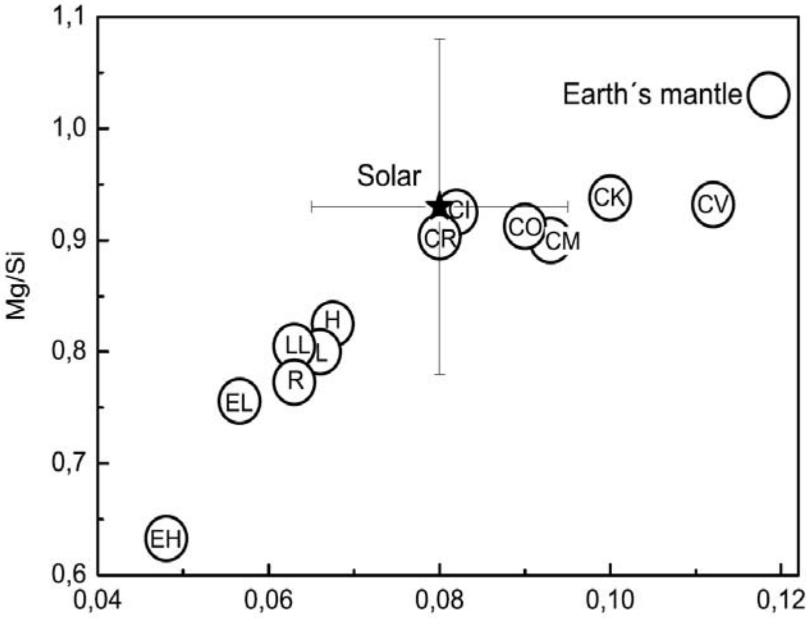

Fig. 3.1-1: Major element compositions of the Earth’s mantle and chondritic meteorites

The multistage core formation model gives poor results when the bulk composition of accreting material remains constant (homogeneous accretion). A single composition for all accreting embryos cannot reproduce the current mantle composition of the Earth. In contrast, heterogeneous accretion produces excellent results for all non-volatile elements. The best fit is obtained when the initial 60-70 % of Earth's mass accretes from material that was highly reduced (> 99 % of Fe initially present as metal) and the final 30-40 % from material that was more oxidized (~ 60 % of Fe initially present as metal). The reduced composition is considered to represent the average composition of material that accreted early in the inner regions of the solar nebula where temperatures were high, whereas the more oxidized material originated further out. The model is thus consistent with radial mixing in the solar system. However, enstatite chondrites do not provide a good fit for the reduced component because they are rich in volatile elements. A volatile-poor enstatite chondrite composition would require a comparatively volatile element enriched oxidized component, that would still be within the range of existing chondrite compositions, *i.e.*, volatile elements would still be depleted in this component. However, a volatile-free enstatite composition with very low Mg/Si and Al/Si ratios (Fig. 3.1-1) would also require an oxidized component with much higher Mg/Si and Al/Si ratios than are known from chondritic meteorites to compensate for the low Mg/Si and Al/Si of the reduced component. The excess Fe in the bulk Earth can be explained by collisional erosion which removes early formed crusts from embryos by collisions.

In conclusion, in contrast to common assumptions, the major part of the Earth cannot be made of material that is represented in the meteorite record, in agreement with stable isotope systematics. Thus meteorites formed in separated, local areas unrelated to the major planetary formation regions.

b. *Conditions and timing for metal diapir breakup and equilibration in terrestrial magma oceans (H. Samuel)*

Understanding the conditions for iron diapir breakup in a magma ocean context is of prime importance for the interpretation of cosmochemical chronometers, and to determine the heat distribution within a young terrestrial planet, which influences the subsequent long-term planetary thermal evolution.

Although this scenario has been previously investigated using conceptual models, numerical modeling, laboratory experiments, and theoretical calculations, no general agreement has clearly emerged. Some studies argue for the rapid breakup of metal diapir down to cm- or mm-sized droplets, while other investigations conclude that despite turbulent processes large diapirs (*i.e.*, of radius > 10 km) can survive complete erosion and preserve most of their initial volume as they reach the bottom of a ~ 1000 km thick magma ocean, therefore leading to metal-silicate disequilibrium.

To clarify the discrepancies and the differences among such studies I have conducted a series of simulations and theoretical calculations to derive the conditions and the timing for the breakup of metal diapirs of any size, sinking through a silicate magma ocean, with a large range of plausible viscosity values.

Scaling analysis combined with numerical experiments was used to derive general and more precise criteria than the one presented in last year’s report for diapir breakup as a function of the Webber and Reynolds numbers (based on the terminal sinking velocity v^{∞}):

$We^{\infty} > 2\,10^{4}(\mathrm{Re}^{\infty^{-1}} - 1.3\,10^{-2}\,\mathrm{Re}^{\infty^{-1/3}})$ for the intermediate regime (*Re* = 0.5-500),
$We^{\infty} > 7$ for the Newton regime (*Re* > 500).

Using this criterion, I have re-evaluated the sizes of stable iron bodies sinking through a silicate magma ocean. These new estimates yield stable iron droplet radii lower than 0.2 meters for plausible magma ocean viscosities (Fig. 3.1-2).

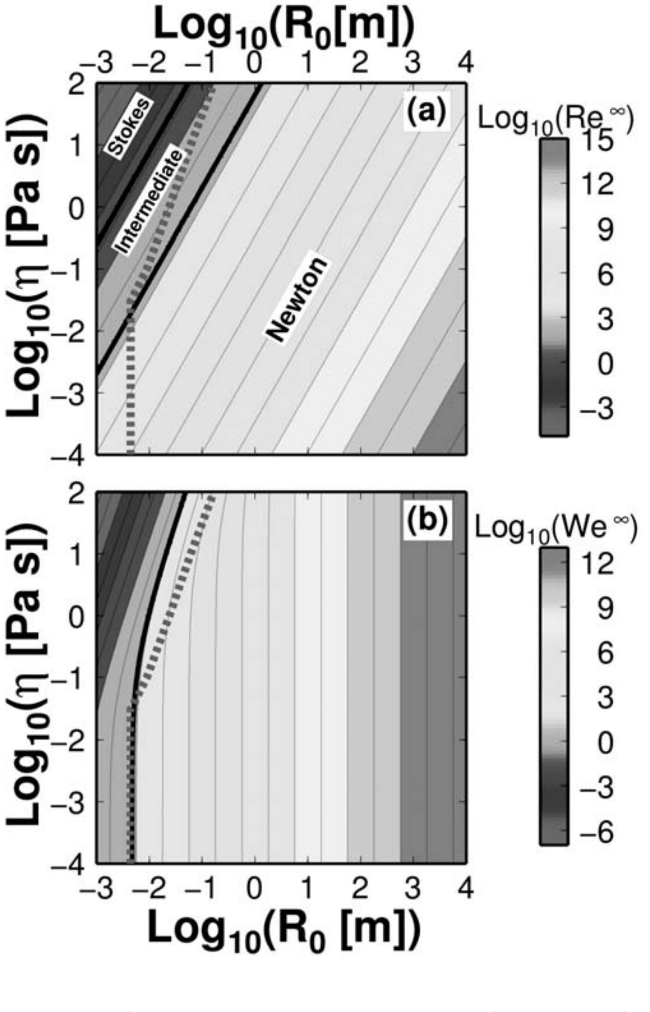

Fig. 3.1-2: Plausible range of governing parameters as a function of diapir radius R_0 and magma ocean viscosity η. Top: Reynolds number with the boundaries of the three dynamic regimes (Stokes, intermediate and Netwon) indicated by the thick lines. Bottom: Webber number with the thick black curve indicating $We^{\infty} = 1$. The dotted curves indicate the stable radius according to the criteria defined in the text.

To complement these estimates I have investigated the timing for unstable diapir breakup, using numerical experiments and analytical theory. The numerical experiments reveal the upstream formation of a stagnation point flow that favors diapir deformation at a rate proportional to the diapir sinking velocity. This behaviour is also observed in laboratory experiments carried out in the turbulent regime (see Fig. 3.1-3). In the context of a magma ocean, this implies that iron diapirs larger than the maximum stable size breakup within distances comparable to their initial radius into smaller sized bodies. This breakup process is repeated until the new iron bodies reach their stable sizes.

Finally, using a simple equilibration model, I show that with such small stable diapir sizes, equilibration is achieved before the iron bodies reach the bottom of the magma ocean. Even for a large value of η=100 Pa s for magma ocean viscosity an equilibration of > 99 % is reached within a sinking distance of 2 km. These results contrast in part with recent studies, where the assumption that iron diapirs systematically sink without breaking up was made. However, the present study shows that such an assumption is reasonable only if the initial iron diapir sizes are larger than the thickness of a magma ocean (*e.g.*, as would be appropriate for a giant impact). Otherwise, for diapir sizes smaller than the thickness of a magma ocean, rapid breakup and metal-silicate equilibration seem inescapable.

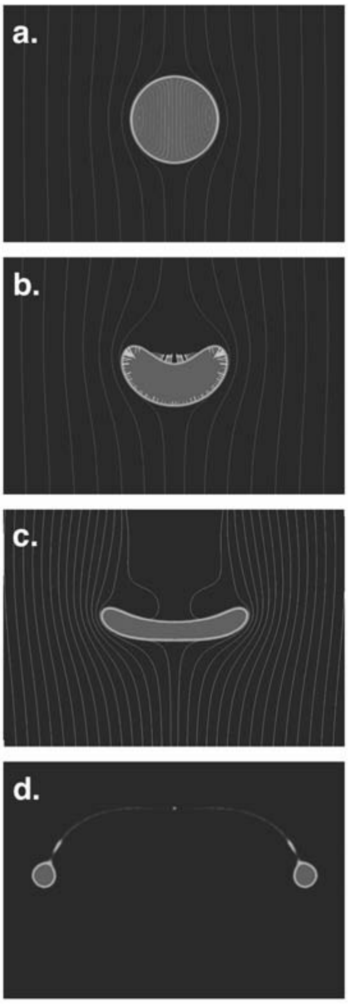

Fig. 3.1-3: Result for a numerical simulation in the intermediate regime. A typical breakup sequence of an unstable iron diapir initially at rest sinking though a silicate liquid magma ocean displayed in four snapshots in time. Internal and external motions are shown by streamlines in snapshot (a-c). The surface tension vector is displayed in snapshot b.

c. *Kinematic model of subducting slab with variable thermal properties (P. Maierová and G. Steinle-Neumann, in collaboration with H. Čížková and O. Čadek/Prague)*

Subduction is a strongly non-linear system and even small changes in parameters can influence its behaviour significantly. This has been shown in various numerical studies where the influence of rheology, phase transitions and model setup on the subduction dynamics have been examined. However, most of them assume constant or only depth-dependent thermal properties (thermal diffusivity and conductivity). At the same time, data from laboratory measurements indicate that thermal properties are strongly temperature- and pressure-dependent and vary considerably among different mantle phases. According to both experiments and first-principles computations, thermal diffusivity and conductivity generally decrease with temperature and increase with pressure, and the variations in the subducting slab and surrounding mantle can be as large as 50 %.

In order to implement variable thermal properties in a numerical model of subduction, we have compiled analytical relationships that approximate pressure and temperature dependence of thermal diffusivity for major mineral phases of the upper mantle and transition zone: olivine (ol), wadsleyite (wa), ringwoodite (ri), majorite-garnet (mj), clinopyroxenes (cpx) and stishovite (st). We restrict the compositional model to the $MgO-SiO_2$ system and propose simplified petrological models of the different slab components and the ambient mantle: basalt (92 % cpx/mj + 8 % st), depleted harzburgite (80 % ol/wa/ri + 20 % cpx/mj) and pyrolite mantle (60 %atomic ol/wa/ri + 40 %atomic cpx/mj). For these phase assemblages we compute thermal diffusivity using the Hashin-Shtrikman bounds and implement the resulting thermal properties, along with density and heat capacity from thermodynamic mantle models, into a simple kinematic model of oceanic subduction.

In the model, the geometry of the subducting plate is defined and does not change with time. A uniform velocity of 5 cm/yr is prescribed along the upper surface of the subducting slab (100 Ma old plate). We study two types of models: 1) *phb*, where the subducting and overriding plates have a 10 km thick basaltic layer on top, followed by 40 km harzburgite and pyrolite below, and 2) a simpler *p* model where the different lithology of the slab is neglected and the slab is assumed to be pyrolitic. The general conductivity distribution (Figs. 3.1-4A and 3.1-4C) is similar in these two models. Since the subducting slab is colder than the surrounding mantle, it has higher thermal conductivity. The conductivity varies from less than 2.5 $Wm^{-1}K^{-1}$ in the mantle (at 100 to 200 km depth, light shades in Figs. 3.1-4A and 3.1-4C) to more than 5 $Wm^{-1}K^{-1}$ in the slab. From the upper mantle to the transition zone, we observe an increase of conductivity due to ol-wa transition, while the wa-ri transition (~ 550 km depth) is invisible. In the model *phb*, the presence of cpx results in a highly conductive basaltic layer with conductivity of up to 7 $Wm^{-1}K^{-1}$, visible as the narrow dark band in the shallow part of the slab in Fig. 3.1-4A. In the model *p* (Fig. 3.1-4C), the highly conductive band is missing and the conductivity of the slab in the transition zone is lower than in the *phb* model.

The effect of variable thermal conductivity and diffusivity on temperature is demonstrated in Figs. 3.1-4B and 3.1-4D where the temperature difference between the model with variable thermal diffusivity and the one with constant diffusivity of 10^{-6} mm^2s^{-1} is plotted. Variable thermal diffusivity leads to colder subducting and overriding plates and warmer asthenosphere and areas along the slab. In the shallow part of the subducting slab, we mostly observe the effect of faster cooling of the plate prior to subduction. This effect is more pronounced in model *phb* (Fig. 3.1-4B), where the temperature difference is as large as -125 K in the shallow parts of the subducting plate and -80 K in transition zone, while in the *p* model (Fig. 3.1-4D), the maximum difference within the slab is about -80 K. In both models, the asthenosphere below the subducting plate is warmer by about 30 K and the temperature difference in and just above the mantle wedge reaches 60 K. The temperature dependence of thermal diffusivity (and conductivity) thus leads to more efficient thermal insulation of the slab and pronounce the temperature anomaly induced by the subducting slab.

We can also compare the temperature field in the *phb* model and in the *p* model and estimate the effect of basalt and harzburgite in the subducting slab. In Figure 3.1-4E we see that the temperature in the model with layered structure of the slab is generally lower than in the *p* model. However, this difference is rather small, mostly less than 50 K, and reaches its maximum in the shallow portion of the slab.

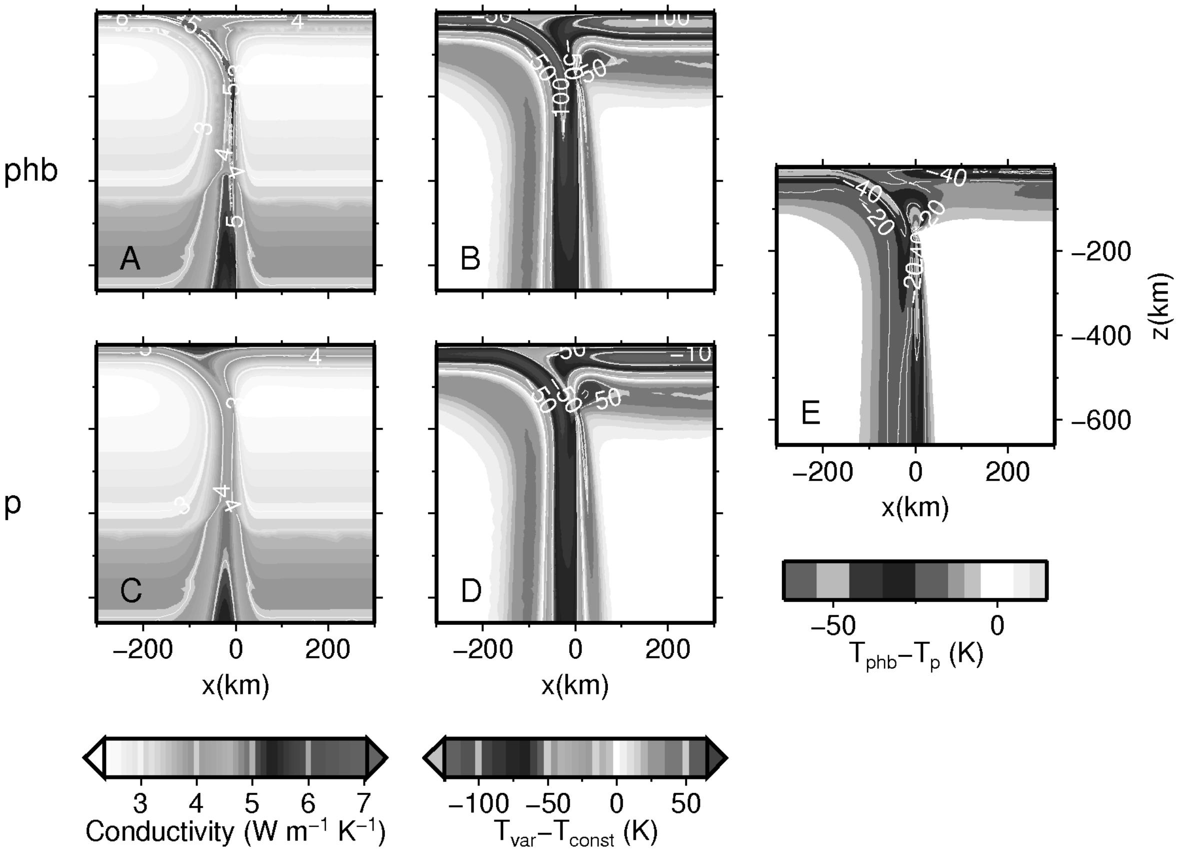

Fig. 3.1-4: Conductivity of a layered (*phb*, upper row) and a homogeneous (*p*, lower row) slab model (left panels). Temperature differences with respect to a model with constant diffusivity (middle panels). Panel E shows the difference of temperature in models *phb* and *p*.

In our kinematic model, the effect on temperature is typically less than 100 K, which is about 10 % of the total temperature anomaly of the slab with respect to the mantle. In a fully dynamic model we expect this effect to play a significant role, as the temperature in the slab is linked to its buoyancy and thus velocity of subduction, and will induce a positive feedback on the slab deformation through non-linear stress-dependent rheology.

d. *Synthetic elastic structure of a subduction system (T. Chust, G. Steinle-Neumann and P. Maierová)*

Using a thermodynamic model for the equation of state and shear modulus for minerals at high pressure and temperature, the temperature fields from the kinematic simulations of subduction presented in the previous section can be converted to density and elastic wave velocity fields. Figure 3.1-5 shows the results for the representative models of a differentiated (*phb*) and homogeneous slab (*p*) as introduced in the previous section of the annual report.

The sinking slab and its immediate surroundings are denser than the ambient mantle in both models. While the slab manifests itself as a coherent feature in the *phb* model through the basaltic layer, it only appears as a diffuse high density region in the pyrolitic model *p*. The basalt layer in *phb* has a marked density contrast to the pyrolite background due to its distinct bulk chemistry and resulting different mineral phase assemblages. For example, at 350 km depth the most abundant phases in the ambient mantle are olivine and majorite, with a density of the assemblage of ~ 3.46 g/cm^3. In the harzburgite layer of the slab the same phases are stable, but olivine is more abundant due to the depletion in SiO_2, and the density of ~ 3.49 g/cm^3 is higher by 1 % only: the compositional change alone would lead to a decrease in density of 1 %, but the lower temperature in the slab region overcompensates for this effect. In the basalt layer of the slab majorite, pyroxene and stishovite are stable, and the density of ~ 3.71 g/cm^3 is higher by ~ 7 % than that for the ambient mantle. The behaviour of the density field matches well with that found in previous studies using more complex mineralogy but a similar model setup.

At the boundary between the upper mantle and the transition zone the phase change from olivine to wadsleyite occurs at different depths in the ambient mantle and the harzburgite component of the slab due to different temperature, but even in the depth intervals where denser wadsleyite in the slab coexists with olivine in the ambient mantle, the density contrast between pyrolite and basalt as well as between harzburgite and basalt is still larger. For the homogeneous model *p* the density increase of pyrolite in the slab region – and hence lateral density variation – is caused by lower temperatures to first order. As a consequence the density contours are simply bent towards lower depths in the slab region.

As can be seen in Fig. 3.1-5 ambient mantle density is very similar in both models. When averaged over the regions away from the slab, *i.e.*, from -300 km to -80 km and from 20 km to 300 km, the density in both models is indistinguishable.

Similar behaviour as for the density field can be observed in v_p and v_s: The slab region is clearly visible due to higher elastic wave velocities in the right panels of Fig. 3.1-5 and the comparison between the *phb* and *p* models exposes thermal features.

The basalt layer in the *phb* model has both higher P- and S-wave velocities than the rest of the slab or ambient upper mantle, but wadsleyite has faster v_p and v_s than majorite; hence with the phase change from olivine to wadsleyite around 400 km the harzburgite layer of the slab becomes seismically faster than the basalt layer, which can be observed well in v_s and, to a lesser degree, in v_p of *phb*.

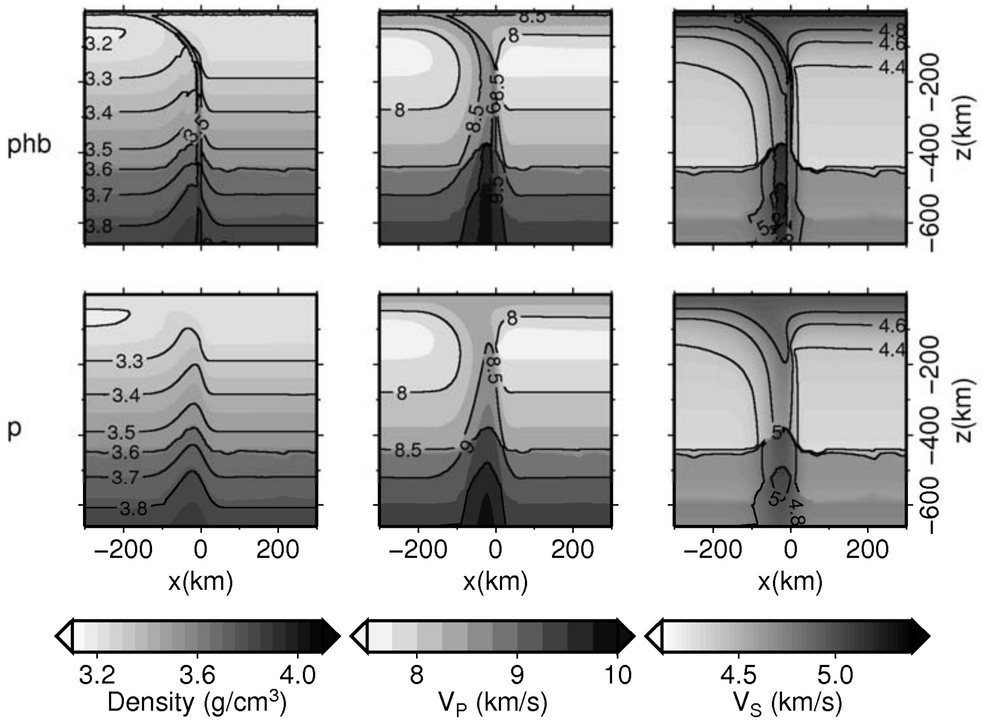

Fig. 3.1-5: Density and wave velocity fields for the differentiated pyrolite-harzburgite-basalt model (*phb*) and the homogeneous pyrolite model (*p*).

e. *Melting phase relations in the lower mantle (D.J. Frost, in collaboration with C. Liebske/ Zürich)*

Seismic studies attest to the presence of ultralow velocity zones (ULVZ) at the base of Earth's mantle. Crossing of the mantle solidus within the thermal boundary layer at the core mantle boundary (CMB) is a plausible explanation for these observations. If the mantle solidus could be determined at these conditions (135 GPa) constraints could be placed on the temperature of the mantle and an origin of ULVZ due to silicate melting could be evaluated. In this study melting experiments in the MgO-$MgSiO_3$ system have been performed to examine the eutectic composition between 16 and 26 GPa in the multianvil press. The eutectic composition places hard constraints on the thermodynamics of silicate melting and can be used to parameterize thermodynamic models that can be extrapolated to the core mantle boundary to investigate the solidus temperature. A model based on mixing properties derived from the eutectic compositions and using literature models for the melting of the MgO and $MgSiO_3$ end member phases, has been extrapolated to core mantle boundary conditions to determine melting temperatures and phase relations at these conditions.

Multi-chamber capsules were spark eroded from a rhenium rod. Up to five different starting compositions with different MgO/SiO_2 ratios were run simultaneously in different experimental chambers in a single multianvil experiment. Recovered samples were polished and examined using the electron microprobe to determine liquid compositions. An example of the resulting phase relations at 24 GPa is shown in Fig. 3.1-6. This also shows the effect of adding 10 mol.% FeO on the liquidus temperature, which is lowered by 280K.

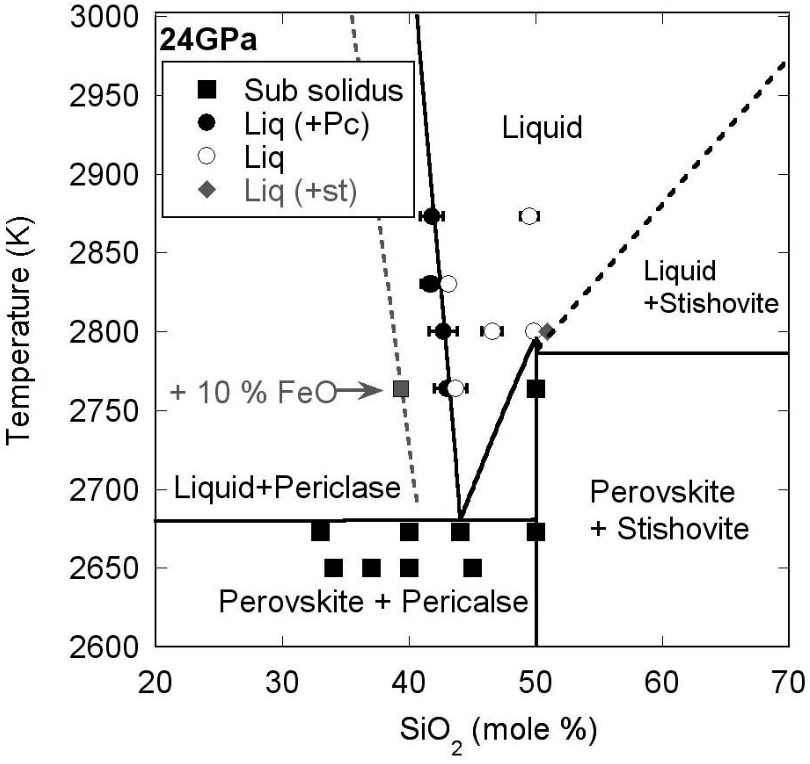

Fig. 3.1-6: Phase relations from experiments using multi-chamber capsules at 25 GPa. Solid circles indicate liquid compositions found to be in equilibrium with periclase. Open circles indicate superliquidus compositions. The grey square shows a liquid composition containing 10 mol.% FeO in equilibrium with ferropericlase. The displacement of the liquidus as a result of this FeO content is indicated by the grey dashed line. Liquidus curves are calculated using a thermodynamic model fit to the data (solid lines). All other symbols are given in the legend.

Figure 3.1-7 shows the eutectic melt composition determined experimentally (symbols) and thermodynamically (curve) using a model fit to the data and to end member melting relations.

The horizontal line shows the mantle bulk composition (BSE). The solidus and liquidus temperatures are very similar to those determined in more complex bulk compositions once the effect of FeO on the melting temperature is considered. The eutectic composition is predicted to cross the BSE composition at approximately 30 GPa, where the liquidus phase will change from periclase at low pressure to perovskite at high pressure. Exactly the same behaviour at the same pressure has been found in literature experiments performed in the multianvil on complex natural BSE bulk compositions. The BSE solidus and liquidus temperatures will remain close together at high pressure because the eutectic composition remains close to that of the BSE , as shown in Fig. 3.1-7. At the core mantle boundary, even accounting for the effects of FeO, the melting interval is not expected to exceed 200 K, in contrast to the findings of recent laser heated diamond anvil cell experiments. The solidus temperature at the core mantle boundary for a BSE composition, accounting for the effect of FeO on the melting temperature, is predicted to be approximately 4700 K, which is higher than expected within the thermal boundary layer at the CMB. A BSE mantle composition is therefore likely to be sub solidus at the CMB unless mineral/melt FeO partitioning changes dramatically at high pressure. If melting causes the ULVZ then it probably indicates enrichment of FeO or H_2O in these regions.

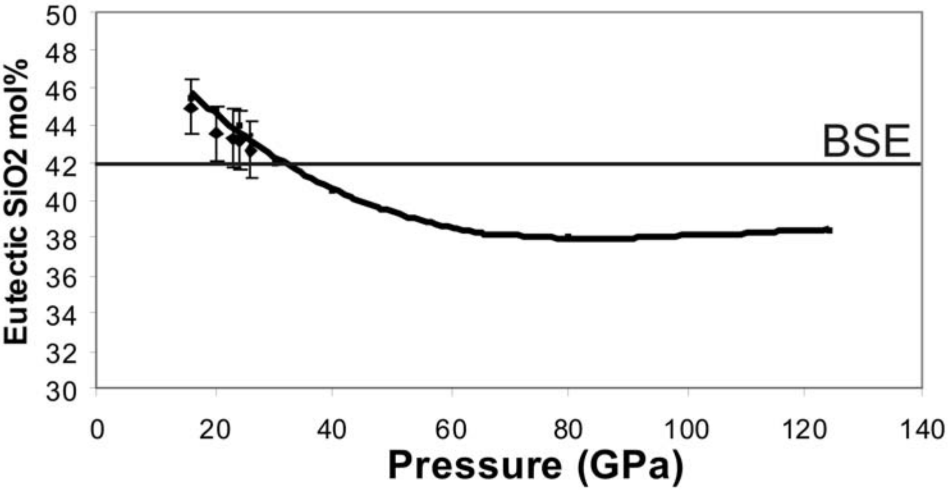

Fig. 3.1-7: The experimentally determined eutectic compositions in the MgO-$MgSiO_3$ system are compared with the thermodynamic model (solid curve), which is extrapolated to core mantle boundary pressures. The bulk silicate Earth (BSE) composition is indicated. As the eutectic crosses the BSE composition the solidus and liquidus temperatures will converge and the liquidus phase changes from periclase at low pressure to perovskite at high pressure.

f. *The influence of post-perovskite rheology on mantle thermal evolution and convective stirring efficiency (H. Samuel, in collaboration with N. Tosi/Berlin)*

Constraining the efficiency of stirring processes in the Earth's mantle is essential to the interpretation of the surface geochemical record. In such a context even the deepest parts of the Earth's mantle play an important role in erasing geochemical heterogeneities through the repeated action of stretching and folding of mantle material.

A range of geophysical and mineral physics considerations strongly support the presence of the post-perovskite (ppv) phase in the lowermost mantle. Recent studies point to the possibility of strong viscosity differences between the perovskite (pv) and the post-perovskite phases. The magnitude and sign however of such a pv-ppv viscosity contrast remains debated, with studies supporting the idea of a weaker ppv, while other suggest a stronger ppv is also possible.

We have therefore investigated the influence of post-perovskite strength on Earth's mantle convective dynamics and stirring efficiency, using numerical experiments and simple analytical theory. We show that the viscosity of the post-perovskite phase can have a dramatic influence on mantle convective dynamics: weak post-perovskite enhances the destabilization of the bottom thermal boundary layer, increasing significantly the heat flux. This yields an increase in mantle temperatures that can be predicted using simple energy scalings. This increase in mantle temperature lowers viscosity, and enhances the convective vigor.

The stirring efficiencies measured in our numerical experiments show a significant increase with decreasing the post-perovskite strength. This observed influence is well reproduced by a simple chaotic mixing model (Fig. 3.1-8).

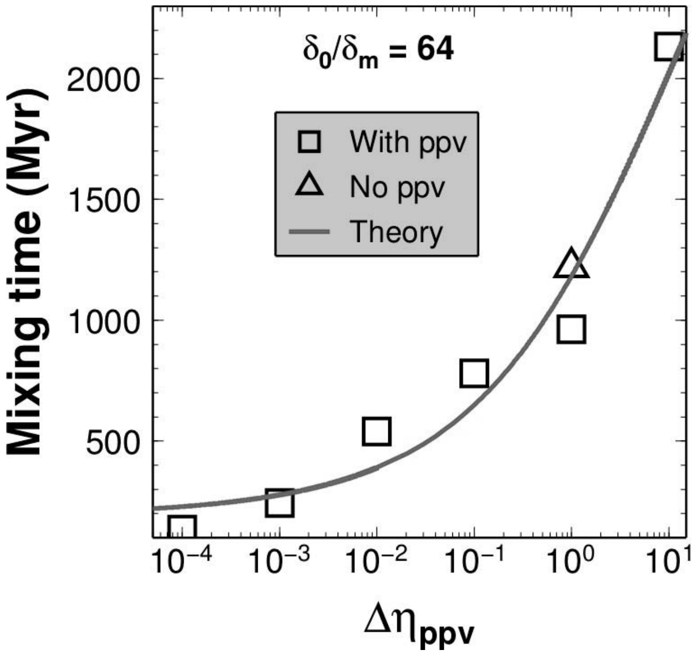

Fig. 3.1-8: Mixing time as a function of the post-perovskite viscosity. Symbols: numerical experiments. A case without ppv phase change is also shown (triangle). Solid curve: chaotic mixing model.

By coupling this mixing model with a parameterized convection evolution, we find that the presence of weak post-perovskite can increase mantle convective stirring efficiency by at least one order of magnitude (Fig 3.1-9). The influence of weak post-perovskite on mantle thermal evolution and convective stirring efficiency is maximized if the post-perovskite phase appears early in the mantle thermal history (Fig 3.1-9), *i.e.*, at relatively high temperatures of T_{ppv}/T_0 =0.5 or 0.7.

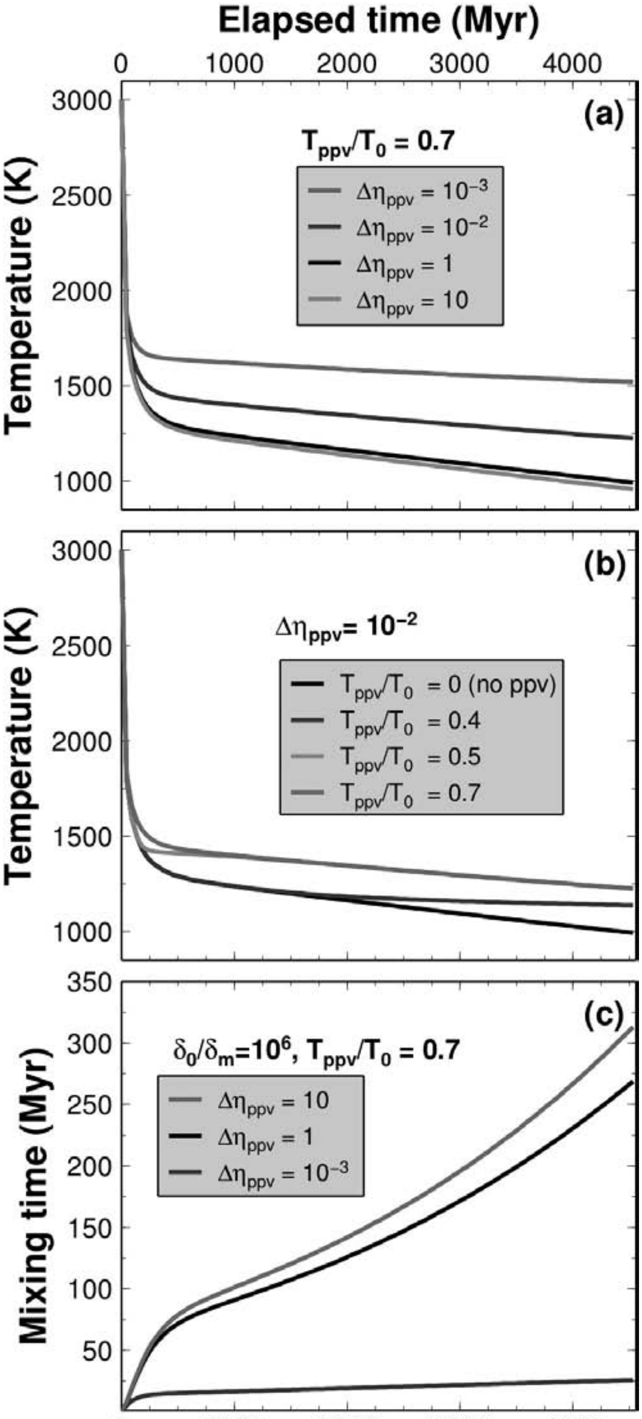

Fig. 3.1-9: Result from the parameterized convection model. Time evolution of average mantle temperature (a-b) and convective mixing time (c) for different prescribed values of ppv strength, $\Delta\eta_{ppv}$, and the average mantle temperature at which ppv is present, T_{ppv}.

Our results suggest that the effect of post-perovskite strength on the thermal and chemical evolution of the Earth's mantle must be accounted for when interpreting surface observations such as heat flow measurements and the geochemical record.

g. *Lattice thermal conductivity of lower mantle minerals and heat flux from Earth's core (M.A.G.M. Manthilake, N. de Koker, D.J. Frost and C.A. McCammon)*

Heat flux from the core into the lowermost mantle critically determines the thermal evolution of both mantle and core. It sets key constraints for the heat production required to be present in the lower mantle, the heat available for the formation of mantle plumes, the details of convection in the lower mantle, the energy available to drive the geodynamo, and the age of the inner core, to name but few. The thermal conductivity (*k*) of the lower-most mantle is a key physical property in determining the CMB heat flux, by controlling the rate at which heat is conducted across thermal boundary layers, in this case the D'' layer

Existing estimates of lattice thermal conductivity for the lowermost mantle range between 4-16 W/m K, primarily based on extrapolation of measurements for pure end member phases (MgO, $MgSiO_3$, SiO_2) at upper mantle pressures. While minor elements have been shown to have a large effect on *k* in upper mantle minerals, their effect at high pressure in lower mantle minerals has not been rigorously considered. In an effort to overcome these challenges, we have performed measurements on the lattice thermal conductivity of pure, Al-, and Fe-bearing $MgSiO_3$ perovskite at 26 GPa up to 1,073 K, and of ferropericlase containing 0, 5, and 20 % Fe, at 8 and 14 GPa up to 1,273 K, to consider dependence of *k* on composition.

We find that the addition of even a small amount of minor elements to the mineral composition strongly reduces the lattice conductivity (Fig. 3.1-10). This reduction is of similar magnitude for larger concentrations of Fe in ferropericlase, as well as for substitution of Al and Fe in perovskite. We extrapolate our results to the lowermost mantle, using an appropriately modified Debye theory relation for perovskite. We subsequently construct a single model for the thermal conductivity of the lower mantle as a function of composition, pressure and temperature, by assuming that the radiative contribution to *k* is negligible in the bulk mantle aggregate and the high-spin to low-spin transition does not notably affect the lattice contribution to *k*.

A model of thermal conductivity constrained from our results indicates that a peridotitic mantle would have k = 9.1±1.2 W/m K at the top of the thermal boundary layer and k = 8.4±1.2 W/m K at its base (Fig. 3.1-11). These values translate into a heat flux of 11.0±1.4 TW from Earth's core, which is within the range of values based on geophysical arguments and also consistent with the minimum bounds of heat flux (3-4 TW) required by geodynamic models to sustain the geomagnetic field. Our results indicate that lateral compositional heterogeneities of Fe and Al in major lower mantle mineral assemblages will not result in large variations of thermal conductivity on its own. However, the lateral variations in temperature and chemistry can change the mineral abundances, either by changing the perovskite-ferropericlase ratio, or by substituting perovskite for post-perovskite. Due to the steep thermal gradient in the basal thermal boundary layer, post-perovskite will occur as lenses surrounded by perovskite. Using a simplified scaling based on measurements in analogue materials, we estimate that a layer of post-perovskite would increase CMB heat flow by about 40 %.

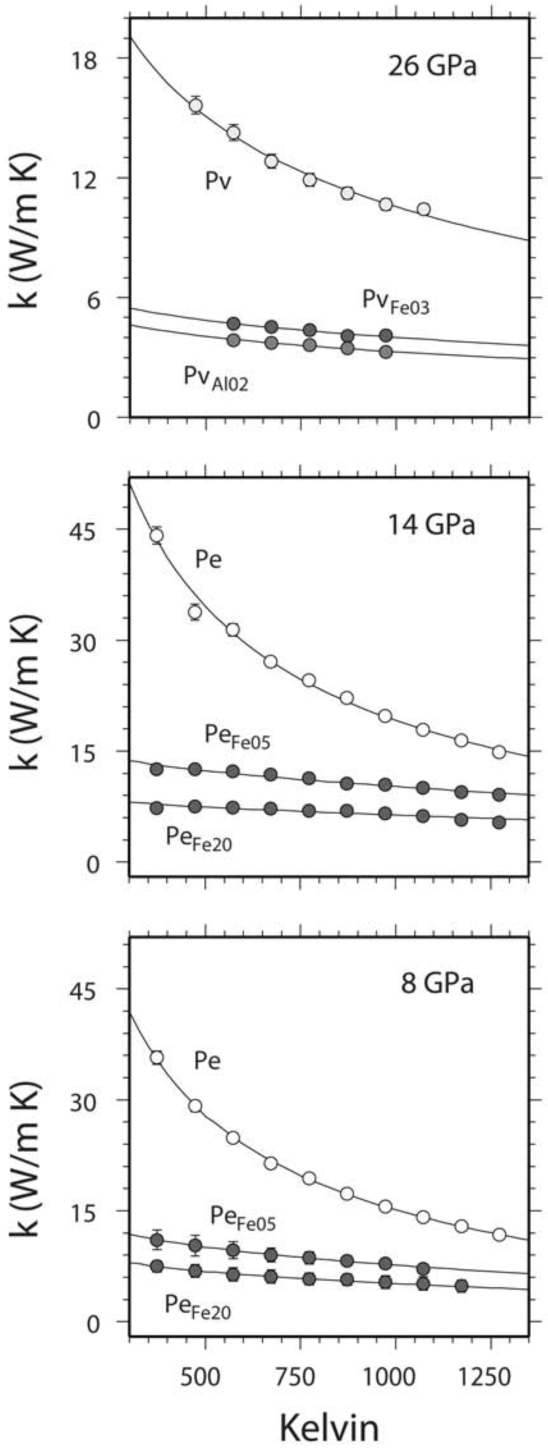

Fig. 3.1-10: Measured lattice thermal conductivities. Measurements are performed for pure $MgSiO_3$, Fe-bearing (3 %) and Al-bearing (2 %) perovskite (upper panel), ferro-periclase (MgO, 5 % and 20 %-Fe bearing MgO) at two pressures (middle and lower panels).

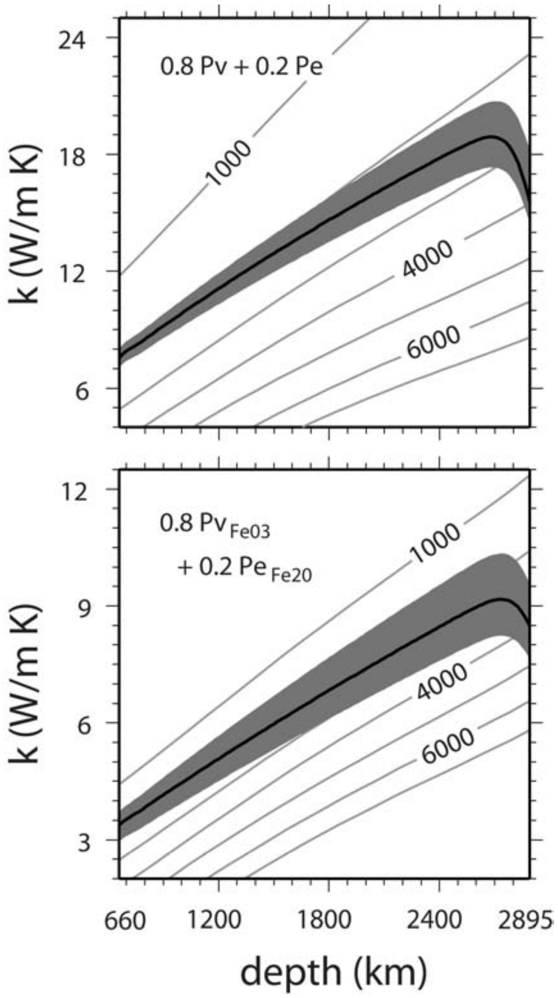

Fig. 3.1-11: Thermal conductivity models computed from our results using Hashin-Shtrikman averaging for aggregates of 20 % Pe + 80 % Pv (top) and 20 % PeFe20 + 80 % PvFe03 (bottom). The mantle geotherm is constructed by combining a 1,600 K pyrolite adiabat with a super-adiabatic temperature increase in the bottom 200 km through the thermal boundary layer to reach the range of temperature estimates for the core-mantle boundary.

h. *Thermal and electrical conductivity of liquid Al at high pressures and temperatures from* ab initio *computations: lessons for geophysics (V. Vlček, N. de Koker and G. Steinle-Neumann)*

Aluminium is considered a simple Drude metal with low number of valence electrons and free-electron-like behaviour. It is thus possible to compute the electronic transport properties with much less computational effort than *e.g.*, for Fe. Moreover, electronic properties of Al can be well described by density functional theory (DFT). By exploring the physical behaviour of simple liquid metals at extreme pressures, we are able to gain insight into the likely behaviour of more complex elements at such conditions, notable Fe in Earth’s core.

Existing estimates of σ and k for the cores of terrestrial planets are based on a series of assumptions. Firstly, σ is assumed to be inversely proportional to T; secondly, σ is assumed constant along the melting curve of the metal; and thirdly, the Wiedemann-Franz law,

$$k = \sigma T L, \quad (1)$$

with $L = 2.44 \times 10^{-8}$ W Ω K^{-2}, is assumed to hold to derive values for k. Our computations allow us to directly test these assumptions.

We calculated electrical (σ) and thermal conductivity (*k*) for compressed aluminium liquid through the Kubo-Greenwood formula employing first principles molecular dynamics and density functional perturbation theory. We investigated *T, P* conditions from 2000 to 8000 K and pressures up to 110 GPa. The method yields independent values of σ and *k*, without assumptions regarding the scaling between the flux of heat and electronic charge. A comparison with experimental data and previous calculations shows that values of the electronic transport properties are reproduced closely.

With respect to previous assumptions in geodynamic models our results indicate that electrical conductivity is not inversely proportional to temperature, but drops less steeply. This implies that current estimates for Earth's core are too low by around 25 %, so that the estimated dissipation rate of the magnetic field generated by the geodynamo is likely smaller.

We further find that the electrical conductivity along the melting curve of a Al is constant to within 5 %, in agreement with the previous assumptions (Fig. 3.1-12). However, computed thermal conductivity values vary significantly along the melting curve (Fig. 3.1-12). Since both quantities are calculated independently, we can test the validity of the Wiedemann-Franz law (Eq. 1), by calculating *L* (Fig. 3.1-12). Our results show that the Wiedemann-Franz law is satisfied only to within 7 % in compressed Al liquid.

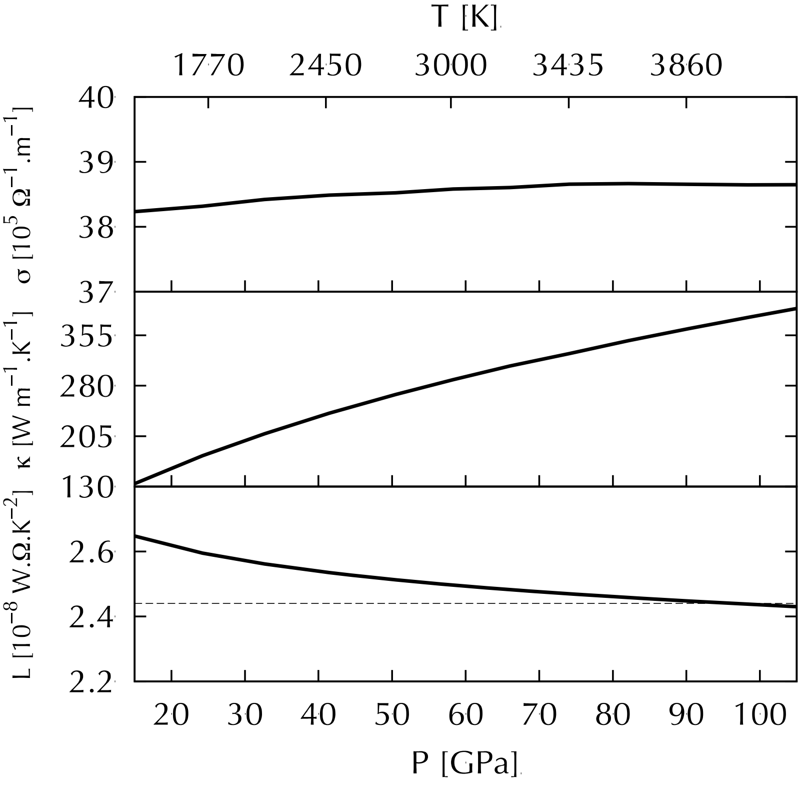

Fig. 3.1-12: (top) Electrical conductivity, (center) thermal conductivity and (bottom) resulting Lorenz number determined via Eq. 1 for aluminium liquid determined along the theoretical Al melting curve (L. Vočadlo and D. Alfè. Phys. Rev. B., 65:214105, 2002). The theoretical value of *L* is indicated by the dashed line in the bottom panel.

This behaviour of a simple liquid metal at high pressure suggests that existing estimates of *k* in the Earth's core are likely too low, by as much as a factor of 3. A higher thermal conductivity for the core would imply that conduction of heat is much more efficient than assumed previously, raising concerns regarding the heat budget required to drive the geodynamo.

i. *Electrical resistivity and thermal conductivity of liquid Fe alloys at high P and T (N. de Koker, G. Steinle-Neumann and V. Vlček)*

Earth's magnetic field is sustained by magneto-hydrodynamic convection within the metallic liquid core. In a thermally advecting core, the fraction of heat available to drive the geodynamo is reduced by heat conducted along the core geotherm, which depends sensitively on the thermal conductivity of liquid iron and its alloys with candidate light elements. The thermal conductivity for Earth's core is very poorly constrained, with current estimates based on a set of scaling relations presented in the previous contribution to the annual report.

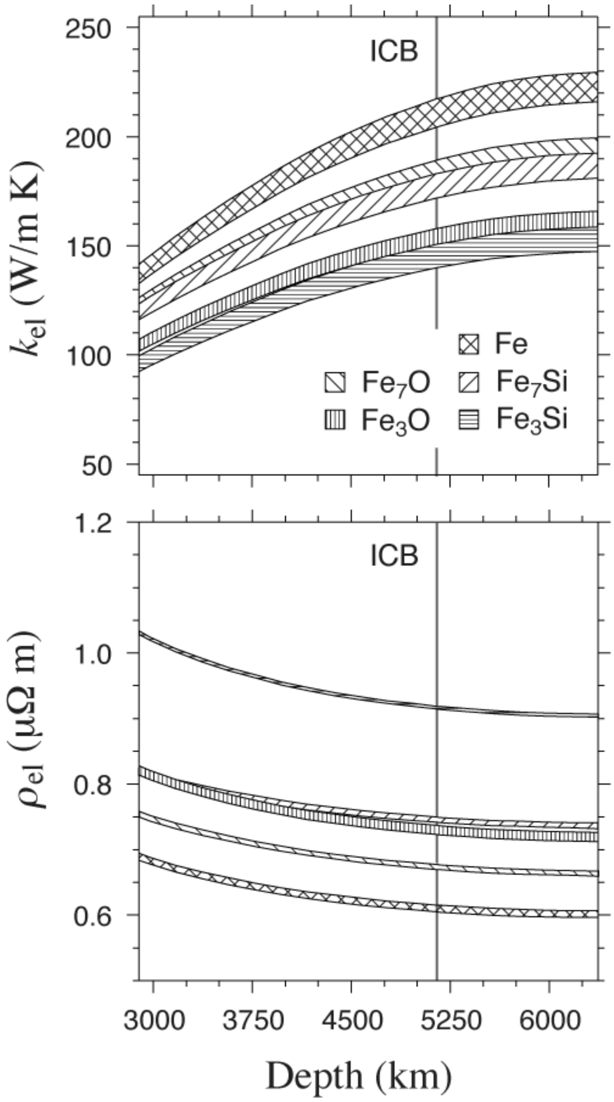

Fig. 3.1-13: (a) Electronic thermal conductivity and (b) electrical resistivity for the various compositions considered in this study, evaluated by interpolating our computations along a range of candidate core adiabats, with pressures converted to depth using the PREM seismic model.

We perform first-principles electronic structure computations to determine k_{el} and ρ_{el} for Fe, Fe_7Si, Fe_3Si, Fe_7O and Fe_3O liquid alloys (6.7, 14.3 wt.% Si; 3.9, 8.7 wt.% O). A series of uncorrelated liquid structure snapshots are generated via First-Principles Molecular Dynamics (FPMD) simulations, for which the electronic transport properties are then computed using the Kubo-Greenwood equation. This approach expresses the electronic Onsager coefficients directly in terms of the expectation values of the electronic velocity operator, thus implicitly capturing both electron-electron and electron-phonon scattering.

Computed resistivities agree very well with existing shock compression measurements, and shows strong dependence on light element concentration and type. Our results further indicate that previous extrapolations to core conditions, on which existing estimates of k_{el} and ρ_{el} for Earth's core are based, are in error; thermal conductivity at pressure and temperature conditions characteristic of Earth's core (Fig. 3.1-13) is higher than previous extrapolations.

Subsequent values for conductive heat flux near the core-mantle boundary are comparable to estimates of the total heat flux from the core but decreases with depth, so that – in the absence of an inner core – thermally driven flow would be constrained to greater depths.

j. *Simulating rotating fluid bodies: When does local vorticity generation via the density-stratification become important? (M. Evonuk)*

Differential rotation is one of the key components needed to maintain a magnetic dynamo, therefore it is important to understand the processes that generate differential rotation in rotating bodies. In a rotating density-stratified fluid, local vorticity generation occurs as fluid parcels move radially, expanding or contracting with respect to the background density stratification, referred to here as LVDS. The convergence of this vorticity forms zonal flow structures as a function of the radius and the slope of the background density profile. While this effect is thought to be of importance in bodies that are quickly rotating and highly turbulent with large density stratifications such as Jupiter, it is generally neglected in bodies such as the Earth's outer core, where the density change is small. Simulations of thermal convection in the 2D rotating equatorial plane are conducted to determine the parameter regime where local vorticity generation plays a significant role in organizing the fluid flow.

2D thermal-convection simulations are performed using the basic anelastic equations in an equatorial disk without a solid non-convecting inner core. The Rayleigh number, Ekman number, Prandtl number, heating distribution and density contrast across the simulation domain are varied to investigate how the fluid behaviour changes in this parameter space.

Three basic regimes can be distinguished for the simulation results. Dipolar flow is at one extreme, where the fluid flows directly through the center of the equatorial plane, with little influence from rotation. At the other extreme is differential flow, where the fluid is strongly influenced by rotation and organizes into a differential frow pattern with radius: two or more jets form a zonal flow structure. An intermediary, transitional flow pattern occurs, when the fluid is influenced by rotation but not strongly enough to form steady jets. In this regime the fluid often oscillates between dipolar flow structures and single jets centered on the origin ringed by smaller vortices or even quasi-two jet structures, where the outer jet does not fully encircle the inner jet.

A power law relationship exists between the convective Rossby number and the density contrast such that a value *C* can be used to determine the behaviour of a rotating convective fluid in the two-dimensional equatorial plane (where *C* is the convective Rossby number divided by the density contrast across the simulation to the 3/2 power), see Fig. 3.1-14. As the value of *C* decreases, the local generation of vorticity (LVDS) becomes increasingly dominant in determining the fluid flow pattern. High values of *C* correspond to dipolar flow patterns, while low values of *C* correspond to differential flow patterns. This correlation holds for simulations with central heating or with uniform heating, and for simulations with varying Prandtl number.

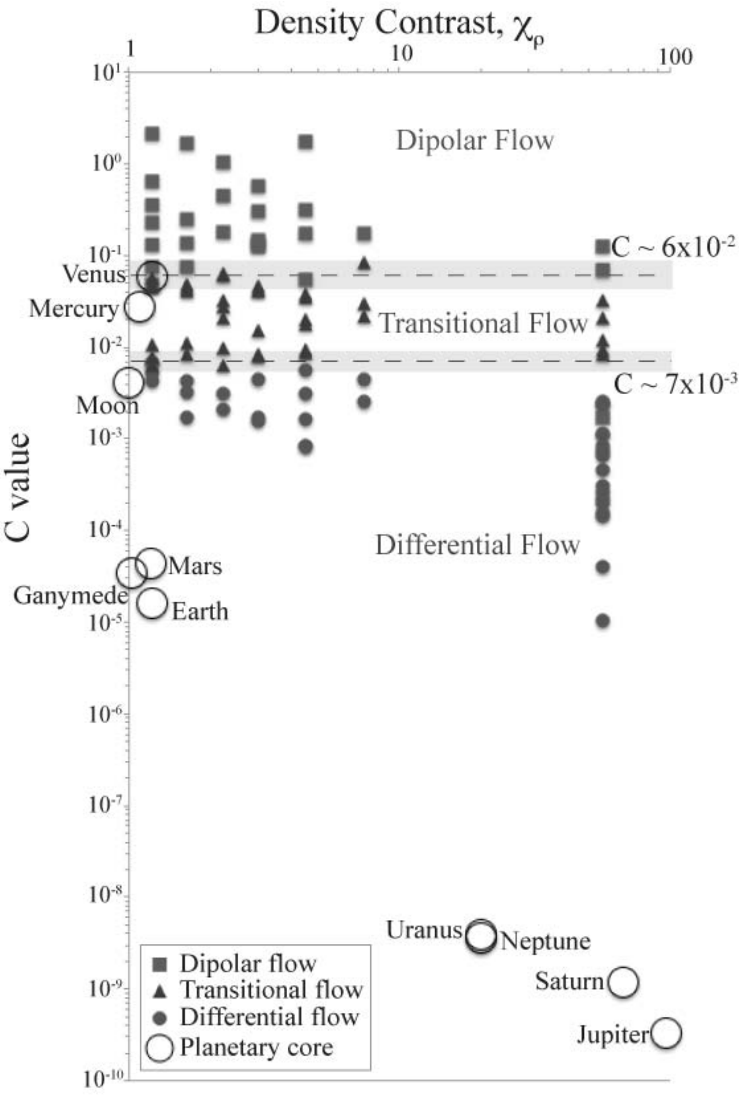

Fig. 3.1-14: Log-log plot of the density contrast versus the *C* value for all the simulations and the planetary bodies. Squares indicate cases with dipolar flow, triangles transitional flow, and small circles differential flow. Dashed lines are shown at the approximate transitions between the three regimes. Grey shaded areas bracketing these lines show regions of overlap in the flow behaviour.

Keeping in mind that this is an extrapolation, a body’s value of *C* can be calculated based on estimates of its parameters to determine if the density stratification needs to be included in simulations. Giant planets are seen to lie in the region of differential flow (therefore including the density stratification is likely very important), while surprisingly the Earth’s outer core also appears to lie in the differential flow region (Fig. 3.1-14). This indicates that LVDS vorticity generation could play a role in forming differential rotation in the Earth’s outer core and therefore in the production and maintenance of the geomagnetic field. Likewise, LVDS may be important in Ganymede and Mars, play some role in Mercury and the Moon, but is likely not to be significant in Venus.

It is important to note that these simulations were done without a non-convecting inner core. This may be the case in the early histories of some planets, and currently for others (*i.e.*, some extrasolar planets), however, most planetary bodies in our solar system currently do possess an inner core of some size. While an inner core would hamper the formation of a dipolar flow structure, it is likely not to effect when LVDS, a local form of vorticity generation, becomes important. Therefore the *C* value should still provide a good estimate for this transition in planets with cores.

3.2 Geochemistry and Cosmochemistry

Chemical fractionation events are recorded in almost all metamorphic and igneous rock samples from the Earth and space and are a recurrent theme in this section of reports. When temperatures are sufficiently high, elements partition between phases to approach an equilibrium state. If chemical equilibrium is obtained the compositions of the ensuing phases can provide information on the conditions of this equilibrium event. If equilibrium was not obtained kinetic information is recorded. Both types of information can be interpreted to provide details of the fractionation event, such as the prevailing temperatures, pressures, oxygen fugacities or the presence of influential chemical species. In most instances, however, experimental data are required to provide the crucial link between the consequences of fractionation and the conditions at which it occurred.

The first three studies in this section seek to trace the conditions in the condensing solar nebular through an appreciation of the distribution of elements in meteorite minerals. The first of these studies describes experiments to relate the oxygen fugacity at which such minerals form to the oxidation state of titanium. The following contributions examine textural and chemical relationships in primitive enstatite chondrite meteorites. Based on different rare earth element patterns it is concluded that such meteorites contain matter that condensed in different regions of the solar system, whereas the following study finds evidence for a condensation sequence that is at odds with thermodynamic calculations. In such a case kinetic factors may have played a crucial role. The following experimental study seeks to identify the conditions at which certain elements partitioned between the core and mantle during the accretion of the Earth. A powerful approach is to study the partitioning of element pairs that have similar relative concentrations in the Earth’s mantle. Conditions that significantly fractionate such elements during core mantle equilibration can thereby be excluded.

The next two contributions (d,e) concern melting of the deep silicate mantle, which likely occurred during the accretion of the Earth and may still occur at the core mantle boundary. The studies seek a fundamental understanding of the effect of pressure and chemistry on the mantle solidus. By building up the effects of chemistry on melting from simple to more complex systems, thermodynamic models can be derived that can be extrapolated over the entire conditions of the Earth’s mantle. The following two contributions (f,g) deal with iron partitioning and oxidation state in the lower mantle. Some samples of lower mantle minerals can be found as rare diamond inclusions. From an experimental knowledge of iron partitioning and oxidation state as a function of pressure, temperature and oxygen fugacity, conditions in the lower mantle can be assessed from such inclusions.

Oxygen fugacity, this time of the upper mantle, is also the theme of the following three reports (h,i,j). The oxygen fugacity of mantle xenoliths can be determined by examining redox equilibria in the mineral assemblages. The thermodynamic properties of these equilibria need to be calibrated and tested. The first study reports experimental tests on such a proposed equilibrium for garnet peridotite rocks. The results indicate that the base of the Archean lithosphere may not be as reduced as previously considered. The following report describes the first attempt to determine the oxygen fugacity of an eclogitic assemblage. The results indicate that the reduction of carbonate minerals and melts to form diamonds occurs at lower oxygen fugacities in eclogitic rocks than in peridotites. The determination of the oxygen fugacity and equilibration pressure in eclogite xenoliths is also the goal of the following study (k), although this time the idea is to experimentally calibrate the partitioning of trace elements between mineral phases as a function of the prevailing conditions.

The next report (l) examines the budget and evolution of nitrogen in the Earth. Preliminary results suggest that nitrogen solubility in the mantle strongly depends on oxygen fugacity, with the solubility being low at oxidized conditions and being high at reduced conditions. This suggests that the evolution of the Earth's atmosphere is linked to the fO_2 evolution in the upper mantle, and that the reduced lower mantle may represent a large nitrogen reservoir.

The trace element signature of primitive basalts provides important insight into the melting mechanisms and source region of these magmas. The contribution of Bali and Keppler (m) deals with the solubility of W and Mo in mantle fluids, which can be used, in combination with the results of earlier studies on U and Th solubility, to constrain the oxygen fugacity and the salinity of fluids in the melting region of arc magmas.

The next two contributions (n,o) are concerned with thermobarometry, the determination of the pressure at which an assemblage equilibrated from mineral compositions. The first presents a critical evaluation of the titanium-in-quartz thermobarometer, which is widely used in the fields of igneous petrology, metamorphism, and hydrothermal mineralization. The previous calibrations are found to be in error and a new calibration is established that is in better accord with independent estimates based on natural occurrences. The second study has established a new oxygen barometer for silicic igneous rocks based on the partitioning of vanadium between magnetite and silicate melt.

In the following contribution (p) the effect of oxygen fugacity on the solubility of hydrogen in plagioclase feldspar is examined. It is found that the solubility is much higher at reducing conditions than at oxidized conditions, but the reason for this behaviour is not entirely clear.

The final two contributions (q,r) deal with hydrothermal and weathering reactions. The first presents a novel method for estimating the solubilities of mineral solid solutions in aqueous fluids at elevated pressures and temperatures. It is based on the volume change occurring during mineral replacement reactions in hydrothermal experiments. The second focuses on the fate of the toxic elements arsenic and chromium in surface waters and sediments and examines the absorption of these elements onto iron compound particles.

a. *The oxidation state of titanium in hibonite: An oxybarometer of the early solar nebula? (M. Giannini and T. Boffa Ballaran, in collaboration with F. Langenhorst/Jena)*

Calcium-Aluminium-rich Inclusions (CAIs) are found in several types of chondritic meteorites and yield the oldest measured ages of any solar system material. The most Al-rich phase found in CAIs is hibonite (nominally $CaAl_{12}O_{19}$), which together with corundum (Al_2O_3) is predicted to be among the first condensates from a hot solar gas. Hibonite belongs to the magnetoplumbite group of minerals, crystallizing in space group $P6_3/mmc$; Al ions are distributed over five different sites: three with octahedral, one with tetrahedral and one with bipyramidal coordination. Substitution of different cations can occur on these sites, thus, the mineral hibonite usually contains significant amounts of Ti, Mg, Fe, Si and V. Among these cations, Ti is of particular interest, because its oxidation state in hibonite has been qualitatively related to the oxygen fugacity (fO_2) at which hibonite has formed and evolved in the solar nebula. However, in order to correlate the Ti^{3+}/Ti^{4+} ratio to the fO_2 conditions, a calibration of the ratio as a function of oxygen fugacity, temperature and composition is necessary. This study addresses the question whether the oxidation state of Ti can be used to quantify the oxygen fugacity at which hibonite has formed and evolved.

We have measured the oxidation state of Ti in meteoritic samples by means of TEM-EELS and compared it to the Ti^{3+}/Ti^{4+} ratio measured in the same way for samples with a similar composition synthesized at different oxygen fugacities.

Meteoritic hibonites from two CAIs within two petrographic thin sections of chondrites Acfer 182 (CH; PL01036) and one of Dar al Gani (DaG) 203 (CO3; PL96274) have been analysed with a JEOL JXA-8200 electron microprobe (EMPA). From each CAI we have chosen one grain of hibonite and prepared it for Transmission Electron Microscope (TEM) analysis using a FEI Quanta 3D Field Emission Gun (FEG) Focused Ion Beam (FIB). Polycrystalline hibonites with Mg + Ti contents analogous to the corresponding meteoritic hibonite grains have been synthesized with a typical ceramic method, starting from the corresponding oxide mixtures heated at 1500 °C for 10 to 14 hours in air or under controlled fO_2 in a gas mixing furnace using a CO/CO_2 flux. Their chemical composition also has been analyzed with EMPA.

The valence state of titanium has been measured with Electron Energy Loss Spectroscopy (EELS) using a Philips CM20 scanning TEM, operating at 200 keV, equipped with Gatan PEELS 666 parallel electron spectrometer. The calibration technique used is based on spectral features and intensities of the $L_{3,2}$ white lines of Ti. The advantage of this technique is that the Ti^{3+}/Ti^{4+} ratio can be determined directly with high lateral resolution at the nano-scale.

Hibonite grains from the analyzed CAIs contain significant amounts of Ti and Mg ranging from 0.8 to 6.1 wt.% and from 0.5 to 5.4 wt.% respectively. Very low amounts of Si, Fe and V were also detected. Their Ti^{3+}/Ti^{4+} ratios obtained with EELS are shown in Fig. 3.2-1. The synthetic analogues (SA) were prepared both in air and at $-\log f\,O_2 = 11$; in one case the sample synthesized under reducing conditions has been subsequently re-equilibrated at 1500

°C and -*log* $f\,O_2$ = 16. EMPA data of the SA shows compositions comparable to the natural samples; their Ti^{3+} content measured with EELS also are reported in Fig. 3.2-1.

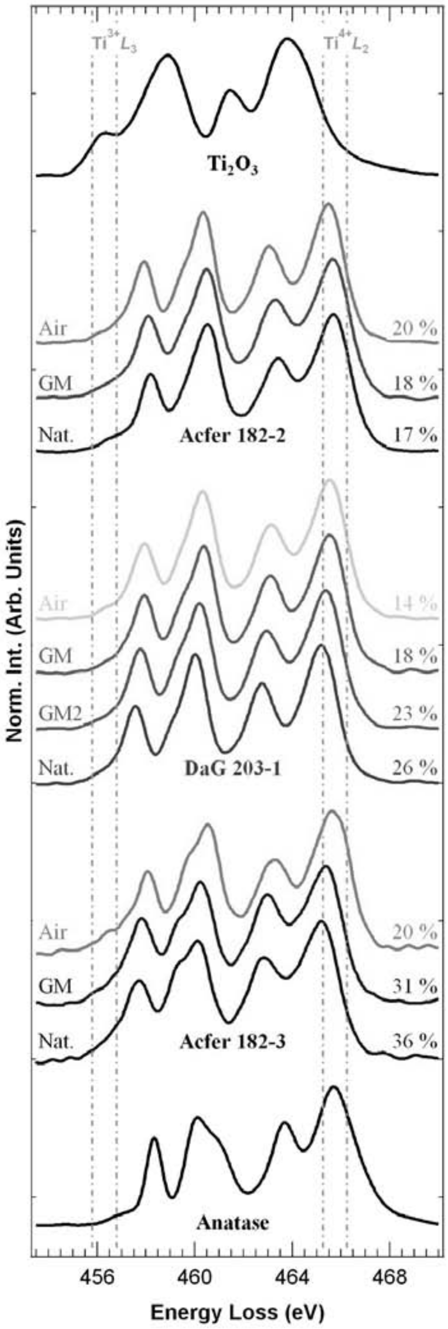

Fig. 3.2-1: EEL spectra collected for meteoritic hibonite crystals and their SA. The tag on the left side of each spectrum indicates natural samples (Nat.) or SA, specifying the conditions at which each was synthesized (where GM and GM2 are -*log* fO_2 11 and 16 respectively). The measured $Ti^{3+}/\Sigma Ti$ are indicated on the right side. The dashed lines show the integration windows for Ti^{3+} and Ti^{4+}.

The variation of Ti^{3+}/Ti^{4+} ratio obtained for the different SA samples are shown in Fig. 3.2-2. The fO_2 appears to have the largest effect on the $Ti^{3+}/\Sigma Ti$ for Acfer 182-3 SA which has the smaller Ti + Mg content but has practically no effect at least down to -11 *log* units of fO_2 for Acfer 182-2 SA, which has the largest Ti + Mg content. Preliminary fits through the data points have been used to make a first approximation of the -*log* fO_2 at which the $Ti^{3+}/\Sigma Ti$ ratio of the meteoritic hibonites has equilibrated. It appears therefore that the Ti^{3+} content in hibonites depends not only on the redox conditions at which they formed and evolved but also on their crystal chemistry. Even at very oxidizing conditions the substitution mechanism $Mg^{2+} + Ti^{4+} = 2Al^{3+}$ is not unique and some $Ti^{3+} = Al^{3+}$ substitution also takes place. Moreover, hibonites with a very large amount of Ti and Mg have a Ti^{3+}/Ti^{4+} ratio practically independent of the oxygen fugacity.

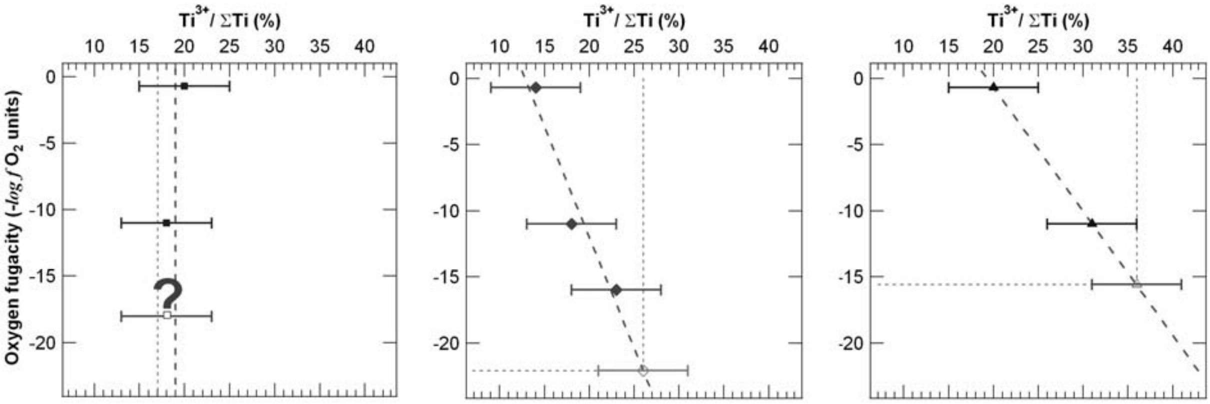

Fig. 3.2-2: Dependence of Ti^{3+} content on oxygen fugacity for SA of Acfer 182-2 (left), DaG 203-1 (centre) and Acfer 182-3 (right). The dashed lines represent preliminary fits through the data obtained so far. Open symbols represent the $Ti^{3+}/\sum Ti$ values obtained for meteoritic hibonites.

b. *REE inventories in oldhamite (CaS) solar condensates in Almahata Sitta MS-17 EL-3 and EH-3 enstatite chondrites: Evidence for different nebular sources (M. Boyet/Clermont-Ferrand, A. El Goresy, Y. Lin/Beijing, L. Feng/Beijing, M. Miyahara/Sendai and A. Gannoun/Clermont-Ferrand)*

Enstatite chondrites reveal evidence for their formation when short-lived isotopic systems, *e.g.*, ^{53}Mn-^{53}Cr ($T_{1/2}$ = 3.7 Ma) were extant. It is generally accepted that mineral constituents in primitive enstatite chondrites condensed and accreted at C/O ratios ≥ 0.83 in the early stage of the solar system. The very low fO_2 leads to drastic changes in the cosmochemical behaviour of nominally lithophile elements like Na, Mg, K, Ca, Mn, Cr, Zn and specifically REE causing them to become chalcophile. These elements occur either as individual sulfides or in solid solution within other multi-element species. More than 60 % of the REE inventory in enstatite chondrites (EH and EL subgroup) are contained as sulfides in solid solution with oldhamite (CaS).

Both EH (High Iron E-chondrites) and EL (Low Iron E-chondrites) contain modal abundances of oldhamite between 0.1 and 1.6 (vol.%). We investigated individual oldhamite-grains in their various assemblages, in chondrules and their REE inventories in several primitive EH-3 chondrites and in the EL-3 chondrite fragment MS-17 from the Almahata Sitta TC_3 2008 asteroid. The main aim of this study was to find out whether oldhamite crystals condensed in different solar regions display different intergrowth textures and retain distinct REE fingerprints characteristic of their condensation source regions.

There is indeed a striking difference between EH-3 and EL-3 in the morphologies of oldhamite, its sulfide-metal-silicate associations and textures. EH-3 chondrites usually contain complex metal-sulfide nodules with various oldhamite morphologies, indicating that some oldhamites were recycled in the nebula prior to their accretion in the metal-sulfide nodules. In comparison, oldhamite in EL-3 occurs in three distinct settings, in matrix, in chondrules and along with sinoite (Si_2N_2O) in FeNi metal nodules (see companion report by El Goresy *et al.*). All three settings are reminiscent of primary accretion processes. Some oldhamite crystals in both EH-3 and EH-4 depict identical intergrowth of schreibersite [$(FeNi)_3P$] spherules or rods (Fig. 3.2-3) interpreted in some reports to be evidence of igneous origin or impact melting. If oldhamites with identical features in EH-3 and EL-3 had emerged from the same solar source or had been produced by the same process, then their REE inventory should be identical.

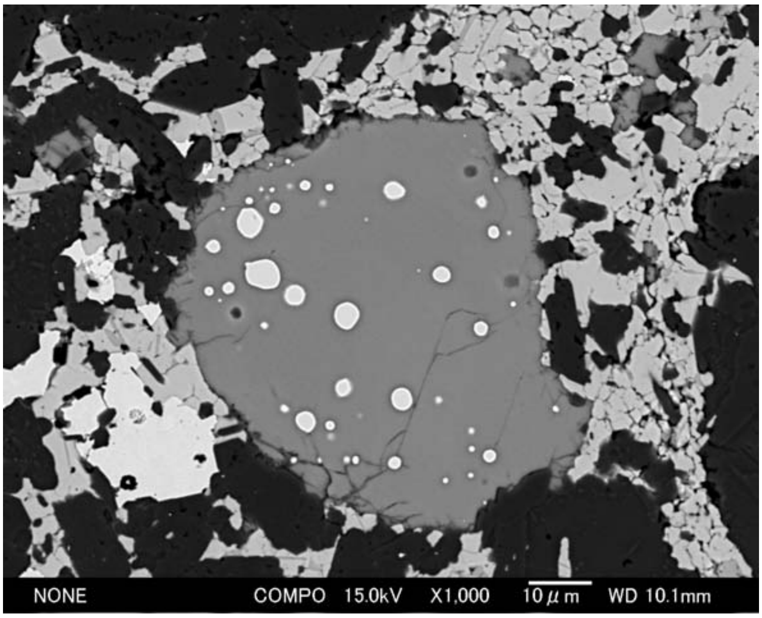

Fig. 3.2-3: An SEM-BSE photograph of a multi-grain oldhamite aggregate (gray in center) with schreibersite inclusions (white spheres). Oldhamite is surrounded by a dispersed sulfide and rarely FeNi accretionary rim. Troilite is the major sulfide and is associated by oldhamite, daubreelite, sphalerite and alabandite (various shades of gray).

Sample EL-3 MS-17 contains oldhamite grains with schreibersite inclusions in the matrix (Fig. 3.2-3). These oldhamite grains are surrounded by dispersed troilite-FeNi metal accretionary rims without any sign of melting (Fig. 3.2-3). This intergrowth texture clearly negates igneous or shock-melting origin. Oldhamite crystals in chondrules are exceptionally large (> 100 µm; Fig. 3.2-4). They engulf numerous enstatite crystals and thus witness that CaS condensed subsequent to enstatite. This is in contrast to thermodynamic condensation calculations predicting that oldhamite condenses at 1379 K prior to diopside at < 1200 K.

LA-ICPMS and SIMS investigations of the REE inventories of numerous oldhamite grains in various assemblages in EH-3 and EL-3 MS-17 fragment indicates two distinct REE patterns of oldhamite in the two groups of enstatite chondrites. Fig. 3.2-5 displays the CI-normalized REE abundance pattern in both chondrule and matrix oldhamite grains in EL-3 MS-17 in comparison to the patterns in the EL-3 MAC 88136. The REE in the asteroid fragment depicts a flat pattern with a CI-normalized enrichment of 100. The patterns have a negative Eu anomaly and no Yb anomalies, different from the predicted patterns of earliest CaS condensates. CI-normalized REE patterns in oldhamite in the EL-3 chondrite MAC88136 indicate enrichment factors between 100 and 1000 (Fig. 3.2-5). Many of these patterns show the negative Eu anomaly also encountered in the EL-3 asteroid fragment. Oldhamite grains in MAC88136 with higher CI/normalized abundances have positive Yb anomalies.

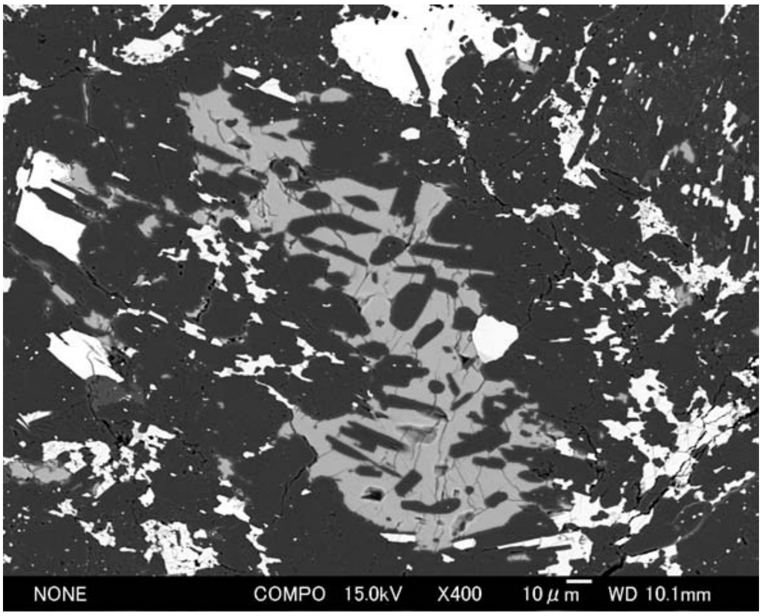

Fig. 3.2-4: An SEM-BSE photograph of a large oldhamite single crystal (light gray) inside a chondrule in the EL-chondrite fragment MS-17 from the Almahata Sitta asteroid. Oldhamite contains numerous inclusions of enstatite and diopside, indicating that enstatite and diopside predated CaS condensation.

CI-normalized REE patterns in oldhamite grains in different associations in the primitive EH-3 chondrites ALHA77295, Sahara97072 and Sahara97158 also clearly deviate from the REE pattern obtained for the earliest CaS condensate. The CI/normalized REE patterns are characterized by both positive Eu and Yb anomalies (Fig. 3.2-5) with CI-normalized enrichment factors between 10 and 100 regardless of the association in which CaS is present.

EuS and YbS are the most volatile sulfides. Hence, the calculated REE patterns for the earliest CaS condensates are predicted to have both Eu and Yb negative anomalies. Such a pattern is rarely encountered in oldhamite crystals both in EH-3 and EL-3 chondrites. Oldhamites in EH-4 and EH-5 chondrites, like in EH-3 also depict both positive Eu and Yb anomalies. Conversely, oldhamites in EL-5 and EL-6 chondrites display a negative Eu anomaly like in the MS-17 asteroid fragment. Occurrence of oldhamite crystals with schreibersite inclusions in EH and EL chondrites may indicate that they condensed during similar episodes using schreibersite crystals as nucleation sites. Their different REE patterns yet convincingly indicate that they emerged from different cosmochemical reservoirs with similar condensation and accretion mechanisms. It is reasonable to conclude that the obtained REE patterns in oldhamite grains in EH and EL chondrites reflect the signature of condensation from two cosmochemically distinct fractionated solar regions.

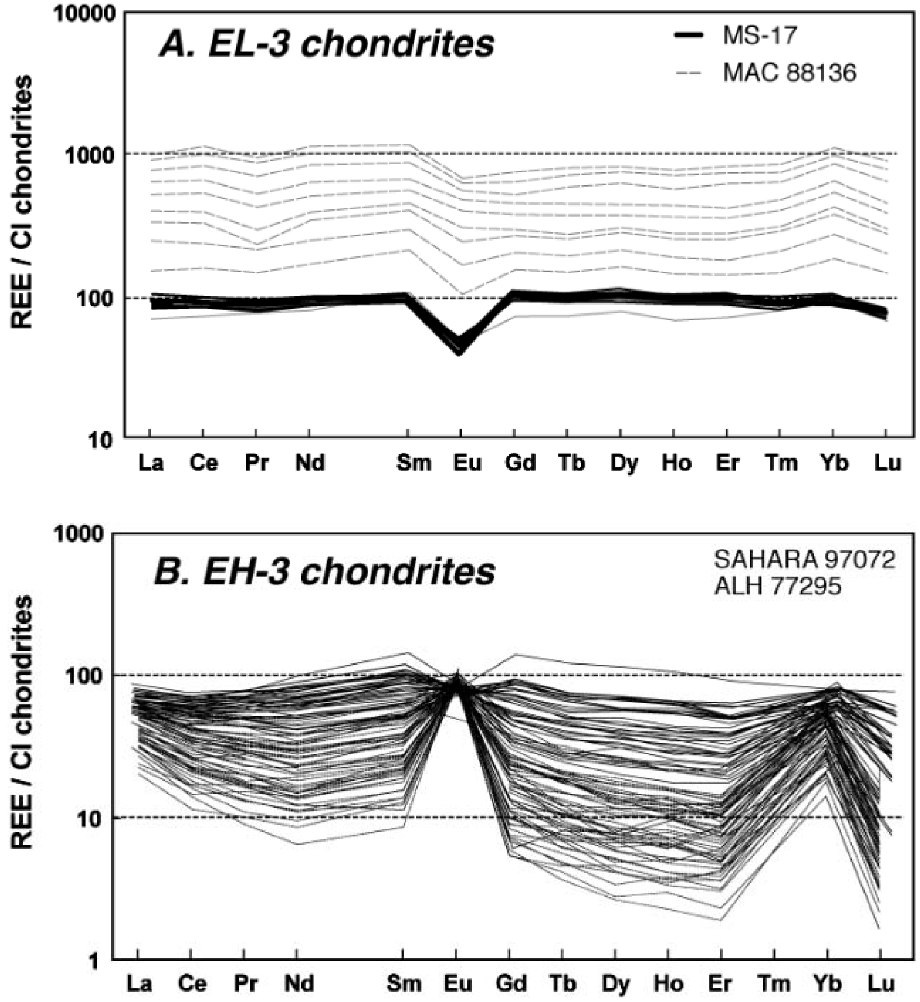

Fig. 3.2-5: CI-normalized REE patterns in oldhamite grains in (a) EL-3 MS-17 and MAC88136, and (b) in EH-3 ALHA77295, Sahara97072 and Sahara97158. REE patterns in MS-17 and MAC88136 show a negative Eu anomaly, which decreases in magnitude with the increase of the CI/normalized REE abundance. In contrast, REE patterns in oldhamite in the three EH-3 are characterized by positive Eu- and Yb-anomalies.

c. *A novel earliest solar condensate assemblage at C/O ratio < 0.83 consisting of oldhamite (CaS), sinoite (Si_2N_2O), graphite and lawrencite ($FeCl_3$), with very high abundances of N_2, Cl_2 and F_2 from the EL-3 chondrite MS-17 of the TC_3 Almahata Sitta asteroid 2008. (El Goresy, M. Boyet/Clermont-Ferrand, Y. Lin/Beijing, L. Feng/Beijing, M. Miyahara/Sendai, J. Zhang/Beijing and J. Hao/Beijing)*

Asteroid 2008 TC_3 is the first planetary object to be detected in space before entering the Earth's atmosphere while approaching the Earth's orbit. The incoming asteroid was observed in space on October 6th, 2008 and its impacting site was precisely predicted to a location near the Railway stop of Almahata Sitta in the Nubian Desert south of Wadi Halfa south of the Egypt and Sudan country border. The bolide exploded 37 km above the Earth surface, disintegrated to numerous fragments that spread in a strewn field with a flat trajectory to the east of Almahata Sitta. The array of thousands of disintegrated fragments covered an area of more than 100 km in length. TC_3 is a second-generation asteroid consisting of a compacted conglomerate of a large variety of meteorite types of ureilite achondrites, ordinary and enstatite chondrites. Meteorite fragments were collected subsequent to impact and the preliminary studies indicated a very low degree of weathering to none.

Fragment MS-17 EL-3 chondrite was particularly selected for search and study of the association of oldhamite (CaS), sinoite (Si_2N_2O) and graphite, minerals predicted to be among the earliest solar condensates from a solar gas with C/O ratio > 0.83, and to study the isotopic composition of both nitrogen and oxygen in sinoite, if encountered. The MS-17 fragment is a compacted conglomerate of enstatite rich chondrules, FeNi metal nodules and dispersed sulphide aggregates. The FeNi metal nodules are well-defined individual objects filling the space between the enstatite chondrules. They are bordered by large idiomorphic enstatite crystals (Fig. 3.2-6). Every FeNi nodule has an accretionary rim of dispersed sulfide crystallites consisting of troilite, alabandite (MnS), sphalerite and daubreelite ($FeCr_2S_4$). Similar FeNi nodules were frequently reported from more equilibrated EL-6 chondrites and were believed to have been produced by impact melting on the parent asteroid. The studied fragment MS-17 did not disclose any sign of shock deformation like closely spaced twin lamellae of troilite crystallites, signs of shock-induced melting like metal-sulfide eutectic textures or high-pressure phase transition of enstatite to majorite or akimotoite.

Fig. 3.2-6: An FeNi metal nodule containing inclusions of three early condensate assemblages: sinoite- and oldhamite-bearing fragments, sinoite-and oldhamite-bearing graphite and lawrencite.

The FeNi nodules contain in their interior a variety of assemblages of sinoite intergrown with oldhamite, graphite intergrown with both sinoite and oldhamite, and thirdly lawrencite (Fig. 3.2-6). Screening of more than 39 metal nodules covering a total surface of 2.3 cm^2 revealed that the abundance of sinoite-bearing assemblages is at least 14 vol.%, thus witnessing an extremely high abundance of both N and O in the metal nodules.

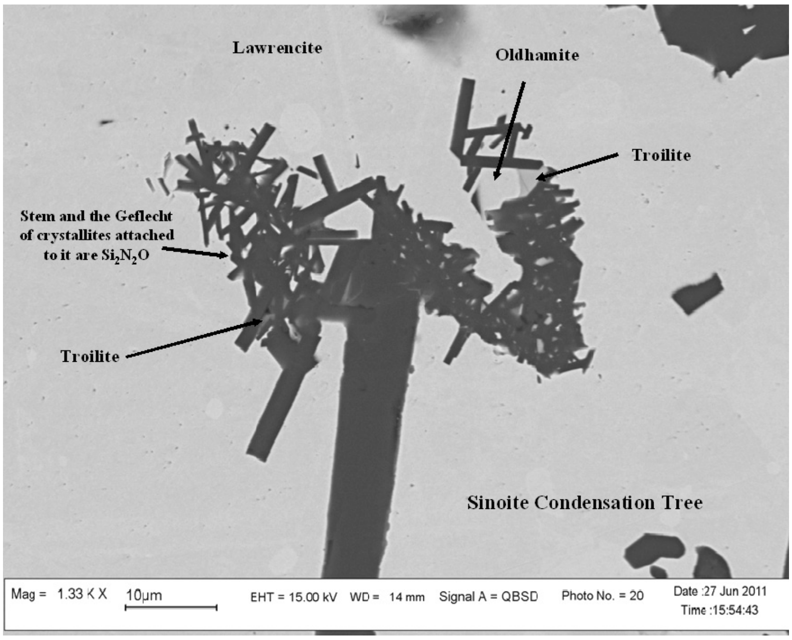

Fig. 3.2-7: A delicate branched accretionary wickerwork of sinoite crystallite condensate with oldhamite inclusions.

Detailed study of the different sinoite-bearing assemblages revealed texture details and mineral associations uncovering a possible sequence of condensation and accretion. Bundles of idiomorphic sinoite crystals always enclose idiomorphic oldhamite (CaS) crystallites (Fig. 3.2-7). This strongly suggests that sinoite nucleated around and encapsulated preexisting oldhamite. Sinoite crystallites are also sprinkled in the FeNi metal host and the coexisting schreibersite $(FeNi)_3P$ (Fig. 3.2-7), thus indicating that their formation predated the accretion of both schreibersite and FeNi metal. The growth textures between sinoite, oldhamite, graphite, enstatite and diopside disclose a sequence of condensation and accretion. Very fragile wickerwork of sinoite whiskers (Fig. 3.2-8) also demonstrates delicately attaching Si_2N_2O crystallite branches that accumulated in a non-turbulent accretionary process. The sinoite whiskers are attached to each other like tree branches and also encapsulate idiomorphic oldhamite crystallites (Fig. 3.2-8). Sinoite crystallites abundantly occur as inclusions and as residual consumed fragments inside both enstatite and diopside (Fig. 3.2-9). We also encounter inclusions of a topotaxial intergrowth of oldhamite and sinoite “geflecht” (Fig. 3.2-9 and Fig. 3.2-10). Feathery graphite (Fig. 3.2-6) contains encapsulated oldhamite and sinoite crystallites. The textures depicted in Fig. 3.2-6 to -9 are strongly suggestive of primitive primary condensation and accretionary textures commenced by oldhamite condensation followed by co-condensation of oldhamite and sinoite. Evaluation of the assemblages, their growth textures and abundances reveal a possible formational sequence including replacement reactions starting with oldhamite condensation followed by co-accretion of oldhamite and sinoite (Fig. 3.2-6), further followed by condensation of graphite and then formation of enstatite and diopside both by partial consumption of sinoite (Fig. 3.2-8). Lawrencite ($FeCl_3$) was probably one of the last minerals to form prior to inclusion in FeNi metal (Fig. 3.2-6).

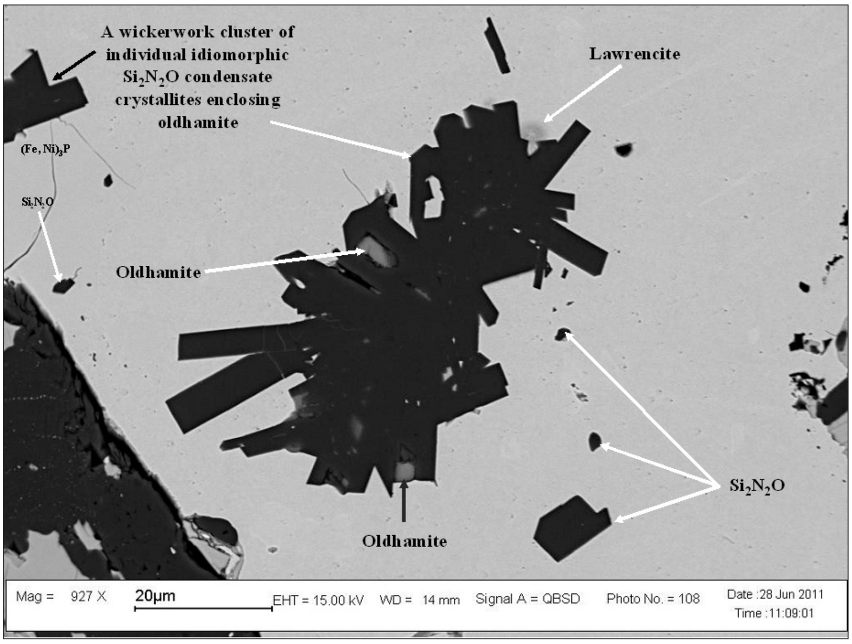

Fig. 3.2-8: Wickerwork of idiomorphic sinoite crystals enclosing oldhamite idiomorphic crystallites.

High resolution ion mapping by NanoSIMS 50L for ^{12}C, $^{12}C^{14}N$ (mass 26), ^{28}Si, ^{16}O, ^{35}Cl and ^{19}F of the assemblage depicted in Fig. 3.2-9 reveals crucial information about the nature of the condensing species, their sequence of formation and possible spatial isotopic heterogeneities within individual grains. ^{12}C and $^{12}C^{14}N$ ion maps indicate that only some of the carbon inclusions in enstatite and diopside contain ^{14}N. The ^{28}Si ion map depicts the occurrences of residual sinoite inclusions in both enstatite and diopside and discloses that numerous unconsumed residual fragments of sinoite are present in both pyroxenes thus supporting the deduced consumption mechanism outlined before. Comparing the ^{35}Cl and ^{19}F ion maps clearly reveals that not all lawrencite fragments have similar abundance of ^{19}F and that we probably encountered an individual unknown novel fluoride condensate that is poor in ^{35}Cl.

It is very unlikely that oldhamite or sinoite crystallized from a FeNi metal melt. The experimentally determined maximum solubility of N in Fe metal melt doesn’t exceed 0.34 %, which is far lower than the volume abundance of sinoite encountered in the FeNi metal nodules in this asteroid fragment.

Condensation calculations from a solar gas at C/O ratio > 0.83 reveal that CaS is one of the earliest condensates at 1379 K. At such reducing conditions the nominally lithophile REE, co-condense as REE-sulphides in oldhamite. More than 60 % of the REE budget in enstatite chondrites is concentrated in oldhamite (see report by Boyet *et al.*). Although all phases encountered in the metal of this asteroid fragment are predicted by thermodynamic calculations as solar condensates from a gas with C/O ratio higher than 0.83, the deduced condensation sequence in the MS-17 asteroid fragment is at odds with the sequence obtained from calculations. Sinoite is listed in such calculations to condense after enstatite and diopside. In addition, the condensation temperature of graphite was calculated at 1766 K thus preceding oldhamite condensation at 1379 K. This is discrepant with the natural occurrence in the asteroid sample. The source of discrepancy in the condensation sequence deduced from our findings in undisturbed natural assemblages in the TC$_3$ asteroid and the thermodynamic calculations probably emerge from the uncertainties of the thermodynamic parameters used in the calculations, specifically the magnitude of $f\text{O}_2$.

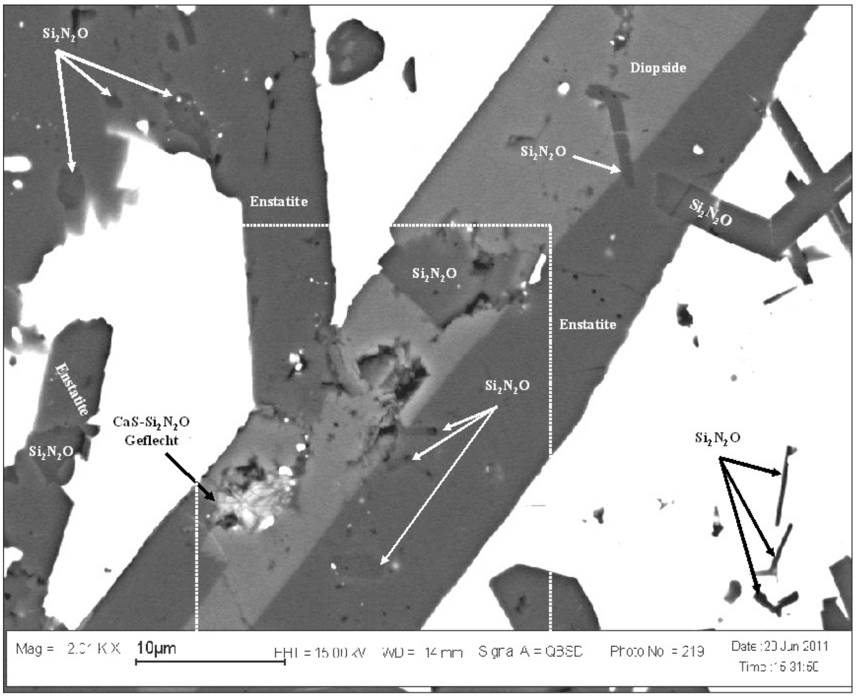

Fig. 3.2-9: Large enstatite and diopside crystals embedded in a metal nodule. Both pyroxenes enclose idiomorphic crystals of sinoite, oldhamite-sinoite topotaxial intergrowth and residuals of partially consumed sinoite fragments.

Minor lawrencite was found in FeNi metal, mainly in the sinoite-bearing metal nodules. Most of the grains are very small (< 1 µm; Fig. 3.2-7) and are partially weathered. ^{32}S, ^{33}S, ^{34}S, ^{36}S and ^{37}Cl in lawrencite were analyzed by NanoSIMS 50L, but only six grains are relatively large (1~2 µm) and reveal $^{35}\text{Cl}/^{34}\text{S}$ ratios > 1000 (1500-5300). Three analyses show significant excess of ^{36}S*, with $\delta^{36}\text{S}^*$ (2σ) of 830±170, 2230±1810 and 510±260, respectively. The inferred $^{36}\text{Cl}/^{35}\text{Cl}$ ratios are $(0.92\pm0.2)\times 10^{-4}$, $(3.8\pm3.1)\times 10^{-4}$ and $(1.42\pm0.74) \times 10^{-4}$, using the relative sensitivity factor of Cl/S of 0.8 measured on NIST 610. The value of $(1.42\pm0.74)\times10^{-4}$ could be referred to as the initial $^{36}\text{Cl}/^{35}\text{Cl}$ ratio of the solar nebula in EL-chondrite forming region, without calibration for the time difference between the condensation of CAIs and lawrencite assuming fast condensation of the solar nebula. The initial $^{36}\text{Cl}/^{35}\text{Cl}$ ratios in CAIs were deduced from the obtained excess of ^{36}S* in sodalite or wadalite which in turn are alteration products of melilite. The time lapsed between melilite condensation at the birth of the solar system and its alteration to sodalite or wadalite when ^{36}Cl was still extant is unknown. Inferred ^{36}Cl/^{35}Cl initial ratios obtained from the study of the ^{36}Cl/^{36}S system in CAIs should be handled with caution because the obtained inferred ratio is short by a still unknown magnitude.

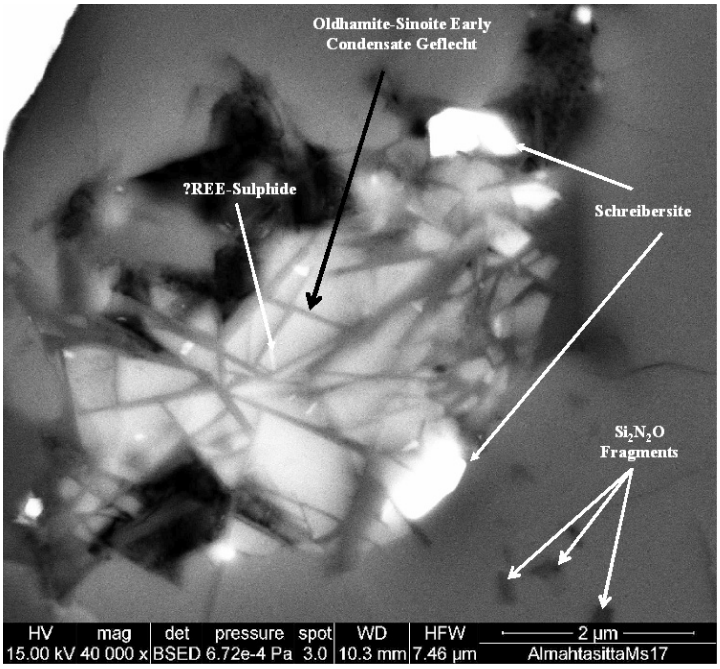

Fig. 3.2-10: A close up of the oldhamite-sinoite inclusion (geflecht) in Fig. 3.2-9. Oldhamite contains brighter lamellae of a presumably REE-sulfide.

d. *The partitioning of volatile and other siderophile elements between metal and silicate at high pressures and temperatures (A.K. Vogel, D.C. Rubie, D.J. Frost and A. Audétat, in collaboration with H. Palme/Frankfurt)*

Volatile elements are depleted in the Earth´s mantle most probably because they failed to condense at high temperatures in the inner part of the solar nebula. However, in the Earth, many of these elements were additionally depleted by core formation processes. We are therefore studying the liquid metal – liquid silicate partitioning behaviour of the volatile siderophile elements Sn and Pb together with the moderately volatile siderophile elements P, Cu, Ge, Sb, As, Ag and Au and the non-volatile elements Ni, Co, W and Mo.

We are performing a series of isobaric and isothermal experiments in a multianvil apparatus, covering a pressure and temperature range of 10.5-23 GPa and 2273-2673 K respectively. Our starting compositions consist of ~ 3 parts by weight silicate (peridotitic composition) and 1 part by weight metal with 95-96 wt.% Fe and 1-3 wt.% pure elements or oxides of the elements of interest. The determined oxygen fugacities vary between -1.9 and -2.4 log units relative to the iron-wüstite (IW) buffer. The experiments are performed under conditions at which both metal and silicate phases are molten. The quenched samples consist of one or more rounded metal blob(s) surrounded by silicate liquid that quenched to phases of elongate skeletal olivine crystals within a silicate matrix (Fig. 3.2-11a). The quenched silicate liquid was analyzed with a laser ablation inductively coupled plasma mass spectrometer (LA-ICPMS) whereas the metal phases were analysed using an electron probe micro analyzer.

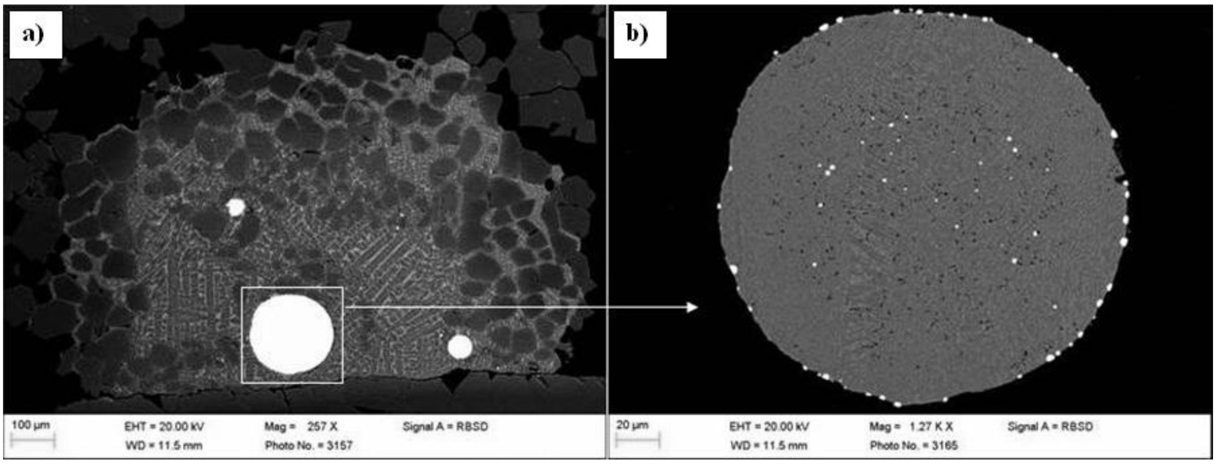

Fig. 3.2-11: a) SEM image of sample H3404a: 11GPa, 2673K, ΔIW -2.3. Three metal spheres (white) are surrounded by quenched silicate that exhibits elongate skeletal olivine crystals. b) Detailed image of the largest metal sphere of a). White blobs within and preferentially at the rim of the metal are Ag- and Au-rich exsolutions.

Currently we are systematically investigating the temperature dependence of the above mentioned elements at 11 GPa covering a temperature range from 2273 K to 2673 K. In addition the effect of S on the partitioning behaviour of these elements is being studied. For this purpose we added 10 wt.% S as FeS to the metal phase of our starting compositions.

The metal-silicate partition coefficient of element M D_M is equal to the concentration of M in the metal divided by its concentration in the silicate. In order to consider results independently of oxygen fugacity, partitioning is expressed as an exchange coefficient $K_D^{M\text{-}Fe}$ that can be described as the ratio of the partition coefficient of element M (the element of interest) and the partition coefficient of Fe with the latter being raised to the power of half the valence n of the element of interest:

$K_D^{M\text{-}Fe} = D_M/(D_{Fe})^{n/2}$.

With increasing temperature, we observed a weak increase in exchange coefficients for the elements Mo, W, Sb, Ge and Pb, whereas Cu and Sn show very little temperature dependence. S has very little influence on the partitioning behaviour of these elements. Fig. 3.2-12 shows the results for the volatile siderophile element pair Sn and Pb, with these elements being particularly informative, because they are depleted to the same amount in the Earth´s mantle, thus requiring the same partition coefficients during core formation. The values for the S-bearing experiments are also given in the diagram. During quenching, the elements Ag, Au and, to a lesser extent, Pb tend to exsolve from the metal phase, forming small highly enriched blobs within and preferentially at the rim of the large Fe-rich metal blobs (Fig. 3.2-11b). In order to take such heterogeneities into account when determining metal compositions, we are performing image analysis, but are also investigating new strategies to prevent those elements from exsolving.

Our goal is to extend our experiments to a wider range of pressures and temperatures and to focus on the influence of the light element S on liquid metal – liquid silicate partitioning. The resulting values for $K_D^{M\text{-}Fe}$ will be incorporated into core formation models in order to understand the timing and nature of volatile element addition to the Earth.

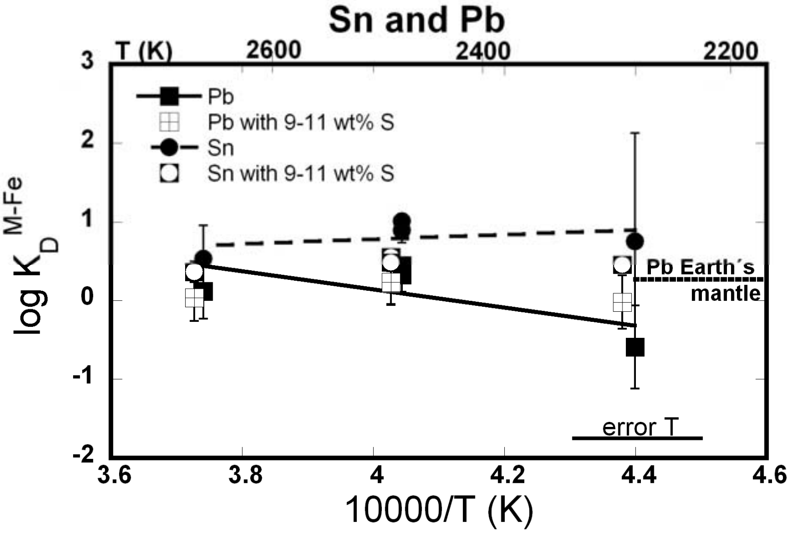

Fig. 3.2-12: Temperature dependence of the volatile siderophile element pair Sn and Pb at 11 GPa. With increasing temperature the values for the exchange coefficient $K_D^{M\text{-}Fe}$ increase for Pb, whereas Sn exhibits hardly any temperature dependence. Unfilled symbols represent S-bearing experiments.

e. *Liquidus phase relations in the systems $AlO_{1.5}$-MgO-SiO_2, CaO-MgO-SiO_2, FeO-MgO-SiO_2 at 17-24 GPa (R.G. Trønnes/Oslo and D.J. Frost)*

During and shortly after Earth's accretion and core segregation, deep and extensive melting and crystallization of the silicate mantle occurred. This might have caused cumulate layering and possibly gravitational segregation of dense late-stage cumulate material in the lowermost mantle. Deep melting in hot ascending plumes shortly after the solidification of the mantle might also have produced melt accumulation and solidification near the boundary between the upper mantle and transition zone. In a hotter Earth this would have been deeper than the 410 km discontinuity. After cooling to ambient temperatures, such igneous rocks might have been sufficiently dense to sink to the bottom of the mantle. The seismically detected antipodal Large Low Shear-Velocity Provinces, stabilized by the Earth's rotation, as well as the thin and irregular Ultra-Low Velocity Zones might have originated during these early magmatic processes.

Although some experimental melting studies on various peridotitic and chondritic model compositions have been performed at pressures of the transition zone and lower mantle, very little systematic work has been done to determine the invariant or univariant melt compositions as a function of pressure. Melting experiments in the multianvil apparatus, with moderate and stable thermal gradients across the samples, are generally well suited to determine the crystallization sequence (first and second liquidus mineral) for a given composition and pressure. The invariant and univariant melt compositions as a function of pressure can then be derived by imposing compositional brackets. Thermodynamic models based on such experimental data can be used to predict the melt compositions to higher pressures, applicable to the lower mantle. Because melting experiments in the laser-heated DAC are very challenging and associated with large uncertainties, such predictions may be very useful.

We have started to determine the cotectic curve locations in three different 3-component systems AMS, CMS and FMS (A, C, F, M and S: $AlO_{1.5}$, CaO, FeO, MgO and SiO_2, respectively). The compositional bracketing approach is facilitated by using multi-chamber Re-capsules. At 17-20 GPa we use two 2 mm OD Re-capsules with a total of 10 cylindrical sample chambers in 18-8 mm (OEL-TEL) assemblies and at 24 GPa we will use a 1 mm OD Re-capsule with three chambers in 10-4 mm assemblies. A representative run product is shown in Fig. 3.2-13. Two such capsules were run in each experiment.

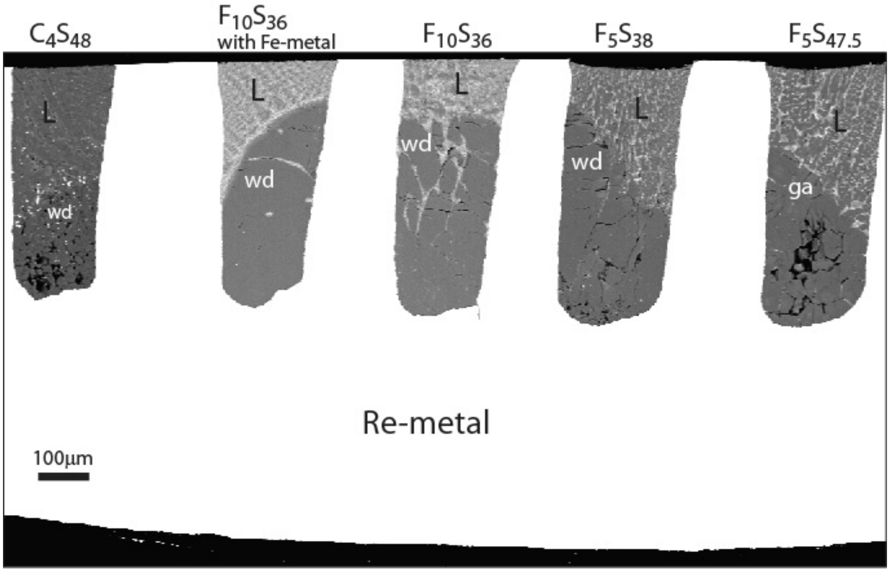

Fig. 3.2-13: Back-scattered electron image of the sectioned surface through the central part of a lower Re-capsule. The five sample chambers are spark-eroded along a diametric plane in the capsule. An axial section through all of the chambers can therefore be made by careful grinding and polishing. The central hotspot within the cell was within the sample chamber plane of the upper capsule, 200-300 µm above the upper border of the image. Abbreviations: L: quenched liquid, wd: wadsleyite, ga: majoritic garnet, C: CaO, F: FeO, S: SiO_2. The bulk sample compositions are given by subscripts for the mol-percent of the components C, F and S. The second sample from the left contains additional Fe-metal. Note the regular thermal gradient with radially increasing T towards the $LaCrO_3$-heater.

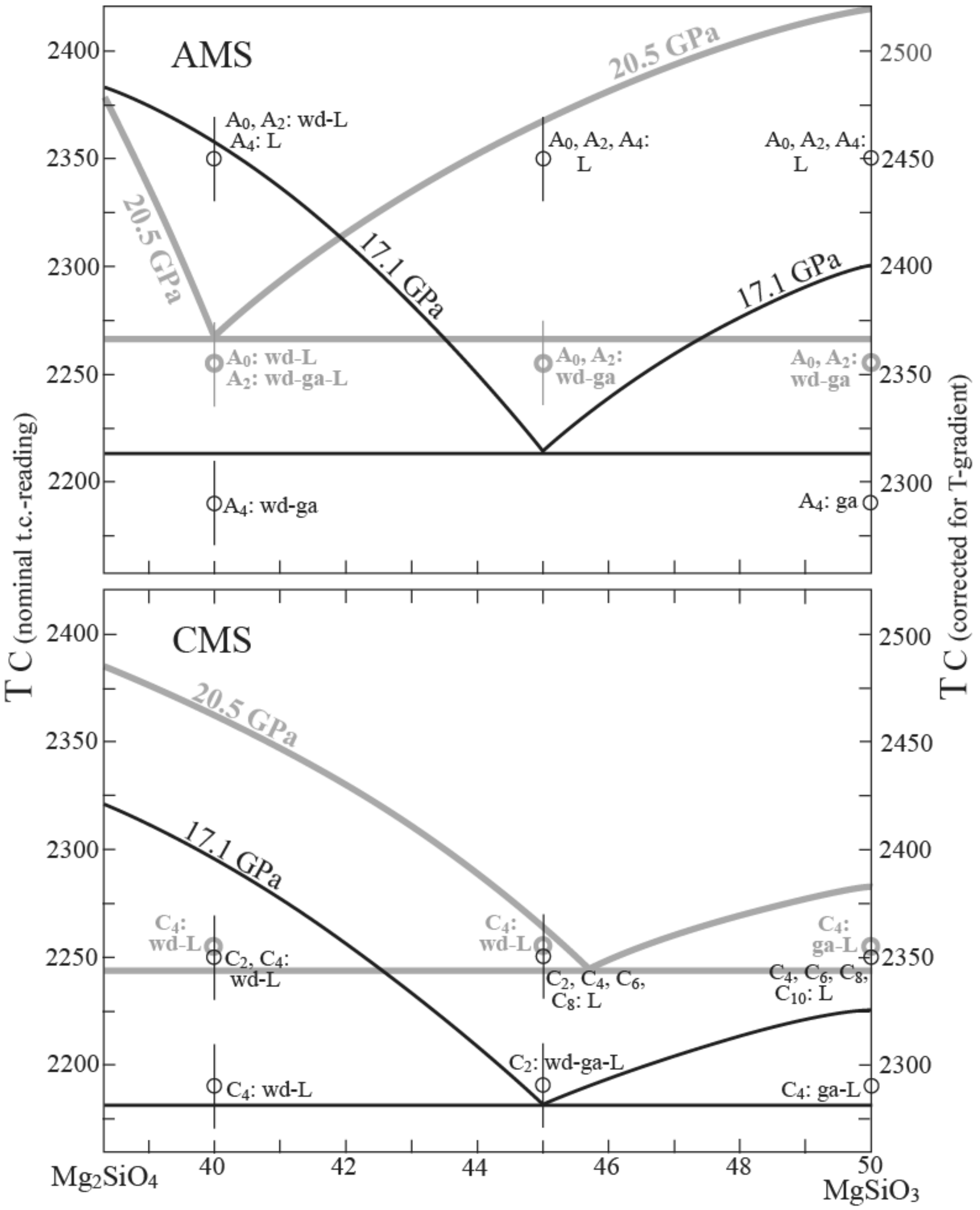

Fig. 3.2-14: Preliminary liquidus surface projections onto the Mg_2SiO_4-$MgSiO_3$ join for the systems AMS and CMS. The different compositions are labelled with the mol.% of $AlO_{1.5}$ and CaO, given as subscripts for the A- and C- component. The three different molecular M/S-ratios (1.5, 1.2 and 1.0) of the sample compositions are given by the positions along the Mg_2SiO_4-$MgSiO_3$ join. The indicated temperature error bars of 80° correspond to the estimated temperature gradient across each of the individual sample chambers. The central hotspots in each of the pressure cells appears to be about 400-600µm from the thermocouple junction. This corresponds to a temperature difference of about 100°. The left and right hand side temperature axes represent the thermocouple reading and the corrected temperatures, respectively. Phase abbreviations: L, wd, ga: liquid, wadsleyite and majoritic garnet. Black and grey lines and text represent 17.1 and 20.5 GPa, respectively.

Preliminary results are shown in Fig. 3.2-14. In the AMS system the garnet-wadsleyite (ga-wd) cotectic seems to move markedly towards MgO-rich melt compositions from 17.1 to 20.5 GPa, associated with increasing liquidus stability field of majoritic garnet with increasing pressure. The 17.1 GPa cotectic seems to have approximately the same molecular MgO/SiO_2-ratio (about 1.2) in the AMS and MS systems. At 17.1 GPa the wadsleyite liquidus surface is lowered considerably by increasing Al-content at a given MgO/SiO_2-ratio.

In the CMS system the ga-wd cotectic does not change considerably from 17-21 GPa, and is located near a MgO/SiO_2-ratio of 1.2. The lime component appears to lower both the ga and wd liquidus surfaces relative to the MS system and this CaO-effect is probably greater than the corresponding effect of alumina. With our preliminary compositional resolution it seems that the effect of FeO on the ga and wd liquidus surfaces may be similar to that of CaO.

f. *The effect of chemistry on the melting of pyroxenite rocks in simplified systems at 6 GPa (O. Savchuk and D.J. Frost, in collaboration with R.G. Trønnes/Oslo)*

Pyroxenites *i.e.*, mafic mantle rocks dominated by pyroxene, are common xenoliths likely formed as cumulates from melts crystallising in the lithospheric mantle. Pyroxenite rocks may be also abundant in the asthenospheric mantle, however, as a result of the recycling of mafic oceanic crust into the mantle at subduciton zones. It is possible that some portion of subducted pyroxenite rocks ultimately form heterogeneities in regions of mantle upwelling beneath melting centres. The geochemistry of lavas erupted in major tectonic settings has been used to argue for a contribution to basalt genesis from such olivine-free mantle source heterogeneities. A fundamental understanding of the melting behaviour of such plausible mantle compositions is therefore important.

The goal of this study is to examine melting phase relations in the $MgO-SiO_2$ and $FeO-MgO-SiO_2$ systems either side of the pyroxene composition. In our approach we compare melting phase relations in the $MgO-SiO_2$ system with those in the FeO bearing system by using multichamber capsules where different compositions can be run at the same temperature simultaneously. To investigate melting phase relations in the above-mentioned systems, a series of high-temperature (~ 1930-2050 °C) multianvil experiments were performed. Several compositions were prepared by mixing powers of Mg_2SiO_4, $MgSiO_3$, SiO_2 and Fe_2SiO_4 in different proportions. Different sample mixtures were placed in multi-chamber Re metal capsules as described in the previous study. Up to 5 samples of different composition were examined in a single experiment. The solid/melt relations in the run products were detected with scanning electron microscopy (SEM), and the chemical composition of the quenched liquids were characterized by electron microprobe.

A preliminary phase diagram summarising the results is shown in Fig. 3.2-15. The results are consistent with congruent melting of $MgSiO_3$. The enstatite-melt two-phase regions are narrow in temperature and challenging to determine as they are of a similar magnitude to the temperature precision in the multianvil (~ 50°). As some single capsules contained samples with differing proportions of FeO, it was possible to precisely bracket the FeO content for the commencement of melting for the $(Mg,Fe)_2SiO_4$ and $(Mg,Fe)SiO_3$ compositions. The depression of melting due to FeO is identical, within error, for both enstatite and olivine melts.

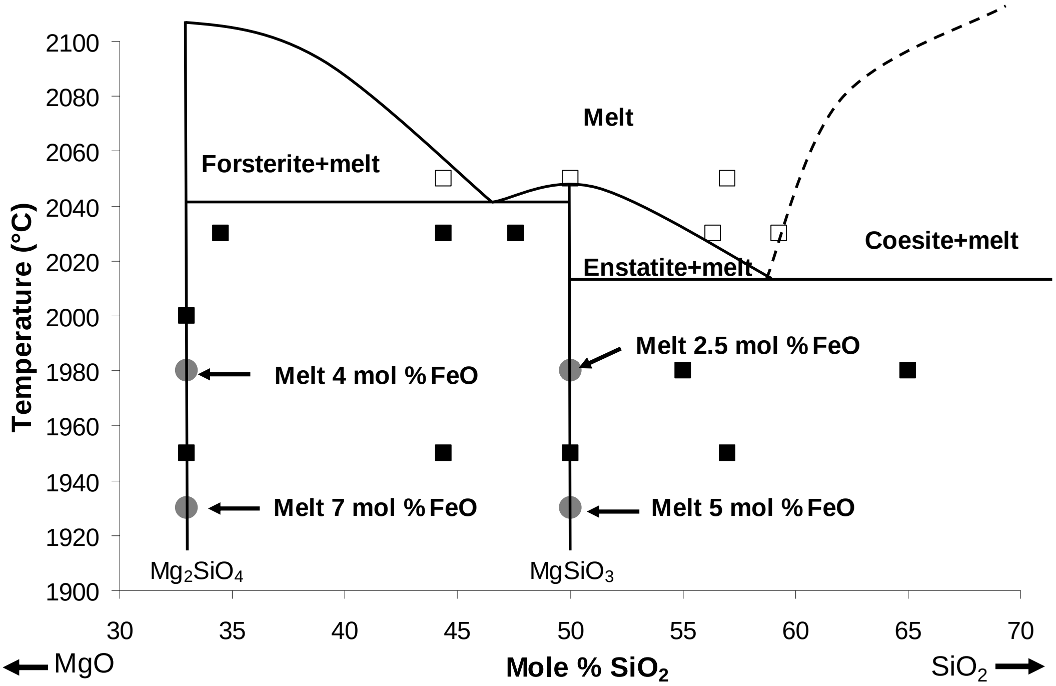

Fig. 3.2-15: Preliminary melting phase relations in the $MgO-SiO_2$ system at 6 GPa. Solid symbols indicate the bulk compositions of solid assemblages, while open symbols indicate melt compositions. The effect of FeO on the melting of olivine and enstatite is also indicated by the grey circles. The molar FeO contents are given for liquids bracketed by the presence of solid and liquid enstatite and olivine.

g. *Ferrous iron partitioning between silicate perovskite and ferropericlase (Y. Nakajima, D.J. Frost and D.C. Rubie)*

$(Mg,Fe)SiO_3$ perovskite (Mg-Pv) and (Mg,Fe)O ferropericlase (Fp) comprise more than 90 vol.% of the Earth's lower mantle. The chemical and physical properties of these phases are, therefore, essential for understanding the structure and dynamics of the lower mantle. The iron content of both phases will influence lower mantle transport properties such as rheology, elasticity, electrical and thermal conductivities. In this study we have examined the exchange coefficient of Fe between Mg-Pv and Fp at the low-oxygen fugacity imposed by the presence of metallic Fe. These conditions ensure low levels of ferric Fe in each phase over the range of composition investigated and thus allow Fe^{2+}-Mg partitioning to be characterized.

Experiments were performed using a multianvil apparatus at 25 GPa and at high temperatures of 2400-2600 K, *i.e.*, close to the silicate solidus, to alleviate kinetic problems observed at lower temperatures in metallic Fe bearing systems. A variety of compositions of

$(Mg,Fe)_2SiO_4$ olivine (Fo#70-95) were prepared as starting specimens and then were packed along with a piece of metallic Fe-wire into an MgO single crystal container. Quantitative chemical analyses were performed by electron microprobe. The oxygen fugacity range in the experiments is 0.4-1.4 log units below the iron-wüstite oxygen buffer.

The Fe^{2+} and Mg exchange equilibrium for Mg-Pv and Fp is

$$MgSiO_3^{Pv} + Fe^{2+}O^{Fp} \leftrightarrow Fe^{2+}SiO_3^{Pv} + MgO^{Fp} \quad (1)$$

The equilibrium coefficient or distribution coefficient is then defined as $K_D = (X_{FeSiO3}^{Pv} / X_{MgSiO3}^{Pv})/(X_{FeO}^{Fp} / X_{MgO}^{Fp})$, where X_i^a is the mole fraction of component *i* in phase *a*. At equilibrium K_D can be equated through the expression:

$$RT \ln K_D = -\Delta G^0(P,T) - W_{FeMg}^{Pv}(1-2X_{FeSiO3}^{Pv}) + W_{FeMg}^{Fp}(1-2X_{FeO}^{Fp}) \quad (2)$$

where R is the gas constant, $\Delta G^0(P,T)$ is the standard state Gibbs free energy change for reaction (1) at the pressure and temperature of interest, and W_{FeMg}^{Pv} and W_{FeMg}^{Fp} are symmetric interaction parameters. The Gibbs free energy change for equilibrium (2) is described by,

$$\Delta G_{P,T}^0 = \Delta H^0 + P\Delta V^0 - T\Delta S^0 \quad (3),$$

where ΔH^0, ΔV^0, and ΔS^0 are changes in enthalpy, volume, and entropy, respectively. Using the present data and results by Frost and Langenhorst (2002; EPSL 199, 227), we can obtain accurate thermodynamic parameters for the reaction (1) over a significant range of temperatures. The fitting result is shown in Fig. 3.2-16.

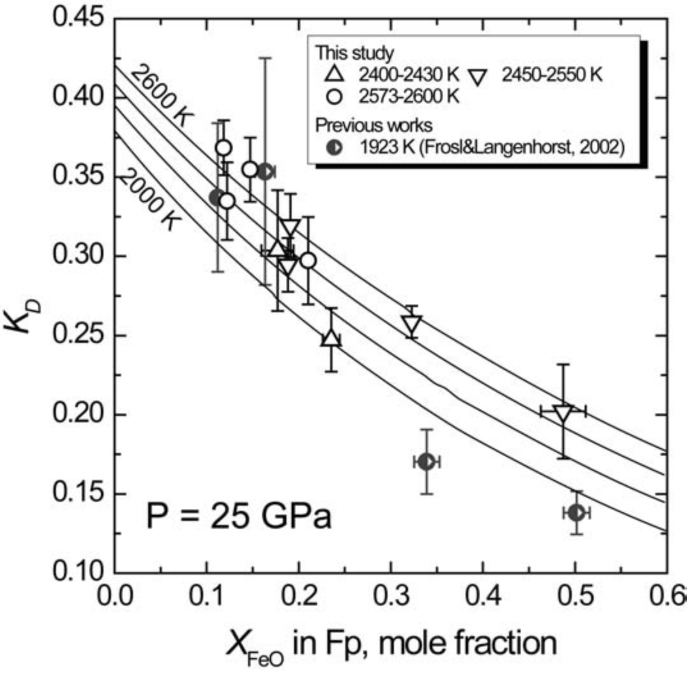

Fig. 3.2-16: Experimental and fitting results of iron partitioning. The distribution coefficients K_D obtained in this study and by Frost and Langenhorst (2002; EPSL 199, 227) are plotted as a function of X_{Fe2+} (=Fe^{2+}/ Fe^{2+}+Mg) of ferropericlase. Solid lines are isothermal K_D (every 200 K) calculated from our results.

With chemical analyses from previous experimental studies at 21-30 GPa, Fe^{2+} contents for Mg-Pv were calculated from the corresponding Fp Fe contents using values of K_D calculated at the P, T conditions of the particular experiments using the thermodynamic parameters obtained in this study. Mg-Pv Fe^{3+} contents were then calculated as the difference between the determined Fe^{2+} contents and reported total Fe content in Mg-Pv (Fig. 3.2-17). For Al-free samples Mg-Pv $Fe^{3+}/\Sigma Fe$ ratios calculated for samples equilibrated in rhenium capsules are in the range 0.1-0.3. The previous experiments with diamond capsules show lower $Fe^{3+}/\Sigma Fe$ values (< 0.1) than those with rhenium capsules and almost negligible ferric iron contents. These estimates show that the Fe^{3+} content of Mg-Pv depends strongly on oxygen fugacity, and varies accordingly with the capsule materials used in experiments.

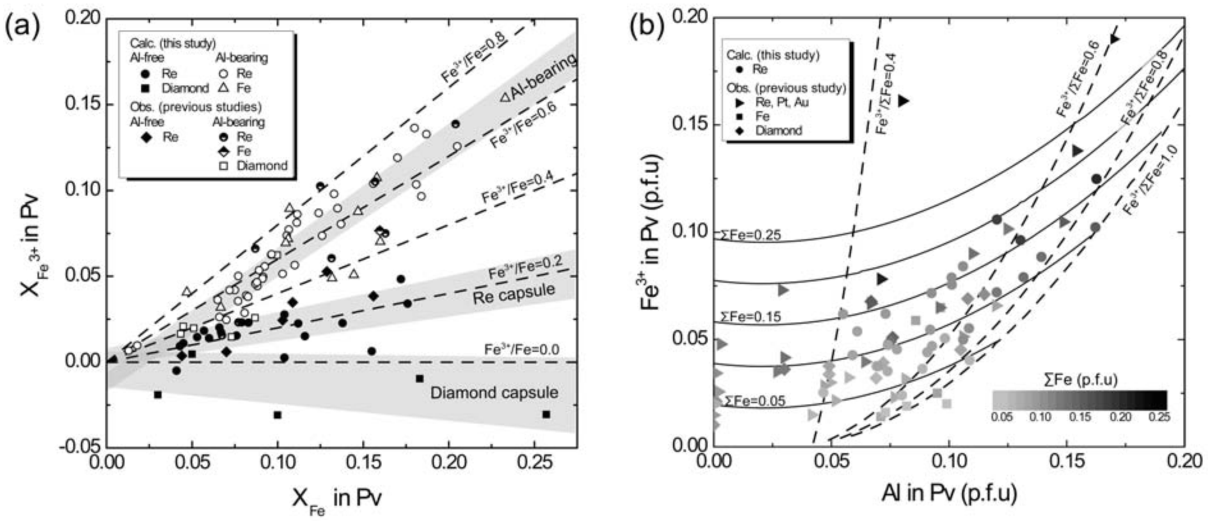

Fig. 3.2-17: (a) Calculated Fe^{3+} contents of perovskite coexisting with ferropericlase in the Al-free and -bearing system. The X_{Fe3+} values are plotted as a function of total iron X_{Fe}. Mg-Pv Fe^{3+} concentrations were calculated for previous experiments in the Al-free and Al-bearing systems with a variety of capsule materials. Broken lines show ferric iron ratios Fe^{2+} / (Fe^{2+} + Fe^{3+}) in Pv. Shaded areas represent linear fitting for data obtained in a variety of capsules and in Al-bearing samples. (b) The relationship between Fe^{3+} and Al concentrations in Mg-perovskite as atoms per formula unit (p.f.u) normalized to two cations. Mg-Pv Fe^{3+} contents are calculated for the previous experimental works using the present thermodynamic model. Observed Fe^{3+} contents of Mg-Pv previously reported are also plotted. Grey scale variation shows the bulk Fe content in Mg-perovskite (Mg-Pv). Solid lines are fitting curves at given total Fe. Broken lines are $Fe^{3+}/\Sigma Fe$ ratios.

For Al-bearing systems, $Fe^{3+}/\Sigma Fe$ ratios are significantly higher than those in the Al-free system and cover a larger range of values 0.2-0.8. Compared with the Al-free system, the influence of capsule materials is negligible. It has been reported that Al contents of Mg-Pv enhances Fe^{3+} contents and the relation between Fe^{3+} and Al contents are nonlinear. We found that Mg-Pv bulk Fe content is also a dominant factor controlling Fe^{3+} contents. At relatively low Al contents less than 0.06-0.08 per formula unit (pfu), the Fe^{3+} contents depend on the bulk Fe contents and weakly on Al contents. At a given bulk Fe content, Fe^{3+} concentration are almost constant or increase slightly up to $Fe^{3+}/\Sigma Fe = 0.5$-0.6 with increasing Al contents. This weaker Al relationship is likely due to trivalent cations being charge balanced by an oxygen vacancy when total trivalent cation concentrations are low *i.e.*, through the components $Mg^{2+}Fe^{3+}O_{2.5}$ and $Mg^{2+}Al^{3+}O_{2.5}$. At higher Al contents (> 0.08 pfu), the Fe^{3+} concentrations increase relatively linearly with Al contents. The linear relationship of Fe^{3+} and Al in Mg-Pv implies the coupled substitution of a $Fe^{3+}AlO_3$ component. This indicates that the substitution mechanism changes at ~ 0.08 pfu of Al, which might be related to the maximum oxygen vacancy level in Mg-Pv.

h. *Ferric iron content of ferropericlase as a function of composition, oxygen fugacity, temperature and pressure: Implications for redox conditions during diamond formation in the lower mantle (K. Otsuka/New Haven, M. Longo/Padova, C.A. McCammon, S.-i. Karato/New Haven)*

The oxidation state of iron in (Mg,Fe)O ferropericlase, the second most abundant phase in the lower mantle, has an important influence in controlling the chemical and physical behaviour of the material including transport properties and phase relations. In ferropericlase, ferric iron (Fe^{3+}) is the most dominant positively-charged point defect, which is charge compensated by the creation of cation vacancies. Therefore, the precise knowledge of Fe^{3+} concentration as a function of composition, oxygen fugacity, temperature and pressure is critical to constrain the charge neutrality conditions and the behaviour of transport properties. Furthermore, an understanding of Fe^{3+} solubility provides an experimental basis for inferring the oxygen fugacity and other thermochemical states in the lower mantle from ferropericlase inclusions encapsulated in diamond.

In this study, we report an investigation of the oxidation state of Fe using the flank method applied to Mg-Fe interdiffusion couples of ferropericlase with a wide range of chemical composition (Mg# 0.44-1) annealed at different pressures (5-24 GPa), temperatures (1673-1873 K) and oxygen fugacities. Oxygen fugacity was controlled by Fe, Ni, Mo, and Re metal capsules and their corresponding oxide phases. Based on our results and available experimental data, we derived an equation for the Fe^{3+} solubility in ferropericlase applicable to depths at the top of the lower mantle: $[Fe^{3+}] = C\ (X_{Fe}^{4}\ fO_2)^{m} \exp\{-((1-X_{Fe})E^*_{Mg}+X_{Fe}E^*_{Fe}+PV^*)/RT\}$, where $C = 2.6(1)\times10^{-3}$, $m = 0.114(3)$, $E^*_{Mg} = -35(3)$ [kJ/mol], $E^*_{Fe} = -98(2)$ [kJ/mol], and $V^* = 2.09(3)$ [cm^3/mol]. The value of the oxygen fugacity exponent m implies that Fe^{3+} mostly occupies tetrahedral sites under these conditions, which is consistent with the results of previously reported Mössbauer spectroscopy studies.

Based on this relationship, we estimated the redox conditions of ferropericlase inclusions preserved in natural diamonds believed to have come from the lower mantle. Although the bulk lower mantle is thought to be at relatively reduced conditions due to the presence of (Fe,Ni) metal, the majority of previously reported Fe^{3+} concentrations occur at oxidized conditions (Fig. 3.2-18). Interestingly, such redox conditions coincide with the upper stability limit of diamond in mantle peridotite at adiabatic or slightly superadiabatic temperature near the top of the lower mantle. We thus infer that ferropericlase inclusions recorded and preserved the redox conditions at which host diamonds was precipitated from carbonates or carbonatite melts. Diamond formation through decarbonation reactions in the lower mantle is consistent with the model of redox freezing and melting, where redox conditions change dramatically due to the change in the capacity of mantle phases to incorporate Fe^{3+}. We cannot, of course, exclude the possibility that the inclusions equilibrated at greater depths in the lower mantle. At such depths, however, the capacity of mantle phases to incorporate Fe^{3+} remains relatively high; hence the oxidation of diamond to produce carbonate melts may not occur in deeper parts of the lower mantle.

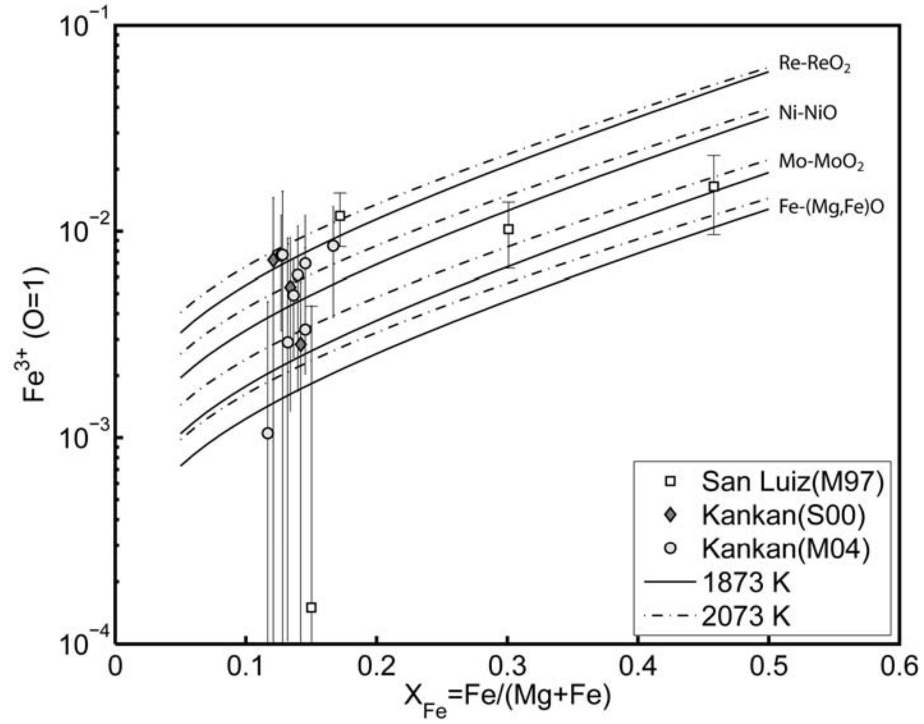

Fig. 3.2-18: Fe^{3+} concentration in ferropericlase inclusions in lower mantle diamonds from San Luiz (M97: McCammon *et al.*, 1997) and Kankan (S00: Stachel *et al.*, 2000; M04: McCammon *et al.*, 2004) compared with values calculated using the derived equation of Fe^{3+} solubility at a pressure of 23 GPa, temperatures of 1873 and 2073 K, and oxygen fugacity buffered by Re-ReO_2, Ni-NiO, Mo-MoO_2, and Fe-(Mg,Fe)O.

i. *Garnet peridotite oxythermobarometry at high pressure and temperature (D. Ojwang, V. Stagno and D.J. Frost)*

The oxygen fugacity at which rocks have equilibrated can be determined through oxy-thermobarometry, which employs redox equilibria between components in mineral phases. To date, the only equilibrium routinely used for garnet-peridotite rocks is,

$$2Fe_3^{2+}Fe_2^{3+}Si_3O_{12} \quad = \quad 4Fe_2SiO_4 \quad + \quad 2FeSiO_3 \quad + \quad O_2 \qquad (1)$$

Garnet Olivine Orthopyroxene

The fO_2 of this equilibrium is calculated from the expression,

$$\log fo_2 = \frac{-\Delta G_r^o}{\ln(10)RT} + 2\log a_{Fe_3Fe_2Si_3O_{12}}^{Gt} - 2\log a_{FeSiO_3}^{Opx} - 4\log a_{Fe_2SiO_4}^{olivine} \qquad (2)$$

where $a_{FeSiO_3}^{Opx}$ refers, for example, to the activity of the $FeSiO_3$ component in orthopyroxene, ΔG_r^O is the standard state free energy of equilibrium (1) and R is the gas constant. The first term in equation (2) can be defined in terms of the equilibrium constant,

$$\log K_1 = \frac{-\Delta G_r^O}{RT\ln(10)} \qquad (3)$$

which, if a suitable activity composition model is employed, should be a constant at a given pressure and temperature. An expression for log K can be derived from thermodynamic data available in the literature, however, experimental data are required then to check whether the oxygen fugacity calculated using equation (2) is indeed correct.

In this study experiments were performed to test the validity of equation (2) for calculating fO_2 at high pressure and temperature. To determine the fO_2 using equation (2) the Fe^{3+} content of garnet needs to be measured with Mössbauer spectroscopy and to determine the accuracy of the equilibrium an independent assessment of the fO_2 must be made. In this study the fO_2 is measured independently using the equilibrium,

$$Fe_2SiO_4 \quad = \quad SiO_2 \quad + \quad 2Fe \quad + \quad O_2 \qquad (4)$$

Olivine alloy

Where the alloy is an Fe-Ir alloy the composition of which becomes sensitive to the imposed fO_2.

The experiments are performed using a starting mineral mixture of olivine, orthopyroxene and garnet in addition to Fe-Ir alloy and graphite and carbonate phases. The fO_2 is nominally buffered by the coexistence of graphite/diamond and carbonate minerals and melts. Graphite capsules are employed inside a Re foil sleeve. In addition, within each experiment a monomineralic layer of garnet is also placed sandwiched between mineral mixes. The layer of garnet is required to facilitate Mössbauer measurements of the Fe^{3+} content of the equilibrium garnet. Many different garnet starting materials were employed. Initially reduced nominally Fe^{3+} free glass was used, however natural garnet layers were also examined in addition to garnet glass compositions that contained 60 % of the total Fe as Fe^{3+}. Experiments were performed in a multianvil press between 3 and 7 GPa.

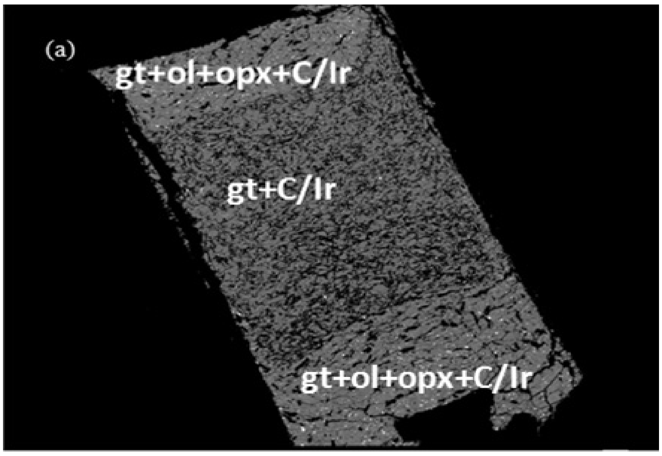

Fig. 3.2-19: Back-scattered electron image showing an experimental run product. A garnet layer formed from oxidised glass contains graphite and Ir-Fe alloy. The layer is sandwiched between layers of mixed garnet, olivine and orthopyroxene in addition to graphite and Fe-Ir alloy. Width of sample is 2 mm.

Figure 3.2-19 shows the results of a garnet layer experiment where the starting material for the garnet layer was an oxidised glass composition. The garnet glass was mixed with carbon and was reduced during the experiment. The fO_2 can be determined through equilibrium (4) and then used with equation (2) to calculate log *K* for equilibrium (1). Figure 3.2-20 shows the results of such a calculation for all the experiments. Log *K(1)* should be a constant at a given P and T and the experimentally determined values are compared with curves calculated from thermodynamic data in the literature. Experimental data at 3 GPa are reasonably consistent with the thermodynamic estimate. As a result of the volume change predicted for equilibrium (1), however, the thermodynamic model predicts a decrease in K with pressure, while the experimental data predicts an increase. The origin of this discrepancy is unclear. It is unlikely to result from an inaccurate estimate of the volume change for equilibrium (1) and is more likely to reflect differences in excess volumetric properties of the garnet solid solutions. If correct, however, the experimental results imply that oxygen fugacities calculated using this oxy thermobarometer are higher at higher pressure than previously considered.

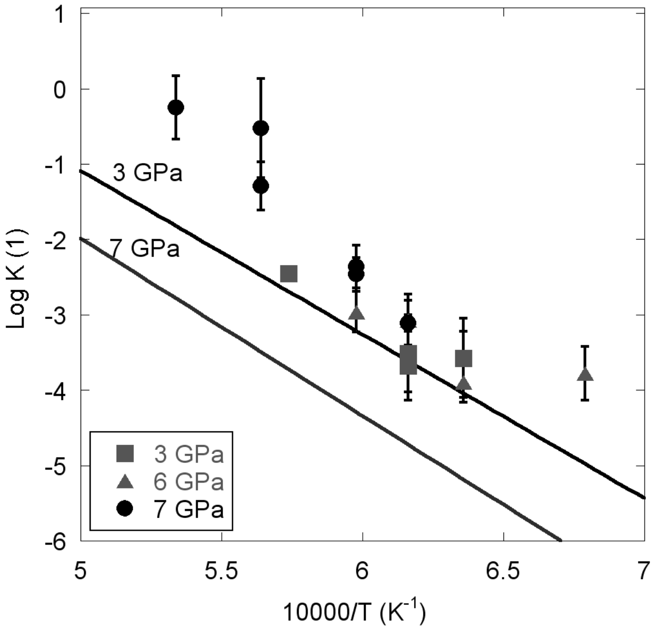

Fig. 3.2-20: Log *K(1),* the equilibrium constant for equilibrium (1) plotted against inverse temperature for experiments performed between 3 and 7 GPa. *K* is calculated using compositional data determined in this study and the fO_2 determined from the Fe-Ir-alloy sensor. Plotted for comparison are curves for Log *K* calculated from thermodynamic data in the literature. As can be seen the pressure dependence of the experimental data seems to be opposite to that predicted from the thermodynamic data.

j. *The oxygen fugacity of eclogitic rocks (V. Stagno/Washington, D.C., D.J. Frost and C. McCammon)*

Eclogitic rocks occur as xenoliths from deep cratonic lithosphere. Diamonds are often associated with eclogites and for this reason it is of interest to be able to determine the fO_2 in such assemblages and in particular to determine the fO_2 at which carbonate melts reduce to form diamonds. A further aspect is to understand the coincident iron redox equilibria that occur in such rocks and to determine the effects of pressure on redox reactions that would occur in eclogitic rocks during subduction. It is plausible that as pressures increase oxygen fugacities decrease in eclogitic rocks as a result of ferric/ferrous component equilibria being driven in a particular direction. This could result in carbonates being reduced to graphite or diamond in subducting eclogites simply due to the change in pressure.

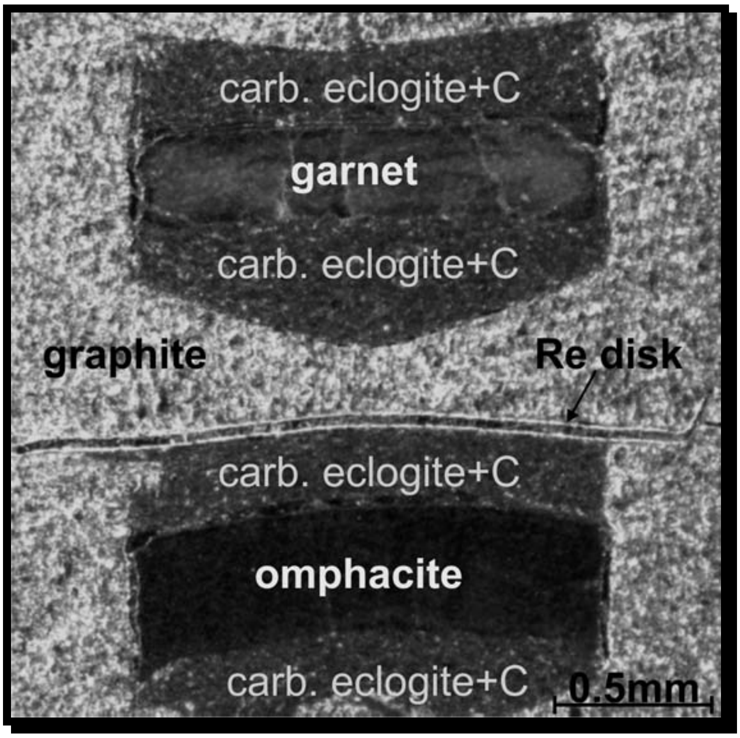

Fig. 3.2-21: Binocular microscope photograph of a recovered capsule showing two experimental charges in graphite sleeves. Both charges consist of carbonated eclogite layers sandwiching a monomineralic garnet layer in the upper change and an omphacitic pyroxene in the lower. Monomineralic layers are to facilitate Mössbauer spectroscopy measurements.

The coexistence of carbonate minerals and graphite/diamond in eclogites under subsolidus conditions is controlled by the equilibrium DCDD,

$$\underset{\text{dolomite}}{CaMg(CO_3)_2} + \underset{\text{coesite}}{2SiO_2} = \underset{\text{diopside}}{CaMgSi_2O_6} + \underset{\text{graphite/diamond}}{2C} + O_2 \qquad [1]$$

Although the fO_2 buffered by this reaction can be calculated from thermodynamic data, there are uncertainties surrounding the thermodynamic properties of dolomite and such calculations cannot, of course, be performed effectively above the carbonate solidus. We require an assemblage that enables us to measure the fO_2 buffered by equilibria involving graphite or diamond and carbonate minerals or melt in an eclogite assemblage.

We have performed a series of experiments on carbonated eclogite compositions where the fO_2 was measured using a sliding redox sensor. 5 wt.% of iridium metal was added to the starting charge as a redox sensor and following equilibrium was employed to then measure fO_2,

$$\underset{\text{garnet}}{Fe_3Al_2Si_3O_{12}} = \underset{\text{kyanite}}{Al_2SiO_5} + \underset{\text{coesite}}{2SiO_2} + \underset{\text{alloy}}{3Fe} + 1.5O_2 \qquad [2]$$

where the oxygen fugacity is calculated by,

$$\log f_{O_2} = \frac{-\Delta G^o[2]}{1.5RT\ln(10)} - 2\log a_{Fe}^{metal} + \frac{2}{3}\log a_{Fe_3Al_2Si_3O_{12}}^{Garnet}$$

Mineral starting mixtures of natural kyanite, quartz, synthetic omphacite, synthetic garnet, graphite, $MgCO_3$, $CaCO_3$ and Na_2CO_3 were run in multianvil apparatus at pressures between 3 and 7 GPa and temperatures of 800-1300 °C. Starting powders were placed within graphite liners inside platinum capsules. In most experiments monomineralic layers of garnet and omphacite were also placed between layers of the carbonate bearing eclogitic material in order to facilitate sufficient material for Mössbauer spectroscopy determinations of $Fe^{3+}/\Sigma Fe$ ratios. Recovered charges such as that shown in Fig. 3.2-21 were analyzed to determine mineral and carbonate melt compositions and the fO_2 was then calculated from the garnet and alloy compositions using equation 3.

Figure 3.2-22 shows the results of the experiments where the fO_2 buffered by an eclogite assemblage containing both graphite, or at high pressure diamond, and carbonate minerals or melts is indicated. At oxygen fugacities above each data point carbonates are stable in the eclogite assemblage, while below graphite or diamond form. For comparison the same carbon-carbonate buffer is shown for peridotite rocks determined through the use of similar experiments. The implication is that the carbonate stability field extends to lower fO_2 in eclogitic rocks compared to peridotites, potentially implying that carbonate melts have greater mobility in mantle eclogites compared to peridotite rocks. To fully employ these data, however, requires some knowledge of the complimentary Fe redox reactions in eclogites, which will be obtained from these experiments once all monomineralic omphacitic and garnet layers have been analyzed to determine the $Fe^{3+}/\Sigma Fe$ ratio using Mössbauer spectroscopy.

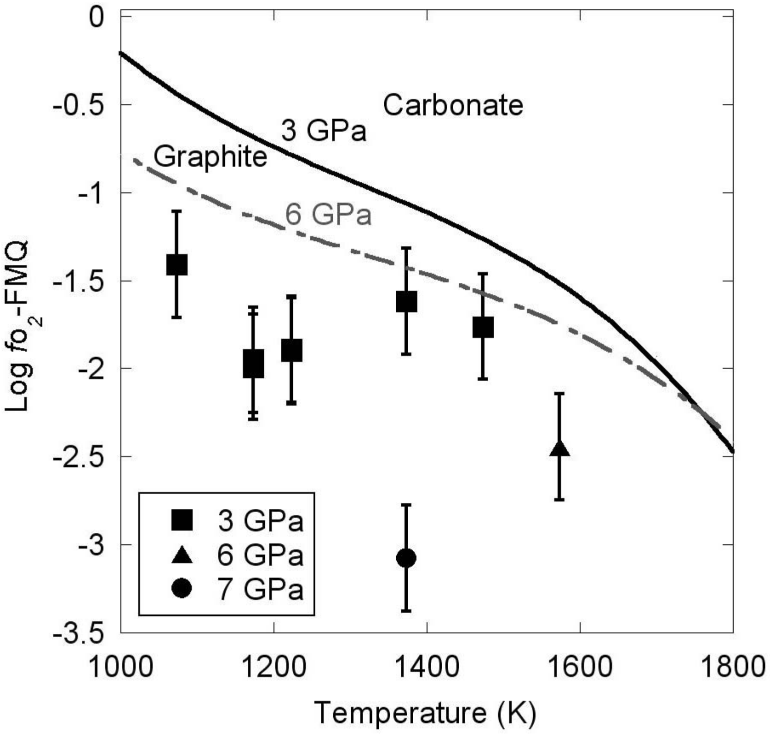

Fig. 3.2-22: Oxygen fugacities (normalized against the FMQ buffer) determined for eclogite assemblages buffered through the equilibrium between graphite or diamond and carbonate minerals or melts. Curves calculated for the same carbon-carbonate equilibrium in peridotite rocks are shown for comparison, calculated at 3 and 6 GPa. The stability fields of graphite and carbonate in peridotites at 3 GPa is indicated.

k. *Trace element partitioning between clinopyroxene, garnet and melt in a hydrous eclogitic system (C. Beyer, D.J. Frost and A. Audétat)*

Eclogitic rocks occur as xenoliths from cratonic lithosphere. An important issue is to be able to determine the temperature, pressure and oxygen fugacity of equilibration of these xenoliths using major and trace element partitioning relations between the main minerals. There is abundant evidence that cratonic rocks have equilibrated with ephemeral melts or fluids. In addition at conditions of the Archean lithospheric geotherm experimental equilibration between minerals is virtually impossible in the absence of a melt phase. To date most of the high-pressure experimental trace element studies on garnet and clinopyroxene were carried out in simplified systems (*e.g.*, CMASF) or in more complex basaltic/eclogitic but dry systems. The effect of H_2O or CO_2 on the partition coefficients has not been studied, however the presence of such volatile species is essential for the formation of melts in the lithospheric mantle.

We are investigating the partitioning of trace elements (first row transition metals, Ga, Ge, Y, Li, Na) between garnet solid solutions, omphacite and corresponding quenched melt in a hydrous natural eclogitic system containing ~ 2 % water under upper mantle conditions (3-6 GPa and 1200-1400 °C). Experiments are performed in the multianvil using a range of capsule materials, such as Re, Pt and graphite to impose different oxygen fugacities. The presence of a melt phase not only aids equilibrium but promotes the growth of large mineral grains that can be analyzed using the laser ablation ICPMS.

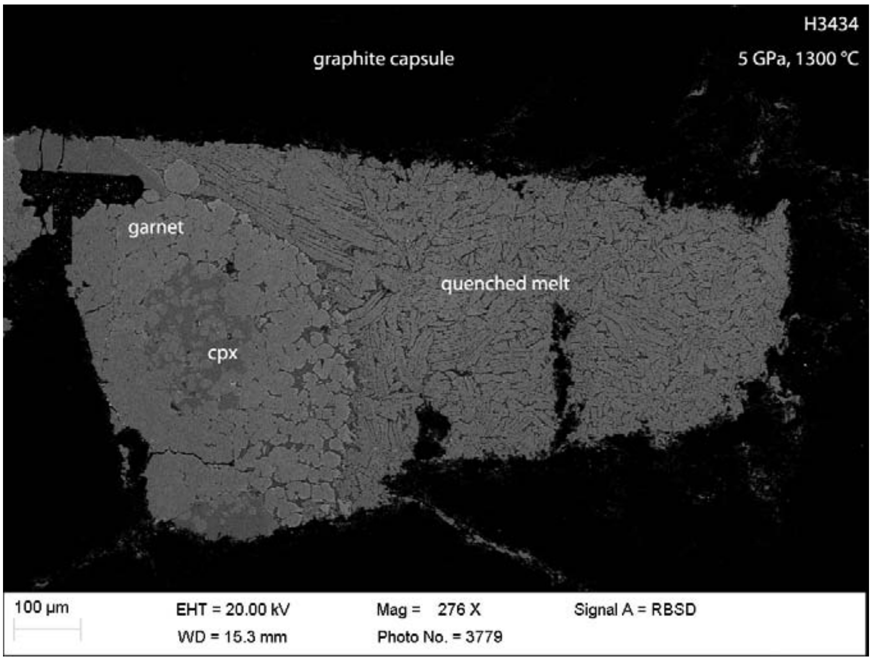

Fig. 3.2-23: BSE-image of a run from 5 GPa and 1300 °C. A large pool of hydrous quenched melt coexists with an eclogitic assemblage comprising clinopyroxene and garnet. The sample is inside a graphite capsule.

A recovered experimental change from an experiment at 5 GPa and 1300 °C is shown in Fig. 3.2-23. The garnet solid solution comprises 53 % pyrope, 20 % almandine, 25 % grossular and minor amounts of NaTi-garnet and majorite. The coexisting omphacite contains 34.2 % jadeite. The results of trace element analyses performed using LA ICP-MS are reported in Fig. 3.2-24. By making a comparison with lower pressure studies changes in the partitioning of Y and Ti between garnet and clinopyroxene can be recognised that look promising as indicators of pressure.

The next step will be to perform experiments at a range of oxygen fugacities. In order to perform these experiments, we will use a double capsule setup built up of an inner graphite capsule with the sample material and an outer noble metal capsule. The outer capsule will be filled with a buffer material (mixture of oxides, hydroxides, and carbonates) according to the conditions we want to maintain. Inherent in these experiments will be a variation in the volatile speciation of the melt phase from CO_2-rich conditions at moderately oxidizing conditions to H_2O-rich at more reduced conditions.

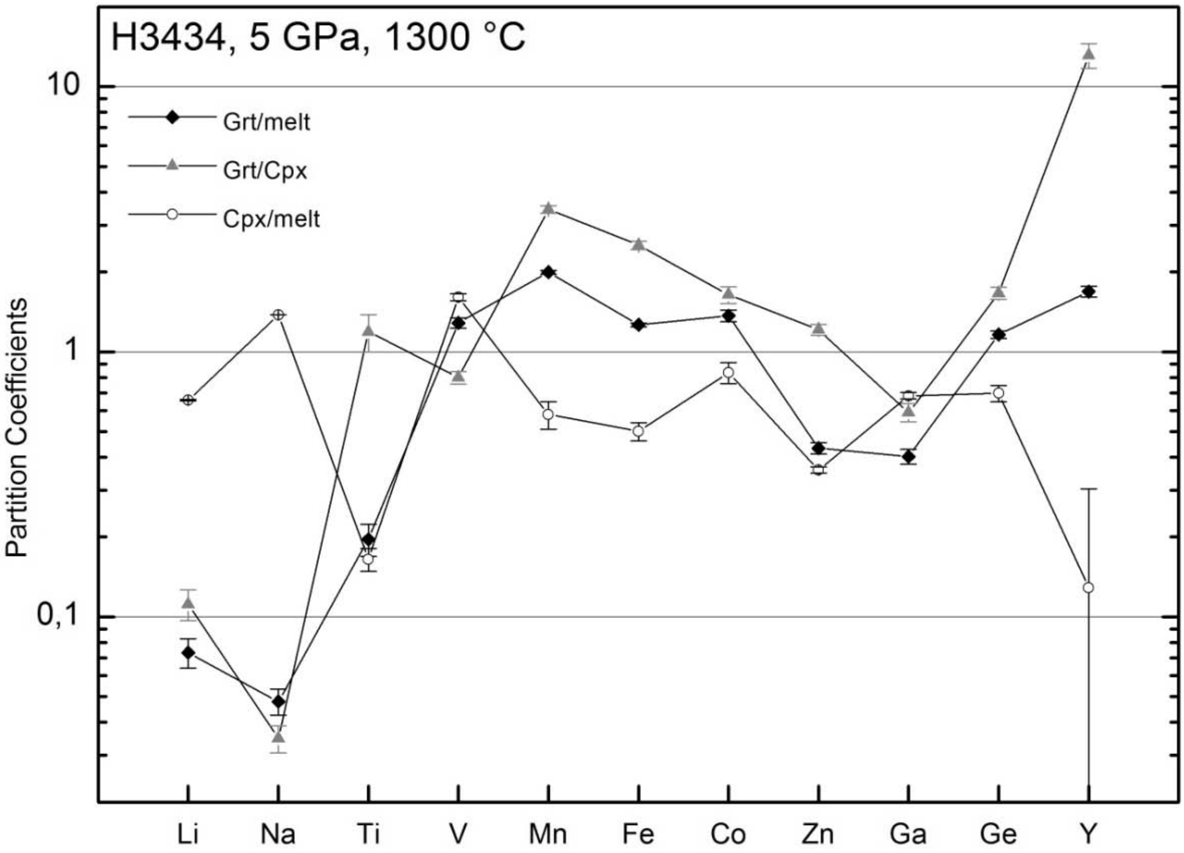

Fig. 3.2-24: Spidergram which depicts the partition coefficients between garnet, omphacite and melt for a range of trace elements. Error bars are shown as one standard error.

l. *Nitrogen solubility in mantle minerals (Y. Li, M. Wiedenbeck/Potsdam, S. Shcheka and H. Keppler)*

The Earth's atmosphere is generally thought to have formed by degassing of the Earth´s interior. If one assumes a chondritic composition of the bulk Earth, mantle and core may still be major nitrogen reservoirs. However, little is known about how much nitrogen could be retained in mantle minerals during the cooling of the magma ocean in the Earth's early history or in residual mantle minerals after partial melting. Consequently, it is not known how efficiently nitrogen could have degassed into the Earth's early atmosphere and the nitrogen abundance in the bulk silicate Earth is poorly constrained. Therefore, we conducted a systematic study of nitrogen solubility in mantle minerals including olivine, clinopyroxene, orthopyroxene, garnet, and spinel. The experiments were done in a piston cylinder apparatus. The temperatures and pressures ranged from 1000 to 1300 °C and from 15 to 35 kbar, to simulate conditions typical of the upper mantle. The minerals were synthesized from well-mixed high purity oxides and hydroxides. About 5 wt.% ^{15}N-labeled $^{15}NH_4{}^{15}NO_3$ was added to the starting mixture as nitrogen source. A modified double capsule technique was used to control oxygen fugacity by three different buffers (Fe-FeO, Co-CoO, Ni-NiO). A total of 52 experiments has been performed to study the effect of oxygen fugacity, pressure, temperature, and chemical compositions on the nitrogen solubility in mantle minerals, and the samples have been prepared for secondary ion mass spectrometer (SIMS) measurement at GFZ Potsdam. First test measurements show that the solubility of nitrogen in olivine, garnet and pyroxenes is very low (< 5 ppm) under oxidizing conditions. However, the solubility under reducing conditions is increased up to 200 ppm in pyroxenes and garnet possibly due to the incorporation of NH_4^+. The primary results demonstrate that the reduced Earth's young mantle must retain a large amount of nitrogen and the presently still reduced lower upper mantle may be an important nitrogen reservoir.

m. *Mo-Ce-W-U-Th systematics in arc magmas: an indicator of fluid salinity and oxygen fugacity in the source of Island Arc basalts (E. Bali/Göttingen and H. Keppler)*

We have studied the solubility of W- and Mo-oxide in aqueous fluids and mantle minerals at 26.1 kbar, 600 to 800 °C at variable controlled oxygen fugacity conditions, relevant to subduction zones. We observed that the solubility of W-oxide in aqueous fluids is only slightly dependent on fO_2 between conditions buffered by CoCoO and $ReReO_2$. In contrast, Mo-oxide solubility is strongly dependent on both oxygen fugacity and fluid salinity at the same conditions. At 26.1 kbar, in the fO_2 range between CoCoO and $ReReO_2$ their solubility can be formulated by the following equations:

$$\log W = 0.07 * \log fO_2 - 4.7236 * 1000/T + 4.4271$$

and

$$\log Mo = 0.435 * \log fO_2 + 0.42 * \log Na - 1.8 * 1000/T + 4.8$$

where W, Mo and Na are concentrations in molalities, fO_2 is oxygen fugacity in bar and T is temperature given in Kelvins.

Both W and Mo are incompatible in the structure of major mantle minerals (including garnet and clinopyroxene) in the presence of aqueous fluid, but they are compatible in rutile. Thus, the presence or absence of rutile controls the mobility of these elements at mantle conditions.

Based on the determined partition coefficients we calculated the composition of aqueous fluids released from an N-MORB eclogite source (Fig. 3.2.-25). We found that the Mo-Ce-W-Th-U systematics of arc magmas can generally be modeled by the mixing of depleted mantle with an aqueous fluid phase that was released from a rutile-bearing N-MORB source in fO_2-conditions between FMQ-1.6 and FMQ+1.7 having a maximum salinity of 20 % $NaCl_{equiv}$ (Fig. 3.2-25). Moreover, Mo/W ratios are found to be indicative of oxygen fugacity during mantle melting.

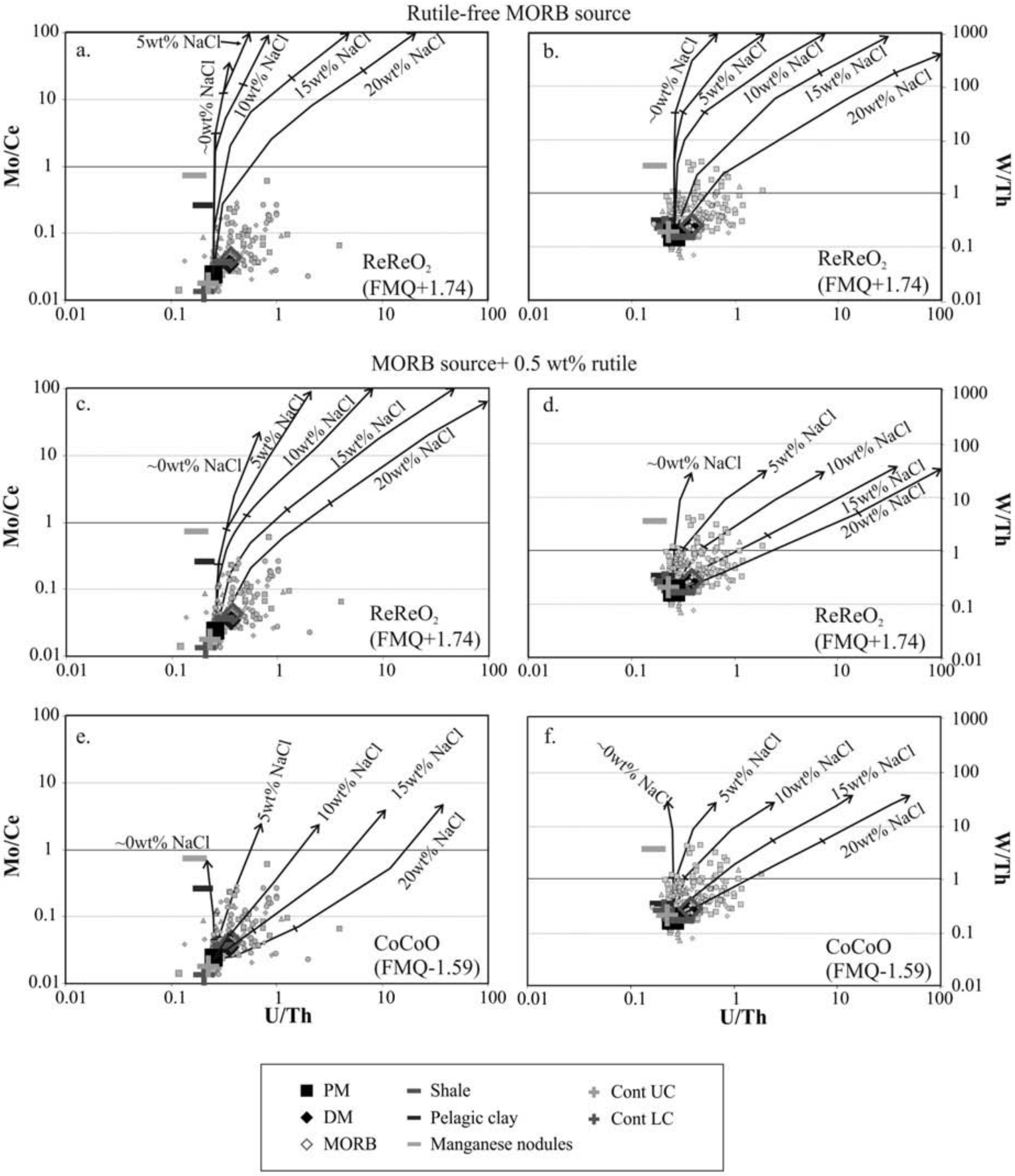

Fig. 3.2-25: Relationship between Mo/Ce, W/Th and U/Th distribution in various sets of primitive arc magmas. Figures also contain the composition of primitive mantle (PM), depleted mantle (DM) and marine sediments, continental lower (ContLC) and upper crust (ContUC) as possible source contaminants. Arrows indicate mixing lines between primitive mantle and aqueous fluid released from N-MORB eclogite. The hypothetic eclogite had a garnet to cpx ratio of 30:70; and contained 0 (a, b), or 0.5 wt.% (c-f) of rutile. The released fluid had a salinity of 0 to 20 wt.% $NaCl_{equiv}$. Fluid compositions were calculated in equilibrium with $ReReO_2$ and CoCoO buffers, which correspond to ~FMQ+1.7 and ~FMQ-1.6 at 26.1 kbar and 1000 °C. U, Th and Ce partition coefficients for garnet, clinopyroxene and rutile are from the literature. Marks on mixing lines indicate fluid contributions of 1 wt.%.

n. *The titanium-in-quartz (TitaniQ) thermobarometer: A critical examination and re-calibration (R. Huang and A. Audétat)*

The titanium-in-quartz thermometer was recently found to be dependent also on pressure (Thomas *et al.*, CMP 160:743, 2010). The pressure effect was calibrated in the range of 5 to 20 kbar. In an attempt to extend this calibration to lower pressures we obtained results that are in strong disagreement with the previous data. In contrast to the previous experiments, in which quartz was synthesized from amorphous SiO_2 and TiO_2 powder, we grew our quartz by dissolution and reprecipitation of quartz in a small thermal gradient. Slightly higher temperatures in the upper part of the assembly resulted in partial dissolution of the upper quartz piece and re-precipitation of SiO_2 onto the lower piece. Experiments in which time markers were generated by small pressure drops show that variations in the thickness of new quartz overgrowth are directly proportional to growth rate. Furthermore, rapid attainment of TiO_2 saturation in the fluid is demonstrated by the occurrence of euhedral rutile crystals at the contact between old quartz substrate and new quartz overgrowth. Titanium concentrations in old quartz and new quartz of various thickness were measured by laser-ablation ICP-MS.

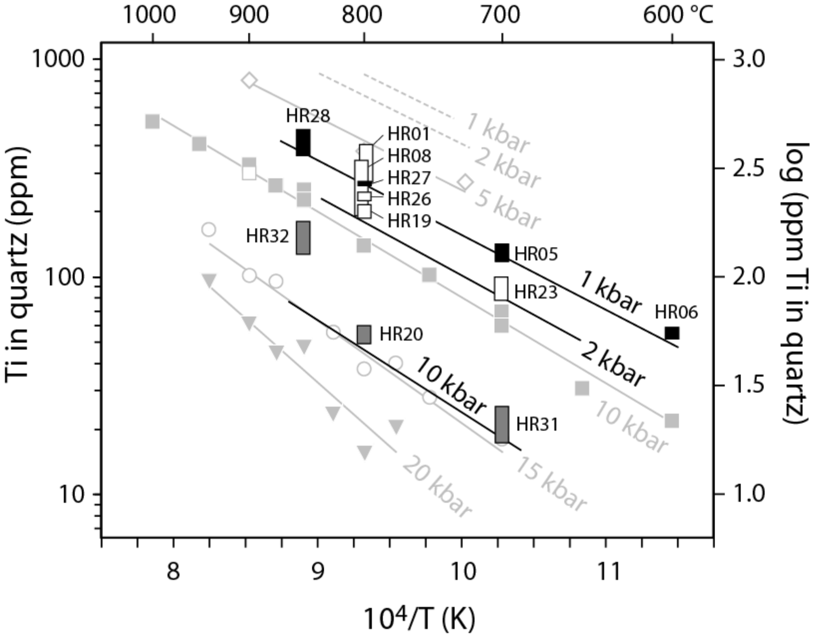

Fig. 3.2-26: Comparison of our experimental data with those of Thomas *et al.* (2010). Black boxes: 1 kbar data; white boxes: 2 kbar data; grey boxes: 10 kbar data. Black lines represent isobars calculated by equation (1), which was fitted through the lowest Ti concentration / most slowly grown quartz obtained at each P-T condition (excluding sample HR32, which Ti content is deemed too high because of rapid crystal growth). The calibration of Thomas *et al.* (2010) is shown in light gray.

Titanium concentrations in new quartz overgrowth depend strongly on growth rate and correlate positively with the concentrations of Al, Li and Na in individual experiments, but otherwise show no dependence on the abundance of the latter elements. This implies that rapid crystal growth leads to a high abundance of all trace elements. Consequently, the composition of the most slowly grown quartz should be closest to equilibrium. Titanium concentrations in our most slowly grown quartz are about three times lower than those obtained by Thomas *et al.* (2010) (Fig. 3.2-26). This may be explained by the fact that our quartz samples grew 10-50 times slower than the samples analyzed by Thomas *et al.* (2010). Our data can be fitted by the equation

$$\log \mathrm{Ti}\ (\mathrm{ppm}) = -\,0.27943 \cdot 10^4/T - 660.53 \cdot (P^{0.35}/T) + 5.6459 \qquad (1)$$

where T is given in Kelvin and P in kbar.

An independent test was made by analyzing igneous quartz from eight plutonic / volcanic magma systems that crystallized at known conditions of 0.8-2.7 kbar and 675-780 °C. The activity of TiO_2 in these magmas was constrained by the composition of melt inclusions analyzed next to the investigated quartz. To allow comparison with experimentally derived TiO_2 solubilities, the Ti contents of the natural quartz samples were re-calculated to a TiO_2 activity of unity. Although the results depend significantly on the model chosen to calculate TiO_2 activity, they agree much better with our calibration than with those of Thomas *et al.* (2010) (Fig. 3.2-27).

If the TiO_2 activities calculated based on the Hayden and Watson (EPSL 258:561, 2007) model are correct, then our calibration would be still not perfect. It would mean that even our most slowly grown quartz contained excess Ti, and that it would be practically impossible to calibrate TitaniQ by means of hydrothermal experiments. In either case, our findings imply that TitaniQ should not be applied to quartz grown from hydrothermal fluids, because growth rates in these environments are extremely variable. TitaniQ is more likely to work in igneous quartz, but the present models for TiO_2 solubility in both quartz and silicate melts may still need to be refined before accurate results can be obtained.

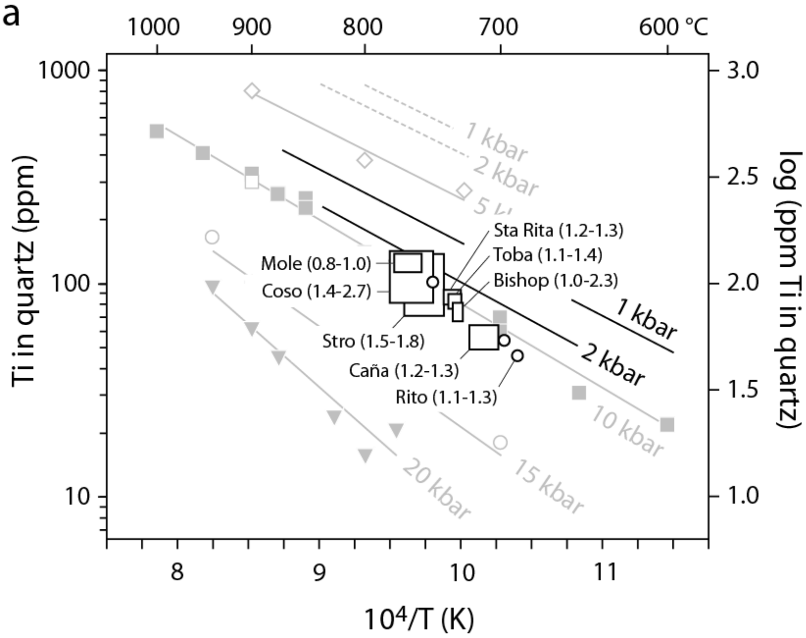

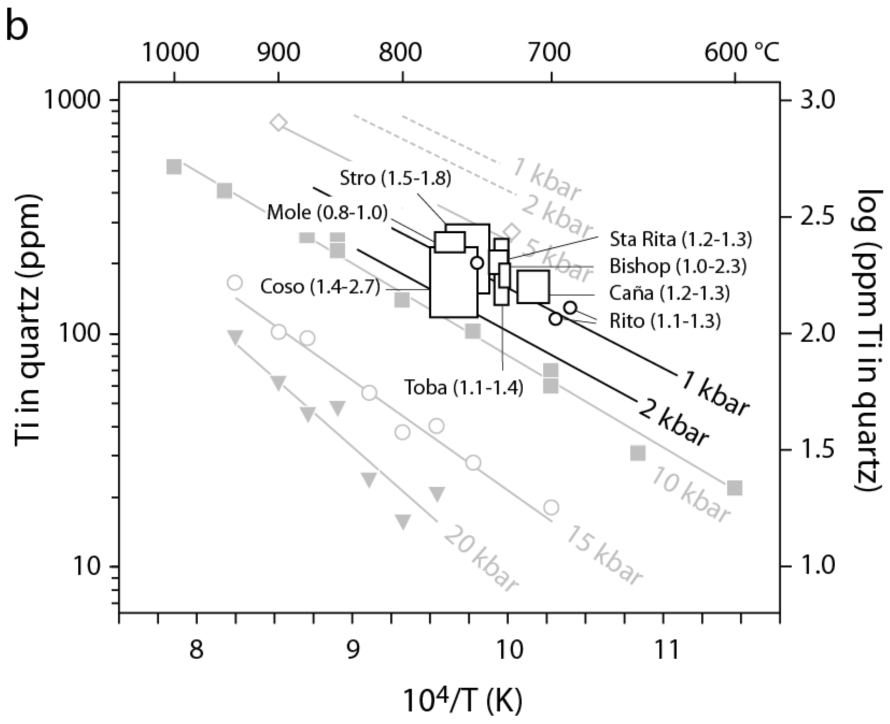

Fig. 3.2-27: (a) Titanium concentrations of natural igneous quartz crystallized at known pressure and temperature, recalculated based on the TiO_2 solubility model of Hayden and Watson (EPSL 258:561, 2007) to a TiO_2 activity of unity. Independent pressure estimates (in kbar) are shown in parentheses behind the sample names. Black lines represent isobars calculated by equation (1); the calibration of Thomas *et al.* (2010) is shown in light grey. (b) Same plot as above, but with TiO_2 activities calculated using MELTS.

o. *Vanadium partitioning between hydrous rhyolite melt and magnetite (L. Zhang and A. Audétat)*

Vanadium occurs in various oxidation states and thus its partitioning behaviour between minerals and silicate melt is sensitive to redox conditions. This characteristic of vanadium could become particularly useful for felsic magma systems, for which fO_2 commonly is difficult to estimate. In terrestrial samples vanadium occurs mostly as V^{3+} in spinel, and as V^{4+} and V^{5+} in silicate melts. The partitioning of vanadium between magnetite and melt thus depends on fO_2 and can potentially be used as an oxybarometer. Corresponding calibrations have already been performed in mafic melt systems.

In this study we measured vanadium partitioning between hydrous rhyolite melt and (titano-) magnetite at different temperatures (from 750 to 850 °C), magnetite compositions, oxygen fugacities (from Ni-NiO to MnO-Mn_3O_4) and sulfur fugacities, all at a fixed pressure of 200 MPa. Three approaches were used to conduct the experiments: (1) magnetite was grown from the decomposition of pyrrhotite; (2) V-free magnetite was equilibrated with V-bearing melt;

and (3) V-rich magnetite was equilibrated with V-free melt. After 7-10 days run time, recovered glass samples and contained magnetite inclusions were analyzed by LA-ICP-MS.

Measured magnetite/melt partition coefficients of vanadium range from about 30 to 3600 and are the same in both forward and reverse runs, suggesting that equilibrium was obtained (Fig. 3.2-28).

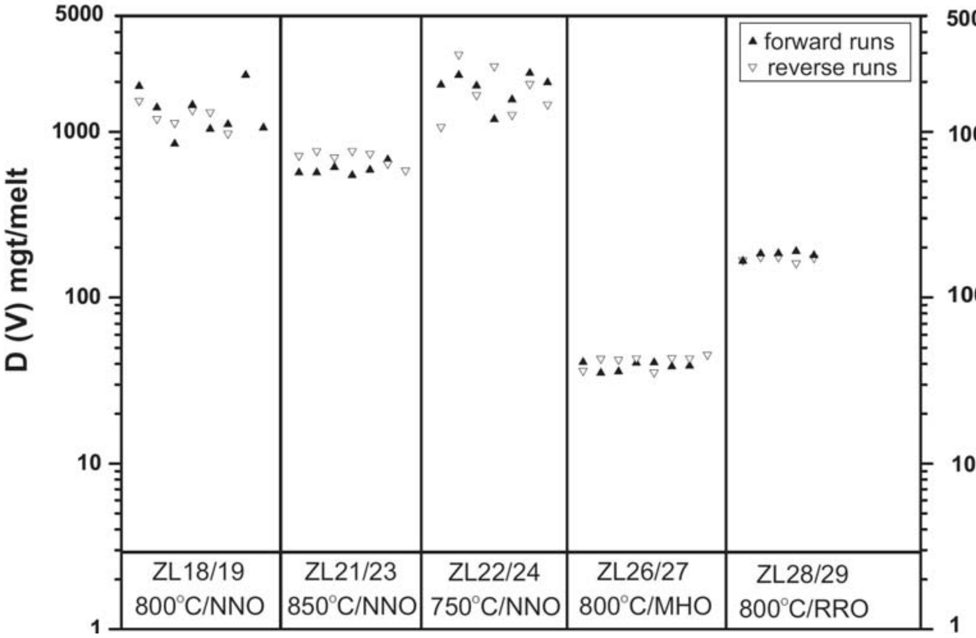

Fig. 3.2-28: Summary of data from equilibration runs performed at different temperatures and oxygen fugacity conditions. Buffer conditions: NNO-Ni/NiO; RRO-Re/ReO_2; MHO-MnO/Mn_3O_4. Each data point represents a partition coefficient derived from the analysis of one magnetite inclusion and surrounding silicate melt. Solid triangles represent forward runs in which V-bearing glass equilibrated with magnetite; open triangles represent reverse runs in which glass was equilibrated with V-doped magnetite. The similarity of $D_V^{mgt/melt}$ in forward and reverse runs suggests that equilibrium was attained.

Magnetite/melt partition coefficients of vanadium increase with temperature, but decrease with oxygen fugacity (Fig. 3.2-29). The TiO_2 content of magnetite has only a small effect on vanadium partitioning, whereas sulfur fugacity has no effect on vanadium partitioning. Our partitioning data can be fitted by following equation:

$$\log D_V^{mgt/melt} = -5713.19/T - 0.44 \log fO_2 + 2.31 \qquad (1)$$

where $D_V^{mgt/melt}$ is the partition coefficient of vanadium between magnetite and melt, fO_2 is oxygen fugacity in bar, and T is temperature in Kelvin. The observed dependence on fO_2 suggests that the dominant valence of V in the melt is V^{5+}. In comparison with previous studies performed on basaltic melt systems, our vanadium partition coefficients are significantly higher, which may be due to the more polymerized nature of our melt.

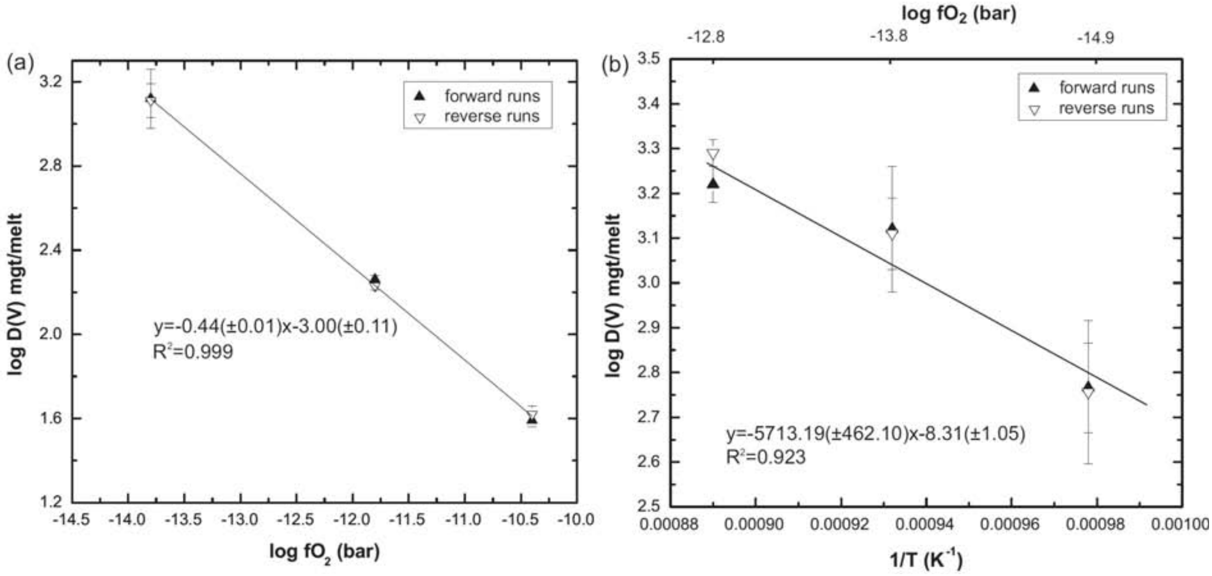

Fig. 3.2-29: Vanadium partition coefficient between magnetite and melt as a function of oxygen fugacity and temperature for experiments carried out at 200 MPa. (a) $D_V^{mgt/melt}$ as a function of fO_2 for experiments carried out at 800 °C. The solid line represents the least square fitting through the averages of each pair. (b) log $D_V^{mgt/melt}$ vs. 1/T (K^{-1}) for experiments carried out at the Ni-NiO buffer at temperatures ranging from 750 °C to 850 °C. The displayed data have been corrected for the effect of changing fO_2 with changing temperature along the Ni-NiO buffer by using the equation shown in (a).

A first test has been made with natural samples. Melt and magnetite inclusions in quartz and plagioclase phenocrysts from three natural silicic magmas formed at known fO_2 conditions were analyzed to obtain $D_V^{mgt/melt}$ and temperature (the latter via zircon saturation thermometry). From these values, fO_2 was calculated based on our empirical equation (1). Calculated oxygen fugacities are within 0.7 log units from independent estimates in all three cases. This suggests that our empirical equation can already be reasonably applied to natural systems, despite the fact that compositional effects of magnetite and melt have not been accounted for.

p. *An experimental study of H solubility in plagioclase: Effect of oxygen fugacity (X. Yang)*

Feldspars, dominated by plagioclase and alkali feldspar, are the most abundant minerals in the Earth's crust, occurring in volcanic and metamorphic rocks with felsic to mafic composition. The majority of feldspars consist of corner-sharing (Al, Si)O_4 tetrahedra arranged around polyhedral sites that contain charge-balancing cations, mainly Na^+, K^+ and Ca^{2+}, and are usually classified chemically as members of the ternary system $NaAlSi_3O_8$-$KAlSi_3O_8$-$CaAl_2Si_2O_8$. While nominally anhydrous, feldspars can contain H on the level of less than 100 to more than 1000 ppm H_2O (by weight). The presence of H in feldspars has substantial effects on their mechanical properties, on the rate of diffusion-controlled processes, on the Al/Si ordering and disordering and even on the colors. However, the solubility of H in feldspars and its dependence on other thermodynamic parameters have been poorly constrained. In this study, we investigated the effect of oxygen fugacity on H solubility in plagioclase.

The starting material was a natural gem-quality crystal of labradorite plagioclase, $Na_{0.41}K_{0.02}Fe_{0.01}Ca_{0.59}Al_{1.59}Si_{2.40}O_8$. The annealings in H_2O were conducted at 2 kbar and 800 ºC in Au-Pt double capsules and oxygen fugacity buffered at Fe-FeO (IW), Ni-NiO (NNO), Re-ReO_2 (RRO), Fe_2O_3-Fe_3O_4 (HM), respectively. Different run durations (100 to 200 hours) were used to check the approximation to equilibrium.

Polarized spectra along three mutually perpendicular directions were measured. All the spectra show typical OH-related bands that are similar with respect to band shapes and frequency positions (Fig. 3.2-30). H solubility at the experimental conditions ranges from ~ 100 to 285 ppm H_2O depending on oxygen fugacity (Fig. 3.2-31). The most interesting result is that the H solubility is very high at the IW-buffered conditions, and first decreases sharply and then increases slowly with increasing oxygen fugacity (Fig. 3.2-31). The observed relation between oxygen fugacity and H solubility cannot be simply explained by a variation of the chemical valence of some species or by a variation of the oxygen vacancy in the plagioclase. Some unknown mechanism(s) may be responsible for the dependence of H solubility on oxygen fugacity in plagioclase.

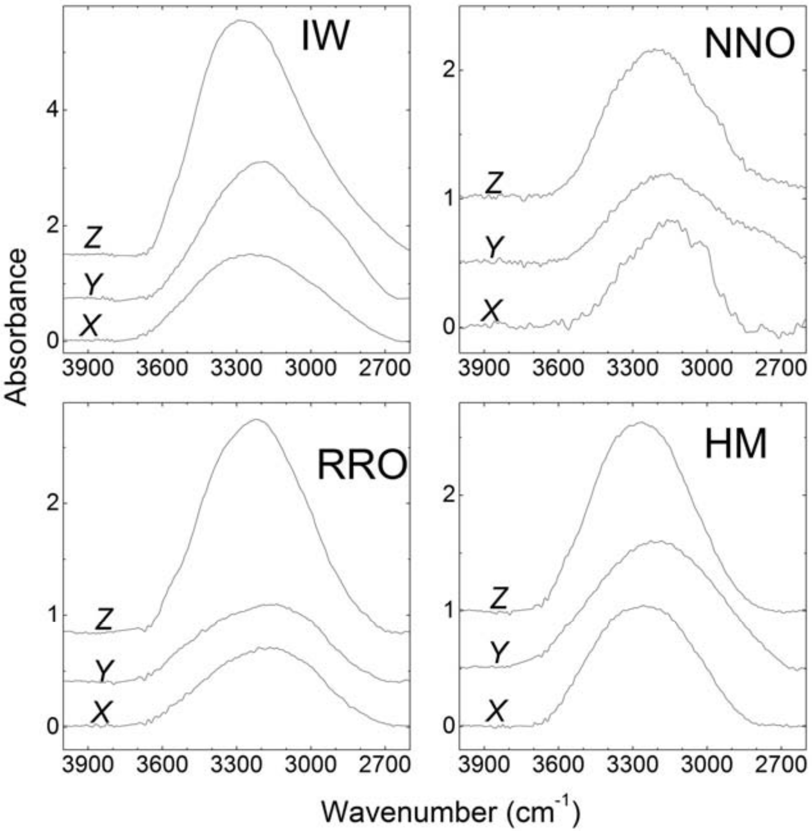

Fig. 3.2-30: Polarized IR spectra of plagioclase along three mutually perpendicular directions (*X*, *Y* and *Z*). The spectra were normalized to 1 cm thickness and are vertically offset.

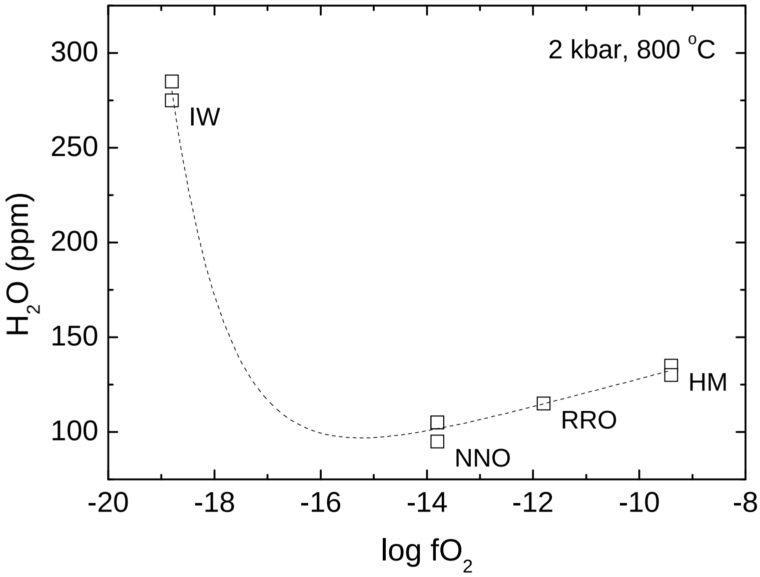

Fig. 3.2-31: Plot of H solubility in plagioclase as a function of oxygen fugacity. Dashed line is the best apparent fit to all the measured data.

q. *Constraints on solubility differences of solid solutions from observed volume changes during replacement reactions (K. Pollok; C.V. Putnis and A. Putnis/Münster)*

Mineral-fluid reactions towards equilibration involve readjustment of the phase assemblage and its composition. Such reequilibration is commonly accomplished by dissolution and precipitation reactions at Earth's surface and at crustal conditions when fluid flow is pervasive. As most rock-forming mineral systems are, to various extents, solid solutions, they respond to the fluid chemistry by readjusting their composition. This can be often observed as a pseudomorphic replacement.

The volume change of solid phases during mineral replacement is a critical factor for the advancement of the reaction boundary. Only interconnected porosity (small negative volume changes) ensures the advancement of reaction fronts by an interface-coupled dissolution-precipitation reaction. Large negative volume changes ($\Delta V^r < -30$ %) do not permit to produce pseudomorphic replacement, when the amount of material precipitating is not enough to produce a connected rim around the dissolving crystal. Any positive volume change ($\Delta V^r \geq 0$) will seal the primary crystal from the surrounding fluid and a slower reequilibration by diffusion must take place. Contributing parameters to the relative volume change of a replacement reaction are the ratios of molar volume of parent and product and their solubility ratio within a given solution which defines the number of moles dissolving and precipitating:

$$\Delta V^r [\%] = \frac{n_p V_{M,p} - n_d V_{M,d}}{n_d V_{M,d}} \cdot 100 = \frac{n_p V_{M,p}}{n_d V_{M,d}} \cdot 100 - 100 \qquad (1)$$

Figure 3.2-32A describes the dependence between the change in solubility and the ratio of molar volumes which results in lines of equal relative volume changes.

Data on the solubility of solid solutions in complex aqueous fluids at higher temperature and pressure is still limited. However, the determined porosity in partly replaced minerals (either natural or experimental) can be used to roughly estimate the solubility difference of the parent and product phases. For the replacement of chlorapatite by hydroxylapatite the ratio of molar volume is 0.976. Experiments in KOH fluid at hydrothermal conditions (500 °C, 100 MPa) show a porous replacement layer of hydroxylapatite. The porosity can be estimated as about 10 % from BSE images (Fig. 3.2-32B). Therefore, the solubility ratio between the dissolving and precipitating phase must be in the rage of 0.9-1. This result implies that the solubility of phases which allow interface-coupled dissolution-precipitation reactions must be always very close to each other (within the same order of magnitude) with the dissolving phase being slightly more soluble than the precipitating one as long it is not counterbalanced by a molar volume ratio less than 1. As the molar volumes are usually not changing very much within a solid solution (*e.g.*, feldspar, U- and REE-enriched zircon, garnet), the porosity observed in natural replacement is thus a direct consequence of the solubility ratios.

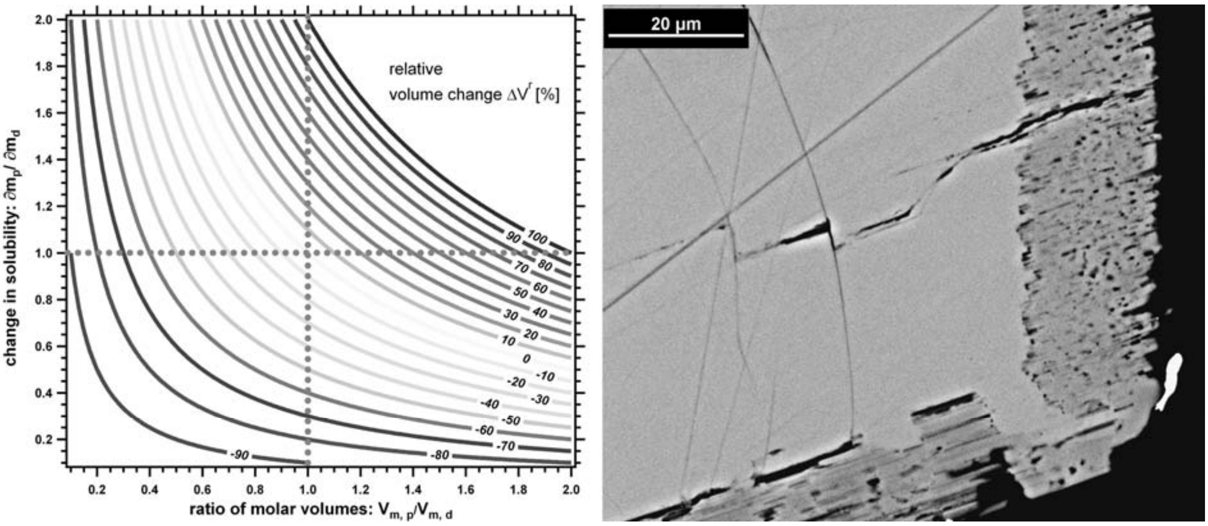

Fig. 3.2-32: (A) Relative volume change of a dissolution-precipitation reaction as function of the change in solubility and the molar volume ratio of the involved phases. (B) Backscattered electron image of chlorapatite (bright) partly replaced by hydroxylapatite (darker rim). The porosity in the replaced part indicates that the solubility of chlorapatite was slightly higher than the solubility of hydroxylapatite at the experimental conditions.

r. *The fate of As and Cr sorbed on goethite and ferrihydrite during sulfidation (K. Pollok and D. Scheiter)*

As and Cr are common redox sensitive contaminants in surface waters and sediments, *e.g.*, from mining operation and industrial waste disposal and pose a severe threat to the environment. These toxic trace elements readily adsorb onto surfaces of ferric (oxyhydr)oxides and their fate at the oxic/anoxic boundary will thus be governed by mineral reactions of ferric (oxyhydr)oxides with dissolved sulphide (produced by sulphate-reducing bacteria) to sulphide minerals. Sulphide formation is conventionally associated with the black-coloured layers in recent anoxic sediments indicating so-called acid volatile sulphide (AVS) which has been widely assumed to consist of nanocrystalline mackinawite (tetragonal FeS) as a major component which transforms to the stable disulphide pyrite (FeS_2) with time. Therefore, such biogeochemical redox reactions have a high impact on contaminant dynamics.

Ferrihydrite starting material was synthesized from 0.1M $Fe(NO_3)_3$ solution by adding KOH until a pH of 7-8 was reached. The suspension was centrifuged, the supernatant decanted and the solid was dialyzed for 2 days and air-dried at room temperature. XRD and TEM confirmed the sample to be pure 2-line ferrihydrite with a grain size of about 5 nm. Goethite was precipitated by adding KOH to a 1 M $Fe(NO_3)_3$ solution before diluting to up with millipore water. The suspension was stored in a closed polypropylene flask at 70 °C for 60 h and the solid was dialyzed for 2 days and air-dried at room temperature. The resulting goethite was as well confirmed by XRD and TEM. The acicular crystals have a size of a few hundred nanometers.

Adsorption experiments were performed at near neutral pH using AsO_4^{3-} and CrO_4^{2-} anions as adsorbates (c = 0.025 – 1 mM). Sorbent concentrations for ferrihydrite and goethite are 1.8 g L-1. The sorbed fraction has been determined by ICP-OES and BET surface area. Due to the higher surface area of ferrihydrite almost 100 % of both anions have been sorbed while only 65 % of chromate and less than 50 % of arsenate were bound to goethite. Reduction experiments were done by subsequent argon purging of the reactor and addition of Na_2S create anoxic sulphidic conditions. The arsenate-on-ferrihydrite suspension is darker compared with the chromate-on-ferrihydrite.

TEM has been used to detect secondary phases after sulphidation. Surprisingly, ferrihydrite with sorbed arsenate has not reacted towards more stable iron (oxyhydr)oxides as it was observed in experiments without sorbents. In contrast, nanocrystalline iron arsenate with d-spacing in line with scorodite ($FeAsO_4 \cdot H_2O$) has been found together with 2-line ferrihydrite. This finding implies that arsenate is not completely sorbed but transforms a part of the ferrihydrite to iron arsenate. Some iron sulfide was detected by STEM-EDX mapping, but its structural state is not yet conclusive. Ferrihydrite with sorbed chromate reacted towards goethite and lepidocrocite which leads to a smaller surface area of the reacted sample. Chromate was mainly found in connection with residual ferrihydrite. The formation of mackinawite (FeS) was also observed. However, whether Cr is bound to this phase and in what oxidation state it may be will be determined in future XAS measurements. The change in the colour of the suspension, however, can be explained by the higher grain size of solid phases in the chromate-on-ferrihydrite experiment. The goethite with sorbed chromate sample shows the presence of a Cr-hydroxide after sulphidation, probably as consequence of reducing surface bound species. This finding implies that dissolved sulphide did not initiate the reductive dissolution of goethite because Cr^{6+} at the surface is mainly taking electrons from the dissolved sulphide, which also suppresses sulphide formation.

3.3 Mineralogy, Crystal Chemistry and Phase Transformations

The bulk of the Earth's interior consists of crystalline phases; hence the crystal structures of Earth materials and their behaviour with pressure, temperature and composition are of fundamental importance to geosciences. Recent breakthroughs at the Bayerisches Geoinstitut have been made by combining the precision of single-crystal X-ray diffraction with the high signal quality available from third-generation synchrotron facilities. This chapter reports details of the first *in situ* single crystal X-ray diffraction study of α-FeOOH, including its equation of state and the nature of a structural phase transition at 45 GPa. A similar approach applied to Cr_2O_3 showed no phase transition to at least 70 GPa, contrary to several previous reports. The dominant phase of the lower mantle, silicate perovskite, continues to attract interest, and a single crystal study in a laser-heated diamond anvil cell showed smooth compression to at least 80 GPa, disproving suggestions in the literature of a high-spin to low-spin transition of ferric iron in the lower mantle. These results were confirmed by a study involving a new method of synchrotron Mössbauer spectroscopy on a wider range of silicate perovskite compositions. The single-crystal approach was also applied to laser-heated diamond anvil cell experiments on the candidate core material Fe_7C_3, enabling an accurate refinement of the crystal structure and determination of its compressibility at pressures corresponding to those within the core.

Knowledge of the Earth's interior requires not only a characterisation of mineral behaviour under high-pressure and high-temperature conditions, but also an understanding of processes taking place. This chapter reports the potential for sodium transport into the deep Earth to take place through Na-majorite, based on a study of its stability at mid-mantle conditions. An investigation into the solubility of aluminium and silicon into high-pressure polymorphs of the common accessory phase, TiO_2, shows their potential for use as an indicator of high-pressure conditions. Surface reactivity studies of pyrrhotite show variations in reaction rate depending on pH conditions and crystallographic orientation of the crystal surfaces. A study of cation site distributions in Cr-spinels shows the influence of oxygen fugacity and their potential use as an oxygen barometer. Synthesis experiments to produce single-crystal silicate perovskite show the strong effect of metal-oxide reactions in controlling iron valence states in mineral phases.

Mineral phases provide not only a record of processes taking place within the Earth's interior, but also of extra-terrestrial processes such as those in the early solar nebula. The importance of gas-solid interactions with volatile species involving nitrogen is shown in a study of sulphide and chromium nitride nanophases in chondrites. Finally, a crystallographic study of pristine metal nuggets in the Murchison meteorite provides constraints on condensation processes in the early solar nebula.

a. *High-pressure behaviour of α-FeOOH (E. Bykova, K. Glazyrin, L.S. Dubrovinsky, N.A. Dubrovinskaia and T. Boffa Ballaran; E. Greenberg/Tel Aviv, V. Prakapenka/Chicago and M. Hanfland/Grenoble)*

Goethite, α-FeOOH, is widely present in the Earth's crust as a component of soils, sediments and ore deposits. The mineral crystallises in an orthorhombic structure (*Pnma*, a =9.9510(5), b =3.0178(1), c = 4.5979(2) Å) and is isostructural with diaspore, AlOOH. Figure 3.3-1 (left) shows the α-FeOOH structure at ambient conditions. It consists of distorted $FeO_3(OH)_3$ octahedra linked together by shared edges to form infinite bands. The bands are connected via shared octahedral vertices that result in infinite channels parallel to the *b* axis. Investigations of the crystal structure of goethite as well as calculations of the equation of state (EoS) based on experimental data at high pressures (up to 29.4 GPa and 250 °C) have already been performed by several authors. At higher pressures (up to 57 GPa) the behaviour of the material has been studied only theoretically using density-functional theory (DFT). A phase boundary between goethite and its high-pressure polymorph, ε-FeOOH, has not been established unambiguously. While DFT predicted the transition at 6-7 GPa, a sluggish transition was observed experimentally above 5 GPa only under heating above 200 °C.

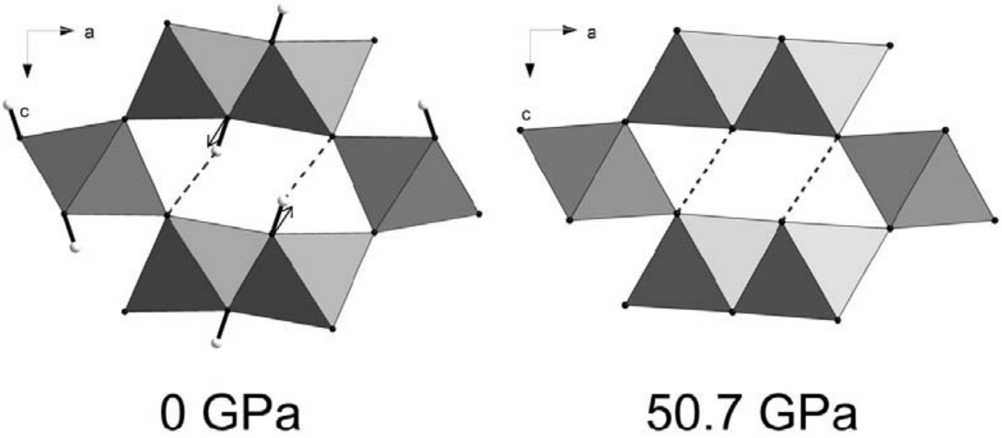

Fig. 3.3-1: The α-FeOOH crystal structure consists of distorted $FeO_3(OH)_3$ octahedra linked together by shared edges to form infinite channels parallel to the *b* axis. Arrows show the direction of the compression, which is linked to decreasing of the channel size and shortening of the hydrogen bond.

Our work presents the first *in situ* single crystal X-ray diffraction (XRD) and Raman spectroscopy study of α-FeOOH in a diamond anvil cell under compression to ~ 51 GPa. Single crystal XRD measurements were carried out both with in-house and synchrotron facilities at the ID09a beam line at ESRF. Ne was used as a pressure transmitting medium and the pressure was determined by the ruby fluorescence method. In-house experiments were performed using a Xcalibur X-ray diffractometer equipped with a CCD detector (MoKαradiation). The data were collected in the pressure range 0 to 44.5 GPa with steps of ~ 2 GPa. For each pressure point a Raman spectrum was also measured. At ESRF the data were collected up to 50.7 GPa with steps of ~ 5 GPa. Data treatment (integration, absorption correction) was performed with CrysAlis RED software. The structure was solved by the direct method and refined by full matrix least-squares using SHELXTL software. The number of independent peaks varied from 61 to 39 for in-house data and from 70 to 46 for synchrotron data with a total number of refined parameters of 10 to 13. Below 40 GPa R_1 values were in the range 2-11 % for in-house datasets, and 2-5 % for data obtained at ESRF. Above 40 GPa the R_1 values for in-house and synchrotron data increased to 25 and 11 %, respectively. Despite degradation in the quality of the crystal near and above the phase transition at ~ 45 GPa, the atomic positions could still be defined.

Figure 3.3-2 demonstrates that the volume-pressure dependence of data obtained with in-house and synchrotron facilities are consistent with each other. The accuracy of the data allowed a fit using a 2nd-order Birch-Murnaghan equation in both cases. The obtained values (bulk modulus and unit cell volume at ambient pressure) are in good agreement with each other as well as with literature data.

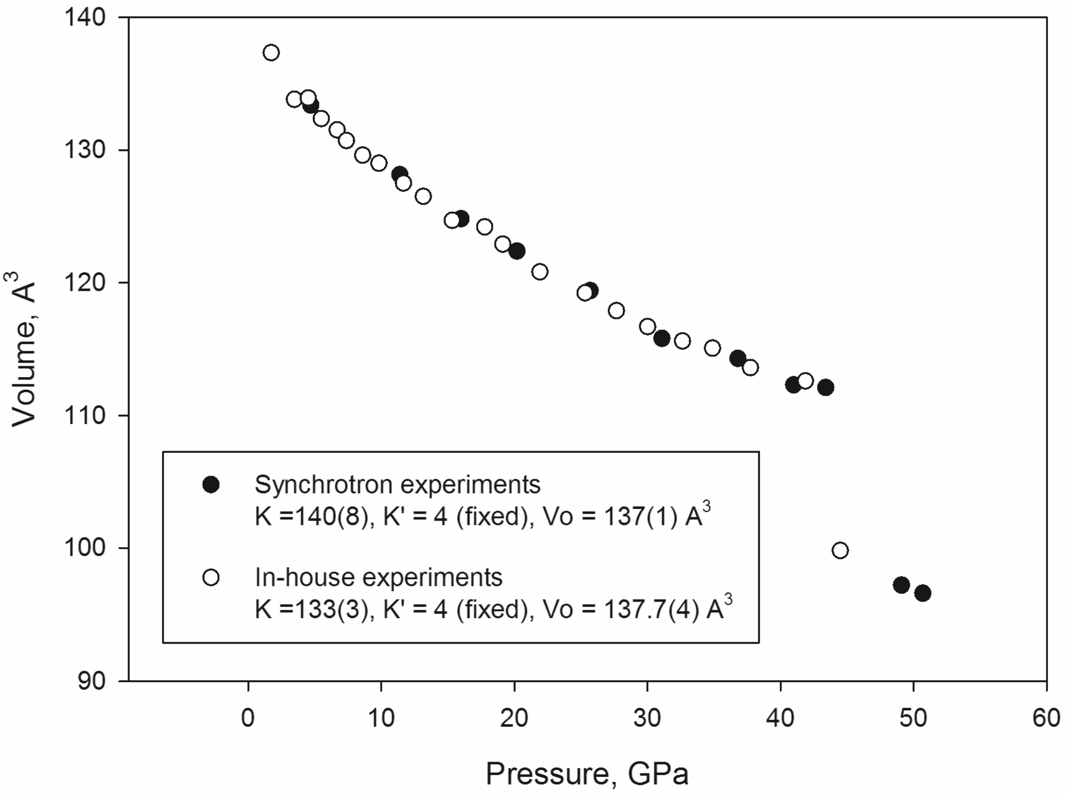

Fig. 3.3-2: Unit-cell volume change of FeOOH as a function of pressure, obtained with in-house (open circles) and synchrotron (filled circles) facilities.

Like diaspore, AlOOH, the goethite structure compresses anisotropically, where the *c* compression is larger than *a* and *b*. Referring to the crystal structure, it appears that major compression occurs due to a decrease of channel size and therefore it leads to a shortening of the hydrogen bond (Fig. 3.3-1, left). During experiments a phase transition that was not predicted by theoretical calculations was found: we observed a first order phase transition at ~ 44 GPa characterised by a sharp reduction in volume (Fig. 3.3-2). In the Raman spectra all lines disappear above 44 GPa, but during decompression they re-appear again, indicating a reversible phase transition. The new phase can be described in the *Pnma* space group with the following unit cell parameters: *a* = 9.27(5), *b* = 2.6420(9), *c* = 3.975(2) Å (at 50.7 GPa). No significant structural changes compared to the low-pressure phase occurred (Fig. 3.3-1, right). However after the transition, the distortion of FeO_6H_3 octahedra was considerably reduced (Fig. 3.3-3). At ambient pressure O-Fe-O angles deviate from 90º by up to 13º, while after the transition the deviation is below 5º. Before the transition the three Fe-O distances where oxygen is directly connected to hydrogen are longer than the non-bonded ones (Fig. 3.3-3, left), while after the transition the length of all Fe-O bonds become more equal (Fig. 3.3-3, right).

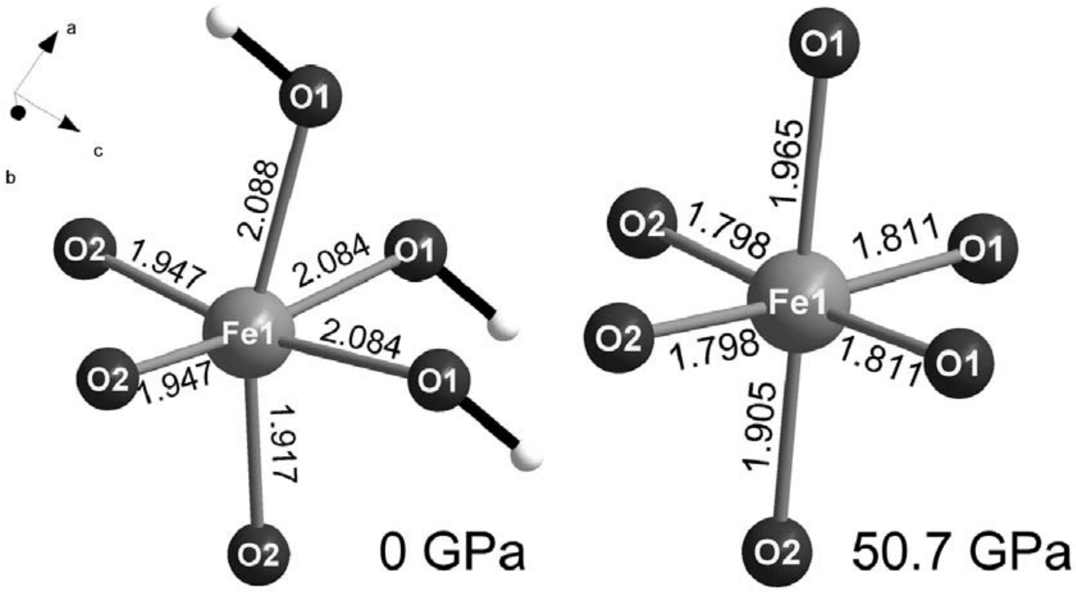

Fig. 3.3-3: Change in the distortion of FeO_6H_3 octahedra due to the phase transition.

b. *High-pressure structural studies of Cr_2O_3 using single-crystal X-ray diffraction (A. Kantor, L.S. Dubrovinsky, K. Glazyrin, and C. Prescher; M. Merlini/Milano and M. Hanfland/ Grenoble)*

Cr_2O_3, similar to other X_2O_3 transition metal oxides, continues to attract the interest of solid-state physicists, chemists and geoscientists. At ambient conditions, chromium (III) oxide (the mineral eskolaite) adopts a corundum-type crystal structure with $R\bar{3}c$ symmetry. The crystal structure consists of a hexagonal close packed framework of oxygen anions with 2/3 of the octahedral voids occupied by chromium. In the (0001) plane CrO_6 octahedra form so-called corundum-type patterns with each filled octahedron sharing common edges with another three octahedra (Fig. 3.3-4). Along the *c*-axis these layers alternate in such a way that each octahedron shares one common face with another.

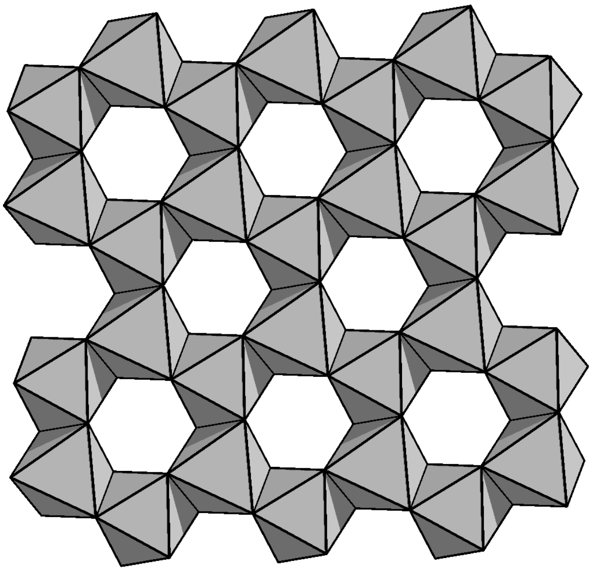

Fig. 3.3-4: "Corundum" layer of $[MO]_6$ octahedra. Every third octahedron in the layer is empty.

The high-pressure phase diagram of Cr_2O_3 remains unclear, despite a number of studies. Due to slow reaction kinetics of dense oxides, it is difficult to study the equilibrium phase relations at low and moderate temperatures. It has been predicted from first principles calculations that at high pressure (above 15 GPa) Cr_2O_3 should transform from the hexagonal corundum-type structure to the orthorhombic Rh_2O_3-II type structure. Subsequently this phase transition was confirmed experimentally, but it occurred at higher pressure (~ 30 GPa) and only after laser heating. However, the recorded powder X-ray diffraction spectra of the high-pressure chromium oxide phase could also be interpreted as a perovskite-type orthorhombic structure, which is also very common among X_2O_3-type transition metal oxides.

To clarify the nature of the transition we investigated the structural behaviour of Cr_2O_3 under quasi-hydrostatic pressure and room temperature using single-crystal X-ray diffraction. No phase transition was found up to the highest reached pressure of 70.4 GPa. The structure remained rhombohedral, and upon compression the oxygen atoms approached an ideal hexagonal close-packing arrangement. The isothermal bulk modulus of Cr_2O_3 and its pressure derivative were found to be 245 (4) GPa and 3.6 (2), based on a third-order Birch-Murnaghan equation of state. The experimental *P-V* data are presented in Fig. 3.3-5.

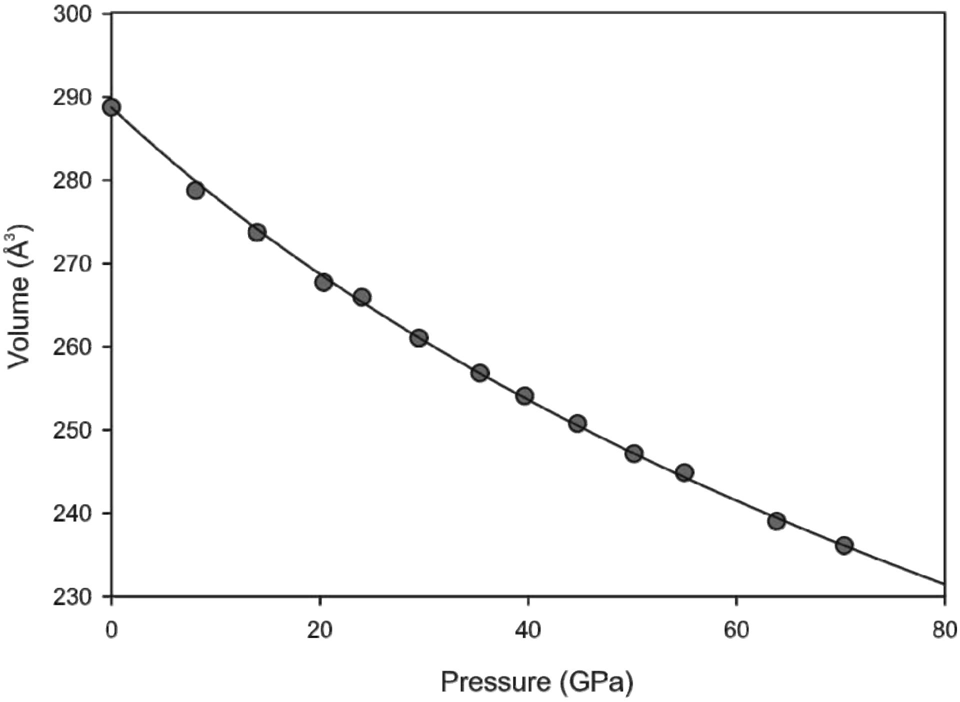

Fig. 3.3-5: Compressibility of eskolaite, Cr_2O_3 (error bars are smaller than the symbols).

c. *Single crystal X-ray diffraction of iron-aluminium-bearing magnesium silicate perovskites under high pressure-high temperature conditions (K. Glazyrin, L.S. Dubrovinsky, T. Boffa Ballaran, I. Kupenko, A. Kurnosov, C.A. McCammon and D.J. Frost)*

Magnesium silicate perovskite is considered to be the most abundant phase of the lower mantle by volume. Although the exact composition of the lower mantle is not well constrained, it is believed that the perovskite phase may contain non-negligible amounts of iron and aluminium incorporated into its lattice by different substitution mechanisms. For example, it has been shown that ferrous iron substitutes exclusively for magnesium at the distorted dodecahedral site (A-site). Aluminium, on the other hand, may occupy both the dodecahedral and the octahedral site (B-site) and tends to stabilise ferric iron on the A-site. In this study we determined the equation of state for two different compositions of iron-aluminium-bearing magnesium silicate perovskite (Pv) at pressures corresponding to the middle of the lower mantle. We performed static compression experiments at ambient and high temperatures on material loaded into diamond anvil cells.

We selected two different compositions, $Mg_{0.63}Fe_{0.37}Si_{0.63}Al_{0.37}O_3$ (Pv1) and $Mg_{0.87}Fe_{0.13}Si_{0.89}Al_{0.11}O_3$ (Pv2). The chemical composition, sample homogeneity, iron valence state and the crystal structure (depending on composition) were studied using Mössbauer spectroscopy, single crystal X-ray diffraction, the electron microprobe and EELS measurements. We verified that almost all iron in Pv1 is ferric iron substituting for magnesium at A-sites. The relative amount of ferric iron in Pv2 is smaller (0.09 Fe^{3+} and 0.04 Fe^{2+}) than in Pv1; however even in Pv2 the ferric iron occupies exclusively the A-sites.

We conducted a single-crystal study at beamline ID09a at ESRF. After loading samples into diamond anvil cells together with ruby spheres (pressure standard) and Ne (quasi-hydrostatic pressure medium used also as a secondary pressure standard), we collected single crystal X-ray diffraction data during sample rotation along the ω axis (±30º or ±40º depending on the loading) with a step of 0.5º. We measured diffraction patterns using an X-ray wavelength of 0.415Å with a flat X-ray CCD detector, MAR555. To heat the samples we used a portable laser heating system designed at Bayerisches Geoinstitut. This compact system allows visual observation of the sample, homogeneous heating and reliable measurement of the temperature of the heated area.

Figure 3.3-6 shows the variation of volume as a function of pressure for the two different compositions. The following parameters were obtained from a fit to the Birch- Murnaghan equation of state: K=235(4) GPa, V_0=168.9(4) Å for Pv1, and K=248(2) GPa, V_0=163.9(1) Å for Pv2. In both cases we fixed the pressure derivative of the bulk modulus to K'=4. It is clear that incorporation of Fe and Al increases the volume of Pv at a given pressure and increases the compressibility of material where the double substitution mechanism occurs (ferric iron for Mg and trivalent aluminium for Si).

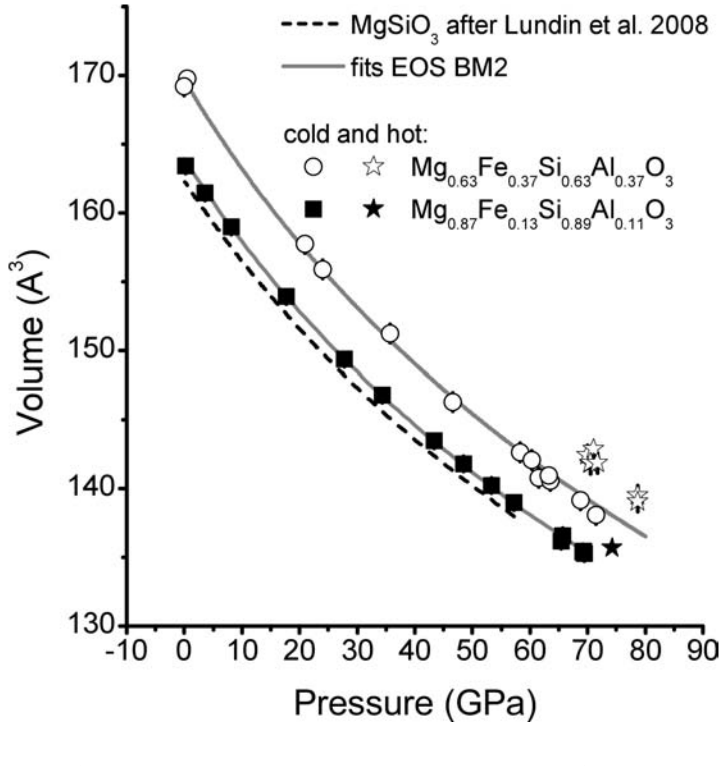

Fig. 3.3-6: Volume of samples Pv1 and Pv2 as a function of pressure and temperature. Stars indicate the high-temperature points. Dashed and solid lines correspond to the equations of state (EOS) for pure $MgSiO_3$ and Fe-Al bearing perovskite, respectively.

Combining our data for Pv1 obtained in the current experimental run with previous experiments, we calculated the volumes of individual sites (A and B) for pressures up to ~ 80

GPa (Fig. 3.3-7). We observe no anomalous contraction of the A-site volume with compression, so based on the large amount of ferric iron and taking into account that the A-site is occupied by ferric iron and magnesium at all conditions of the experiment, we conclude that there is no spin transition in ferric iron occupying the A-site.

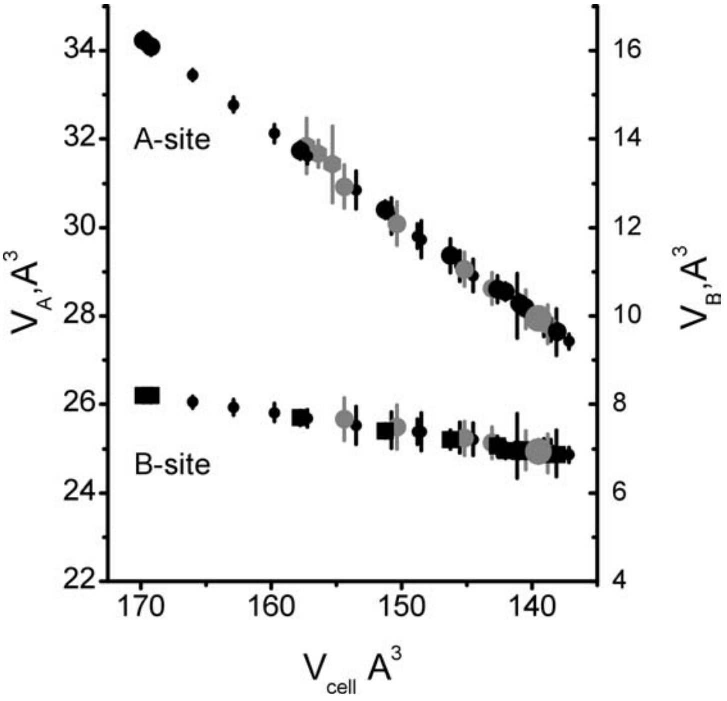

Fig. 3.3-7: Polyhedral volumes of the A- and B-sites as a function of unit cell volume. At ambient temperature (black symbols) the smaller volume means a higher pressure. High-temperature points are shown in grey.

d. *Spin state of ferric iron in magnesium silicate perovskite at lower mantle pressures (V. Potapkin, C.A. McCammon, L.S. Dubrovinsky, K. Glazyrin, A. Kantor, I. Kupenko, C. Prescher and R. Sinmyo; A.I. Chumakov and R. Rüffer/Grenoble; G.V. Smirnov and S.L. Popov/Moscow)*

Iron-containing magnesium aluminium silicate perovskite is the most abundant component in the Earth's lower mantle, and at least half of the iron in this phase is believed to be Fe^{3+}. The high-spin (HS) state of Fe^{3+} (which is stable at ambient conditions) contains five unpaired *d* electrons, but some recent studies have suggested that at high pressure a transition takes place to the low-spin (LS) state (where four of the *d* electrons become paired). HS-LS crossover is predicted to have significant implications for lower mantle properties, thus understanding the behaviour of ferric iron in silicate perovskite is important.

Conventional ^{57}Fe Mössbauer spectroscopy measured in the energy domain remains one of the best methods to determine iron valence and the nature of spin transitions in lower mantle phases. Because it allows individual spin and valence states to be identified separately, it can provide a clear answer to the question of whether Fe^{3+} undergoes a HS-LS transition in silicate perovskite. However, this technique is not well suited to study samples with a size less then ~ 100 microns, because focusing of radiation from radioactive sources is extremely difficult, resulting in a low count rate and a high background. To overcome these problems we have developed an energy domain Synchrotron Mössbauer Source (SMS) on beamline ID18 at the European Synchrotron Radiation Facility, enabling rapid collection of high quality energy domain Mössbauer spectra (see BGI Annual Reports 2009 and 2010).

We used this new technique to investigate the spin state of ferric iron in lower mantle silicate perovskite by studying the silicate perovskite sample $Mg_{0.63}Fe_{0.37}Si_{0.63}Al_{0.37}O_3$ (~ 80 % $Fe^{3+}/\Sigma Fe$). We collected SMS spectra at room temperature and increasing pressure up to 93 GPa using a diamond anvil cell, including measurements made after laser annealing. SMS spectra are extremely well resolved (Fig. 3.3-8). We fit the data to three quadrupole doublets, one assigned to Fe^{3+} and two assigned to Fe^{2+} (high QS and low QS) based on their centre shifts. Visually there appears to be no change to the Fe^{3+} doublet over the entire pressure range.

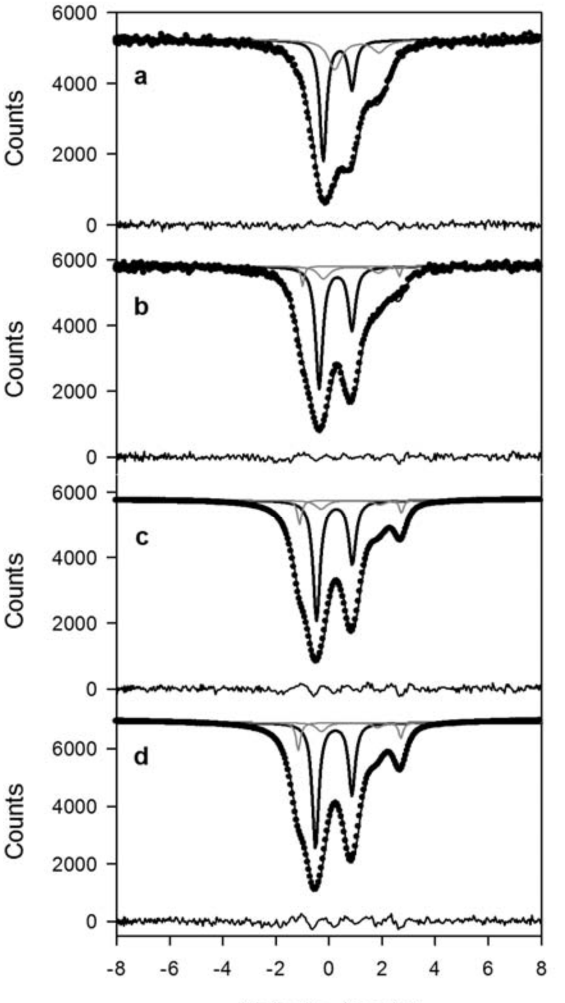

Fig. 3.3-8: SMS spectra of $(Mg_{0.6}Fe_{0.4})(Si_{0.6}Al_{0.4})O_3$ perovskite at room temperature showing their evolution with pressure: (a) 2.5 GPa; (b) 37.9 GPa; (c) 67 GPa; (d) 93 GPa. The data were fit to one Fe^{3+} doublet (black) and two Fe^{2+} doublets (grey), and the fit residual is shown below each spectrum. Area asymmetry is due to preferred orientation of the sample, and the velocity scale is given relative to α-iron.

The hyperfine parameters of the low QS Fe^{2+} doublet (dominant doublet in Fig. 3.3-8) correspond to the high-spin state, while the doublet with high quadrupole splitting corresponds to intermediate-spin Fe^{2+}, or less likely to a distortion of the site occupied by high-spin Fe^{2+}. Irrespective of the interpretation of the Fe^{2+} spin state, the conclusion regarding the absence of a spin transition in Fe^{3+} remains the same. The hyperfine parameters of Fe^{3+} corresponds to a high-spin state throughout the entire pressure range, even after laser annealing, so we conclude that there is no Fe^{3+} HS-LS transition in silicate perovskite in the lower mantle.

e. *Structure and properties of a novel Fe_7C_3 carbide up to 160 GPa from single crystal X-ray diffraction data (L.S. Dubrovinsky, E. Bykova, K. Glazyrin, A. Kantor, C.A. McCammon, M. Mookherjee, Y. Nakajima; N.A. Dubrovinskaia; M. Merlini and M. Hanfland/Grenoble)*

Following the discovery of the Earth's core about a century ago, the idea of iron or an iron-based alloy (with Ni and some light elements such as S, O, Si, C, and H) being the dominant component of the core has been supported by cosmochemical and geochemical observations, seismic data, the theory of geomagnetism, and high-pressure studies. The properties of pure iron have been intensively studied and examined experimentally under the relevant conditions (*i.e.*, at pressures of 136-364 GPa). However, the effect of light elements on the structure and physical properties of iron at core conditions is still unclear.

While significant reservoirs of carbon are thought to exist in the deep Earth's interior rather than in the exosphere, the partitioning of carbon between the metallic core and the silicate mantle is inadequately understood. In addition, the host mineral phases of carbon are largely unknown. Based on experimental estimates of carbon solubility, it is likely to partition into the metallic core at conditions relevant for planetary accretion and differentiation. Such ideas are further strengthened by the occurrence of graphite and metal carbides in iron meteorites. These meteorites are likely the fragments of cores of planetesimals with radii of at least 100-400 km. The discovery of carbides as inclusions in ultra-deep diamonds suggests that Fe-C phases may be present in the Earth's lower mantle. Recent experimental studies of the Fe-C and Fe-C-S systems suggest that Fe_7C_3 is the liquidus phase of Fe-C melt at high pressure and might be a stable carbide phase at the P-T conditions relevant to the lower mantle and inner core. However, the structure and elastic properties of Fe_7C_3 at core conditions are poorly constrained.

We synthesized single crystals of Fe_7C_3 in a multianvil apparatus from iron and graphite at a pressure of 18 GPa and a temperature of ~ 1773 K. Based on the single crystal X-ray diffraction data collected in house at ambient conditions, we solved and refined the structure of the high-pressure Fe_7C_3 orthorhombic phase (space group *Pbca*, Z = 8) (Fig. 3.3-9). Iron atoms are arranged in two types of octahedra and two types of tetrahedra. Carbon atoms are at the centre of trigonal prisms formed by six iron atoms, three of which belong to an octahedron, and the other three to the opposite tetrahedron (not shown in Fig. 3.3-9).

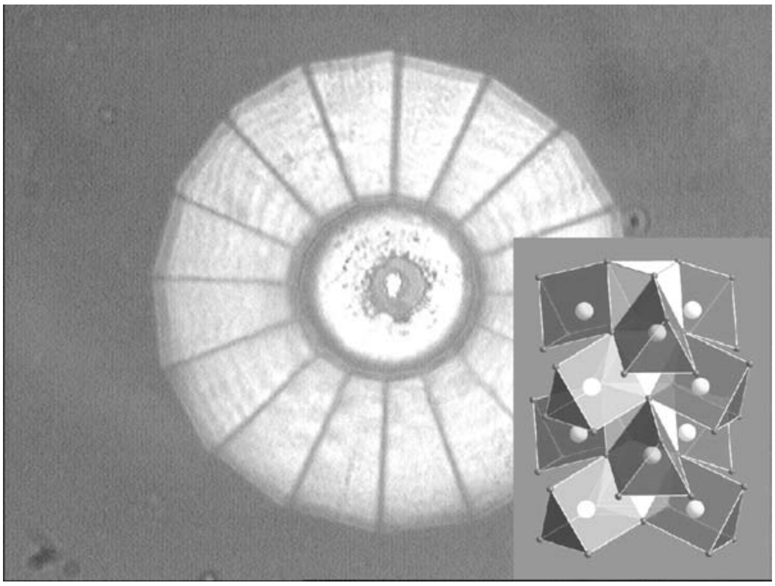

Fig. 3.3-9: Optical micrograph of the Fe_7C_3 crystal in a diamond anvil cell with Ne pressure transmitting medium at 160 GPa. The insert shows the structure determined from *in situ* X-ray single crystal diffraction data.

We investigated the effect of pressure on the lattice parameters and structure of Fe_7C_3 using single-crystal X-ray diffraction at ambient conditions and in laser-heated diamond anvil cells at the ID09 beam line at ESRF. In four different loadings we were able to compress Fe_7C_3 crystals to 160 GPa in a Ne pressure medium and collect over 400 independent reflections even at the highest pressure. This enabled an accurate refinement of the structure and a determination of the lattice parameters and compressibility of Fe_7C_3 at pressures corresponding to the Earth's core (Fig. 3.3-10).

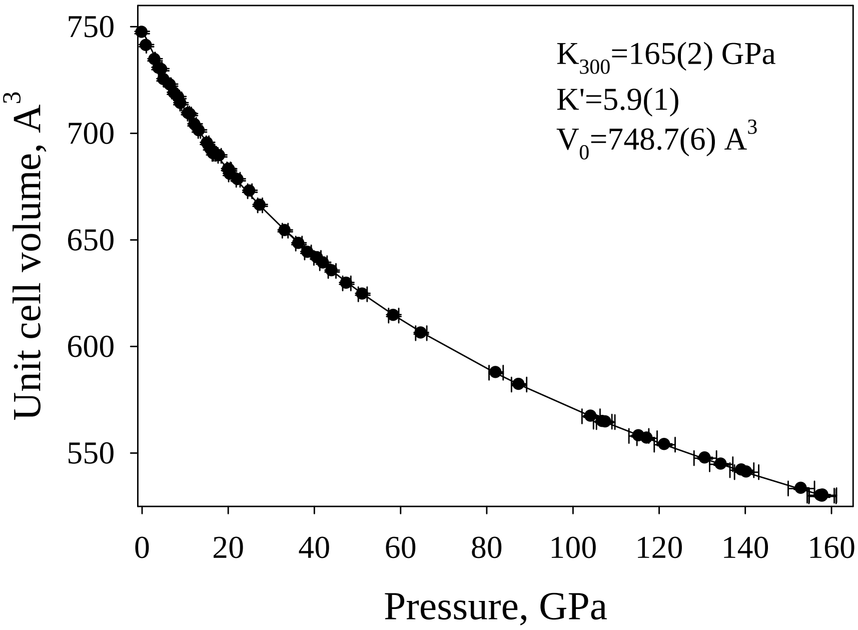

Fig. 3.3-10: Unit-cell volume of the high-pressure orthorhombic phase of Fe_7C_3 as a function of pressure, obtained by single crystal X-ray diffraction experiments at pressures up to 160 GPa.

f. *Stability of $Na_2MgSi_5O_{12}$ under conditions of the transition zone (A.V. Bobrov/Moscow, Yu.A. Litvin/Chernogolovka and L.S. Dubrovinsky)*

The solubility of alkalis in the structures of high-pressure minerals, as well as their abundance under conditions of the upper mantle and transition zone, attracts considerable interest from experimental geologists and mineralogists. Na-bearing majoritic garnet is important as a potential host of sodium at high pressures and temperatures. Although pure sodium majorite $Na_2MgSi_5O_{12}$ has not been found in natural samples (*e.g.*, inclusions in diamonds or mantle xenoliths in kimberlites), the concentration of the $Na_2MgSi_5O_{12}$ end-member in majoritic garnets sometimes exceeds 10 mol.%. Recently the stability of Na-garnet was followed up to 19.5 GPa (2100 °C). Although the stability of this phase at higher *P–T* is not yet confirmed, by analogy with pyrope and majorite we may assume its decomposition at pressures above 20-22 GPa with the formation of $MgSiO_3$ perovskite and new sodium-rich phase(s). The main aim of this project was to determine the upper pressure limit of Na-majorite stability.

A gel with $Na_2MgSi_5O_{12}$ composition was dried at 100 °C and used as the starting material. Our experiments were performed over a wide pressure range (15-35 GPa) and comprised two series: multianvil runs at 15-24 GPa (1600-1900 °C) and runs in laser-heated diamond anvil cells at 17-35 GPa (1600-2200 °C). The run products were characterised using X-ray powder diffraction, scanning electron microscopy, and Raman spectroscopy; the chemical compositions were determined by electron microprobe analysis.

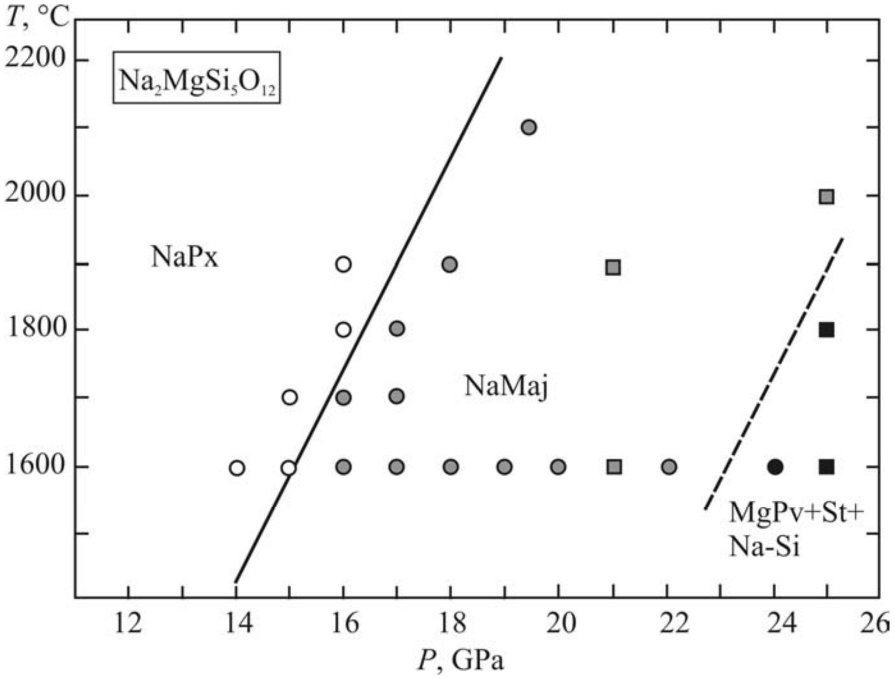

Fig. 3.3-11: *P–T* phase diagram demonstrating the stability of Na-pyroxene (empty symbols), Na-garnet (gray symbols) and $MgSiO_3$ perovskite + stishovite + Na-Si phase (black symbols) in multianvil (circles) and diamond anvil (squares) experiments.

The results of the experiments are shown on a *P–T* phase diagram (Fig. 3.3-11) which illustrates the stability fields of Na-pyroxene (NaPx, $NaMg_{0.5}Si_{2.5}O_6$) and Na-majorite (NaMaj). The latter is represented by small (10-30 µm) semi-transparent crystals with tetragonal symmetry (space group $I4_1/acd$) and lattice parameters a = 11.3966(6), c = 11.3369(5) Å, V = 1472.5(1) Å^3. As seen in our experiments, the upper pressure limit of Na-majorite stability is recognised by its decomposition and the formation of $MgSiO_3$ perovskite, SiO_2 stishovite (both are clearly observed on XRD patterns), and a Na-Si ($NaSiO_3$?) non-quenchable amorphous phase (Fig. 3.3-12). These data were reproduced at higher pressures (> 25 GPa) using diamond anvil cells.

The results of our study thus allow Na-majorite to be considered a potential host phase of sodium under the *P-T* conditions of the upper mantle and transition zone. However more experiments need to be performed to verify the results of Na-majorite transformations at higher (> 22-23 GPa) pressures, in particular runs with *in situ* estimations of the structural features of phases.

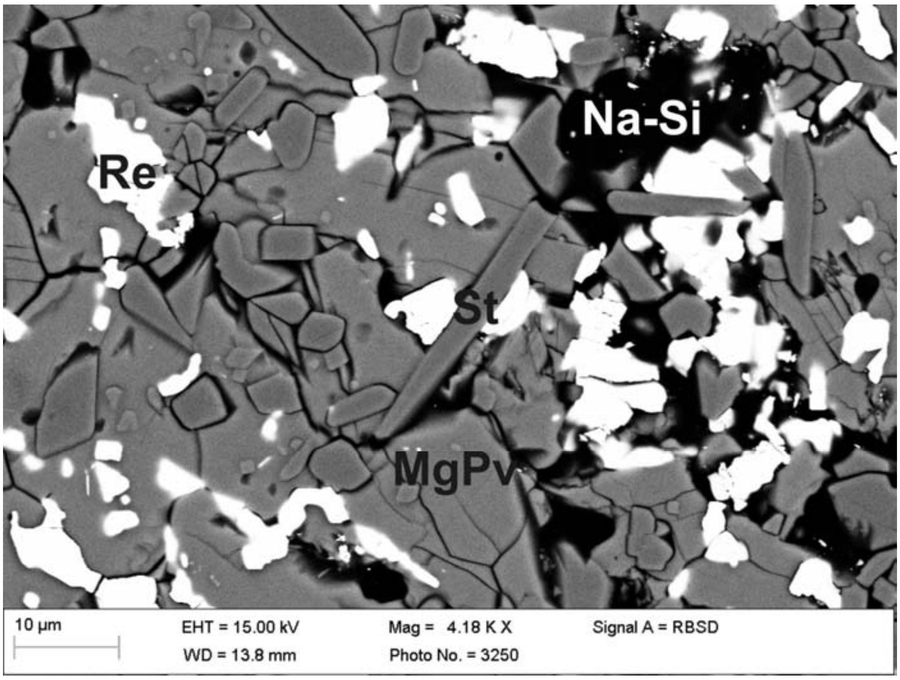

Fig. 3.3-12: BSE image of the phase assemblage ($MgSiO_3$ perovskite, SiO_2 stishovite and Na-Si phase) obtained in multianvil run at 24 GPa and 1600 °C.

g. *Incorporation of aluminium and silicon into high-pressure polymorphs of TiO_2 (A. Escudero/Sevilla and F. Langenhorst)*

Titanium dioxide (TiO_2) has been intensively studied for a number of decades due to its fundamental and applied interest for geology and material science. Rutile is a common accessory mineral in metamorphic and igneous rocks. It transforms to high-pressure TiO_2 polymorphs with the α-PbO_2 and ZrO_2 baddeleyite structures, the latter recently named akaogiite. The solubility of trivalent cations in TiO_2 rutile increases drastically with pressure, with two different mechanisms of solubility. There are two clear indications of high-pressure conditions: (1) enhanced aluminium or chromium concentration in TiO_2 rutile; and (2) (110) twinned TiO_2 grains with the $CaCl_2$-type structure. However, in order to evaluate the possibility of using the incorporation of trivalent cations into TiO_2 phases as a possible indicator of high-pressure conditions, the effect of the nature of the different TiO_2 polymorphs at higher pressure on Al incorporation into TiO_2 phases should be determined. We report here the aluminium incorporation into the high-pressure polymorph of TiO_2 with the α-PbO_2-type structure from 10 to 20 GPa and 1300 ºC. For comparison, the analogous Si-doped system is also presented.

XRD data indicate that α-PbO_2-type TiO_2 can be recovered after quenching from high pressure in both Al and Si-doped TiO_2 systems. However, the transition to TiO_2 akaogiite, expected at 17 GPa at 1300 ºC for pure TiO_2, has not been directly observed. The solubility of both dopants increases with increasing synthesis pressure, as shown in Fig. 3.3-13. However, the incorporation of aluminium into α-PbO_2-type TiO_2 is much more efficient than that of silicon in the Si-doped system. In both cases, a substitutional solid solution takes place. Dopants replace Ti^{4+} on the normal octahedral α-PbO_2-type TiO_2 sites, as indicated by both XRD and MAS NMR data. On one hand, a linear decrease of both Al and Si-doped α PbO_2-type TiO_2 lattice parameters with increasing synthesis pressure is observed up to 16 GPa. The slightly different ionic radii of the cations explains the slight decrease of the unit cell parameters when this substitution takes place. On the other hand, high-resolution ^{27}Al MAS-NMR data indicate the presence of a unique Al environment in Al-doped α-PbO_2-type TiO_2. A unique octahedral Si environment for Si-doped α-PbO_2-type TiO_2 has also been reported in the literature. In case of the Al system, charge is balanced with the formation of oxygen vacancies.

A drop in the solubility of both Al_2O_3 and SiO_2 in TiO_2 is, however, observed between 16 and 20 GPa. Samples synthesised at 20 GPa are recovered as α-PbO_2-type TiO_2 after quenching, but they show less Al and Si incorporation and also higher lattice parameters than would be expected according to the trend observed to 16 GPa. Both samples show a completely different microstructure than the samples synthesised at lower pressures. α-PbO_2-type TiO_2 grains are decorated with pi-fringes stacking faults, as shown in Fig. 3.3-14. All of this evidence points to the non-quenchable character of the TiO_2 akaogiite polymorph. This would be the stable TiO_2 phase at 20 GPa and 1300 ºC in both Al- doped and Si-doped systems, but it would revert to α-PbO_2-type TiO_2 upon pressure release, preserving its original dopant content. Since the structures of both α-PbO_2-type TiO_2 and TiO_2 akaogiite can be related by a continuous topological variation of three-dimensional anion nets with its consequential change in the stacking sequence, the observed stacking faults in the recovered α-PbO_2-type TiO_2 grains from the sample synthesised at 20 GPa can be ascribed to be a consequence of the reversible akaogiite → α-PbO_2-type TiO_2 transition when releasing the pressure.

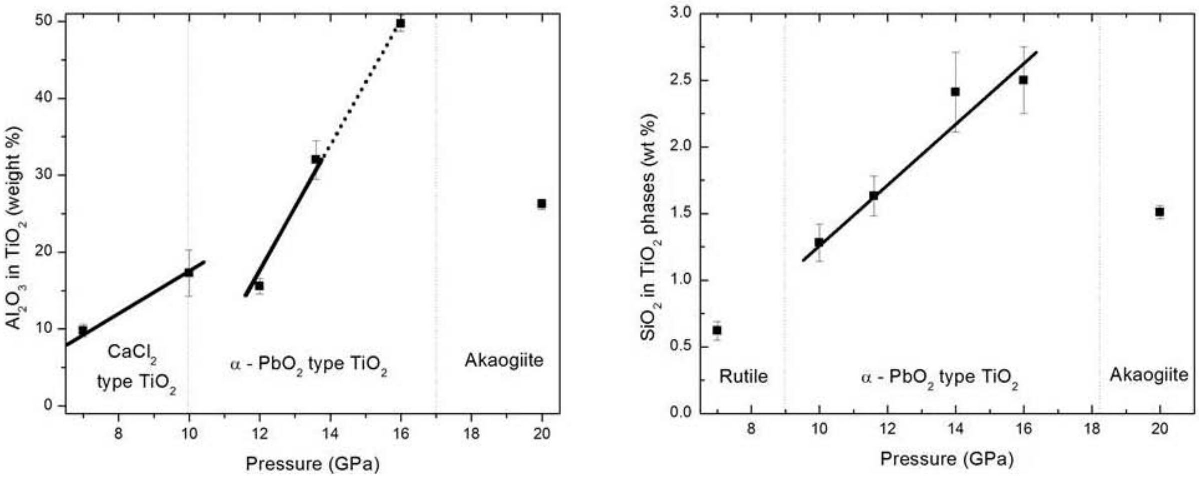

Fig. 3.3-13: Solubility of Al_2O_3 (left) and SiO_2 (right) in TiO_2 phases versus pressure at 1300 ºC. Data were obtained from TEM-EDX analyses. The dotted line between 14 and 16 GPa in the Al system indicates that the composition shown by the TiO_2 grains synthesised at 16 GPa may not correspond to Al_2O_3 in TiO_2 but to another aluminium titanium phase.

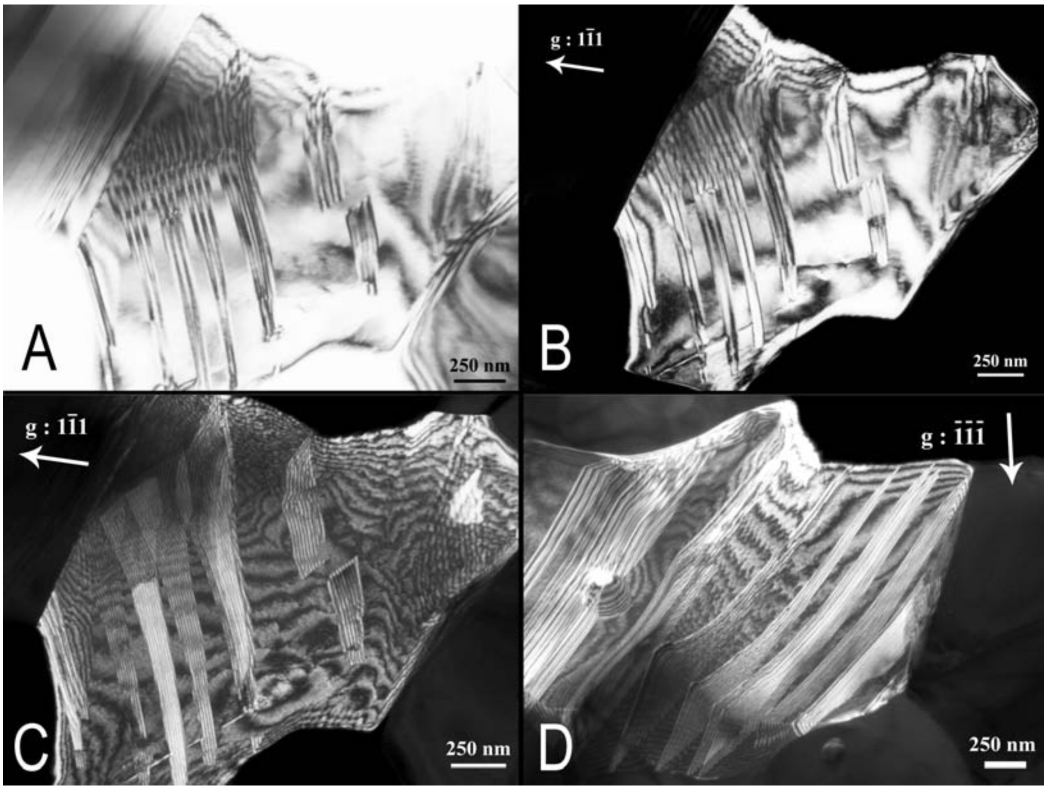

Fig. 3.3-14: A) Bright field TEM image of a Si-doped α-PbO_2-type TiO_2 grain recovered from 20 GPa and 1300 ºC. B) Dark field TEM image of the same grain, g: $[1\bar{1}1]$. C) Weak beam dark field image of the same grain, g : $[1\bar{1}1]$. D) Weak beam dark field image of another α-PbO_2-type TiO_2 grain, g : $[\bar{1}\bar{1}\bar{1}]$

h. *Crystallographic and microstructural controls on pyrrhotite dissolution under oxidising conditions (D. Harries; K. Pollok and F. Langenhorst/Jena)*

To study differences in the surface reactivity of varieties of pyrrhotite ($Fe_{1-x}S$ with variable non-stoichiometry: $0 \leq x \leq 0.125$), we conducted oxidative dissolution experiments on carefully polished pyrrhotite surfaces containing crystallographically coherent intergrowths of 4C-pyrrhotite ($x = 0.125$) and NC-pyrrhotite ($N = 4.81$-4.87, $x \approx 0.100$). These samples offer the possibility to eliminate the effect of crystal anisotropy and to study intrinsic differences of 4C and NC superstructures. Experiments were done at 30-35 °C using Fe^{3+} and H_2O_2 as oxidants. Surface cross sections were prepared using the FIB technique and were studied using analytical TEM. The surface topography after reaction was recorded by vertical scanning confocal microscopy and used to deduce individual reaction rates of the intergrown pyrrhotite varieties.

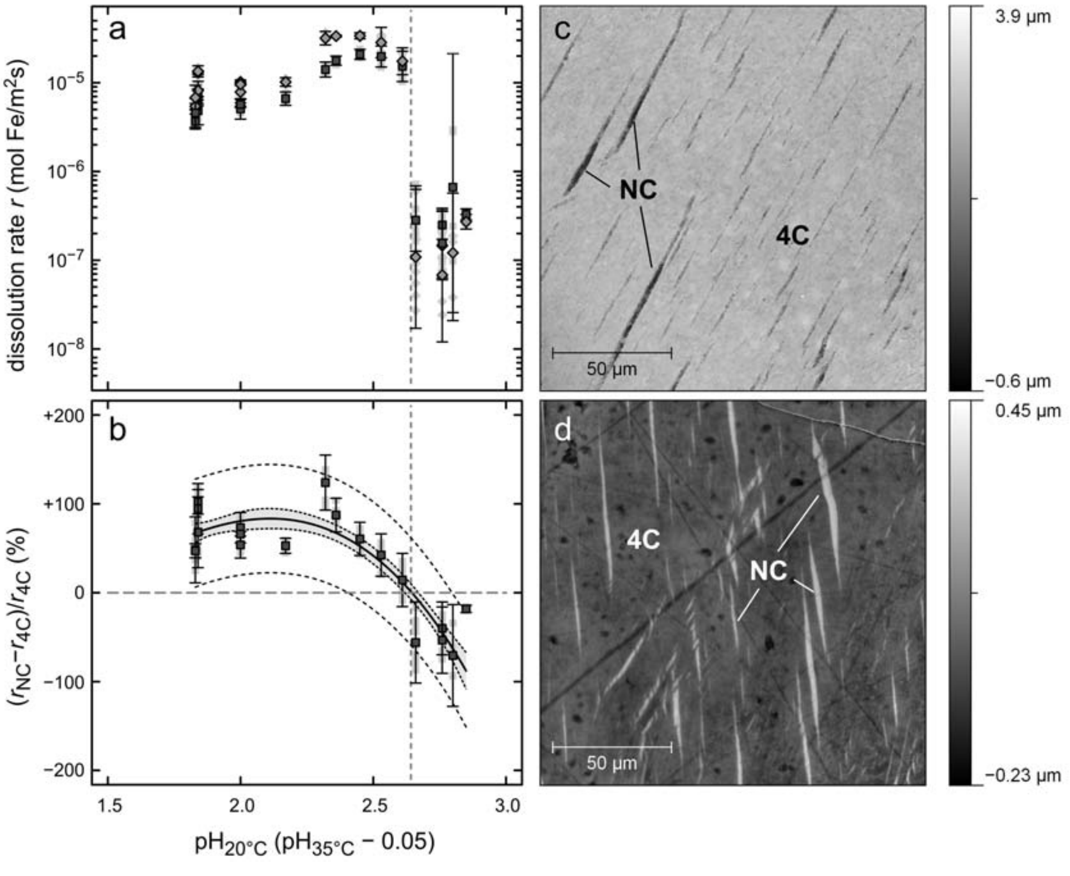

Fig. 3.3-15: (a) Absolute rates of oxidative dissolution of a {hk0} surface of pyrrhotite in 0.1 mol/L H_2O_2 as function of pH (adjusted by H_2SO_4). Pyrrhotite from Sta. Eulalia (Mexico). Squares: 4C, diamonds: NC. A strong drop occurs at pH 2.70. (b) Dissolution rates of NC relative to 4C. Below pH 2.70 the NC phase reacts faster; above pH 2.70 the 4C phase reacts faster. (c) Height map of {hk0} surface reacted at pH 2.05. Pyrrhotite from Dalnegorsk (Russia). NC lamellae are preferentially dissolved. (d) Height map of the sample in (c) reacted at pH 2.92. Under these conditions the 4C matrix is preferentially dissolved.

Our results show in Fig. 3.3-15 that reaction rates on a $\{hk0\}_{NiAs}$ surface strongly and abruptly decrease as pH becomes larger than 2.70 (close to the isoelectric point). At pH < 2.70, NC-pyrrhotite oxidises and dissolves faster than 4C-pyrrhotite and abundant elemental sulphur precipitates among ferric oxyhydroxides. At pH > 2.70, 4C-pyrrhotite reacts faster and sulphur is always absent, while strong precipitation of 2-line ferrihydrite occurs. High resolution TEM and TEM-EDX do not show evidence for the formation of S-enriched sulphides (*e.g.*, Fe_2S_3, FeS_2) below the reaction interface at any pH studied.

Comparison of different orientations reveals that the reactions at pH < 2.70 proceed much more slowly on $(001)_{NiAs}$ surfaces than on $\{hk0\}_{NiAs}$ surfaces. At pH > 2.70 the opposite is observed. On corroding $\{hk0\}_{NiAs}$ surfaces at pH < 2.70 the reaction proceeds along basal cleavage planes and leads to the formation of pyrrhotite flakes dominated by $(001)_{NiAs}$ faces, which are the most resistant against dissolution under these conditions. The result is strongly enhanced roughness of the reaction interface. On the same $\{hk0\}_{NiAs}$ surfaces above the transition at pH 2.70, the change in direction dependence of dissolution speed causes smooth reaction interfaces, as flakes no longer form due to preferred dissolution on the $(001)_{NiAs}$ faces. These observations exemplify complex physicochemical and microstructural processes at the reaction interface.

i. *Cation order-disorder in natural and synthetic Cr-spinels: Electron channelling spectroscopy in TEM (N. Miyajima and W. Sun)*

Electron channelling spectroscopy is a powerful technique to determine site occupancy of elements in complex mineral solid solutions (*e.g.,* garnet, spinel and perovskite). We can localise an inelastic scattering along specific atom planes or columns by setting excitation error(s) around a Bragg condition. This phenomenon is known as an electron channelling effect. The effect has been used in ALCHEMI (Atom Location by CHannelling Enhanced Microanalysis) for energy dispersive X-ray spectroscopy (EDXS) and electron energy loss spectroscopy (EELS) in the transmission electron microscope (TEM). However, ALCHEMI is more difficult to perform even qualitatively, because the signal-to-noise ratio is usually very low under the planner channelling conditions due to the off-axis measurement by EELS-aperture under the two-beam excitation condition. We report preliminary results for atomic site-specific analyses of Cr-spinels in electron energy loss near edge structure (ELNES) under electron channelling conditions.

Cr-spinels in a harzburgite assemblage, coexisting with olivine (Fo_{90-91}) and orthopyroxene (Fs_{90-91}), were synthesized using a piston-cylinder apparatus at 1200 °C and 2 GPa under different redox conditions (fO_2). The recovered samples were studied by EDXS and EELS in a TEM. The chemical compositions of the synthesised Cr-spinels ($Cr^{\#}$ = 0.3-0.4) are as follows:

starting material (STM): $^{[4]}(Mg_{0.64}Fe^{2+}_{0.36})_{\Sigma 1.00}{}^{[6]}(Al_{1.20}Cr^{3+}_{0.69}Fe^{3+}_{0.13})_{\Sigma 2.01}O_4$
iron-wüstite (IW): $^{[4]}(Mg_{0.73}Fe^{2+}_{0.27})_{\Sigma 1.00}{}^{[6]}(Al_{1.35}Cr^{3+}_{0.62}Fe^{3+}_{0.04})_{\Sigma 2.01}O_4$
magnetite-hematite (MH): $^{[4]}(Mg_{0.72}Fe^{2+}_{0.16}Fe^{3+}_{0.12})_{\Sigma 1.00}{}^{[6]}(Al_{1.12}Cr^{3+}_{0.68}Fe^{2+}_{0.11}Fe^{3+}_{0.09})_{\Sigma 2.00}O_4$,

where the chemical formulae are based on the assumption of no positional disorder of mixing of Mg and Al cations and distributions of Fe^{2+} and Fe^{3+} were based on the EELS results described below.

The ALCHEMI-ELNES method for the STM-spinel with $Fe^{3+}/\Sigma Fe = 0.17(5)$ indicates a preferential distribution of ferric iron into the octahedral sites and ferrous iron into the tetrahedral sites (see Fig. 3.3-16) and almost no positional disorder of mixing of Mg and Al cations, estimated from ALCHEMI-EDXS spectra. However, the Cr-spinel synthesized in the magnetite-hematite buffer sample has more magnetite component ($Fe^{3+}/\Sigma Fe = 0.43(4)$) than the other samples, which may represent a change from normal spinel to inverse spinel (Fig. 3.3-17), *i.e.*, positional disorder of Fe^{2+} and Fe^{3+} cations between the tetrahedral and octahedral sites. The EDXS spectra under the same channelling conditions did not display any relative intensity changes in Mg-K and Al-K lines, which implies disorder of Mg^{2+} and Al^{3+} cations as well as iron. In the recovered mineral assemblages from different fO_2 experiments, the $Fe^{3+}/\Sigma Fe$ ratios and total Fe contents in Cr-spinels increase with increasing fO_2, which indicates the potential to be used as an oxygen barometer in the Earth's upper mantle. However, the above-mentioned cation disorder might be considered problematic in the application of oxygen barometers at the high temperature studied here.

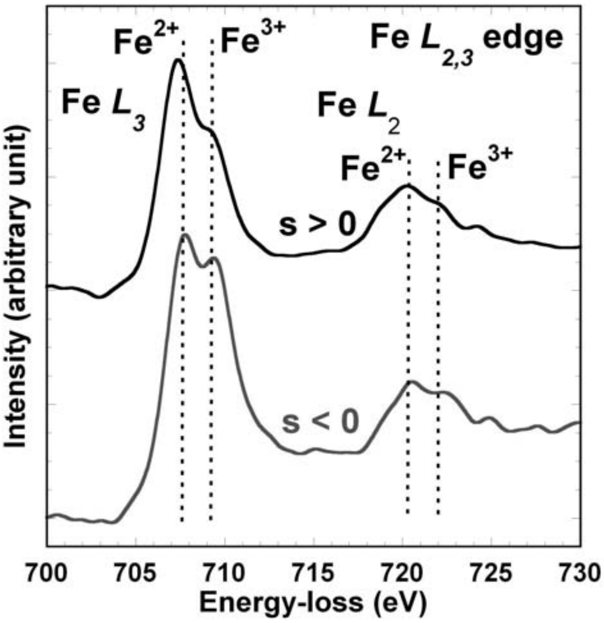

Fig. 3.3-16: Fe-$L_{2,3}$ edge ELNES in the starting Cr-spinel (STM) taken under two different orientation conditions. Lower: Octahedral sites preferentially selected with s < 0 against ***g*** = 400. Upper: Tetrahedral sites selected with s > 0. Relative intensity of the right shoulder in the doublet peaks of Fe-$L_{2,3}$ edges increases under the s < 0 condition, which indicates a preference of ferric iron in the octahedral site.

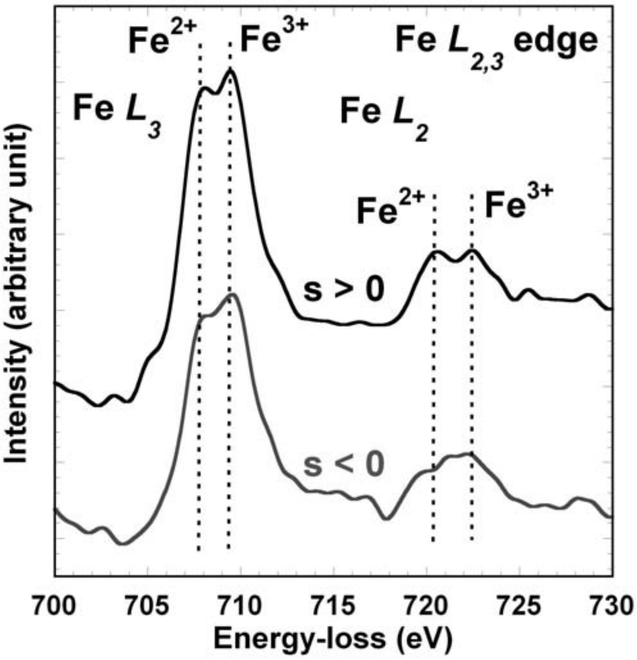

Fig. 3.3-17: Fe-$L_{2,3}$ edge ELNES in the most oxidized Cr-spinel (in the MH-buffered experiment) taken under two different orientation conditions. The configurations are the same as the previous figure. Relative intensities of the doublet peaks in the Fe-L_3 edge do not change under the two conditions, but fine structures in the Fe L_2 edge become more complex. The former indicates no preferential distribution of ferric irons in the octahedral site.

j. *Synthesis of single-crystal (Mg,Fe)SiO_3 perovskite (R. Sinmyo, L.S. Dubrovinsky, C.A. McCammon, E. Bykova, K. Glazyrin and I. Kupenko)*

The chemical composition of the lower mantle can be estimated from a comparison of observed seismic wave velocities with laboratory-measured elastic wave velocities of rocks and minerals. According to this approach, it is now believed that Earth's lower mantle is mainly composed of silicate perovskite and ferropericlase. However, the elastic properties of these phases at lower mantle pressure and temperature conditions (up to about 135 GPa and 4000 K) are still controversial, and therefore the chemical composition of the lower mantle is not well constrained. Hence, a number of studies have attempted to measure elastic properties of lower mantle minerals using various methods. In particular, the combination of single-crystal X-ray diffraction (XRD) and nuclear inelastic scattering measurements has the advantage that it can be applied to iron-bearing minerals under high pressure. Here, we have synthesised a single-crystal of (Mg,Fe)SiO_3 perovskite as the first step for such a combined method.

Fine grained MgO, SiO_2 and Fe_2O_3 (95 % enriched in ^{57}Fe) were ground together for 1 hour and then dehydrated at 1273 K in air, while Fe_2O_3 was used without reducing. A Kawai-type multianvil press was used for high-pressure and -temperature generation. The sample was loaded into a Re capsule and then packed into an MgO container. $LaCrO_3$ was used as a heater. Pressure and temperature conditions were 26 GPa at 2073 K, and the heating duration was 50 min. The recovered sample was chemically analysed using a scanning electron microscope (Fig. 3.3-18). The sample was carefully removed from the Re capsule, and subsequently crushed into several pieces for powder X-ray diffraction (XRD) measurements. After phase identification, the sample was crushed further to separate out the single-crystals. Selected single crystals were examined by XRD using an Oxford Diffraction Xcalibur diffractometer. The $Fe^{3+}/\Sigma Fe$ ratio of the synthesised silicate perovskite was determined by synchrotron Mössbauer spectroscopy at ESRF.

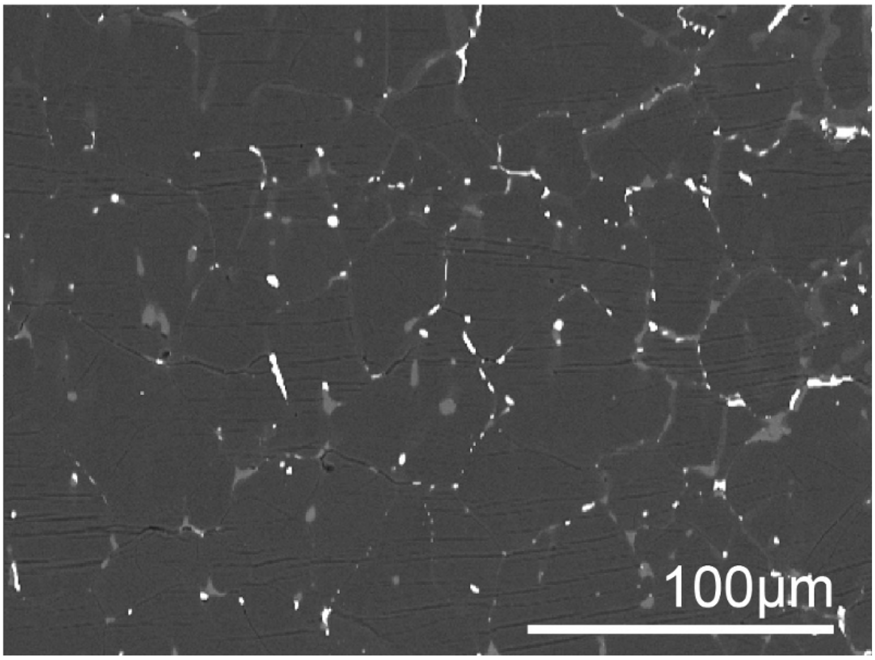

Fig. 3.3-18: Back-scattered electron image of $(Mg_{0.94}\ Fe_{0.06})SiO_3$ perovskite recovered from 26 GPa and 2073 K.

The results of chemical analysis showed that perovskite is chemically homogeneous with a composition of $(Mg_{0.94}\ Fe_{0.06})SiO_3$. The typical grain size is ~ 50 µm at the centre portion. While trace amounts of heavier material were observed in the electron microscope image (Fig. 3.3-18), powder XRD measurements indicated that the main phase of the sample is silicate perovskite. The $Fe^{3+}/\Sigma Fe$ ratio of the synthesised perovskite was determined to be 20 %, even though all iron was Fe^{3+} in the starting material. Iron was possibly reduced by the surrounding metallic capsule during heating. Crystal structure refinement was performed by SHELXL97 software with single-crystal XRD data. We found from structure refinement that all iron substitutes in the A-site of the perovskite structure. This result is in good agreement with previous studies of Al, Fe-bearing perovskite.

k. *Nanocrystalline sulphide and chromium nitride in CM2 chondrites (D. Harries and F. Langenhorst/Jena)*

Phosphorous-bearing Fe,Ni sulfides are characteristic accessory phases in CM2 chondrites, but enigmatic in their mineralogy and origin. We have prepared several FIB sections of P-bearing sulphides from two selected CM2 chondrites. TEM shows that grains in both meteorites are not internally homogeneous. As shown by an earlier TEM study, the sulphide is nanocrystalline (< 20 nm). Surprisingly, in certain grains we found myriads of < 100 nm sized platelets of chromium nitrides, which show preferred alignment in the isotropic, nanocrystalline sulphide matrix. The d-values derived from selected area electron diffraction (SAED) patterns are consistent with CrN (carlsbergite) in Y-791198 and CrN+Cr_2N in Y-793321. The presence of chromium and nitrogen has been confirmed by EDX and EELS. This is the first reported observation of chromium nitride in chondritic meteorites.

SAED patterns of the nanocrystalline sulphides in Y-791198 show two broad rings corresponding to d-values of 0.30 and 0.18 nm (Fig. 3.3-19). In Y-793321 the principal rings appear at the same positions, but splitting occurs and additional, weaker rings join. The corresponding d-values of strong and weak rings in Y-793321 match to a pentlandite structure. HR-TEM imaging shows that the nanocrystallites in Y-793321 are larger (close to 20 nm) and better defined than in Y-791198. Hence, the difference in SAED patterns is due to better crystallinity in Y-793321, which we interpret as a result of thermal annealing. This is supported by the development of a lattice preferred orientation (LPO) of sulphide nanocrystallites in Y-793321, which is evident as circumferential intensity variations along the diffraction rings. The LPO is likely a transitional state during recrystallization toward a single pentlandite crystal. The chemical shift of P Kα determined by EMPA-WDS suggests a mix of phosphate and phosphide and EELS indicates abundant oxygen in the sulphide portion. While phosphide is likely incorporated into the pentlandite structure, phosphate groups probably reside on the large internal boundary surfaces.

HR-TEM imaging of CrN platelets revealed that the dominant face is the (100) form. It is known in metallurgy that CrN precipitating rapidly from metal alloys at temperatures around or below 500 °C forms thin (100) platelets in a specific orientation relationship with the host ferrite/kamacite. The orientation relationship governs the extremely thin shapes of the precipitates and causes preferred orientation. Taken together, the unusual shape and preferred alignment of carlsbergite in the sulphide grains strongly indicates that the platelets originated as precipitates in a Cr- and P-bearing Fe,Ni alloy before sulphidation. We did not find nitrides inside relict metal grains of Y-791198 and Y-793321, but in one case nitride crystals were found in contact with corroded metal. Explaining the abundance of carlsbergite and therefore of high nitrogen concentrations up to 2 wt.% in the bulk sulphide grains poses a challenging problem. N_2 partial pressures on the order of many hundreds of bars would be needed to reach comparable nitrogen contents in molten Fe-Ni-Cr. This is hardly compatible with the conditions of the solar nebula. The absence of nitrides in the metal and the association with sulphides strongly suggests a concurrent formation during sulphidation. This in turn indicates that not only H_2 and H_2S played roles in this process, but also gas-solid interactions with other volatile species such as N_2, and potentially H_2O and NH_3.

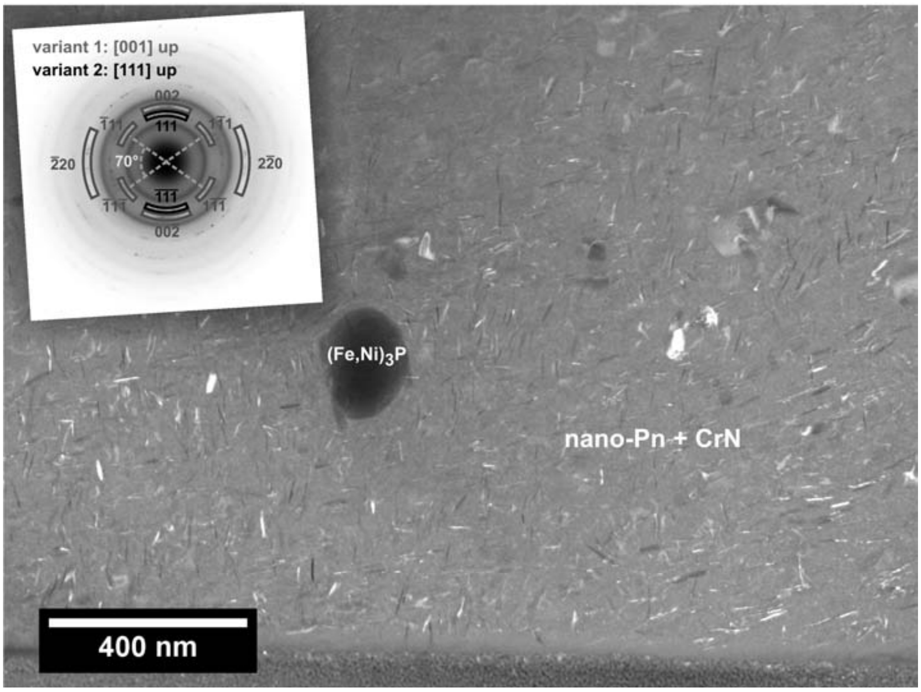

Fig. 3.3-19: STEM-DF image of CrN platelets in nanocrystalline pentlandite (nano-Pn). A large inclusion of schreibersite is present. The inset shows the SAED pattern with broad rings of nano-Pn and reflections of CrN particles, which occur in at least two major orientation variants.

l. *Crystallography of sub-µm sized, pristine refractory metal nuggets from the Murchison meteorite (D. Harries, T. Berg/Mainz, H. Palme/Frankfurt and F. Langenhorst/Jena)*

Metallic minerals are important constituents of chondritic meteorites and maintain a record of solar nebula processes. Os-Ru-Mo-Ir-bearing refractory metal nuggets (RMNs) are excellent candidates for the first solids condensed from the solar gas and some appear to be unaltered since their formation. Their chemical compositions agree remarkably well with predicted condensation into a single metal alloy, which has been calculated in the literature to constrain formation temperatures to between 1400 and 1600 K at 10^{-4} bar total pressure. Alternative models suggested condensation of refractory metal alloys into three different crystal structures: as hcp alloys of Ru and Os, bcc alloys of Mo and W, and as fcc alloys with Ir, Fe, Ni. Subsequent mixing produced the observed opaque assemblages (OA) in CAIs. Earlier predictions of condensation into a single refractory metal alloy were based on the observation of micrometre sized OA, which contain oxidised, sulphidised, and exsolved phases. In these assemblages Mo occurs as molybdenite, W as scheelite, Os and Ru as hcp alloy and Pt and Ir in Fe,Ni alloy, sometimes associated with Fe,Ni sulphides (Fig. 3.3-19a). Understanding the mode of formation of these assemblages, and thereby the conditions of CAI processing, clearly requires knowledge about the initial state of refractory metal condensates. Furthermore, knowledge of the speciation and processing of Mo, Ru, Os, and W appears interesting in terms of understanding of the origin and preservation of nucleosynthetic anomalies observed in isotopes of these elements.

We used FIB-TEM to study the crystallography of a population of submicrometre-sized particles chemically extracted from the Murchison CM2 chondrite, where they most likely resided initially enclosed within CAI mineral grains. These RMNs described by previous authors escaped oxidation and sulphidation and presumably retained their original structure and composition. We found that all particles studied are monophase, often euhedral, single crystals (Fig. 3.3-19b). The electron diffraction patterns of all grains can be unequivocally indexed in terms of a hcp metal structure (space group $P6_3/mmc$). This also includes grains which are compositionally dominated by metals that are non-hcp structured at ambient conditions, such as Mo and Ir (amounting up to ~ 67 at.%). The diffraction patterns show no evidence for exsolution, compositional modulation (*e.g.*, spinodal decomposition leading to diffuse satellite reflections) or superstructure formation. Results of EDX spectroscopy in scanning TEM mode at high spatial resolution (< 10 nm) indicate the absence of compositional zoning across individual grains, except for small Fe (and likely Ni) deficits at the outermost margins of some grains (less than 20 nm from the surface).

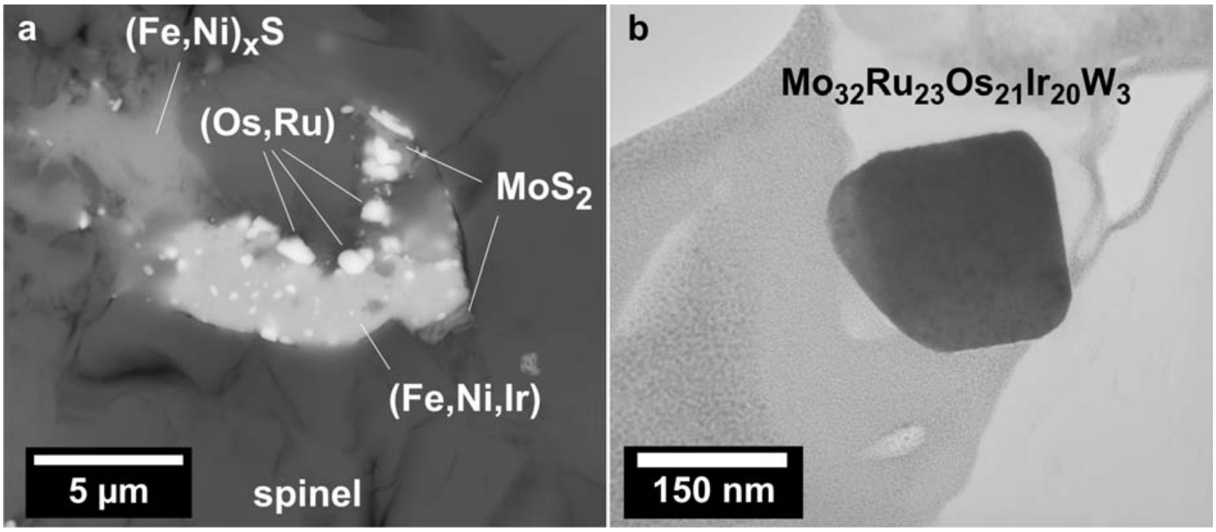

Fig. 3.3-20: (a) SEM-BSE image of a heterogeneous opaque assemblage in an Allende CAI. (b) TEM-BF image of a homogeneous RMN from Murchison.

Our results clearly support the condensation of refractory metals into a single alloy phase. The condensation model proposed by previous authors indicates that upon cooling of a solar gas the metal condensates become increasingly Fe-rich. The fact that we only find hcp-structured

RMNs suggests that the condensation of cubic Fe,Ni alloys, accounting for the bulk metal content of chondrites, did not proceed in a continuous manner. The initially homogeneous formation of refractory metal grains strongly supports the idea that heterogeneous OAs observed in CAIs are secondary products. The processing of OA-bearing CAIs must therefore have happened at conditions significantly different from those during formation of RMNs and their initial incorporation into these CAIs.

3.4 Physical Properties of Minerals

Constraining the physical properties of minerals at pressures, temperatures and compositions of the Earth's interior remains a focal point of research at the Bayerisches Geoinstitut, since their knowledge is essential for relating seismic observations and geophysical models to the actual chemical and thermal state of the Earth's interior. To this end the use of materials synthesised under controlled conditions and well characterised in terms of their chemistry and structure as well as computational techniques which overcome many of the limitations imposed by experiments, have been employed to obtain information on the elasticity, electrical conductivity and magnetic properties of minerals spanning the whole range of the Earth's interior conditions from the crust down to the core. A range of functional materials have also been examined.

In the last couple of years efforts have been made in order to set up a system at BGI which allows the simultaneous measurement of sound velocities and density of single-crystal samples (see annual report 2010) at high pressure and high temperature. This system is so far an unique in-house facility and the first results of full elastic tensors of minerals measured at high pressure are being obtained, not only for "cubic" systems such as pyrope but also for low-symmetry minerals like orthorhombic $MgSiO_3$ perovskite. These results combined with high-pressure and -temperature ultrasonic measurements up to 25 GPa and 1200 K as well as with accurate compressibility data collected on single-crystals up to 75 GPa for $MgSiO_3$ perovskites with different amounts of Fe^{2+}, Fe^{3+} and Al are providing strong constraints on the behaviour of such minerals at the conditions of the Earth's lower mantle.

The study of elastic properties has not been focused only on $MgSiO_3$ perovskite, however. In particular, first principle calculations have been used to elucidate the effect of chemistry on the stability and elasticity of Fe and Al- bearing $MgSiO_3$ post-perovskite phases, as well as to constrain the seismic signature of aluminous phases in subducting slabs. Moreover, powder diffraction at high-temperature has been used to quantify accurately the thermal expansion of forsterite and wadsleyite, whereas the structural evolution of β-realgar, a rare example of a molecular inorganic material, has been investigated by means of high-pressure X-ray single-crystal diffraction.

Another important physical constraint on the Earth's interior is represented by the conductivity profiles versus depth which reveal conductivity anomalies and electrical anisotropy in many regions of the oceanic and continental mantle. Three contributions deal with the electrical conductivity of mantle minerals, the first study focuses on the grain size effect on the conductivity of clinopyroxene, providing thus a basis for extrapolating laboratory data to natural settings, whereas the other two contributions give accurate constraints on the effect of water on electrical conductivity of oriented single-crystals of olivine and of policrystalline wadsleyite.

In the last two contributions the use of diamond anvil cell techniques, coupled in one case with Synchrothron Mössbauer spectroscopy and in the other with laser heating, have allowed the characterisation of the magnetic behaviour of Fe_7C_3 up to 72 GPa and to determine the phase stability and melting properties of calcite up to 43 GPa and 3900 K.

a. *Elasticity of pyrope (M.G. Pamato, T. Boffa Ballaran, D.J. Frost, A. Kurnosov and D.M. Trots)*

Seismological studies are essential for understanding the chemistry and structure of the inaccessible Earth's interior. The velocity of seismic waves through the Earth depends on the elastic properties of the minerals through which they travel in the interior. By comparing the elastic properties of relevant mantle minerals with seismic properties it is possible to relate those observations to the chemical and thermal state of the Earth's interior. Therefore, knowledge of elastic properties of mantle minerals at realistic pressures and temperatures is of crucial importance.

Among mantle minerals, pyrope rich garnet is considered to be an important constituent of the Earth's interior, with a pressure and temperature stability ranging from the Earth's crust down to the upper part of the lower mantle. Although many studies have been conducted on the elastic properties of pyrope, the majority of measurements have been performed either at high pressure (up to 20 GPa) and at room temperature, or at high temperatures (up to 1100 K) and at room pressure. To date, elasticity data at simultaneously high pressure and temperature are missing.

The main aim of this project is to determine the *P-V-T* equation of state and Vs and Vp sound velocities of single crystals of natural pyrope-rich garnet. Brillouin scattering spectroscopy will be used in order to measure single crystal sound velocities at high pressure and temperature. Simultaneously, mineral densities are measured to high precision using single crystal X- ray diffraction in a 4-circle diffractometer to determine *P-V-T* equation of state.

A doubly side polished crystal of natural pyrope (from the ultrahigh pressure metamorphic rocks of the Dora Maira massif, Western Alps) of 90×70×18 μm in size, was loaded in a piston cylinder cell using anvil diamonds with culets of 350 μm in diameter, with a rhenium gasket pre indented to 70 μm and with a hole of 200 μm in diameter. A neon gas, as hydrostatic pressure transmitting medium, was loaded into the sample chamber using a high-pressure gas loading device and a in-house designed external resistive heater was prepared and placed for high-temperature measurements. The unit-cell parameters of pyrope single crystal were determined using a four-circle Huber diffractometer (with Mo*K*α radiation) equipped with an ultrahigh-intensity rotating anode. A Verdi laser with wavelength of 532 nm and a six pass Sandercock interferometer, employing a symmetric/platelet forward 80° scattering geometry, were used for Brillouin measurements.

Preliminary results on the single crystal elasticity of pyrope at room conditions are here reported. Pyrope velocities were measured in different crystallographic orientations and, as shown in Fig. 3.4-1, it is practically elastically isotropic at ambient conditions. Full elastic constants (C_{ij}) were derived by inverting the velocity data with a least square method. The C_{ij} constants obtained in this study are in good agreement (about 1 % difference) with those reported in the literature for both natural and synthetic pyrope. We are planning now to obtain *P-V-T* data as well as Vs and Vp data up to 40 GPa and ~ 1200 K.

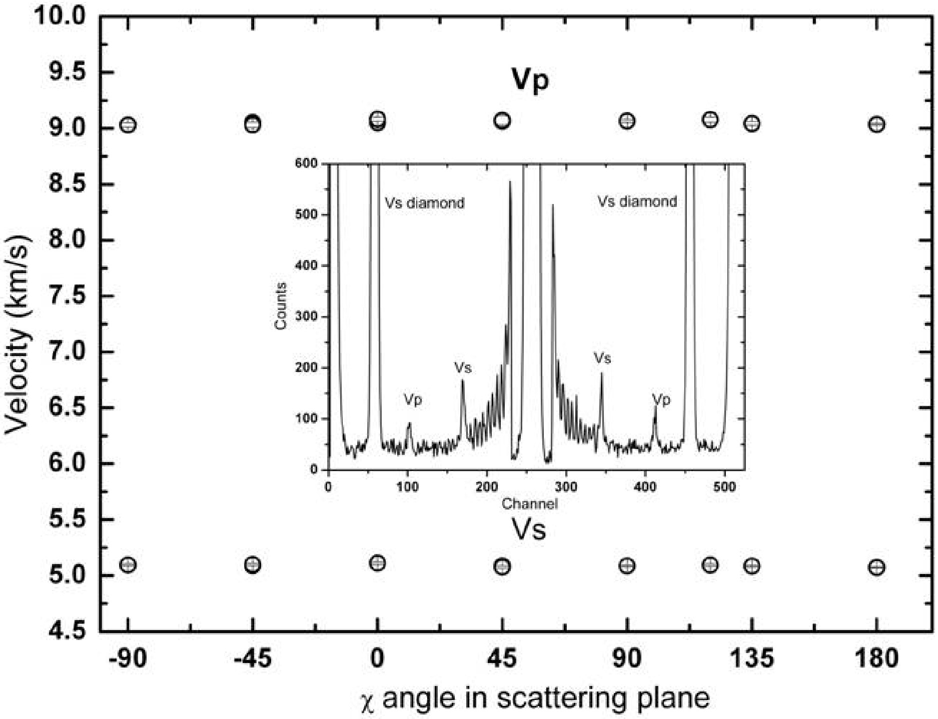

Fig. 3.4-1: Compressional and shear wave velocities of pyrope as a function of crystallographic directions at room pressure and temperature.

b. *High-pressure single-crystal elastic properties of $MgSiO_3$ perovskite obtained by simultaneous X-ray diffraction and Brillouin measurements (A. Kurnosov, D.M. Trots, T. Boffa Ballaran, D. Harries and D.J. Frost)*

Simultaneous measurements of density and sound velocities of single crystals with different orientations is the unique way to determine the full set of elastic constants for low-symmetry materials. However such experiments are a very challenging task when undertaken at pressure and temperature conditions of the Earth's interior. It is, thus, not surprising that the main information on the full elastic tensor of orthorhombic $MgSiO_3$ perovskite, the dominant mineral of the Earth's lower mantle, comes from first principle calculations, whereas experiments are limited to room pressure conditions or deal with aggregate materials and therefore give only average elastic properties.

A combined single-crystal X-ray diffraction/Brillouin scattering system has been recently set up at BGI and it is now possible to measure sound velocities and densities of materials simultaneously as a function of pressure and temperature. The aim of this study is to determine the elastic properties of $MgSiO_3$ perovskite at pressures and temperatures relevant for the lower mantle, as well as to constrain how such properties are affected by Fe and Al substitution. So far orthorhombic $MgSiO_3$ perovskite single crystals have been selected. A platelet sample was prepared using focused ion beam (FIB) cutting to obtain a thin (< 20 µm) single crystal with parallel high-quality surfaces for Brillouin spectroscopy (Fig. 3.4-2). The sample was loaded in a diamond anvil cell with an optical opening angle of 80° with He as pressure transmitting medium and studied both by Brillouin spectroscopy and X-ray diffraction in the pressure range 0 - 31 GPa. A typical Brillouin spectrum of $MgSiO_3$ perovskite still at room conditions, but with the crystal already inserted in the DAC is shown in Fig. 3.4-3. Several efforts were made to improve the collection of the Brillouin signal and at the same time to reduce correlation between the elastic constants during the fitting procedure. For example, the crystal is aligned with respect to the diamond anvils in a way that the minimum of the anisotropic dispersion curve of V_P for the sample corresponds to the maximum of the dispersion curve of V_S for the diamond anvils (both anvils are aligned with respect to each other). Additionally, a mask slit has been installed to reduce the angular distribution of the collected signal and consequently to reduce the halfwidth of the diamond V_S signal. Thanks to these efforts we are able to observe the V_P signal of the sample up to 30 GPa.

To extract the full set of Cij constants for orthorhombic crystals and consequently calculate bulk and shear moduli, however, requires at least two crystals with different random orientations. A second crystal with a random orientation is currently being prepared.

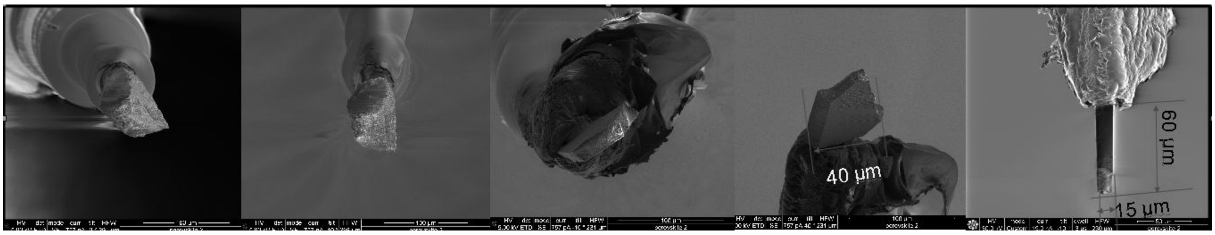

Fig. 3.4-2: Sample preparation using FIB.

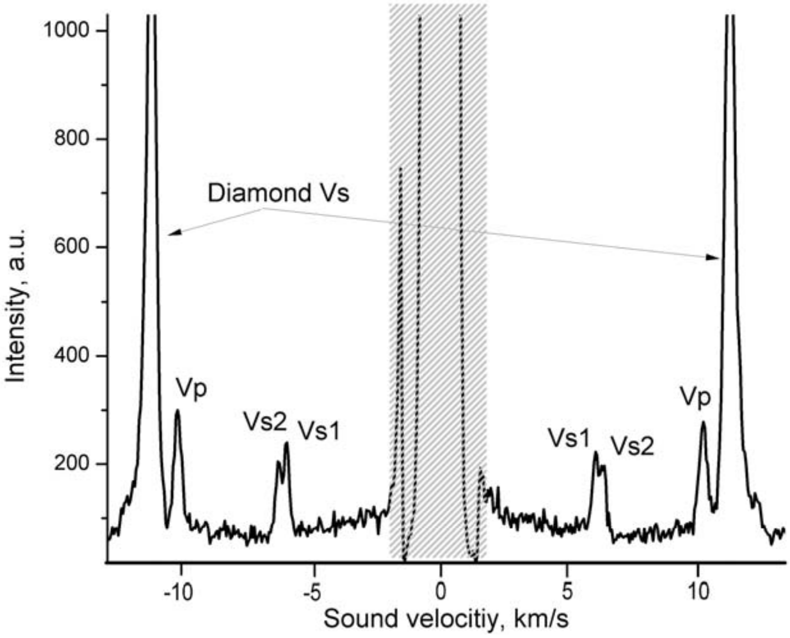

Fig. 3.4-3: Example of a Brillouin spectrum of $MgSiO_3$ perovskite collected with the crystal in the diamond anvil cell and at room pressure.

c. *Sound velocities of (Mg,Fe)SiO_3 perovskite measured up to 25 GPa and 1200 K (J. Chantel and D.J. Frost, in collaboration with Z. Jing and Y. Wang/Chicago)*

The only rigorous method for determining the composition of the Earth's lower mantle is to compare estimates for seismic velocity within the lower mantle with experimentally determined estimates for the appropriate rock compositions. Magnesium-silicate perovskite is the dominant mineral of the Earth's lower mantle. The composition of silicate perovskite forming within a typical Bulk Silicate Earth (BSE) composition is dominated by the $MgSiO_3$ component but will also contain sub equal proportions of Al and Fe. The lower mantle may also contain a significant proportion of remnant subducted basaltic crust, from which more Al and Fe-rich silicate perovskite would form. Fe and Al substitution in perovskite will therefore be a significant source of chemical variability in the lower mantle and potentially the main cause of observed seismic heterogeneity in this region. The study of this substitution on elastic properties is therefore crucial for interpreting seismic observations made on a global and regional scale to place constraints on the variation in temperature, adiabatic gradient and chemical composition in the lower mantle.

Ultrasonic interferometry can be used to measure travel times of P and S-wave velocities. In this study we have measured densities and S and P velocities of monomineralic aggregates of magnesium silicate perovskite at conditions encompassing the top of Earth's lower mantle (up to 25 GPa and 1200 K). Experiments were performed on both the $MgSiO_3$ end member perovskite, and Fe bearing perovskite with 3.6 wt.% FeO. In this way we have constrained the influence of the one of the main chemical variants in the lower mantle on seismic wave velocities.

Combined *in situ* X-ray and ultrasonic measurements were conducted at the 13-ID-D, GSECARS beamline of the Advanced Photon Source in Chicago. Hot pressed polycrystalline aggregates of $MgSiO_3$ and $(Fe,Mg)SiO_3$ with 3.6 wt.% of FeO were presynthesized in Bayreuth. Ultrasonic measurements were performed using a 10/4 multianvil assembly utilizing a Re furnace and an Al_2O_3 buffer rod to make an acoustic junction between the cubic anvil and the sample. The ultrasonic transducer was glued to a cubic truncation directly oppose the truncation employed in the high-pressure experiment. Gold foils separated the sample from the surrounding materials and a pressure calibrant of Au and NaCl was placed next to the sample. A thermocouple was inserted axially on the opposite side of the sample from the buffer rod. X-ray diffraction from the sample and pressure calibrant materials were collected using an energy-dispersive detector. The sample length was measured with a high-resolution (1 pixel ~ 2 µm) CCD camera. Ultrasonic measurements were conducted for both P- and S-waves using the pulse-echo method. The overall uncertainties of the present velocity measurements are within 0.5 % in both V_P and V_S.

Ultrasonic measurements on $MgSiO_3$ perovskite samples are in good agreement with previous studies at room temperature. High-temperature measurements were also performed up to 1200 K at 24 GPa, which are conditions not previously achieved for $MgSiO_3$ perovskite. In addition, for the first time, sound wave velocities were measured for $(Mg,Fe)SiO_3$ perovskite (Fig. 3.4-4). The velocities are approximately 1.5 % lower than those measured for $MgSiO_3$. These results were used to derive a model for the equation of state of $MgSiO_3$-$FeSiO_3$ perovskties to describe wave velocities as a function of pressure, temperature and composition.

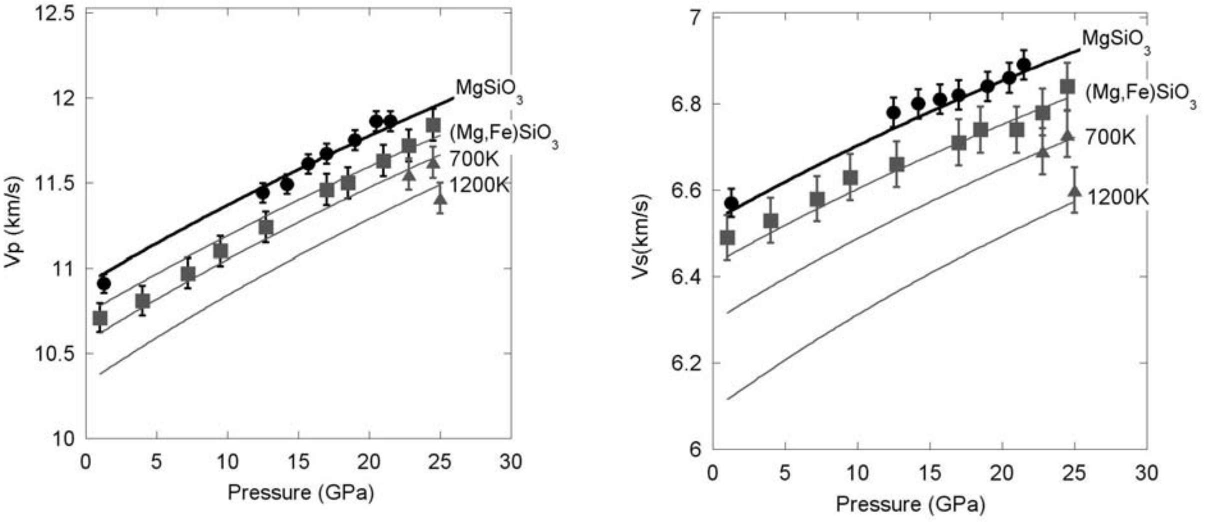

Fig 3.4-4: V_P and V_s measurements as a function of pressure for $MgSiO_3$ perovskite (circles) at room temperature and $(Mg,Fe)SiO_3$ perovskite containing 3.5 wt.% FeO at room temperature (squares) and at 700 and 1200 K (triangles). Results of an equation of state fit to the data are shown by the curves.

Using the derived model and literature models for the other lower mantle minerals, ferropericlase and $CaSiO_3$ perovskite, velocities for a lower mantle BSE rock were calculated along a suitable lower mantle geotherm. These velocities are compared to seismic models for the lower mantle in Fig. 3.4-5. If ultrasonic experimental results on $(Fe,Mg)SiO_3$ perovskite are employed, velocities estimated for a model BSE composition lower mantle are in good agreement with seismic models, within the experimental uncertainties. The only issue that now remains is to examine the combined effect of Fe and Al on perovsktie acoustic velocities.

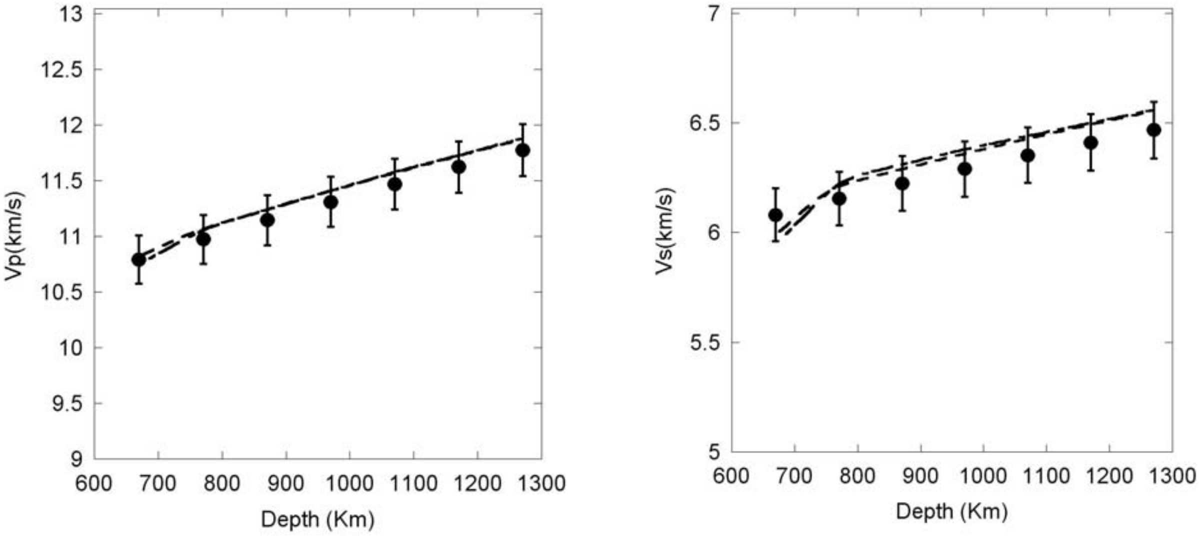

Fig. 3.4-5: Estimates for Vs and Vp of a BSE bulk composition comprising $(Mg,Fe)SiO_3$ perovskite, $(Mg,Fe)O$ ferropericlase and $CaSiO_3$ perovskite are shown as the solid symbols calculated at the pressures and temperatures corresponding to the lower mantle depths indicated. Data for $(Mg,Fe)SiO_3$ perovskite are taken from the equation of state model determined in this study, while models for the other phases are taken from the literature. The dashed lines show PREM and AK135 seismic reference models for the lower mantle.

d. *The effect of chemistry on the compressibility of $MgSiO_3$ perovskite at pressures of the Earth's lower mantle (T. Boffa Ballaran, A. Kurnosov, K. Glazyrin, M. Merlini/Grenoble, M. Hanfland/Grenoble, D.J. Frost and R. Caracas/Lyon)*

A number of studies have identified seismic velocity anomalies extending from the base to the middle of the lower mantle, so called large low shear velocity provinces (LLSVP), Such anomalies have likely a chemical origin and since the major phase stable at the conditions of the lower mantle is magnesium silicate perovskite, we can expect that these regions will contain perovskite with a composition distinct from that of the surrounding mantle. An understanding of the plausible chemical variation of perovskite in addition to its effect on density and elastic properties is, therefore an important issue. Chemical heterogeneities in the lower mantle may be caused by a number of processes. For example the persistence of unequilibrated sections of subducted mid ocean ridge basalt would form regions comprised mainly of Fe-Al rich $MgSiO_3$ perovskite, whereas the persistance of primordial chondritic material would likely form regions low in SiO_2 and consequently lower in ferropericlase, however, such regions may also have an elevated bulk FeO content as found for most meteoritic compositions.

In order to address the effect of such chemical anomalies on the density and seismic velocities at depths of the lower mantle we have studied the compressibility at room temperature of three single-crystals of magnesium silicate perovskite with compositions of the pure end-member $MgSiO_3$, as well as containing 4 mol.% of Fe^{2+} substitution [$(Mg,Fe)SiO_3$] and 37 mol.% of Fe^{3+}- Al coupled substitution [$(Mg,Fe)(Al,Si)SiO_3$]. The crystals were loaded in diamond anvil cells with He as pressure transmitting medium and diffraction intensities have been collected by means of synchrotron X-ray diffraction from room pressure up to 75 GPa at the ESRF on beam line ID-09. The high-quality of the collected data allows a detailed examination of the effect of different chemical substitutions on the compression mechanism of perovskite and on its equation of state (EoS). The bulk modulus and first pressure derivative determined for $MgSiO_3$ perovskite obtained by fitting a 3rd order Birch-Murnaghan are found to be quite insensitive to the maximum pressure to which the data are fitted. The EoS parameters obtained by fitting data from room pressure to 10, 40 or 75 GPa are almost identical. This insensitivity of fitting range, however, is not the case for either $(Mg,Fe)SiO_3$ or $(Mg,Fe)(Al,Si)SiO_3$ perovskites, for which the EoS parameters obtained from fitting data up to 40 GPa deviates with the actual measured data when extrapolated to higher pressure. In the case of $(Mg,Fe)SiO_3$ perovskite this deviation appears to be related to the change in compression of the octahedral tilting as revealed by analysis of the lattice strain variation with pressure (Fig. 3.4-6) and is likely a consequence of the high-spin to intermediate spin transition of Fe^{2+}. In the case of $(Mg,Fe)(Al,Si)SiO_3$ perovskite, instead such effect is clearly due to a change in the compressibility of the *c*-axis (Fig. 3.4-7) and no evidence for effects due to a change in Fe spin state are observed. The two types of substitutions also affect differently the elastic properties of $MgSiO_3$ perovskite, Fe^{2+} in fact has a large negative effect on the bulk sound velocity and a large increase in density in contrast with Fe^{3+}-Al which have a very modest effect both on the bulk sound velocity and on density. The latter may be, therefore, more compatible with causing the observed seismic anomalies in the lower mantle.

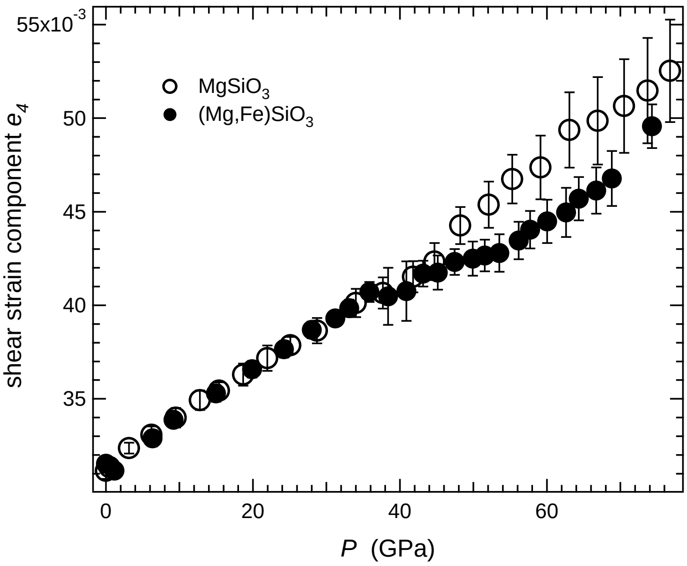

Fig. 3.4-6: Variation as a function of pressure of the shear strain component e_4 related to the variation of the tilting of the orthorhombic $MgSiO_3$ and $(Mg,Fe)SiO_3$ perovskites.

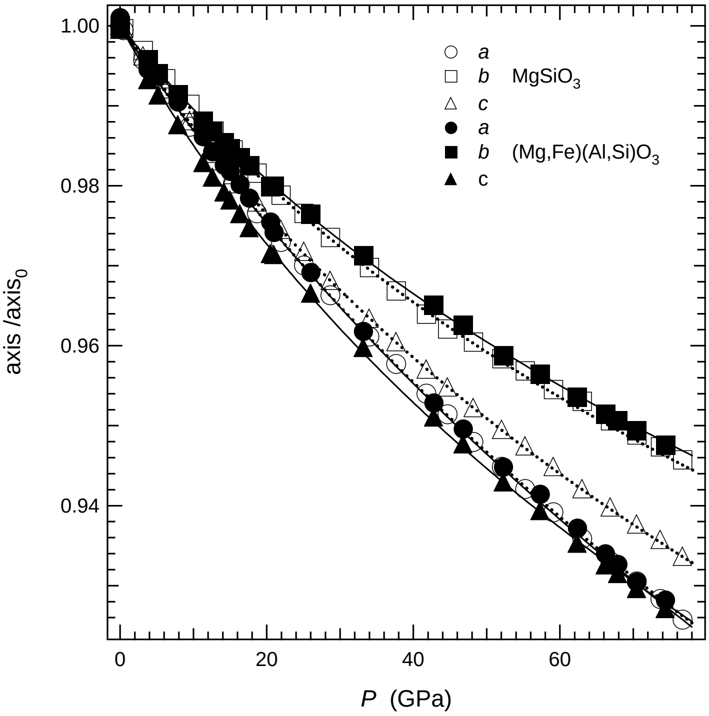

Fig. 3.4-7: Variation as a function of pressure of the unit-cell axes of $MgSiO_3$ and $(Mg,Fe)(Al,Si)O_3$ perovskites scaled with respect to their values at room pressures. Note the different behaviour of the *c*-axis between the two samples.

e. *Stability and compressibility of FeO, Fe_2O_3 and Al_2O_3 bearing-$MgSiO_3$ post-perovskite from* ab initio *calculations (M. Oussadou, G. Steinle-Neumann and M. Mookherjee)*

High-pressure/-temperature experiments and *ab initio* calculations have shown that $MgSiO_3$ perovskite (pv), the dominant phase of Earth's lower mantle, transforms to a $CaIrO_3$-type structure, named now post-perovskite (ppv) phase at ~ 120 GPa and ~ 2500 K, conditions at the base of the lower mantle (D" zone). As $MgSiO_3$ perovskite includes considerable amounts of FeO, Fe_2O_3 and Al_2O_3 in its bulk composition, these minor elements could also have a significant effect on the stability of the ppv phase.

In the current work we explore the energetics and compressibility of Fe^{3+}-, Al^{3+}-, and Fe^{2+}-bearing $MgSiO_3$ post-perovskite using first-principle theory based on density functional theory with the Vienna *Ab initio* Simulation Package. In a supercell of 80 atoms ($Mg_{16}Si_{16}O_{48}$) we have investigated the following charge coupled substitution mechanism on the A (Mg^{2+}) and B (Si^{4+}) sites of $MgSiO_3$ ppv:

- $Fe^{2+}\leftrightarrow Mg^{2+}$ with compositions $(Mg_{15}Fe)Si_{16}O_{48}$, $(Mg_7Fe)Si_8O_{24}$, $(Mg_3Fe)Si_4O_{12}$, and $FeSiO_3$.
- $Fe^{3+}Al^{3+}\leftrightarrow Mg^{2+}Si^{4+}$ with compositions $(Mg_{15}Fe)(Si_{15}Al)O_{48}$, $(Mg_7Fe)(Si_7Al)O_{24}$, $(Fe_{15}Mg)(Al_{15}Si)O_{48}$, and $FeAlO_3$.
- $Al^{3+}Fe^{3+}\leftrightarrow Mg^{2+}Si^{4+}$ with compositions $(Mg_{15}Al)(Si_{15}Fe)O_{48}$, $(Mg_7Al)(Si_7Fe)O_{24}$, and $AlFeO_3$.
- $2Fe^{3+}\leftrightarrow Mg^{2+}Si^{4+}$ with composition $(Mg_{15}Fe)(Si_{15}Fe)O_{48}$, $(Mg_7Fe)(Si_7Fe)O_{24}$, and $(Fe_{15}Mg)(Fe_{15}Si)O_{48}$, Fe_2O_3.
- $2Al^{3+}\leftrightarrow Mg^{2+}Si^{4+}$ with composition $(Mg_{15}Al)(Si_{15}Al)O_{48}$, $(Mg_7Al)(Si_7Al)O_{24}$, and Al_2O_3.
- $Fe^{2+}2Fe^{3+}\leftrightarrow 2Mg^{2+}Si^{4+}$ with composition $(Mg_{14}Fe_2)(Si_{15}Fe)O_{48}$.

- $Fe^{2+}Al^{3+}Fe^{3+}$↔$2Mg^{2+}Si^{4+}$ with composition $(Mg_{14}AlFe)(Si_{15}Fe)O_{48}$.
- $Fe^{2+}Fe^{3+}Al^{3+}$↔$2Mg^{2+}Si^{4+}$ with composition $(Mg_{14}Fe_2)(Si_{15}Al)O_{48}$.
- $Fe^{2+}2Al^{3+}$↔$2Mg^{2+}Si^{4+}$ with composition $(Mg_{14}FeAl)(Si_{15}Al)O_{48}$.

Using these compositions we have calculated the excess static enthalpy of mixing for post-perovskite for solid solutions along different joins with $MgSiO_3$. For the Fe^{2+} substitution along $MgSiO_3$-$FeSiO_3$ we find that Fe^{2+} incorporation is energetically not favorable, in agreement with previous computations. Along the $MgSiO_3$-$FeAlO_3$ and $MgSiO_3$-$AlFeO_3$ joins we predict that both substitutions are favored with respect to the end-members, and that Al^{3+} favors the A-site over Fe^{3+}. Coupled trivalent and Fe^{2+} substitutions are energetically stable over their respective end-members, suggesting that the coupled Fe^{2+}-trivalent cation substitution provides an effective route to incorporate Fe^{2+} into the A-site of $MgSiO_3$ ppv.

A third-order Birch Murnaghan equation of state has been fit to the *P-V* results for the different compositions, and we find that the zero pressure volume is increasing from $MgSiO_3$ to Fe^{2+}- and Fe^{3+}-bearing post-perovskites. Zero pressure bulk moduli and their pressure derivates are plotted with confidence ellipses in Fig. 3.4-8. While Fe^{2+}-bearing ppv phases (inset of Fig. 3.4-8) have values close to those of $MgSiO_3$ end-member, the Fe^{3+}-bearing ppv phases (Fig. 3.4-8) show larger variations in K_0 and K_0', with the coupled $Fe^{2+}Fe^{3+}Al^{3+}$ substitution showing the largest zero pressure bulk modulus of all phases.

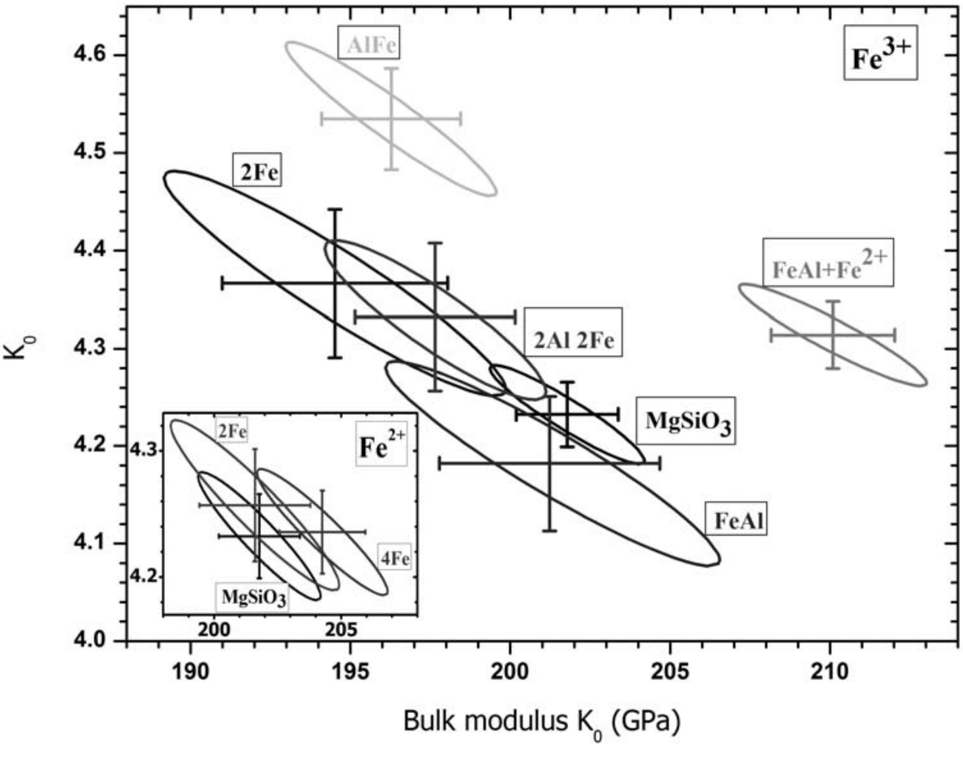

Fig. 3.4-8: Zero pressure bulk modulus K_0 and its pressure derivative K_0' computed for different compositions of Fe^{3+}- and Fe^{2+}- (inset) bearing post-perovskites. Results on *P-V* relation are fit with a 3rd-order Birch-Murnaghan equation of state (Eosfit52). Note that the limit of the 1σ error bar obtained from the variance of the two parameters correspond to the limit of a confidence ellipse calculated with $\Delta = 2.30$.

f. *Elasticity of aluminous phases in subducted MORB (M. Mookherjee)*

Seismological and chemical evidence indicates that heterogeneity is ubiquitous in the mantle. Subduction and separation of oceanic crust from the slab is one of the processes that may produce this heterogeneity. Subducted mid ocean ridge basalt (MORB) has very different major and trace element chemistry in comparison to the surrounding pyrolitic mantle. While the bulk silicate Earth contains 4 wt.% alumina, MORB is significantly enriched with 16 wt.% alumina. MORB is also enriched in iron and alkali elements. As a result of the differing chemistry, the phase relations in MORB are quite different from that of pyrolite in the deep mantle. At lower mantle depths, MORB consists of Mg-perovskite, Ca-perovskite, stishovite and an aluminous phase. The aluminous phase has various crystal structures, including a phase with the calcium ferrite-type structure (CF) and a phase with calcium titanate-type structure (CT). The volume fraction of the aluminous phases (CF and CT) in MORB is around 20 %. These phases vary widely in chemistry between the end members $MgAl_2O_4$ and $NaAlSiO_4$. Although high-pressure phase equilibria and equation of state of major subducting phases has been a subject of major interest, there is a paucity of studies on the elasticity of these aluminous phases.

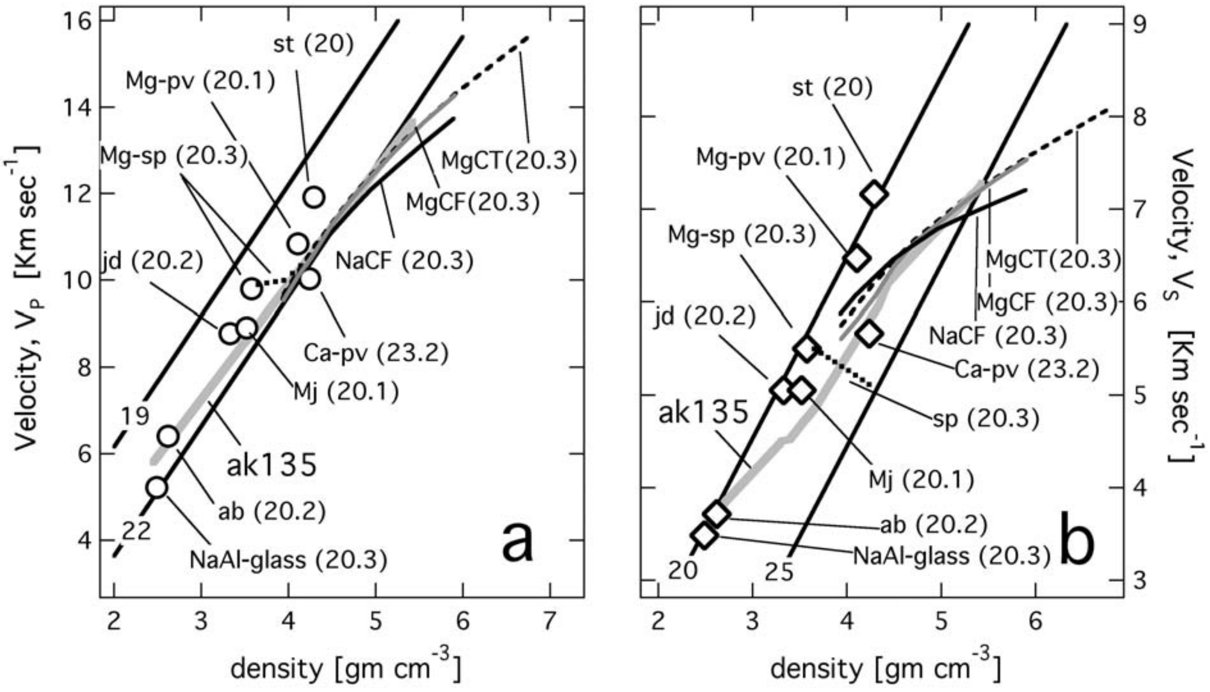

Fig. 3.4-9: Velocity density systematics, (a) compressional and (b) shear wave velocities, the solid black lines refer to constant mean atomic weights. MgCF phase: grey solid curve, MgCT phase: dark grey dashed curve, NaCF: black solid curve, $NaAlSi_3O_8$ glass (NaAl-glass), albite (ab), majorite (Mj), jadeite (jd), spinel (sp), Mg-perovskite, (Mg-pv), Ca-perovskite (Ca-pv), stishovite (st), reference Earth model: ak135.

Using first principle simulations, we calculated the equation of state and elasticity of $NaAlSiO_4$ (NaCF) and $MgAl_2O_4$ (MgCF and MgCT) up to > 150 GPa, encompassing the full range over which NaCF, MgCF and MgCT has been observed experimentally. We calculate the isotropically averaged elastic wave velocities and the anisotropy from our single crystal elastic constants. The compressional (V_P) and shear (V_S) wave velocities of these aluminous phases are significantly slower than those of silica polymorphs (Fig. 3.4-9). Heterogeneity due to subducted oceanic crust might be difficult to detect based only on the velocity heterogeneity since mid-oceanic ridge basalt is enriched in both silica and aluminous phases which have fast and slow velocities which likely compensate each other. Moreover, the elasticity of these aluminous phases is sensitive to the chemistry. The bulk modulus decreases with $MgAlNa_{-1}Si_{-1}$ substitution with a $\partial K_0/\partial x \sim$ -15 GPa, whereas the shear modulus stiffens with a $\partial G_0/\partial x \sim$ 10 GPa. At lower mantle conditions, the temperature derivative of bulk, $\partial K/\partial T$ and shear $\partial G/\partial T$ modulus are -0.006 and -0.013 GPa K^{-1}, respectively. Slab penetrating the lower mantle often develops significant anisotropy. The full elastic constant tensor of these aluminous phases reveal significant anisotropy and are likely candidates to account for the large delay times observed in the Tonga-Kermadec subduction zones.

g. *High-temperature structural behaviour of anhydrous wadsleyite and forsterite (D.M. Trots, A. Kurnosov, T. Boffa Ballaran and D. J. Frost)*

The Mg_2SiO_4 polymorphs forsterite and wadsleyite are major mineral components within the Earth's upper mantle and transition zone. The olivine-wadsleyite (or α-β) transition of $(Mg,Fe)_2SiO_4$ is considered to cause a seismically detectable discontinuity in elastic properties at approximately 410 km depth. Precise information on the physical properties and stability fields of wadsleyite and olivine at high temperatures and pressures is of primary importance to geophysics. In order to calculate stability fields and seismic wave velocities of mantle minerals, thermodynamic parameters are often refined from high-pressure experimental phase relations and equation of state data. This permits phase boundaries and seismic wave velocities to be determined at conditions beyond the range of experimental measurements and allows multiple studies to be compared and uncertainties in pressure and temperature to be addresses. Such calculations benefit immensely if parameters such as thermal expansivity and bulk modulus, can be accurately determined independently. Thermal expansion measurements provide particularly useful constraints on elastic properties due to very low experimental uncertainties. However, there is significant divergence between results of previous thermal expansion studies performed on Mg_2SiO_4 polymorphs and strong divergence in some equations used to parameterize these measurements when extrapolated beyond the measured range. This fact provoked us to perform high-temperature powder diffraction experiments on anhydrous wadsleyite and forsterite and to examine a suitable methodology for fitting and extrapolating the data. We compare our results with previous studies and with analyses of previous studies reported in the literature. In addition, temperature-induced structural variations in anhydrous wadsleyite are examined through Rietveld refinement of synchrotron powder diffraction data.

Thermal expansion measurements and *in situ* structural investigation of the two samples of anhydrous wadsleyite (z626 and z627) were performed at the synchrotron facility HASYLAB/DESY (Hamburg, Germany) with the powder diffractometer at beam-line B2 while the thermal expansion of forsterite was measured using a Philips Xpert powder diffractometer at BGI. The high-temperature data of forsterite (Fig. 3.4-10a) can be reproduced equally well by fitting both a 1st or a 2nd order Grüneisen approximations and a Debye model for the internal energy, however, while the 1st order fit provides an estimate of the Debye temperature consistent with independent elasticity determinations, the supposedly more appropriate 2nd order fit underestimates the Debye temperature. Extrapolation of volumes to higher temperature using these equations shows that they diverge above 1600 K but differ by only 0.4 % at the forsterite melting temperature (~ 2150 K). The high-temperature data of wadsleyite (Fig. 3.4-10b) also can be fitted equally well by means of a 1st or a 2nd order Grüneisen approximation and both fitting provide estimates for the Debye temperature that are in agreement with independently determined literature values.

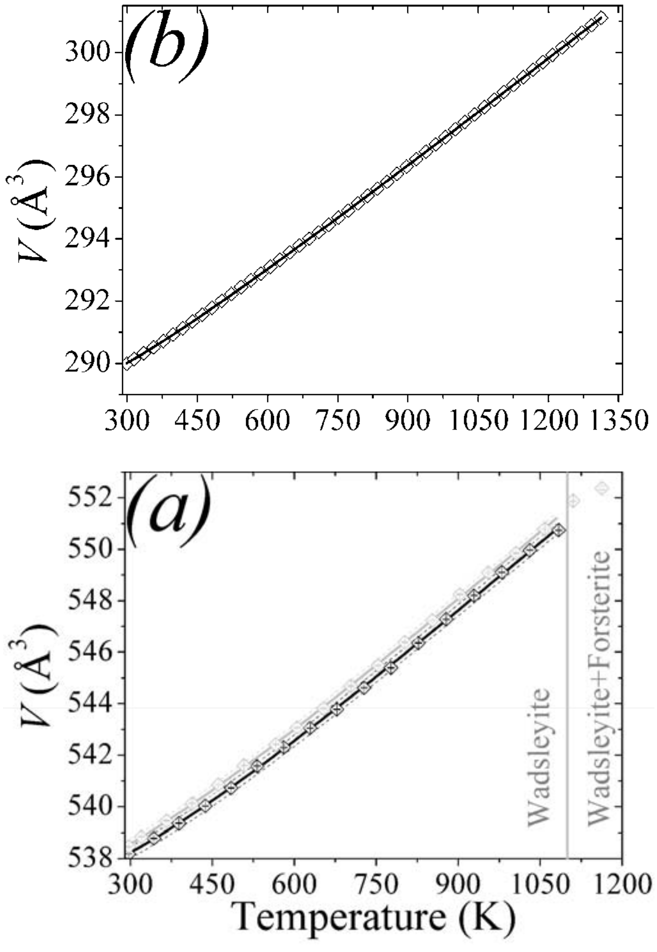

Fig. 3.4-10: Variation of the unit-cell volume of (a) forsterite and (b) wadsleyite measured by means of X-ray powder diffraction. Black and grey symbols in (b) are experimental data obtained from Rietveld refinements for z626 and z627 samples, respectively. Solid lines through the symbols denote results of fits of 1st order Grüneisen approximation $V(T) = \frac{\gamma}{K_0} U(T) + V_0$ to experimental data (V_0 is hypothetical volume at $T = 0$, γ is the Grüneisen parameter, assumed to be pressure and temperature independent, K_0 is the isothermal bulk modulus at $T = 0$ K, the internal energy $U(T)$ can be calculated using the Debye model to describe the energy of the lattice vibrations). Dashed lines in (b) represent confidence intervals at the 99 % confidence level.

h. *Compressibility of synthetic β-As_4S_4:* In situ *high-pressure single-crystal X-ray study (G. Lepore/Firenze, T. Boffa Ballaran, F. Nestola/Padova, L. Bindi/Firenze, P. Bonazzi/Firenze and D. Pasqual/Padova)*

Various compounds belonging to the As-S system are of interest to physicists and material scientists and are thus widely studied because of their potential applications. These materials are in fact characterized by a strong photostructural sensitivity which leads to reversible and/or irreversible changes in their physico-chemical properties, making them very important for their actual or potential use in fields like optics and optoelectronics. They also are very important in examination and conservation of art objects, since many arsenic sulfides minerals, characterized by colours ranging from yellow to red, were largely used as pigments.

Most of these materials consist of a packing of cage-like, covalently bonded As_4S_n (n = 3, 4, and 5) molecules held together by van der Waals forces, and the investigation of their thermodynamic properties, such as thermal expansion and compressibility, can usefully contribute to the understanding of the interactions governing the structure and its stability.

The crystal structure of the α modification of As_4S_4 (*i.e.*, the mineral realgar) has been recently investigated by energy-dispersive X-ray diffraction technique up to 8 GPa and *in situ* X-ray single-crystal and powder diffraction methods up to 43 GPa. On the other hand, no data on the compressibility and structural behaviour of β-As_4S_4 at high pressure have been reported in the literature so far. The investigation of the variation of β-As_4S_4 structure and properties with pressure is of great importance since this compound is an interesting and quite rare example of a molecular inorganic crystal with closed globular molecules. The character of the molecule displacements in the lattice cell during compression may be a precursor of possible phase transitions. The bulk modulus value and its variation with pressure directly reflect the character of intermolecular forces.

Under ambient-pressure conditions, β-As_4S_4 crystallizes in the $C2/c$ space group with a = 9.957(3), b = 9.335(4), c = 8.889(5) Å, β = 102.48(4)°. The structure consists of As_4S_4 cage-like molecules, characterized by a D_{2d} molecular symmetry, with each As atom bonded to one As and two S atoms. Crystals of β-As_4S_4 were obtained by heating crystals of realgar under vacuum at 295 °C for 24 hours. The quenched product was used to collect single crystal intensity data at pressures up to 6.86 GPa using two different diamond anvil cells loaded with different crystals in a methanol-ethanol (4:1) mixture. Unit-cell measurements have been performed in a ETH-type DAC using a STOE STADI IV four-circle diffractometer equipped with a point detector (University of Padova). The measurement of unit-cell parameters became impossible beyond 2.8 GPa because of a dramatic broadening of reflections. The whole intensity data collections were carried out at different pressure steps up to 6.86 GPa using an Oxford Diffraction -Xcalibur2 diffractometer equipped with a CCD detector (Bayerisches Geoinstitut) using a Böhler-Almax DAC. The diffraction study has been combined with a microRaman investigation throughout the whole experiment. The P-V data

(Fig. 3.4-11) were fit using a Birch-Murnaghan equation of state truncated at the 3rd-order with resulting bulk modulus K_0 = 10.9(2) GPa, and its first pressure derivative K' = 8.9(3). These values are substantially identical to those found for the low-temperature polymorph (realgar), characterized by the same kind of molecule. The response to pressure is almost isotropic and the dramatic decrease of the unit-cell volume (from 805.17 to 632 Å^3 at 6.86 GPa) is mainly due to the reduction of intermolecular distances, whereas the intramolecular distances remain substantially unchanged. In particular, the volume of the As_4 tetrahedron does not decrease significantly while the molecular volume contracts by approximately 2 %, due to the shortening occurring along the S3-S3 $[30\bar{1}]$ and S1-S2 [010] directions. Further experiments, carried out at higher pressures with a thinner crystal, only led to a rough measurement of the unit-cell parameters showing that β-As_4S_4 does not undergo any phase transition in the whole pressure range investigated, in spite of a compression to about 80 % of its initial volume.

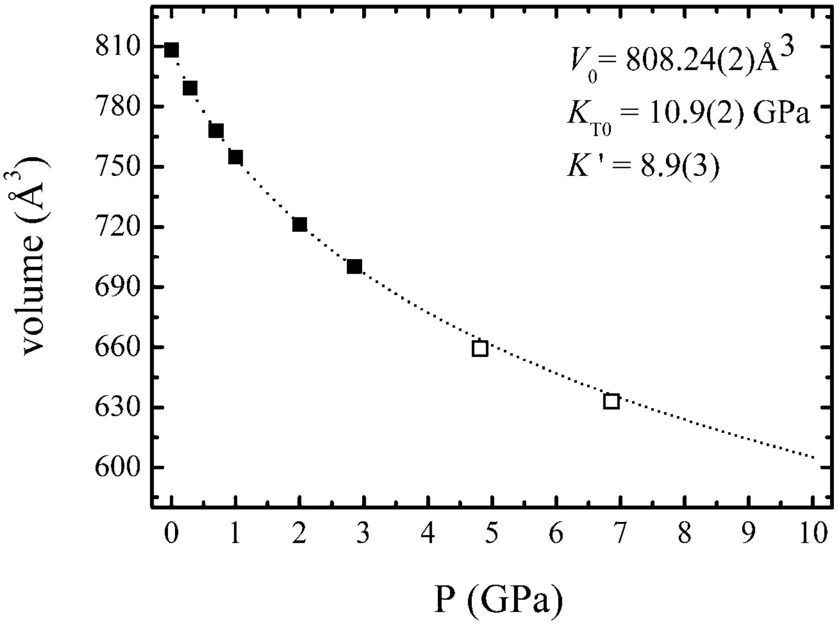

Fig. 3.4-11: Pressure dependence of the unit-cell volume of β-realgar. The dotted curve represents the 3rd order Birch-Murnaghan EoS fit of the P-V data. The e.s.d.'s values are smaller than the size of the symbols. Empty symbols refer to volumes measured at 4.81 and 6.86 GPa with the CCD detector and were not used for the EoS fitting.

i. *Grain size effect on the electrical conductivity of clinopyroxene (X. Yang and F. Heidelbach)*

The electrical properties of Earth materials are strongly dependent on factors such as chemical composition, temperature, oxygen fugacity and crystallographic orientation but slightly on pressure, and the influence of these parameters has been investigated in previous studies. The grain size of minerals in the Earth's interior varies from ~ 10 µm (*e.g.*, some ultra-mylonites in strong shear-zones) to several mm or even larger depending on the thermal and mechanical history. Many laboratory electrical conductivity measurements are conducted on fine-grained polycrystalline samples, and the grain sizes, *e.g.*, from < 10 to tens of µm, are usually different from those inside the Earth. Therefore, there is a potential gap between laboratory measured electrical conductivity of fine-grained minerals and geophysically resolved electrical conductivity of the Earth's interior, and it is necessary to address to what extent the results of laboratory determinations can be applied to natural settings.

We have measured the electrical conductivity of polycrystalline clinopyroxenes with different grain size fractions (~ 5-63, 63-160 and 160-250 µm) and single crystal clinopyroxene with orientation parallel to *b*, using impedance spectroscopy at simultaneous high-pressure and temperature conditions. The starting material was a natural single crystal augite, and the experiments were conducted at 10 kbar and 500 to 1000 ºC with a piston cylinder apparatus. The results show that the electrical conductivity of all the samples is similar at given temperatures (Fig. 3.4-12). As has been shown previously that the orientation-induced electrical anisotropy of dry clinopyroxene is negligible, the electrical conductivity of dry clinopyroxene is independent of grain size changes above ~ 5 µm. The conduction is controlled by the bulk material rather than the grain boundaries. The activation enthalpy over the measured temperature range is 83±3 to 90±3 kJ/mol due to conduction by small polarons. Our data provide a solid basis for extrapolating laboratory electrical conductivity data to natural settings.

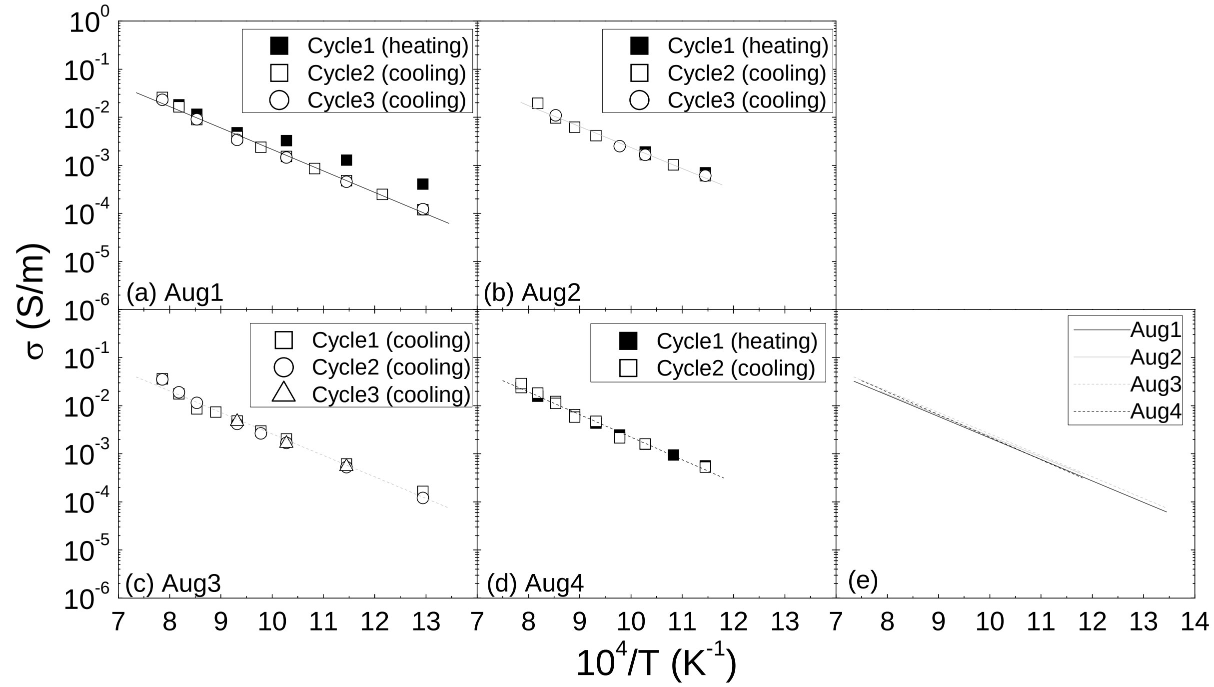

Fig. 3.4-12: Electrical conductivity of dry augites as a function of temperature. (a) 5-63 µm, (b) 63-160 µm, (c) 160-250 µm, (d) sing crystal (//*b*), and (e) comparison of electrical conductivity between different samples. Solid and dashed lines are from linear regression.

j. *Orientation-related electrical conductivity of hydrous olivine (X. Yang)*

Results from laboratory studies of the electrical conductivity of Earth materials are important in the interpretation of conductivity profiles versus depth derived from field observations and of conductivity anomalies inside the Earth. Electrical anisotropy has been reported concomitantly with electrical anomalies and synonymously with seismic anisotropy in many regions of the uppermost oceanic and continental mantle (~ 40-200 km depth) and the resolved electrical conductivity can be up to ~ 0.01-0.1 S/m along some direction(s). In spite of many studies in the past decades, the origin of electrical anisotropy in the uppermost mantle remains a poorly constrained issue.

Olivine is the most abundant mineral in the uppermost mantle, and is probably characterized by significant lattice-preferred orientation (LPO) due to mantle flow. Because the conductivity of dry olivine is usually very low, *e.g.*, < 0.001-0.01 S/m at mantle conditions, some people argued that mantle electrical anisotropy may be caused by the LPO of hydrous olivine due to H-enhanced conductivity. In this study, we measured the orientation-related electrical conductivity of H-bearing olivine under well-controlled pressure, temperature, water content and oxygen fugacity conditions. Starting materials were gem-quality natural olivine crystals, and hydrous samples with ~ 40 ppm H_2O were annealed at 2 kbar and 800 ºC with a hydrothermal vessel.

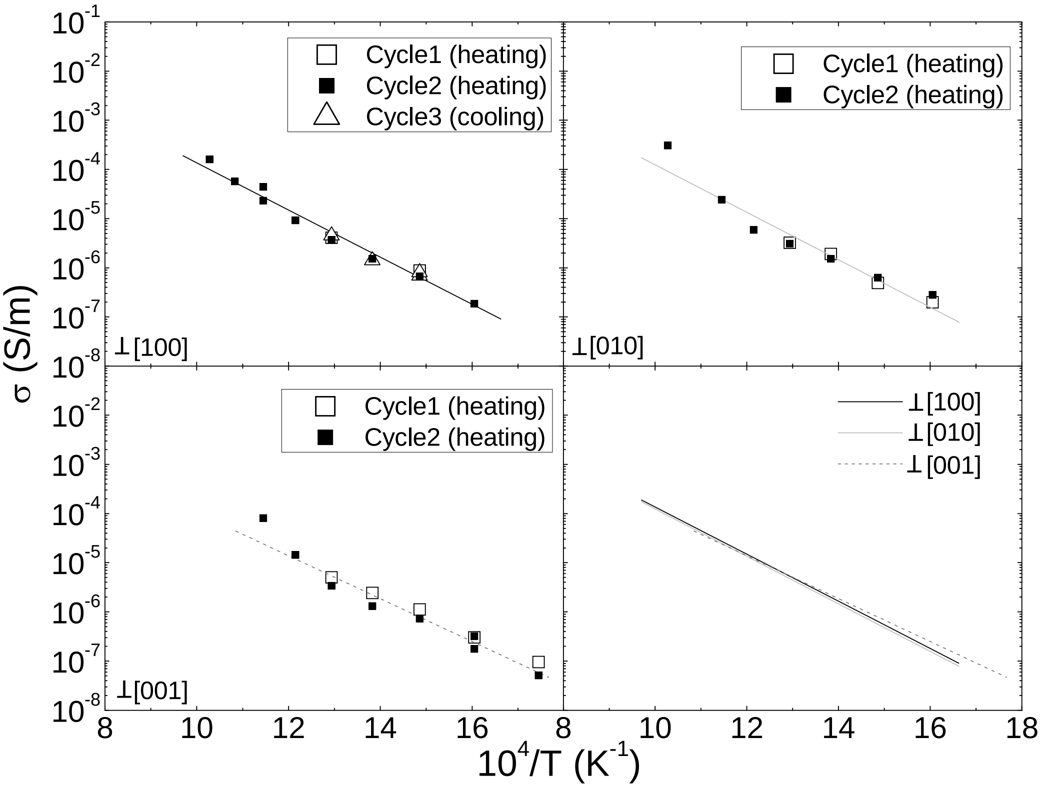

Fig. 3.4-13: Electrical conductivity of hydrous olivine (40 ppm H_2O) along different orientations (10 kbar and Ni-NiO buffer).

Because electrical conductivity of silicate minerals is not sensitive to pressure, the experiments were conducted at 10 kbar with an end-loaded piston cylinder apparatus. To avoid serious sample dehydration at high temperatures, complex impedance was measured mainly from 300 to 700 ºC, and electrical conductivity was calculated from the measured complex spectra and sample dimensions. The results show that the activation enthalpy is 84±6 to 92±7 kJ/mol, in good agreement with available reports for H-conduction in olivine, and that the orientation-related conductivity anisotropy is negligible (Fig. 3.4-13). Assuming that H-conduction also occurs at mantle temperatures, the resolved electrical anisotropy in the uppermost mantle cannot be attributed to the LPO of hydrous olivine.

k. *Re-evaluation of electrical conductivity of anhydrous and hydrous wadsleyite (T. Yoshino/Misasa and T. Katsura)*

Recent laboratory electrical conductivity measurements of the main mantle constituent minerals have made a lot of effort to accurately determine the effect of water content on electrical conductivity. However, at least in the case of wadsleyite, there is a large discrepancy among the results present in the literature with some work suggesting a relatively high hopping and low proton conduction, implying a negligible effect of water on electrical conductivity and some other suggesting the opposite tendency, and therefore emphasizing a large water effect. The discrepancy of these results leads to the impossibility of a clear understanding of the role of water in the mantle, and therefore, we have decided to reinvestigate hydrous and anhydrous wadsleyite to accurately determine their electrical conductivity and possibly to give some insight on the reasons causing such divergent results.

We have measured the electrical conductivity of wadsleyite with different water content as well as of a wadsleyite sample with a very small amount of water (< 2 ppm) by means of impedance spectroscopy. Moreover, in order to test the effect of temperature on the dehydration of wadsleyite with consequent formation of free fluid we conducted the experiments up to 1100 K. Change of the measured impedance spectra up to 1100 K are shown in Fig. 3.4-14. The impedance spectra in the heating path (Fig. 3.4-14a) show one single almost perfect semicircular shape. Once the temperature reaches 1100 K (Fig. 3.4-14b), however, the impedance spectrum appears suddenly distorted, and consist of more than two arcs. In the successive cooling path (Fig. 3.4-14c and 3.4-14d), the arcs have a similar distorted shape. Measurement of water content by means of infrared spectroscopy reveals that the water content of the recovered wadsleyite sample is much lower than that of the same sample before the conductivity measurements, suggesting that free fluid formed above 1000 K. Our results are consistent with a previous work by Yoshino *et al.* (Nature, 451(7176), 326-329, 2008) and indicate that there is no effect of water on the electrical conductivity of wadsleyite. Moreover, our results show that experiments conducted at temperatures higher than 1000 K may be affected by the presence of free fluid and therefore lead to incorrect conclusions.

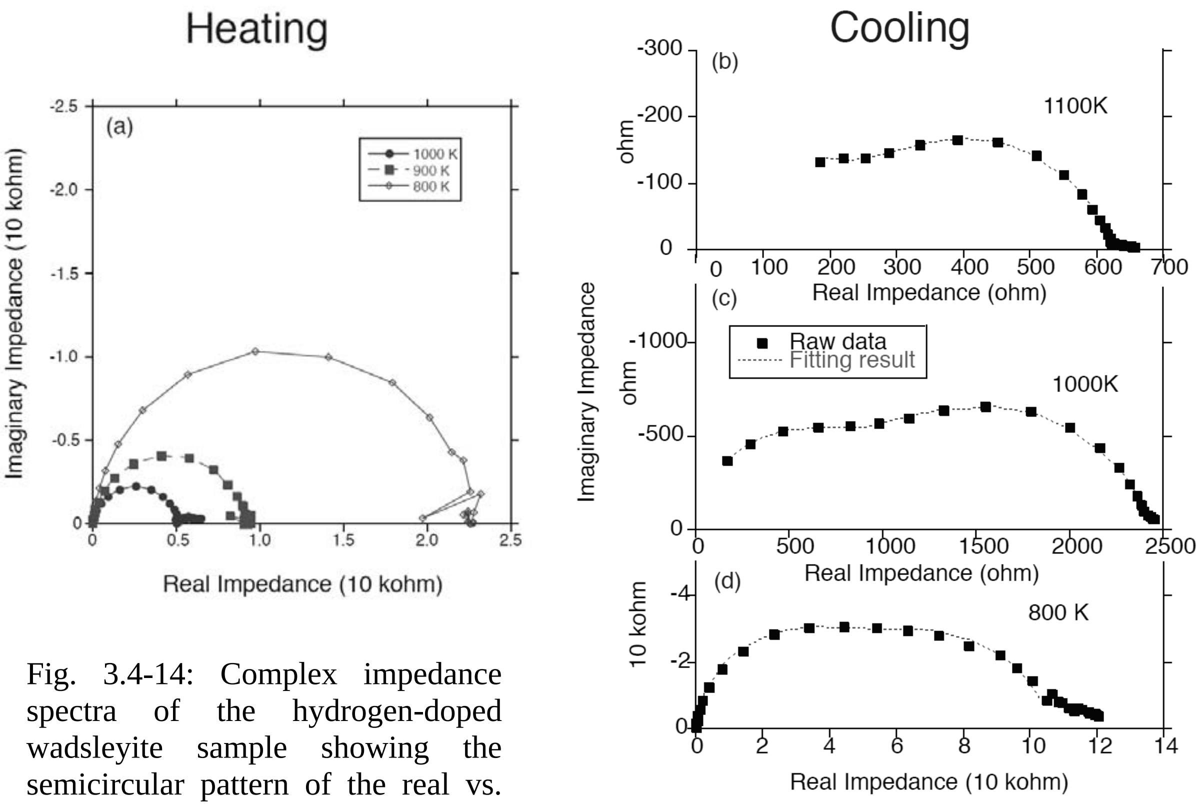

Fig. 3.4-14: Complex impedance spectra of the hydrogen-doped wadsleyite sample showing the semicircular pattern of the real vs. imaginary component at frequencies ranging from 1 MHz to 0.1 Hz. (a) Impedance spectra as a function of temperature obtained during a first heating path. (b), (c) and (d) Impedance spectra obtained during cooling at 1100, 1000 and 800 K, respectively.

l. *Magnetic transition in Fe_7C_3 observed with Synchrotron Mössbauer spectroscopy (C. Prescher, M. Mookherjee, K. Glazyrin, Y. Nakajima, V. Potapkin, C. McCammon and L. Dubrovinsky)*

Metal carbides are important compounds in material science and solid state physics due to their anomalous properties and for the understanding of the electronic states in interstitial metal compounds in general. The behaviour of Fe_7C_3 under high pressure is also especially interesting for planetary sciences; an increasing amount of studies suggests Fe_7C_3 to be the liquidus phase of an Fe-C mixture at conditions of the Earth's core and Carbon is widely believed to be one of the main constituents causing the density deficit in the Earth's core relative to pure iron.

We conducted Synchrotron Mössbauer measurements of Fe_7C_3 up to 72 GPa (Fig. 3.4-15) at the nuclear resonant beamline ID18 at ESRF. The sample was pre-synthesized in a multianvil apparatus and loaded into a diamond anvil cell with Ne as pressure transmitting medium and ruby as pressure marker. The spectra were fitted with the full transmission integral with a squared Lorentzian source line by MossA.

Fe_7C_3 has 3 different crystallographic iron sites with a 3-3-1 occupancy. This leads to 3 sextets with different hyperfine parameters but with area ratios between the different sites being constraint by crystallography. With this constraint it was possible to reasonably fit the very complex spectrum at low pressures (Fig. 3.4-15). The magnetic hyperfine splitting decreases with increasing pressures and vanishes at 16.5 GPa. At this pressure the spectrum collapses to just one slightly asymmetric broad doublet (Fig. 3.4-15). The local environment of the iron atoms seems to be very similar above this pressure and the resolution of the measurement is not good enough to separately fit a doublet for each iron site. No change in the behaviour can be seen up to 72 GPa.

The pressure of the magnetic transition (16.5 GPa) is larger than in Fe_3C (10 GPa) but still not as high as predicted by numerical calculations. A contribution from the second order Doppler shift to the central shift can be seen like in Fe_3C above the transition pressure. The central shift of the doublet first increases and then decreases linearly to lower values.

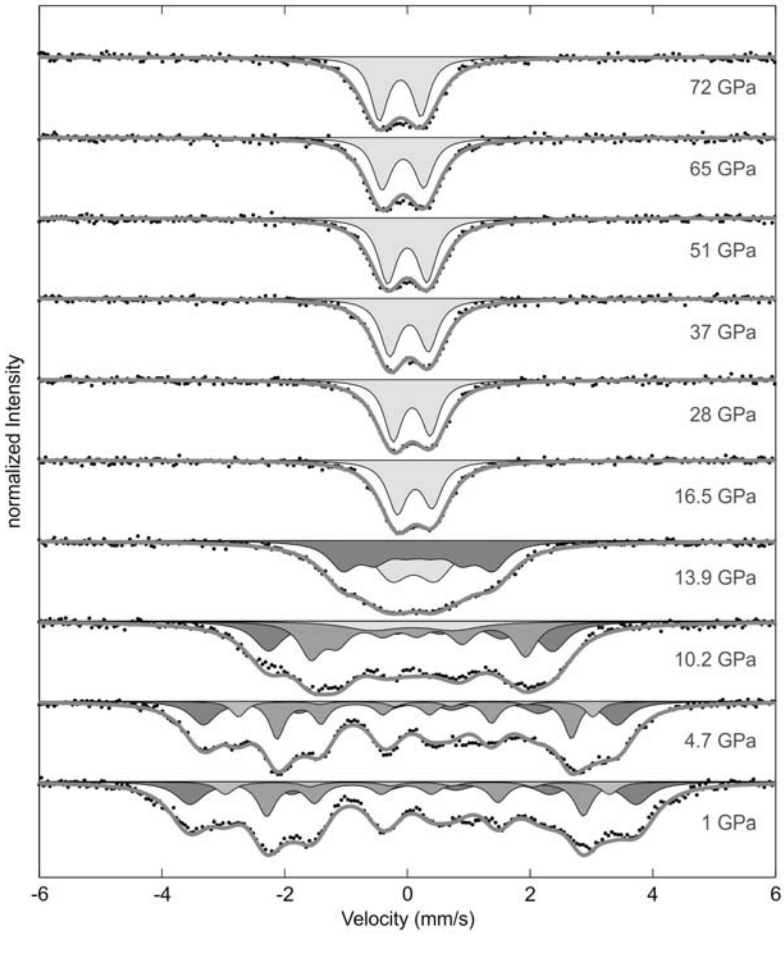

Fig. 3.4-15: Synchrotron Mössbauer spectra of Fe_7C_3 compressed up to 72 GPa showing the loss of ferromagnetism.

m. *Stability and breakdown of* $Ca^{13}CO_3$ *associated with formation of* ^{13}C*-diamond in static high-pressure experiments up to 43 GPa and 3900 K (A.V. Spivak and Yu.A. Litvin/Chernogolovka; S.V. Ovsyannikov, N.A. Dubrovinskaia and L.S. Dubrovinsky)*

Calcium carbonate ($CaCO_3$) is one of the most common materials of rocks and skeletons of living organisms. Being collected in sediments, calcium carbonate is involved in rock-forming processes including those ones, which due to subduction happen in the deep Earth's interior at elevated pressures and temperatures. However, information about high-pressure high-temperature phase states of $CaCO_3$ and its stability at non-ambient conditions is still limited. The main task of the work was to investigate experimentally the conditions of chemical stability and the *PT*-field of congruent melting of $CaCO_3$ at 10-43 GPa (probably, one of the main carbonatic component in diamond forming media at conditions of the transition zone and lower mantle).

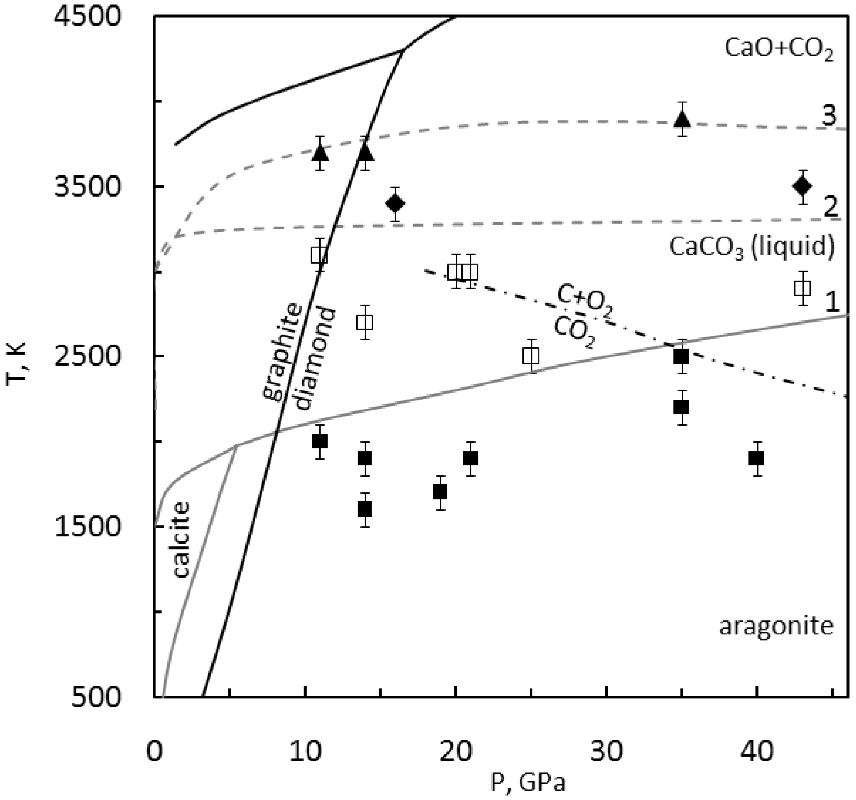

Fig. 3.4-16: The *PT* phase diagram of $CaCO_3$. Experimental points (DAC): filled squares indicate experiments where there is no melting of $CaCO_3$; empty squares and filled diamonds indicate experiments with melting of $CaCO_3$ and diamond or graphite formation respectively. All other phase diagram features are taken from the literature and are the following: gray curves are boundaries of $CaCO_3$ phases: calcite, aragonite and liquid of $CaCO_3$. Black curves are diamond-graphite equilibrium boundaries. Line 1 represents the decomposition boundary of CO_2 to C and O_2; whereas line 2 and 3 represent the decomposition boundary of $CaCO_3$ to CaO and CO_2. Line 4 is the decomposition boundary of $CaCO_3$ to CaO and CO_2 according to the present study.

$Ca^{13}CO_3$ was used as starting material for the experiments. The ^{13}C isotope was used for the purpose of identifying possible carbon phases. Experiments were carried out in diamond anvil cells with laser heating (DAC-LH) at in the pressure range 11-43 GPa and at temperatures of 1600-3900 K. Raman spectra of temperature-quenched samples were collected using a Dilor XY system (514 nm excitation laser).

In the present work we show that isotopically pure ^{13}C-diamond crystallises from the $Ca^{13}CO_3$ melt oversaturated with dissolved ^{13}C-carbon at pressures of 8.5 GPa and 20 GPa. Our static compression experiments in laser-heated DACs suggested that calcium carbonate melts congruently and the *PT* field of the chemically stable melt is quite wide (Fig. 3.4-16), extending from 2100 to 3400 K at 11 GPa and from 2500 to 3400 K at 43 GPa. The existence of a high-temperature decomposition boundary for the phase field of the $CaCO_3$ melt was confirmed. The decomposition boundary was marked by formation of diamond (above ca. 16 GPa) and graphite (below 16 GPa) and may be explained by a two-stage decomposition reaction: $CaCO_3 = CaO + CO_2$; $CO_2 = C + O_2$.

3.5 Fluids, Melts and their Interaction with Minerals

The chemical evolution of our planet is largely the result of processes involving silicate melts and fluids. Fluids in the crust and the upper mantle are often water-rich. In a reducing environment, hydrous fluids contain appreciable amounts of hydrogen (H_2), which is generally believed to be completely miscible with water in the upper mantle. New experimental results presented in the first contribution in this section show that this is not so. Water and hydrogen may occur as two immiscible phases in Earth's upper mantle. This observation has major implications for the redox evolution of our planet; it may explain the rapid oxidation of Earth's mantle shortly after core formation and the stabilization of a reduced Hadean atmosphere.

Water released from subducted slabs triggers melting in subduction zones, while melting under mid-ocean ridges is primarily a consequence of adiabatic decompression. However, even this process is significantly modified by the presence of traces of water. A quantitative understanding of the effect of small amounts of water on the formation of low-degree partial melts is still in its infancy. Two contributions address this problem. Measurements of mineral/melt partition coefficients of water in a peridotite system using an iterative sandwich technique suggest that these partition coefficients are only slightly pressure dependent in the upper mantle. In a complementary study it was found that the amount of water required to produce a given melting point depression in the $MgSiO_3$-H_2O and Mg_2SiO_4-H_2O system is smaller than expected. In another contribution, the conditions of diamond crystallization from silicate-carbonate melts in the transition zone were simulated in the laboratory.

In volcanic systems, chlorine and sulfur are important factors both in the enrichment of metals to hydrothermal ore deposits and in the impact of volcanic eruptions on climate. A Raman spectroscopic study in this chapter shows that a significant fraction of sulfur in high-temperature aqueous fluid may not be present as SO_2 or H_2S, but as H_2SO_4, *i.e.*, as hexavalent sulfur that may be directly injected into the stratosphere during explosive eruptions. Adsorption of sulfur and chlorine on volcanic ashes in an eruption cloud is believed to be important for reducing the climatic impact of eruptions. Some preliminary data on HCl adsorption on rhyolitic ashes are presented here. Importantly, the adsorption of HCl on ashes appears to be nearly irreversible and is therefore likely an important process in limiting the effect of volcanoes on the ozone layer.

A very interesting contribution in this chapter addresses the formation of porphyry copper deposits. Here, it was widely believed that copper is strongly fractionated into a vapor phase coexisting with a saline brine, due to the formation of hydrosulfide complexes in the vapor. The corresponding enrichment of copper in vapor inclusions from natural ore deposits is now shown to be an artifact of post-entrapment modification, implying that available models of the formation of porphyry copper deposits need to be revised.

a. *Immiscibility between water and hydrogen in Earth's upper mantle (E. Bali, A. Audétat and H. Keppler)*

The oxygen fugacity in Earth's upper mantle is quite variable, but generally decreases with depth. Close to the Fe-FeO buffer, hydrous fluids contain roughly 50 mol.% of molecular hydrogen (H_2). Previous experiments in the H_2-H_2O system located the critical curve at low pressures (0.2 GPa) close to 400 °C, with little pressure dependence. Accordingly, it is generally believed that water and hydrogen form homogeneous mixtures throughout the mantle. In a series of experiments, we were able to show that this assumption is in error and that water and hydrogen actually form two coexisting, immiscible phases in reducing parts of the upper mantle.

Experiments were carried out in the piston cylinder apparatus at Fe-FeO buffer conditions. Pre-cracked olivine or quartz crystals were loaded together with pure water into platinum capsules. An outer Fe capsule containing water and FeO was used to buffer the system. After quenching of the runs, synthetic fluid inclusions that had formed during the experiment were studied by Raman spectroscopy.

Figure 3.5-1 shows fluid inclusions trapped in olivine at 26 kbar, 1000 °C and Fe-FeO buffer conditions. Two different types of inclusions are clearly visible, indicating the coexistence of two immiscible phases at run conditions: (1) Inclusions with a dark rim indicating a large difference in refractive index to the host olivine; Raman spectroscopy shows that these inclusions are filled with nearly pure, high-density H_2; and (2) liquid-filled inclusions with a much weaker optical contrast to the host olivine. According to Raman spectra, these inclusions contain nearly pure water with minor amounts of dissolved H_2. Only rarely, mixed inclusions can be observed that formed by accidental trapping of both coexisting phases. These inclusions contain an H_2-rich gas-bubble in liquid water. Similar immiscibility was also observed at 26 kbar and 1100 °C, while at 1150 °C, only one phase of intermediate composition was detected, indicating closure of the miscibility gap. We therefore suggest that with increasing pressure, the critical curve in the H_2O-H_2 system raises steeply, such that in reducing parts of the upper mantle, water and hydrogen will coexist as separate fluid phases.

Our observations have a number of important consequences for the redox evolution of Earth's mantle. If immiscibility between H_2 and H_2O occurs, the H_2-rich phase will be very buoyant and will likely separate quickly from the hydrous phase. Upon further ascent in the mantle, interaction with nominally anhydrous minerals may strip this phase from the residual traces of water, and thereby produce an extremely reducing fluid. This could be the cause for the formation of phases such as moissanite SiC that are sometimes found as inclusions in kimberlite minerals. The origin of these phases was considered to be enigmatic, as they require oxygen fugacities some five log units below the Fe-FeO buffer to be stable. Immiscibility between water and hydrogen and rapid ascent of the immiscible H_2 to the surface may also be a mechanism that allows a rapid oxidation of Earth's upper mantle shortly after core formation. The corresponding outgassing of nearly pure hydrogen may have helped to stabilize a reducing early atmosphere.

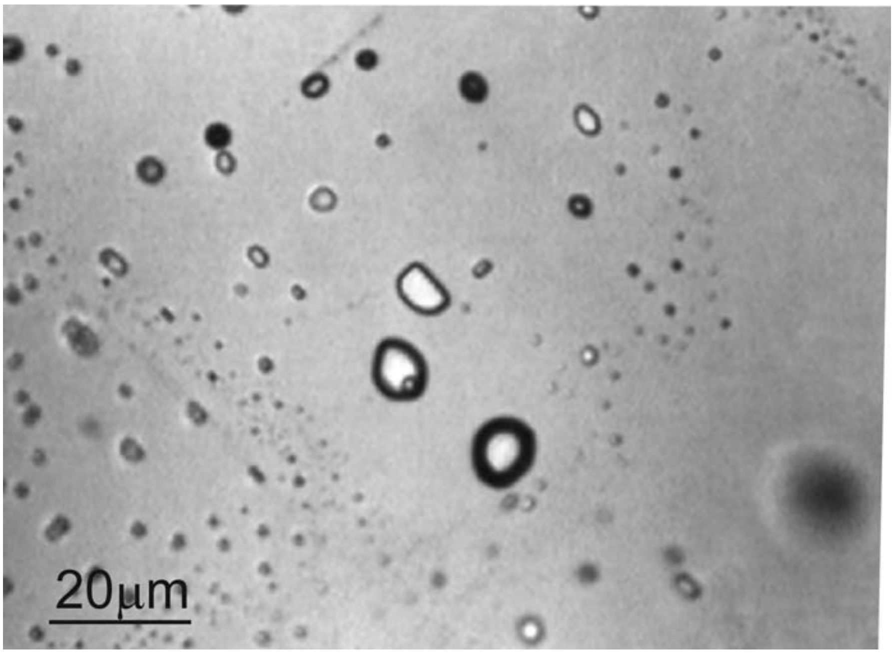

Fig. 3.5-1: Synthetic fluid inclusions in olivine, trapped in the system H_2O-H_2 at 1000 °C, 26 kbar and Fe-FeO buffer conditions. Note the coexistence of H_2-rich fluid inclusions (with a dark rim) with water-rich inclusions (light rims).

b. *Water partitioning between low-degree peridotite melts and mineral phases in the upper mantle (D. Novella and D.J. Frost)*

During adiabatic decompression, the presence of H_2O in the mantle can cause low-degree partial melting to occur at much greater depths than under dry conditions. The formation of such melts in the deep upper mantle has important implications for geochemical and geophysical properties of the lithosphere and asthenosphere. The partitioning of H_2O between peridotitic mineral phases and melt is a key parameter in determining the depth at which melting commences and the resulting melt fraction as a function of depth and bulk H_2O content. Hydrous melts produced at depths > 100 km will most likely be in proportions small enough that the major element compositions of coexisting mantle minerals will be unaffected by melting. Melt and mineral compositions likely play a role in H_2O partitioning. In experiments to determine H_2O partitioning it is, therefore, important that near solidus phase compositions are employed, which for the mineral phase assemblage implies compositions close to those expected under anhydrous conditions, while the melt phase must be in equilibrium with this assemblage.

In the present study we have conducted sandwich experiments at 6 GPa and the corresponding adiabatic temperature, 1400 °C, employing a synthetic composition based on a natural peridotite. Following this approach, the chemical composition, including H_2O content, of a low-degree, hydrous partial melt formed by melting an upper mantle peridotite at approximately 180 km has been determined. In our experiments, the mantle peridotite mixture was equilibrated at high pressure and temperature with a large proportion (60-90 %) of an 'initial guess' hydrous melt composition. After the experiment, a new melt was formed by reaction with the peridotite that was closer in composition to being in equilibrium with the peridotite. This product melt composition was then fabricated and re-equilibrated with the peridotite in similar proportions to the first experiment. After this process was repeated numerous times a melt composition was found that was in equilibrium with olivine, clinopyroxene and garnet, *i.e.*, the same solid assemblage as found under anhydrous conditions at the same conditions. The mineral phases also converged to be of similar chemical composition to those found at subsolidus conditions.

The low-degree melt produced in equilibrium with this peridotite phase assemblage contained 11 wt.% H_2O. The H_2O content of the melt was determined through a mass balance calculation. It was found that the best approach is to mix only small proportions of peridotite with the melt. Although this slows convergence of the melt composition, it ensures a large melt pool that makes mass balance calculations more accurate and aids the formation of large crystals. The mass balance also assumes minimal loss of H_2O from the capsule. Double capsules were employed with an outer capsule containing the same melt composition as the inner capsule, in order to minimize H_2O loss. Significant H_2O loss can be discounted as a series of experiments mixing different proportions of peridotite and hydrous melt demonstrated dramatic differences in phase relations and the proportion of crystallization when bulk H_2O contents were lowered by even small amounts.

The H_2O contents of all coexisting mineral phases were measured by means of Fourier-transform infrared spectroscopy (FT-IR). Unpolarized FT-IR measurements were performed on doubly polished sections when sufficiently large (50 to 150 µm) and clear crystals were synthesized in the high-pressure experiments (Fig. 3.5-2). Water contents of olivine, clinopyroxene and garnet produced in our experiments were found to be respectively 150 ppm H_2O, 570 ppm H_2O, and 117 ppm H_2O by weight. From the mineral and coexisting melt H_2O contents, the H_2O mineral- melt partition coefficients ($D^{H2O}_{min/melt}$= H_2Omineral/H_2Omelt) can be determined as 0.0015, 0.0052, and 0.0011 for olivine, clinopyroxene, and garnet, respectively.

When compared to literature data at lower pressures, the data indicate that $D^{H2O}_{min/melt}$ does not increase significantly with increasing pressure up to 6 GPa. While the values for olivine stay almost constant over this pressure range, the values of $D^{H2O}_{cpx/melt}$ and $D^{H2O}_{gt/melt}$ slightly decrease with pressure between 2 and 6 GPa. Moreover, using the derived H_2O partition coefficients of each phase and knowing the proportion of each phase in the peridotitic rock, the partitioning of water between peridotite and melt at 6 GPa is 0.00264. Using these results, the proportion of hydrous melt that can be produced in adiabatically upwelling mantle at 6 GPa can be calculated as a function of bulk mantle H_2O content. Our results indicate, for example, that to produce a melt fraction of 0.1 wt.% at 180 km would require a bulk mantle H_2O content of 390 ppm. This value is larger than that typically proposed for basalt source rocks.

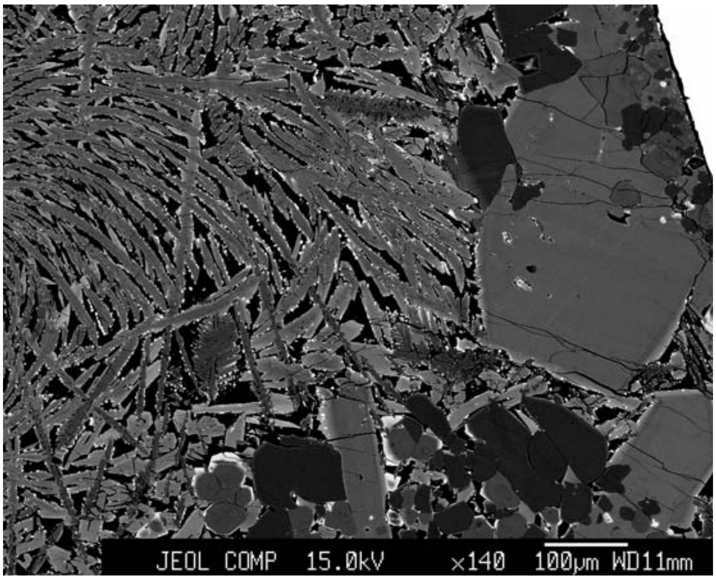

Fig. 3.5-2: Backscattered electron image of an experimental run performed at 6 GPa and 1400 °C. In this experiment, crystals of olivine (dark), garnet (grey) and clinopyroxene (light grey) are found coexisting with a large pool of quenched melt, which segregates from the crystalline matrix and can be recognized by its dendritic texture.

c. *Melting phase relations in the* Mg_2SiO_4*-*H_2O *and* $MgSiO_3$*-*H_2O *systems at upper mantle conditions (D. Novella and D.J. Frost)*

Olivine constitutes more than 50 % by volume of the upper mantle, and orthopyroxene up to 15 %. In order to understand melting processes that take place in the Earth's interior, the melting behaviour and phase equilibria of major mantle minerals need to be determined at high pressure and high temperature. Volatiles such as H_2O, which are recycled into the deep Earth at subduction zones, have a drastic effect on melting temperatures and melt productivity. There is abundant evidence, for example, for the passage of deep hydrous melts in lithospheric samples. The effect of H_2O on the melting of mantle rocks in complex chemical systems is hard to quantify at high pressures, however, due to factors such as the necessity to control oxygen fugacity, attainment of equilibrium and H_2O-loss from experimental capsules. As a result, experiments on simplified chemical systems, *e.g.*, MgO-SiO_2-H_2O, can provide crucial quantitative information on the effect of H_2O on melting processes, which can be modeled and extrapolated with relatively simple thermodynamic treatments.

In this study, multianvil experiments have been performed to investigate the melting relations in the systems Mg_2SiO_4-H_2O and $MgSiO_3$-H_2O at upper mantle conditions. Here results are presented from experiments performed at 6 GPa (~ 180 km depth in the mantle) and temperatures between 1300 to 1600 °C. Starting compositions of forsterite and enstatite containing different amounts of H_2O were prepared by mixing different proportions of

Mg_2SiO_4, $MgSiO_3$, SiO_2 and brucite. Capsules were fabricated from a 2 mm diameter platinum rod, cut into sections and spark-eroded with holes approximately 0.6 mm deep and 0.25 mm in diameter. Each of the produced capsules contained 4 chambers where different starting mixtures containing different H_2O contents were loaded in each experiment (see Fig. 3.5-3).

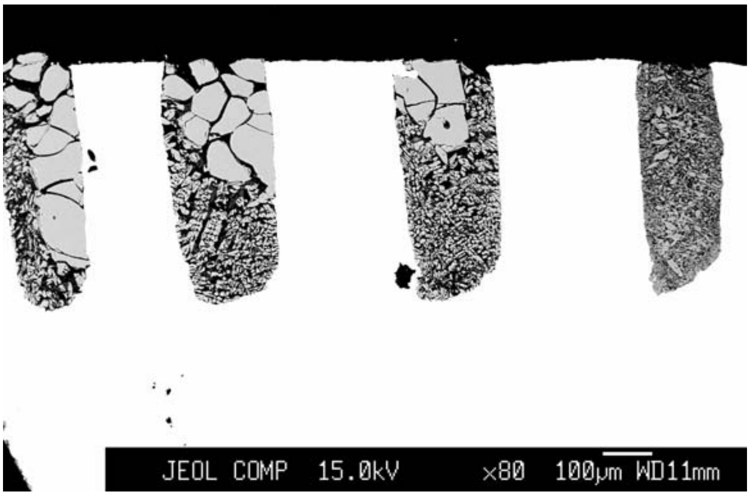

Fig. 3.5-3: Backscattered electron (BSE) image of an experiment performed at 6 GPa and 1400 °C in the Mg_2SiO_4-H_2O system. The bright material is the Pt capsule. In order from left to right are sample chambers where starting mixtures of Mg_2SiO_4 plus 6.7, 8.3, 12.5, and 17.5 wt.% H_2O were employed. Grey crystals (50 to 100 µm across) of forsterite can be easily distinguished from the fine grain quenched melt.

The capsules were closed by placing a second disk of platinum on top of the chambers, which was held closed under pressure. Two experiments performed at the same conditions but with different durations of 5 and 30 minutes were performed to assess whether H_2O may be lost during the experiment. The two experiments showed identical phase assemblages for all the samples in the platinum capsule. This suggests that significant water loss does not occur using the experimental setup on timescales that are reasonable to achieve equilibrium. After quenching, the chemical composition of the produced crystalline phase forsterite and enstatite was confirmed by microprobe analyses. Equilibrium crystals in the charges were easily distinguished from the melt quenched crystals, due to the fibrous textures (Fig. 3.5-3). Melting relations in the system Mg_2SiO_4-H_2O and $MgSiO_3$-H_2O determined in this study are plotted and interpreted on a diagram temperature vs. H_2O-content (Fig. 3.5-4).

At 6 GPa, forsterite and enstatite were found to melt congruently under hydrous conditions over the range of temperatures investigated. However, compared to previous studies performed at a similar pressure, melt H_2O contents were found to be significantly lower. Further experiments are being performed at 12 GPa in the same systems and a simple thermodynamic model is being developed using these data to describe the effects of H_2O on melting in the MgO-SiO_2-H_2O system at high pressures and temperatures.

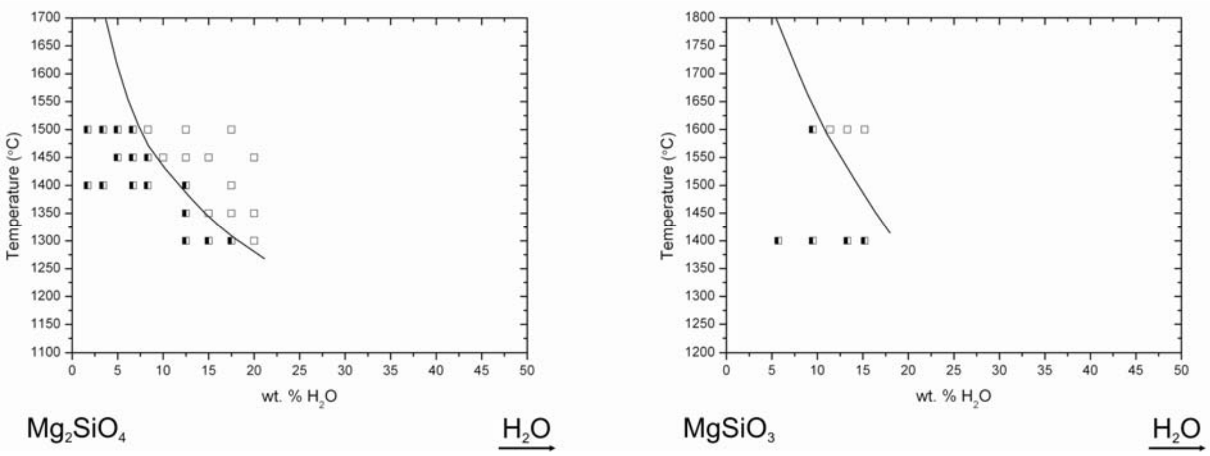

Fig. 3.5-4: Melting phase relations on the joins Mg_2SiO_4-H_2O (left) and $MgSiO_3$-H_2O (right) at 6 GPa. Half-filled squares indicate experiments where the crystalline phase was found in equilibrium with melt; empty squares indicate experimental runs that produced only melt. The black lines are the liquidus curves constrained by the experiments performed in this study. Estimated temperature uncertainty in the experiments is 50 °C.

d. *Crystallization of diamond and majoritic garnet from carbonate-silicate melts (A.V. Bobrov/Moscow; A.V. Spivak and Yu.A. Litvin/Chernogolovka; L.S. Dubrovinsky)*

Most natural diamonds probably crystallized from carbonate-silicate melts in the upper mantle, as is evident from numerous studies of mineral and melt inclusions. Experiments demonstrate that diamond and the minerals occurring in its inclusions (olivine, garnet, and pyroxene) can form in such melts. The formation of diamond under the conditions of the transition zone is not well studied. Particularly important are experiments on diamond crystallzation in carbonate-silicate systems containing majoritic garnet, since its composition may be used for thermobarometry. The aim of this project was to investigate phase relations in the system Na-Fe-Ca-carbonate – majorite ($MgSiO_3$, $Na_2MgSi_5O_{12}$) – C at 20 GPa and 1600-1800 °C.

Gels of $MgSiO_3$ and $Na_2MgSi_5O_{12}$ compositions, crystalline carbonates (Na_2CO_3, $CaCO_3$, and $FeCO_3$), and ultrapure graphite mixed in weight proportion of 24:36:40 were used as starting materials for multianvil experiments. Diamond was synthesized in all runs, which was confirmed by SEM and Raman spectroscopy. At 1800 °C, the experimental run products consisted of quenched carbonate silicate melt containing small (2-5 µm) diamond crystals or their aggregates. At 1700 °C diamond crystals were accompanied by Na-bearing Ca-majorite (SiO_2 54.88, FeO 8.91, MgO 15.78, CaO 19.76, Na_2O 0.51 wt.%) in Na-rich quenched carbonate melt. Majoritic garnets with stishovite were obtained together with diamond crystals at 1600 °C (Fig. 3.5-5); most diamonds were found in the quenched carbonate melt, but sometimes they occurred as inclusions in majorite.

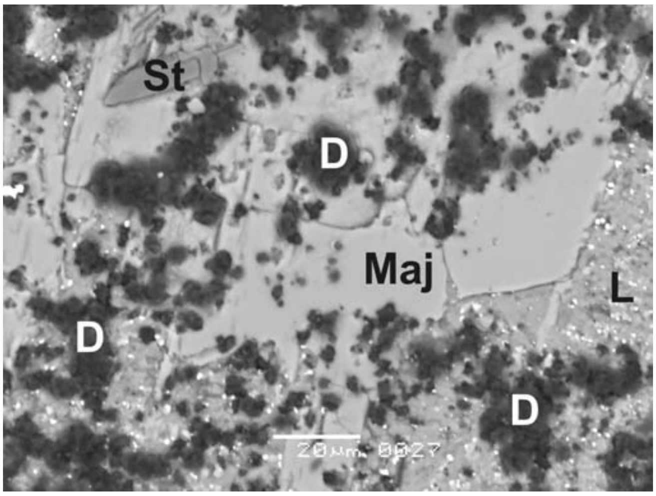

Fig. 3.5-5: Backscatter electron image of a phase assemblage with diamond (D), majoritic garnet (Maj), stishovite (St), and carbonate melt (L) obtained in a multianvil run at 20 GPa and 1600 °C.

Our experiments suggest that diamonds may easily crystallize from carbonate-silicate melts in the transition zone. In further experiments, we will try to vary the experimental conditions such that the compositions of majorite and other transition zone minerals found in deep diamond inclusions can be reproduced in the laboratory to better constrain the conditions of diamond formation.

e. *Sulfur speciation in oxidized magmatic-hydrothermal fluids (H. Ni and H. Keppler)*

Sulfur compounds released by explosive volcanic eruptions can result in large-scale cooling of the atmosphere. Although it is H_2SO_4 aerosol in the stratosphere that absorbs and backscatters solar radiation to cause the cooling effect, this aerosol is generally believed to be the oxidation product of primary SO_2 (and perhaps H_2S) in volcanic gases. However, there has been recent field evidence suggesting that sulfate is directly emitted from the vents of some volcanoes. In this project, we investigated using *in situ* Raman spectroscopy, whether hexavalent sulfur may be stable in hydrous fluids under the conditions prevailing in magma chambers below volcanoes (up to 700 °C and 10 kb).

Dilute sulfuric acid (5 N H_2SO_4) was loaded into a Bassett-type hydrothermal diamond anvil cell with two type IIa diamonds, using a gasket of gold-lined rhenium, gold-lined iridium or plain iridium. In some runs we coated a ~ 40 nm thick gold layer onto both surfaces of a gold-lined Re gasket. Different fluid densities were examined, with one extreme being no air bubble loaded and the other being homogenization into the vapor phase upon heating. To avoid complicating the system, we chose not to load a pressure sensor but to infer pressure from estimated fluid density. After temperature became stable and optical focus was tuned, Raman spectra were collected for 2×18 s every 50 or 100 °C during both heating and cooling. The acquisition setup of our Horiba Jobin-Yvon LabRam HR800 spectrometer involved a 514.5 nm Argon laser of 300 mW output power, a confocal hole of 500 µm diameter, an objective of 50× magnification (N.A. = 0.35), and a spectral range of 200-4000 cm^{-1} with a 1800 gr/mm^{-1} grating, yielding 3.5 cm^{-1} resolution.

Starting from room temperature, SO_4^{2-} disappeared after heating to 100 °C, and SO_2 formed at > 250 °C, probably by reaction with the rhenium or iridium of the gasket, which apparently were not completely shielded by the gold liner. With high fluid densities (such as > 0.9 g/cc), the air bubble was homogenized into the liquid phase upon heating, and more and more H_2SO_4 and SO_2 sulfur formed at the expense of HSO_4^- (Fig. 3.5-6). For low fluid densities (such as < 0.2 g/cc), the system homogenized into the vapor phase upon heating, and molecular H_2SO_4 appeared to dominate in the fluid. In neither case we detected any molecular SO_3.

The above observations confirm that hexavalent sulfur indeed coexists with SO_2 under relatively oxidizing conditions (close to the Re-ReO_2 buffer). Hexavalent sulfur is stabilized by hydration in the form of H_2SO_4 and HSO_4^-, and this stabilization effect is much more effective than suggested by available thermodynamic data. It is therefore entirely plausible for hexavalent sulfur to be directly emitted during volcanic eruptions and to directly contribute to regional cooling without the necessity of photochemical oxidation.

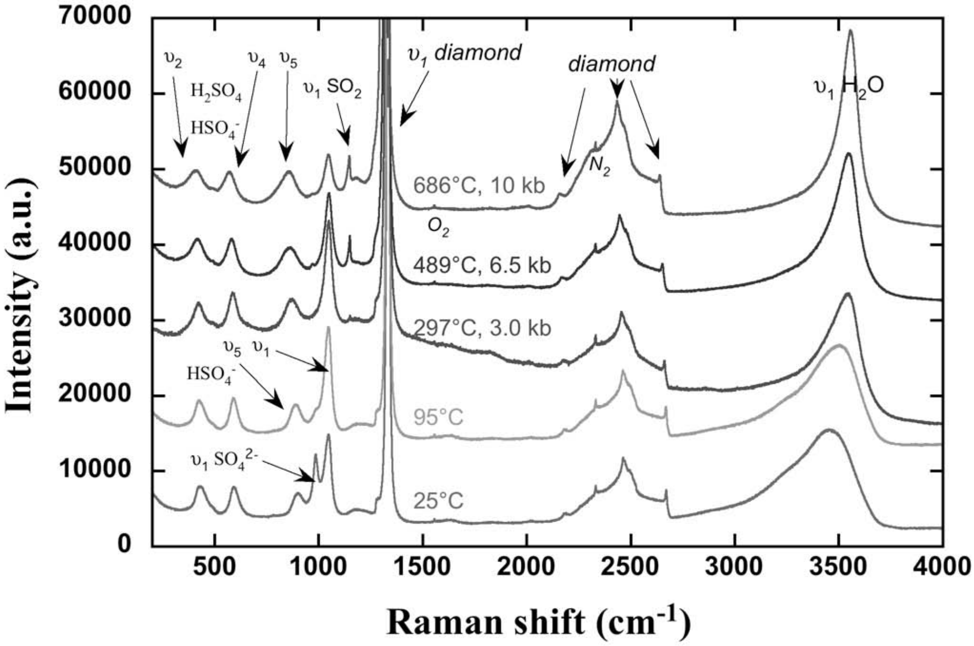

Fig. 3.5-6: Raman spectra of sulfur-bearing aqueous fluid in an experiment with high fluid density (~ 0.93 g/cc). Indicated pressures are estimated from the equation of state for pure H_2O.

f. *The partitioning of copper in two-phase fluids: new insights into the genesis of porphyry copper deposits (L. Lerchbaumer and A. Audétat)*

Porphyry copper deposits are the main economic source of copper. The copper in these deposits is of magmatic origin and was transported by magmatic-hydrothermal fluids from the magma chambers to cooler, shallower sites in the crust. During its ascent, the one-phase fluid started to boil due to decompression and to separate into a vapor-rich, low-density phase and a high-saline liquid phase, the so-called brine. Remnants of these fluids are frequently found as fluid inclusions in minerals such as quartz. Data from natural fluid inclusions in porphyry copper deposits suggest that Cu (plus S, As, B, and Au) commonly is enriched in the vapor phase, whereas most other elements, *e.g.*, Na, K, Fe, Pb, Co, Rb, and Cs, partition into the brine. Therefore, it is widely believed that vapor was the main transporting agent for Cu and thus played an essential role in the formation of these deposits. The inferred enrichment of copper in the vapor may be related to the formation of hydrosulfide complexes. However, numerous experimental studies of various groups failed to find conditions under which copper in the laboratory preferentially partitions into the vapor phase (*i.e.*, the partition coefficient $D_{Cu}^{vap/brine}$ is greater than 1).

In view of recent studies demonstrating that quartz-hosted fluid inclusions can diffusively loose or gain Cu (as well as Na and H) after their formation, we investigated whether this process could also have affected the measured vapor-brine partition coefficients in natural samples, which were exclusively determined on quartz-hosted fluid inclusions. For this purpose, we synthesized quartz-hosted vapor and brine inclusions from a Cu-H_2O-NaCl-S fluid at 800 °C/130 MPa and re-equilibrated them in a second experiment with a similar fluid at 800 °C/70 MPa. After each step some of the inclusions were analyzed by microthermometry, Raman spectroscopy, and LA-ICP-MS.

The results of this study are astonishing: just within 4 days vapor inclusions experienced a dramatic increase in their Cu content (Fig. 3.5-7) from 0.3 ± 0.03 to 8.3 ± 4.9 wt.% while brine inclusions remained unmodified, leading to a change in $D_{Cu}^{vap/brine}$ from a true value (*i.e.*, before re-equilibration) of 0.4 ± 0.05 to an apparent value of 8.3 ± 4.9. Subsequent experiments showed that the requirements for the diffusional gain of Cu in fluid inclusions are a change in pH from ≤ 1 to a more basic value in the surrounding fluid, and the presence of significant amounts of sulfur in the inclusions. The former provides the driving force for the migration of Cu (and Na): H^+ diffuses out of the inclusion due to a concentration gradient between the inner and outer fluid, and the resulting charge disequilibrium is balanced by Cu^+ (and Na^+) diffusing into the inclusion. The sulfur reacts with the copper to sulfides in the vapor inclusions. Figure 3.5-8 illustrates a model for this process and also provides an explanation why Cu concentration changes more dramatically than Na concentration: The diffusion of Na into the inclusion is a direct function of the concentration gradient. This implies that diffusion of Na stops as soon as its concentration inside and outside the inclusion is equal. Copper, on the other hand, can continuously combine with sulfur present in the inclusion and precipitates as sulfide. Hence the only limiting parameter for the diffusion of Cu is the amount of sulfur present in the inclusion, and due to the fact that sulfur usually fractionates into the vapor phase, vapor inclusions end up gaining more Cu than the coexisting brine inclusions. Cooling magmatic-hydrothermal fluids experience a change from acidic to more neutral pH due to buffering along the feldspar-mica join, and natural vapor inclusions typically contain significant amounts of S, so that the conditions for the process described are also found in nature.

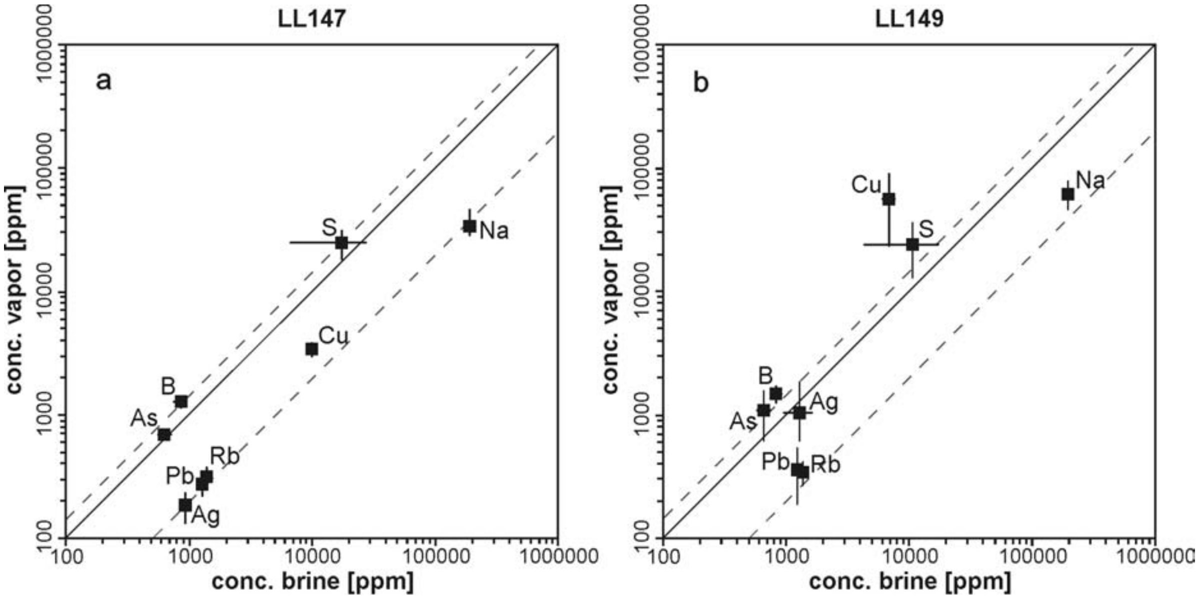

Fig. 3.5-7: Composition of synthetic vapor and brine inclusions before (a; run LL147) and after (b; run LL149) diffusional re-equilibration in a less acidic fluid at 800°C and 70 MPa. Error bars are 1σ standard deviations.

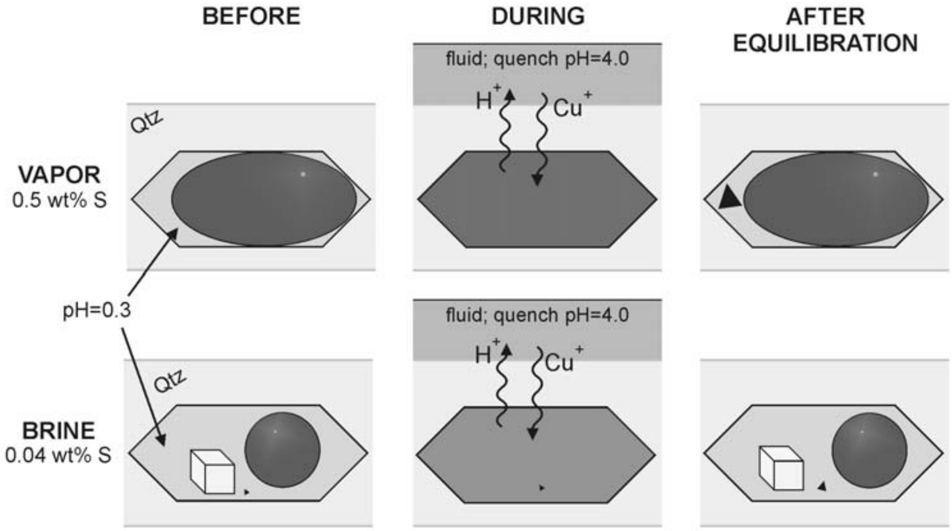

Fig. 3.5-8: Mechanism of Cu diffusion into fluid inclusions. A gradient in fluid acidity causes protons to diffuse out of the fluid inclusions, which in turn causes Cu (plus Na, Ag) to diffuse inward to maintain charge balance. The incoming Cu combines with S to precipitate as sulfides (black triangles).

Definite evidence for our model comes from a re-equilibration experiment performed on a natural quartz sample from the Erongo granite in Namibia. From petrographic and analytical data we were able to reconstruct the chemical composition of the fluid and the temperature and pressure during fluid inclusion formation: the fluid was acidic, sulfur-rich, relatively reduced and was trapped at ~ 600 - 650°C and ~ 80 MPa. The assemblages of coexisting vapor and brine inclusions yield $D_{Cu}^{vap/brine}$ values of 10-66. To check whether cooling and fluid neutralization may have modified the $D_{Cu}^{vap/brine}$ values, we chose one of the trails and re-equilibrated it at its original formation conditions (650°C, 80 MPa, same fluid composition) for 22 days. The idea was to reverse the diffusion process *i.e.*, the gain of Cu in the vapor inclusions. The result was a change in $D_{Cu}^{vap/brine}$ from 11 ± 9.3 to 0.06 ± 0.04 and a change in $D_{Na}^{vap/brine}$ from 0.09 ± 0.01 to 0.06 ± 0.02, *i.e.*, the converse of what we observed in our re-equilibration experiments on synthetic fluid inclusions. The concentrations of all other elements remained unmodified.

We therefore conclude that $D_{Cu}^{vap/brine}$ values > 1 observed on natural boiling assemblages likely are a secondary feature, with original values being 0.11 ± 0.04 to 0.15 ± 0.04. The latter values are based on experiments reproducing the conditions of porphyry copper systems (with a mineral assemblage consisting of chalcopyrite, bornite, magnetite, biotite, orthoclase, albite, muscovite, quartz ± anhydrite that buffers pH, fO_2, fS_2, and the activity of Cu) and with SO_2 as the dominant sulfur species. Consequently, the brines likely carried more Cu to the site of deposition than the vapor-type fluids, even though the mass of brine was lower than that of vapor by a factor of four to nine.

g. *Adsorption of HCl gas onto volcanic ash with rhyolitic composition (F. Schiavi, J. Huber, G. Gollner and H. Keppler)*

Large explosive volcanic eruptions produce high ash- and gas-laden atmospheric columns that penetrate through the troposphere and into the stratosphere. The injections of considerable amounts of gases (*e.g.*, SO_2 and HCl) into the stratosphere disturb its chemical equilibrium and affect Earth’s climate. Chlorine free radicals, which form by breakdown of gaseous HCl molecules via heterogeneous chemical reactions and photolysis, contribute to the destruction of the ozone layer. However, before reaching the stratosphere, a significant fraction of gases may be removed from the eruptive column by adsorption onto volcanic ash surface. Thus, experimental investigations of the adsorption process of HCl on ashes at conditions relevant for volcanic plumes become important to estimate the removal of HCl from the atmosphere during eruptive events.

We performed adsorption experiments on a synthetic glass with rhyolitic composition (SiO_2 ~ 77 wt.%, $Alkali_{tot}$ ~ 6.3 wt.%) and on natural obsidian, with alkali-rhyolitic composition (SiO_2 ~ 74 wt.%, $Alkali_{tot}$ ~ 9.5 wt.%), erupted from Vulcano (Aeolian Islands, southern Italy) in 1739 A.D. Both synthetic and natural glasses were ground to sub-micrometer sized particles using a planetary mill under dry conditions. The glass powder was stored in a simple volumetric vacuum device, which was first evacuated and then purged with pure HCl gas to a desired pressure. The pressure drop caused by adsorption was recorded by a vacuum gauge until an equilibrium pressure was reached within hours or days. The pressure was increased in six steps from 32 to 932 mbar and from 87 to 957 mbar in the experiments on synthetic rhyolite and natural obsidian glasses, respectively. The experiments were conducted at room temperature.

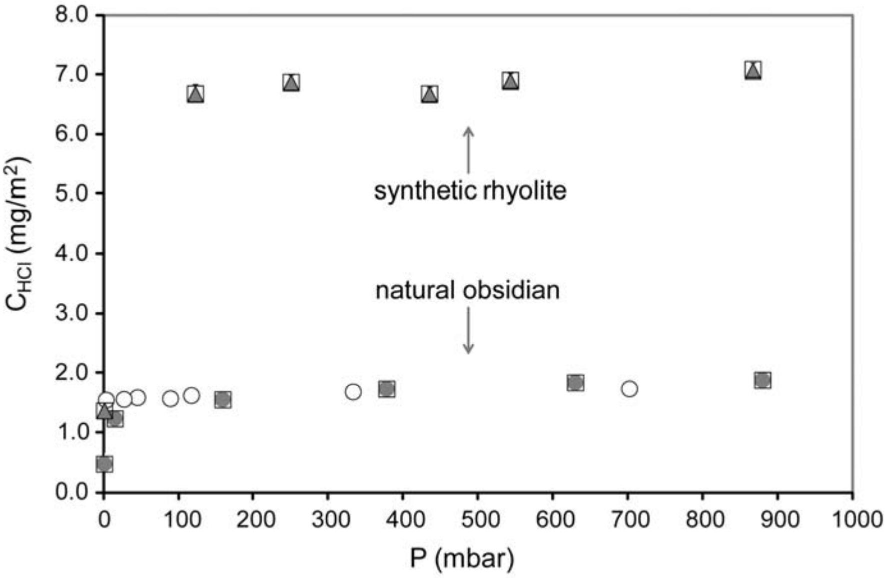

Fig. 3.5-9: Adsorption isotherms of HCl gas on ashes of synthetic rhyolite and natural obsidian. The amount of HCl adsorbed on ash surface during each step was calculated from the recorded pressure drop applying both the ideal gas law (filled symbols) and the van-der-Waals equation (squares). Desorption of HCl from obsidian ashes (white circles) is also shown. Error bars are smaller than symbols.

Preliminary results indicate that adsorption on the order of 6.8 mg/m^2 (synthetic rhyolite) and 1.6 mg/m^2 (natural obsidian) occurs even at low partial pressures of HCl (Fig. 3.5-9). The amount of adsorbed HCl increases rapidly in the first two pressure steps ($P \leq 200$ mbar), whereas at higher pressures, the adsorption isotherm reaches a plateau (synthetic rhyolite) or exhibits a very slight increase (obsidian sample). The shape of the adsorption isotherms resembles that of a Type I isotherm which is characteristic for monolayer adsorption in systems with strong interaction between the adsorbate and the adsorbent (chemisorption). The difference in the HCl amount (mg/m^2) adsorbed on synthetic rhyolite and on Vulcano obsidian may be due to partial crystallization of the natural obsidian. No significant desorption or only very minor desorption (< 10 %) are observed in the experiments on synthetic rhyolite and obsidian powders, respectively. This suggests that the adsorption of HCl on ash particles is largely irreversible and that this process contributes to the removal of volcanic HCl from the atmosphere after explosive volcanic eruptions.

3.6 Rheology and Metamorphism

Ductile deformation and metamorphism are often closely interlinked processes in the deep Earth. They are both governed to a large extent by solid state diffusion of chemical species as well as crystalline defects such as grain and phase boundaries, dislocations and point defects. Additionally, metamorphic reactions and deformation are often interlinked processes that alter and enhance each other. Thus, experimental investigations of rheology and metamorphism often involve the determination of similar microstructural and/or chemical properties at high temperatures and pressures. As such the contributions to this chapter – though dealing with a relatively large variety of materials and (natural or experimental) P,T conditions – are united by the common theme of understanding macroscopic processes like deformation or mineral reactions through their microscopic mechanisms.

The precise determination of the deviatoric stresses acting on a sample in a multianvil press is still technically not feasible due to the gasket-friction; preliminary tests with piezoelectric crystals however are promising and may possibly yield stress measurements with a resolution of a few MPa. Also on the developmental side, the pressure range for controlled deformation experiments with multianvil presses has been expanded significantly by employing a new press with a cubic arrangement of six independently movable anvils (MAVO press). With a composite anvil design deformation experiments at pressures of the mantle transition zone (*e.g.*, on wadsleyite or ringwoodite) are now routinely feasible. Of particular interest are here also transition textures, *i.e.*, the influence of the phase transitions on the rheology. With the D-DIA multianvil press the rheological and microstructural behaviour of upper mantle type mixtures of olivine and orthopyroxene with reactive melt has been studied, indicating that the deformation has a strong influence on the geometry of the melt percolation and that the reaction of the melt may significantly alter the deformation texture of the solid phases.

The determination of intracrystalline slip systems is important for the understanding of the rheological behaviour as well as for the development of physical anisotropy of high-pressure phases. Phase A is a potential carrier of water into the deep mantle in subduction zone environments and its dislocation structure is potentially able to create large physical anisotropy. The rate determining process for plastic deformation or progress of metamorphic reactions is the diffusion of the slowest species. New data presented here indicate that Si diffusion in olivine is much faster than previously thought and as such reconcile a discrepancy existing in the literature between Si diffusion data from direct diffusion experiments and those inferred from deformation experiments. Major element (Ca, Mg, Fe) diffusion in garnets with a high majorite component – as is expected for the high pressures of the deeper mantle – is extremely slow and cannot account for chemical homogenization of the mantle on the time scale of the Earth's history.

In studies of natural samples two aspects of deformation and diffusion were investigated. The mylonitic rocks from the Moresby seamount detachment in the western Pacific near Papua

New Guinea are characterized by a complex interplay between brittle and ductile processes. Diffusional creep assisted by grain boundary sliding of the fine-grained mafic material is intermittently interrupted by the formation of brittle calcite and quartz veins during phases of high fluid pressure, and subsequently the quartz and calcite from these veins are worked into the fine-grained mafic matrix and deformed by diffusional creep. In dunites from the Balmuccia Massif in the Southern Alps reaction with melt derived from nearby gabbros yielded tight intergrowths of stoichiometric kaersutite and diopside with a strong crystallographic orientation relationship. If these intergrowths are primary or formed as exsolutions is currently investigated.

a. *The use of piezoelectric crystals to measure stress in high-pressure deformation devices (S. Shekhar, M.A.G.M. Manthilake and D.J. Frost)*

Rheological measurements and the determination of mineral and rock flow laws rely on the ability to measure stresses in materials undergoing changes in strain. In room or low-pressure devices stress measurements are achieved through the use of a load cell, which resides outside of the sample environment, or high-pressure chamber, but which must be mechanically coupled to the loaded sample. In solid media multianvil high-pressure devices the need for gasketing makes this impossible but a load cell that could be used internally in high-pressure assemblies would be a significant advantage, particularly if it could preserve the accuracy in stress demonstrated by low-pressure devices.

Piezoelectric crystals develop an electrical charge proportional to the applied stress. If the charge response could be calibrated at high pressures they might be developed as internal load cells within multianvil experiments. The charge polarization of a crystal caused by the application stress is related to the applied force through the piezoelectric charge constant, d_{ab}, where a is the direction of the polarization and b is the direction of the applied stress. d_{11} for quartz, for example, is -2.3×10^{-12} C/N but $GaPO_4$, which is isomorphic with quartz, has a value that is twice as high. The charge developed on a piezoelectric crystal can be determined by measuring the discharge voltage; however, as the charge is very small the discharge time is on the order of nS. A method of amplification is required in order to convert the charge on the crystal into a measurable voltage. This can be performed by constructing a charge amplifier or integrator amplifier, which produces an output voltage proportional to the integral of the input voltage with respect to time. An important aspect in the measurement of small charges is the elimination of drift, which is an undesirable change in the output signal over time. Drift originates from leakage of current or charge through the cabling or the crystal itself. If a piezoelectric charge is to be measured from within a high-pressure multanvil assembly, then the cabling within the cell assembly needs to have a very high resistance. As many ceramics can contain H_2O or C extreme caution has to be taken to ensure the resistance across the cables remains extremely high in order to eliminate or minimize drift.

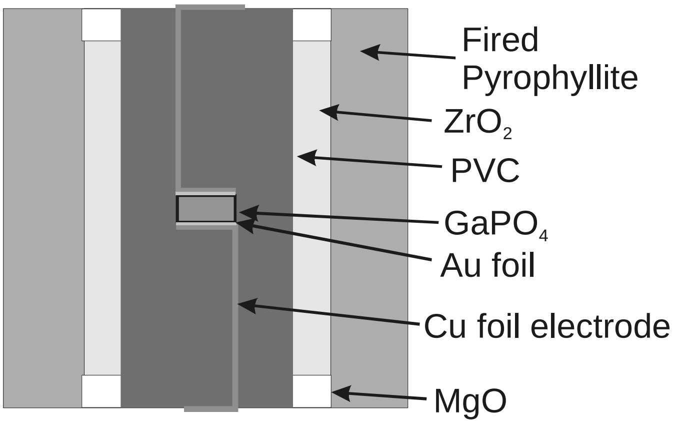

Fig. 3.6-1: Assembly design for piezoelectric measurements at high pressure in the D-DIA and 6-axis multianvil presses. The cube is 8 mm in edge length and is compressed using 6 mm edge length truncations. The $GaPO_4$ crystal is 1.2 mm in diameter and 0.4 mm thick and is coated with Au using vapour deposition.

Figure 3.6-1 shows the cubic assembly developed for measuring piezoelectricity at high pressure in a deformation type multianvil such as the D-DIA or 6-ram MAVO press. The $GaPO_4$ single crystal of 1.2mm diameter and 0.4mm thickness is mounted within a PVC cylinder with a 1.2 mm diameter hole, which is also filled with PVC rods. PVC has an extremely high resistivity and provides a relatively soft pressure medium. Copper foil electrodes connect the crystal faces with the upper surface of the cube. The most successful runs, where drift was minimal, were performed using the 6-axis MAVO press rather than the D-DIA. The success of the MAVO press in these experiments most likely originates from the highly resistive electrical insulation of each individual anvil. Extreme problems with drift occur in the conventional D-DIA press.

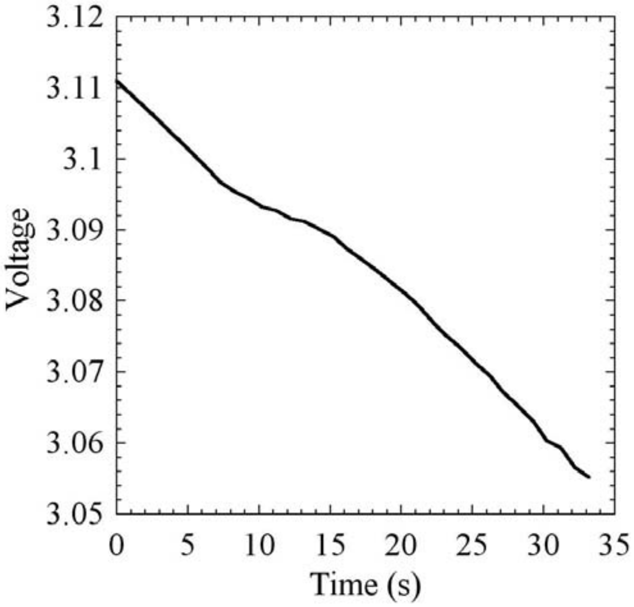

Fig. 3.6-2: Output voltage from the operational amplifier as a function of time for an experiment held statically at 2 GPa and then deformed by driving out the anvils in the horizontal simultaneously after approximately 7 s by 20 microns.

Figure 3.6-2 shows the output voltage as a function of time in seconds for an experiment in the 6-ram press at 2 GPa where the cubic assembly has been deformed by 40 µm approximately 7s after the start of data recording. The vertical anvils are each advanced by 20 µm while the horizontal anvils retract. As deformation of the assembly occurs, a break in slope of the output voltage is observed. As the drift before 7s is linear it can be removed by subtracting a linear background. The charge Q on the crystal is calculated from $Q=V_o.C_r$ where $C_r=10x10^{-9}F$ and V_o is the drift corrected voltage. The force on the crystal can then be calculated using d_{11} and from the surface area of the crystal the stress is determined.

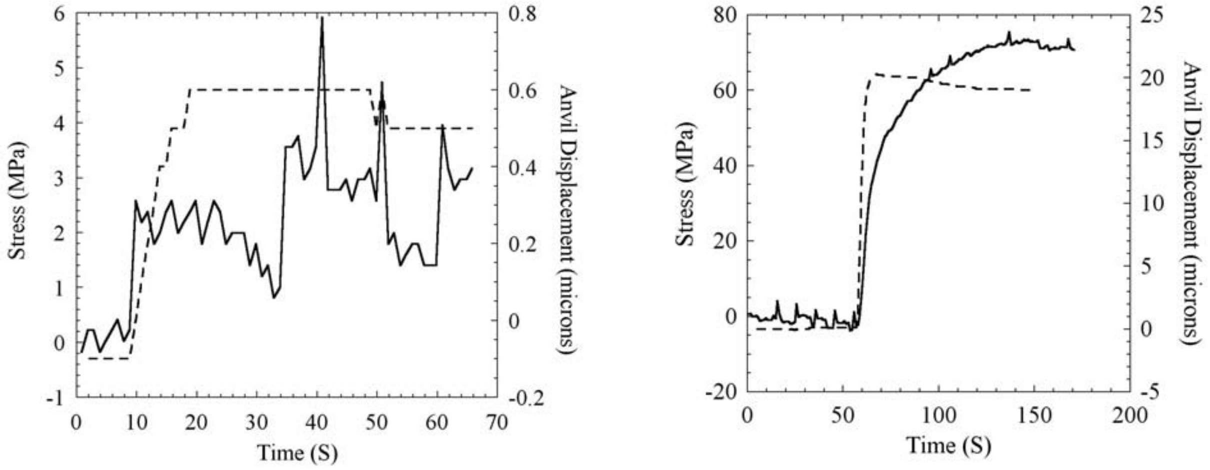

Fig. 3.6-3: Stress (solid line left axis) and anvil displacement (dashed line right axis) versus time for 2 deformation events at high pressure.

Examples of assembly deformation are shown in Fig. 3.6-3 where the stresses determined from the piezoelectric crystal are compared with the corresponding anvil displacement. In the left figure piezoelectric stress developed as a result of deformation by anvil advancement amounting to 0.5 µm. Although the signal is noisy an increase in stress of the order of 2-3 MPa can be observed indicating that the technique is extremely sensitive. In Figure 3.6-3 right the vertical anvils were each compressed by 20 µm and the corresponding stress reached approximately 80 MPa. The timescale for the increase in stress is found, as expected, to be longer than the anvil advancement event as a result of internal relaxation and gasket flow. Further experiments have been performed up to 6 GPa and a high-temperature cell is under development.

b. *Controlled deformation under conditions of the transition zone with the help of composite anvils (N. Walte, M.A.G.M. Manthilake and D.J. Frost)*

Multianvil presses have long been able to generate pressure and temperature conditions of the lower mantle; however, controlled deformation *e.g.*, with the deformation-DIA was largely limited to crustal or upper mantle conditions. Recently developed larger 6-ram presses in Japan and at the BGI have extended the pressure range to conditions of the Earth's transition zone, thereby allowing to investigate deformation of high-pressure phases such as $(Mg,Fe)_2SiO_4$ wadsleyite. One of the problems encountered at the BGI is the concentration of tensile forces at the back of the smaller second stage anvils that are placed between the large first stage anvils (6-6 anvil method), which facilitates cracking of the brittle tungsten carbide. To solve this problem, larger composite anvils were developed, in which a WC core is supported by a jacket of shrunk steel (Fig. 3.6-4).

Fig. 3.6-4: *(left)* Composite anvil with a tungsten carbide core that is supported by a steel jacket. *(right)* Six second stage composite anvils are guided by an aluminium cage and compressed by large first stage anvils.

Room temperature calibration experiments with 3 mm truncations showed that pressures in excess of 15 GPa can easily be achieved repetitively without the occurrence of blowouts and anvil breaks. For further testing of the new anvils heated deformation experiments were performed under conditions of the deep upper mantle and the transition zone. 1.2 x 1.2 mm Rhenium capsules were filled with dried San Carlos olivine and placed in 5 mm edge length cubes of fired pyrophyllite. The assemblies were placed in the press, compressed to ca. 15 GPa and heated to 1000-1400 K with a platinum metal furnace. After 30 min of annealing some samples were deformed by axial compression with a strain rate of 10^{-5} s^{-1} until a bulk shortening of ca. 10 % had been reached. Figure 3.6-5 shows an SEM backscatter image of a partially transformed and deformed sample. Wadsleyite nucleated along grain boundaries of olivine (intergranular) and, to a lesser extent, inside large olivine grains (intragranular). The intragranular wadsleyite is found in the form of oriented spindles or as roundish grains (Fig. 3.6-5). The intergranular wadsleyite is often decorating grain boundaries that are oriented at a high angle to the shortening direction and that may therefore have been subjected to grain-scale shearing (grain boundary sliding). Hence, deformation has apparently aided transformation of olivine to wadsleyite.

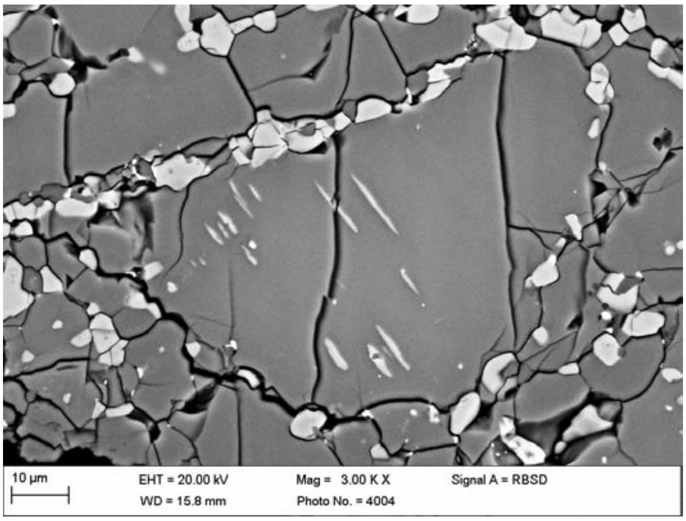

Fig. 3.6-5: SEM backscattered image of a deformed and partially transformed sample. Olivine is dark grey, newly formed wadsleyite light grey.

EBSD measurements of the sample showed that both phases have a weak to moderate crystallographic preferred orientation (CPO) (Fig. 3.6-6). The olivine shows an orientation of the {010} planes perpendicular to the compression axis and a weak girdle of the a-axis. This CPO confirms recent work by S. Shekar at the BGI suggesting that the dominant [100] {010} glide system, which has previously been thought to represent low pressure, low water content dislocation glide in olivine, extends to very high pressure under dry conditions. The pole figure of the wadsleyite shows a weak orientation of the {100} planes perpendicular to the compression axis (Fig. 3.6-6), which may be the result of an interplay between deformation and phase transformation.

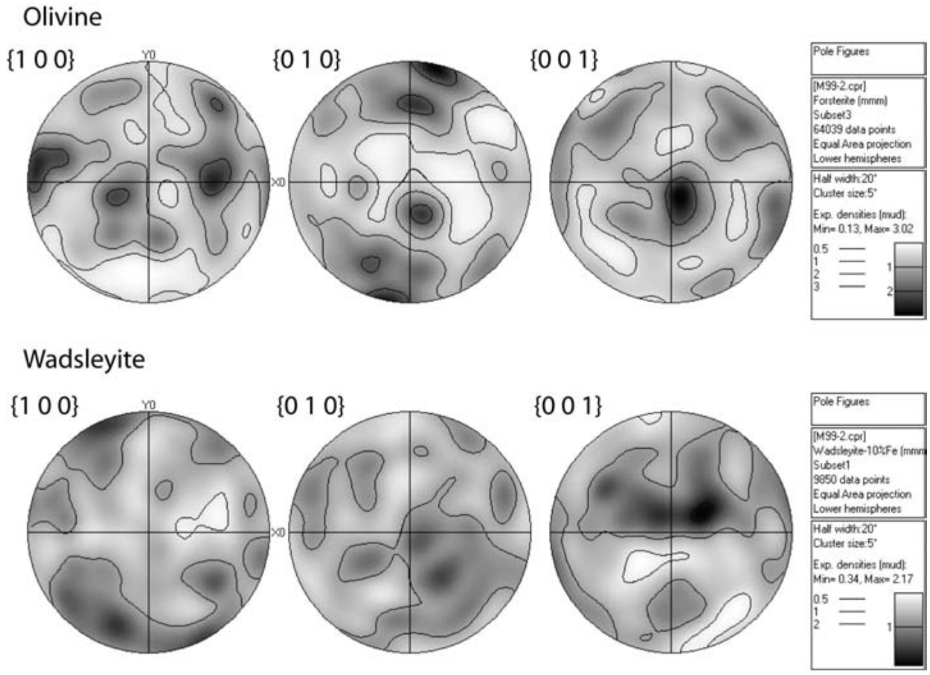

Fig. 3.6-6: Lower heminsphere pole figures of olivine (top) and newly formed wadsleyite (bottom). Vertical shortening direction.

c. *Interactions between deformation and reactive melt percolation in the upper mantle: Deformation-DIA experiments at high pressure and temperature (V. Soustelle, M.A.G.M. Manthilake, N. Miyajima, N. Walte, D.J. Frost and F. Heidelbach)*

Most experiments involving partially molten mantle rocks imply the presence of a melt that is in chemical equilibrium with a solid matrix. In contrast natural samples deformed in the presence of melt often display evidence for petrological reactions between the percolating melt and the surrounding minerals. These reactions occurring during deformation may be responsible for structural and textural differences observed between experimental and natural samples. In this study, we used a D-Dia apparatus to perform deformation experiments at 2 GPa and 1150 ºC on an olivine aggregate mixed with 5 % melt, which has a composition similar to an adakitic magma. The samples were deformed by uni-axial compression at strain rates of 10^{-5}, $5x10^{-5}$ and 10^{-4} s^{-1} and strains ranging from 10 to 30 %.

The reaction between the melt and the olivine induces the precipitation of orthopyroxene and minor amounts of clinopyroxene. The pyroxene-melt ratio is twice to four times higher in the deformation experiments than static ones performed for the same duration time. This implies that deformation enhances the reaction rate as has been described, for example, in experiments performed on partially molten crustal rocks. In all samples, melt-pockets and the pyroxenes are dispersed randomly in the aggregates. The analysis of the melt pockets topology shows, however, that the majority have their long axis at 0-30º to the direction of compression, with an average around 10º (Fig. 3.6-7b). On the other hand, the pyroxenes, occurring as single or small aggregates, are flattened parallel to the extension plane (Fig. 3.6-7c). This result may be fundamental to understanding modally metasomatized mantle rocks, which display a segregation of the reaction products normal or at high angle to the assumed melt percolation direction (*e.g.*, the refertilized spinel-tectonites in the peridotite massif of Ronda). In our experiments, the small size of the sample could explain the absence of melt segregation and/or the development of pyroxene-rich bands.

Crystal preferred orientation (CPO) measurements on olivine show a maximum concentration of the [010] axes parallel to the compression axis, a girdle of the [100] axes in the extension plane, and a random dispersion of the [001] axes. These CPO patterns are consistent with the pure shear deformation and the experimental P, T conditions. The orthopyroxene CPO displays a girdle of the [001] axes in the extension plane, and a maximum concentration of the [010] axes sub-parallel to the compression axis. This is not consistent with orthopyroxene CPO observed in natural upper mantle samples where [100] correspond to the dominant slip plane. This difference may result from: (1) crystallisation of Al-rich orthopyroxene, (2) topotactic relationship between olivine and orthopyroxene neoblasts, or (3) orientated crystallization under stress. Microprobe analyses show that the orthopyroxene neoblasts have a very low Al content (Al_2O_3 range from 0 to 1.6 wt.%), which cannot be responsible for a change of the dominant slip plane. TEM observations display that orthopyroxene neoblasts have no topotactic relationships with olivine, and that they are totally free of dislocations. As orthopyroxenes display a relatively strong CPO intensity, we assume that orientated crystallisation under stress may have been responsible for the observed orthopyroxene CPO features.

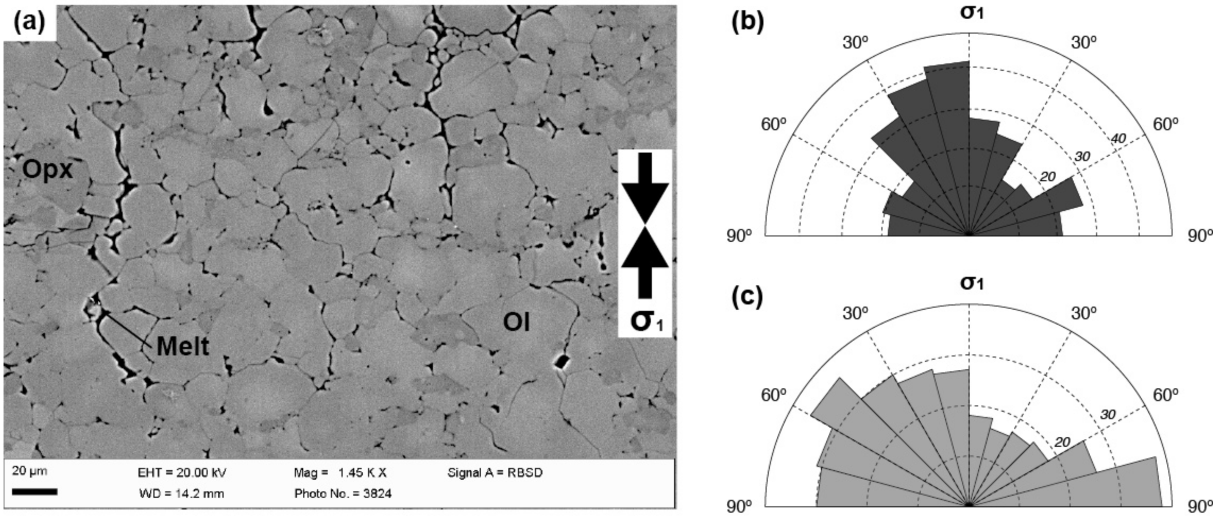

Fig. 3.6-7: Backscattered electron image of the sample DD522 deformed at 1150 ºC, 2 GPa, at strain rate of 5×10^{-5} s^{-1}, for a strain of 20 % (a). Distribution elongation axes of melt pockets (b) and orthopyroxenes (c) elongation axes in the sample DD522.

d. *Transmission electron microscopy characterization of the dislocations of phase A deformed at 400 °C and 11 GPa (P. Cordier and A. Mussi/Lille; D.J. Frost)*

Water transported in oceanic plates plays a major role in the dynamics of subduction. It is carried within hydrous minerals such as serpentines. However serpentines become unstable with increasing pressures and temperatures inducing partial dehydration and fluid release. At greater depths, dense hydrous magnesium silicates (DHMS) are further potential water carriers. Phase A is the first DHMS to appear, beyond ca. 200 km, after the antigorite breakdown. Up to now, nothing is known on the mechanical properties of phase A which may play an important role in the mechanical coupling between the plate and the surrounding mantle below 200 km. Phase A is hexagonal (space group $P6_3$) with an ABCB sequence of close-packed layers of O atoms and hydroxyl groups along the c-axis. One-half of the available octahedral sites and one-fourteenth of the available tetrahedral sites are filled by cations.

Three high-purity oxides (MgO, SiO_2 and $Mg(OH)_2$) have been mixed and annealed at 11 GPa and 900 °C during 210 min, to synthesize the sample. Then, phase A sample has been deformed in a further experiment at 11 GPa and 400 °C during 60 min. In order to get thin foils of the deformed specimen, it was mechanically polished down to a thickness of 24 µm. As noticed in a previous study of phase A (deformed at 700 °C, see last year’s report), it is very sensitive to irradiation damage. To reduce ion irradiation damage, the specimen was milled with an argon ion beam at liquid nitrogen temperature. Then, the thin foil was studied in Lille with a Philips® CM30 transmission electron microscope (TEM) operated at 300 kV. For the same reasons, TEM characterizations have been performed with a Gatan® cold stage (liquid nitrogen), with low illumination conditions.

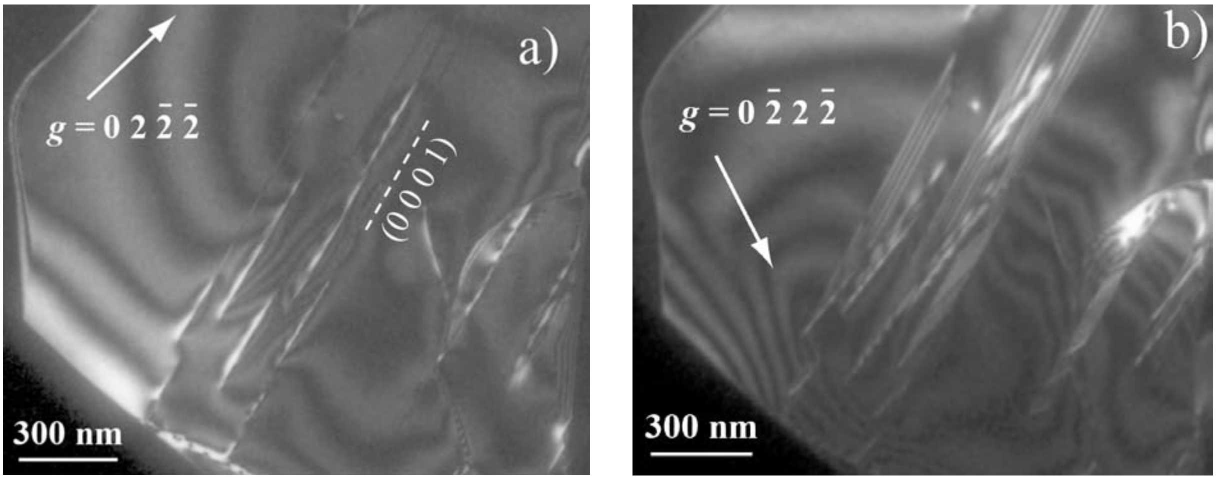

Fig. 3.6-8: TEM micrographs of widely dissociated dislocations on the basal planes in weak-beam dark-field conditions (dashed lines = glide planes, g = diffraction vector).

The specimen microstructure is composed of small grains of 8 ± 2 µm. All the analyzed grains have a high dislocation density ($\rho \approx 2.10^{13}$ m^{-2}). Very few sub-grain boundaries were noted. Contrary to the dislocation population of the specimen deformed at 700 °C (perfect dislocations, essentially), the sample deformed at 400 °C mostly contains widely dissociated dislocations on the basal plane (Fig. 3.6-8). Prismatic and pyramidal slip systems have also been characterized (Fig. 3.6-9).

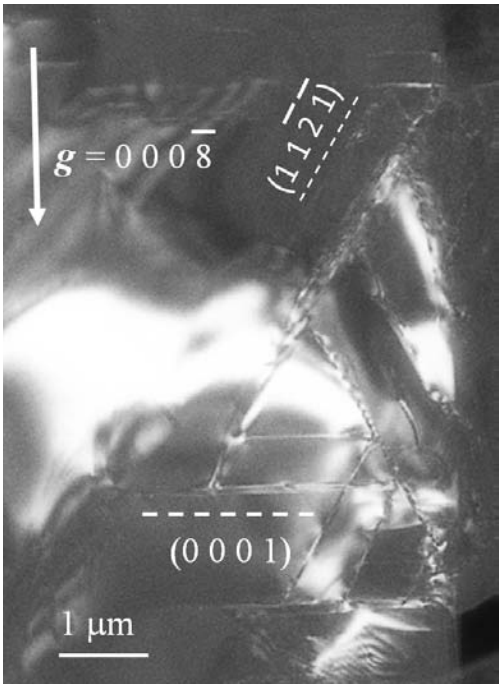

Fig: 3.6-9: TEM micrographs of pyramidal and basal glide planes in weak-beam dark-field conditions (dashed lines = glide planes, g = diffraction vector).

e. *High silicon self-diffusion coefficient in dry forsterite (H. Fei, C. Hegoda and D. Yamazaki/Misasa, S. Chakraborty and R. Dohmen/Bochum, M. Wiedenbeck/Potsdam, H. Yurimoto/Sapporo, S. Shcheka and T. Katsura)*

The plastic deformation of minerals at high temperature is controlled by diffusion or dislocation creep. Diffusion creep is governed by the diffusion of atoms through the volume and along grain boundaries, and dislocation creep is also believed to be rate-limited by diffusional processes if dislocation climb is involved. Silicon is the slowest diffusion species in most mantle minerals and therefore expected to limit the creep rates. Olivine is the main constituent mineral in the upper mantle and forsterite is the Mg-rich end-member of olivine. Hence, the Si self-diffusion coefficient (D_{Si}) in forsterite is essential for understanding the upper mantle rheology. Previous studies of D_{Si} in olivine and forsterite at ambient pressure showed discrepancies of ~ 2-3 orders of magnitude with those estimated from deformation experiments. Hence, it is necessary to reexamine D_{Si}. In this study, we measured D_{Si} in dry forsterite at 1600 and 1800 K and 0-13 GPa. We obtained a much higher D_{Si}, and it well explains the high dislocation climb rates in deformation experiments.

After polishing with diamond powder and a colloidal silica solution forsterite single crystals were coated with 300-500 nm of ^{29}Si enriched Mg_2SiO_4 films and covered by 100 nm of ZrO_2 films. The samples were pre-heated at 1273 K for 2 h to remove water in the coated films. The pre-cooked samples were then annealed at 1600 and 1800 K, 0-13 GPa and different duration (0-43 h) for diffusion. Water contents in the samples were determined to be less than 1 μg/g before and after annealing by infrared spectroscopy. The diffusion profiles were obtained by secondary ion mass spectroscopy and values of D_{Si} with surface roughness calibration were determined by fitting the profiles to the solution of Fick's second law.

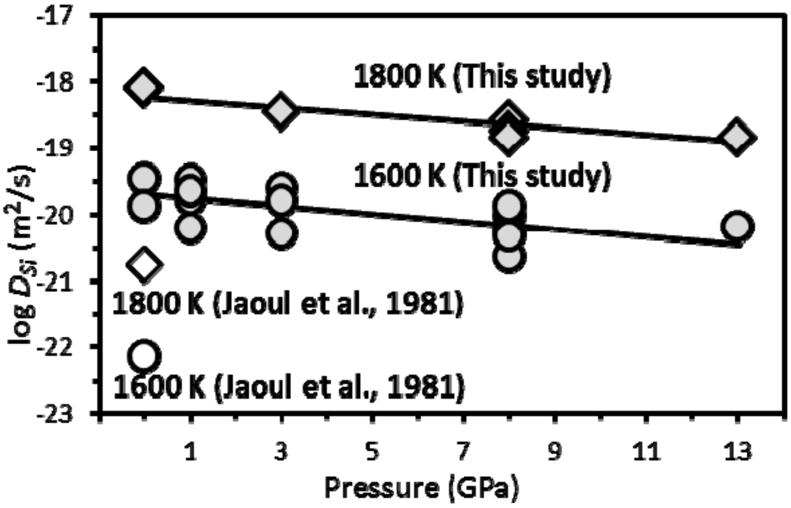

Fig. 3.6-10: Plots of log D_{Si} in forsterite against pressure at 1600 and 1800 K in comparison to data from Jaoul *et al.* (1981), Anelasticity in the Earth, **4**, 95-100.

Results of D_{Si} are plotted against pressure in Fig. 3.6-10. Our results are ~ 2.4 orders of magnitude higher than those measured by Jaoul *et al.* (1981) in forsterite at ambient pressure and 1-2 orders of magnitude higher than those in natural olivine (Fig. 3.6-11). In their studies, ZrO_2 thin film was not used for protecting the isotopic film. Possibly, without ZrO_2, the isotopic film tends to horizontally shrink instead of diffusing into the substrate during high temperature annealing. Such phenomenon was found in some no-ZrO_2 coated samples with much shorter diffusion profile compare with normal ZrO_2 coated samples (Fig. 3.6-12). This phenomenon was not found in high-pressure experiments even without ZrO_2 film, which was not too surprising because the isotopic film was compressed by the surrounding material and well contacted with substrate at high pressures. Our data explain the high dislocation climb rates well and they solve the discrepancy of D_{Si} in olivine or forsterite measured in diffusion experiments and that estimated from deformation experiments.

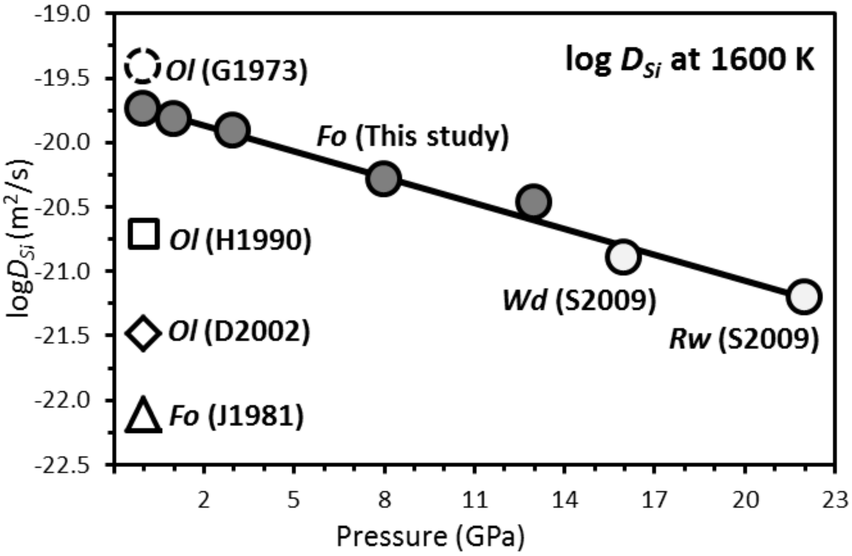

Fig. 3.6-11: LogD_{Si} against pressure at 1600 K. *Fo*: forsterite. *Ol*: natural olivine. *Wd*: iron-bearing wadsleyite. *Rw*: iron-bearing ringwoodite. S2009: Shimojuku *et al.* (2009), EPSL, **284**, 103-112; H1990: Houlier *et al.* (1990), PEPI, **62**, 329-340; D2002: Dohmen *et al.* (2002), GRL, **29**, 2030-2034; J1981: Jaoul *et al.* (1981), Anelasticity in the Earth, **4**, 95-100. G1973: estimated from dislocation climb rate by Goetze and Kohlstedt, (1973), JGR, **78**, 5961-5971. D_{Si} from previous studies are all calibrated to 1600 K.

Olivine, wadsleyite and ringwoodite are the main constituents of the upper mantle. If we extrapolate our data of D_{Si} at 1600 K to higher pressures, it is almost equal to that in iron and water bearing wadsleyite and ringwoodite from published data (Fig. 3.6-11). The linear relationship of logD_{Si} with pressure in dry forsterite, iron and water bearing wadsleyite and ringwoodite implies that temperature and pressure would be essential factors that affect D_{Si} in comparison with other factors, for example, iron concentration, water content, and structural differences of the $(Mg,Fe)_2SiO_4$ polymorphs.

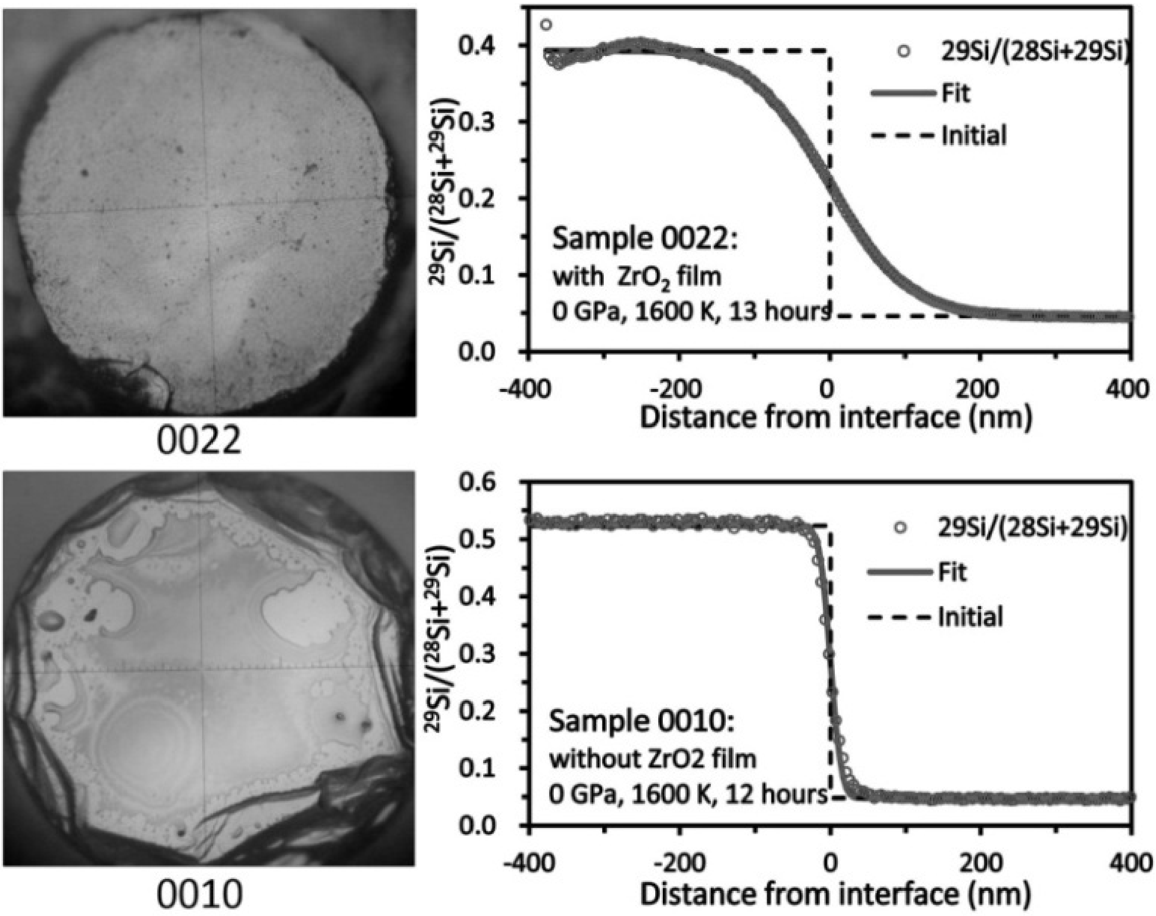

Fig. 3.6-12: Sample 0010 (1600 K, 0 GPa, 12 hours, without ZrO_2 film) and 0022 (1600 K 0 GPa, 13 hours, with ZrO_2 film). In sample 0010 the coated film shrank during the experiment yielding a diffusion profile much shorter than in sample 0022 which has the same pressure and temperature conditions and very similar duration.

f. *Major element diffusion in garnet in Earth's transition zone (W. van Mierlo, F. Langenhorst, D.J. Frost and D. Rubie)*

Majorite is a high-pressure polymorph of enstatite with a garnet structure, and forms a solid solution with the other natural garnets present in the Earth's mantle. It is thought to be the second most important phase in the Earth's transition zone, after the high-pressure polymorphs of olivine (wadsleyite and ringwoodite). Unfortunately, very little is known about the transport properties of this majoritic garnet phase. Especially the major element diffusivity in garnet plays an important role in understanding the dissolution kinetics of pyroxene into garnet in a subducting slab. Also after the oceanic crust has been subducted, it will form an aluminium inhomogeneity in the mantle. The diffusivity of the majorite component will here be of importance in controlling how long such an inhomogeneity can persist. Thus, we have conducted diffusion experiments on garnet diffusion couples to determine the major element diffusivity in the Earth's transition zone.

To determine the major element diffusivities in garnet at transition zone conditions interdiffusion experiments have been conducted in a multianvil apparatus between 2-20 GPa and 1400-1900 °C with diffusion couples made of synthetic majoritic garnet, Dora Maira pyrope garnet and Ötztal almandine garnet. The diffusion experiments with the majoritic garnet – Dora Maira pyrope garnet couples show that the diffusion of the majorite component in garnet is very slow, comparable to the diffusivity of silicon in wadsleyite and ringwoodite. The activation energy, activation volume and the pre-exponential for diffusion of the majorite component in garnet were determined to be 241 ± 54 kJ mol^{-1}, 3.3 ± 0.1 cm^3 mol^{-1} and 2.3 x 10^{-7} cm^2 s^{-1}, respectively (Fig. 3.6-13). The diffusivity of the majorite component in garnet was determined to be 2-3 orders of magnitude slower than the self-diffusivity of Mg, Fe and Ca in garnet at the same conditions. Comparison with diffusion data on wadsleyite and ringwoodite shows that the diffusivity of the majorite component in garnet is very similar to that of the silicon self-diffusivity in the olivine high-pressure polymorphs.

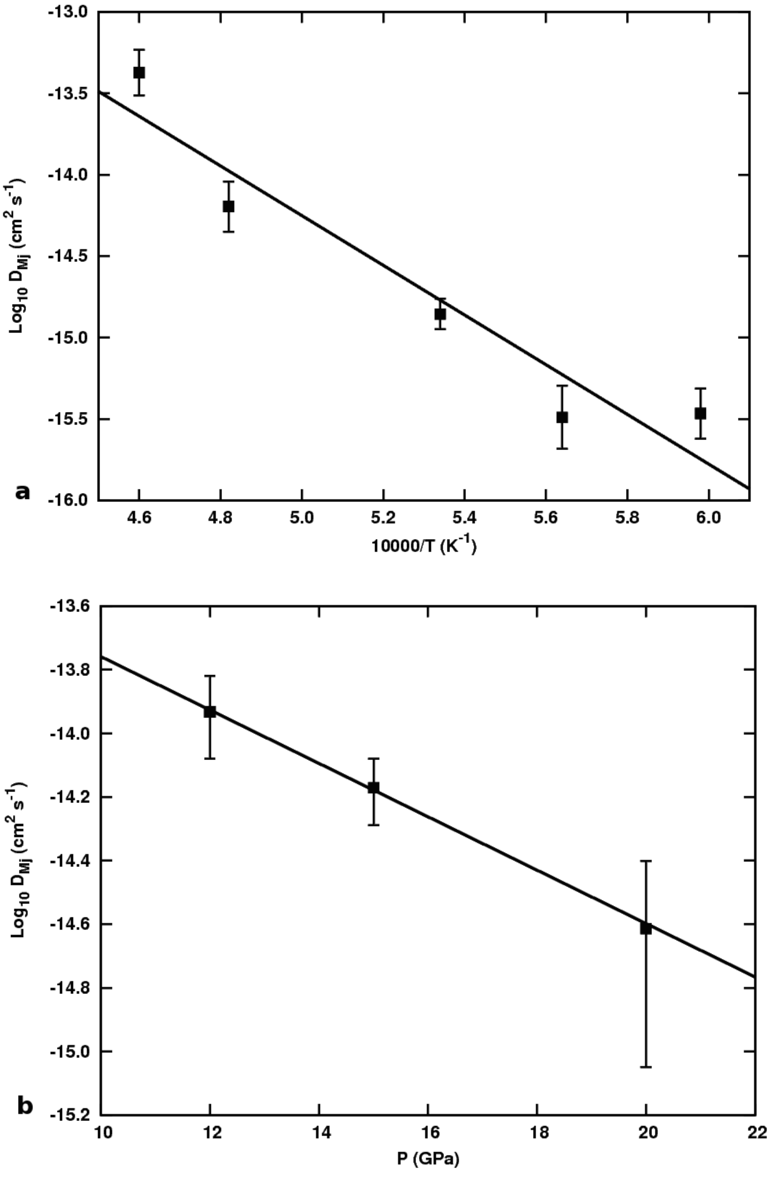

Fig. 3.6-13:
The determined diffusion coefficient for the majoritic garnet – Dora Maira diffusion experiments at 15 GPa (a) and 1800 °C (b).

Another set of diffusion experiments was conducted with Ötztal almandine – majoritic garnet diffusion couples. The diffusion profiles obtained from these experiments are strongly asymmetric, and indicate that there is an increased tracer-diffusivity of Mg and Fe by one order of magnitude in majoritic garnet part of the diffusion couple. The increased diffusivity of Mg and Fe in majoritic garnet appears to be an intrinsic property of majoritic garnet, which can be explained by the fact that the octahedral sites short cuts the diffusion path through the garnet structure. In almandine the octahedral sites are all occupied by aluminium, whereas in the majoritic garnet a part of the octahedral sites are occupied by Mg and Fe, too.

To determine whether solid state diffusion can homogenize the mantle the diffusion distance of the majorite component in garnet, assuming grain boundary diffusion is the dominant diffusion mechanism, has been calculated. The results show that within the range of temperatures prevailing in the transition zone, majorite is able to diffuse 5-15 m on the time scale of the age of the Earth. Solid state diffusion is thus not able to homogenize the mantle. Another important question is if diffusion of the majorite component in garnet is fast enough such that pyroxene can dissolve in garnet forming majoritic garnet in the subducting oceanic slab. A finite difference code that models diffusion in a spherical grain and diffusion controlled growth of a spherical grain has been developed to assess this question. The results show that during the subduction process all pyroxene can be dissolved in garnet in the case of the lithospheric mantle part of the slab. The oceanic crust shows however a different result, due to its lower temperature, and only a small amount of pyroxene can be dissolved into garnet. Metastable phases will thus be preserved in the subducting oceanic crust during the subduction process.

g. *Deformation fabric of quartz-rich and calcite-rich mylonites at the Moresby Seamount detachment (R. Speckbacher and M. Stipp/Kiel, F. Heidelbach)*

The Woodlark Basin (east of Papua New Guinea) is among the most studied examples for an active transition from continental rifting to seafloor spreading. There, the submerged Moresby Seamount detachment is arguably the best exposed active detachment fault in the world, and is the candidate structure for future crustal break and ocean floor spreading. Many experimental studies indicate that continental lithosphere is too strong to be split by plate tectonic forces, if brittle rupture has to occur in typical crustal rocks. However, geological evidence suggests that detachment faults in rifts are weak, and can thus operate under low differential stress. While high fluid pressures assist in maintaining low stress faults in the brittle regime, other processes must be in operation to create ductile mylonites (today exhumed at the seafloor) capable of aseismic flow at greater depth.

The fault rock protoliths are dominantly mafic (gabbros, dolerites etc., as documented by shipboard dredging results). Yet we observed fault rocks derived from these protoliths, which are rich in quartz and calcite. Veins and microcracks suggest that addition of quartz and calcite occurs syntectonically. Our preliminary interpretation is that as soon as a rheologically critical amount of quartz and/or calcite is precipitated in the fault rocks, the deformation mechanism switches from cataclasis to plastic flow (mylonitization). We infer that the infiltration of calcite and quartz by hydrothermal fluids into the fault rocks is deformation related.

One key to understand fault weakening in the Moresby Seamount detachment is the deformation on microstructure that can be analyzed by scanning electron microscopy and electron backscatter diffraction (EBSD) analysis. Pattern acquisition was carried out at 15 - 30 kV acceleration voltage, ~ 3 nA beam current, 20 mm working distance and 70° sample tilt. Crystallographic preferred orientation (CPO = texture) data were determined based on automatically indexed EBSD patterns. EBSD scans were obtained by beam or stage movement on square grids with variable step sizes between 1.3 μm and 100 μm depending on grain size and purpose of the analysis. Between 1 and 4 scans have been analyzed on each of the six samples, in order to achieve large- and small-scale microstructural and textural information.

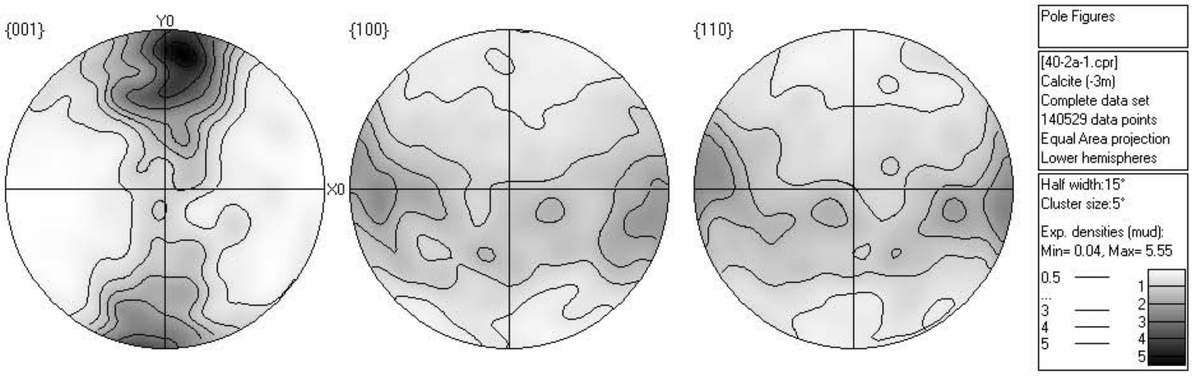

Fig. 3.6-14: Typical calcite CPO in mylonites from the Moresby seamount detachment; here fabric of sample DR40-2a (9°46.495'S, 151°34.478'E); shear plane is horizontal, stretching lineation E-W; lower hemisphere, equal area projection.

The small grain size and the polyphase composition of the mylonites comprising not only quartz and calcite, but also feldspar and chlorite my result in a moderate index; EBSD data with low confidence sometimes make up to 50 % of the entire maps. Nevertheless, pure quartz and calcite areas in the six samples show similar results. In all five calcite containing samples calcite porphyroclasts and recrystallized grains display c-axis pole figures with maxima perpendicular to the macroscopic foliation (Fig. 3.6-14). Related basal planes a-axis orientations are subparallel to the foliation plane. Quartz textures, however, are more complicated to interpret. C-axis pole figures (see Fig. 3.6-15) display weak cross girdle fabrics which appear to be rotated about 30° around the foliation pole. Strongest CPO's are shown by rhomboedric {10-11} and {01-11} planes. The weak lattice preferred orientations suggest that other deformation mechanism than dislocation creeps considerably contribute to strain accommodation in quartz.

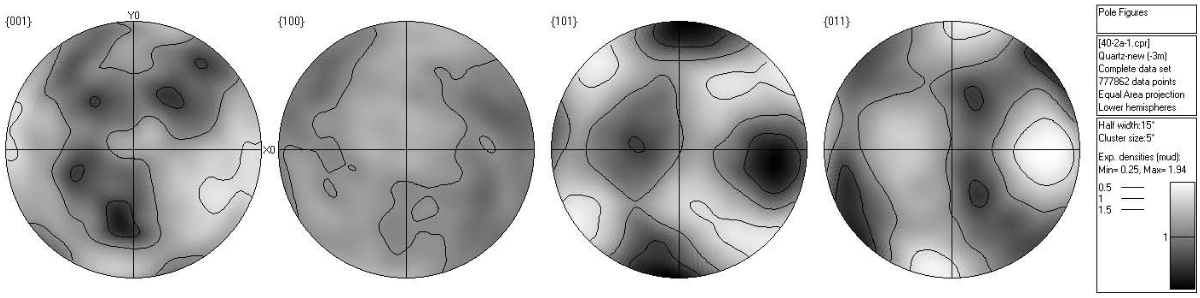

Fig. 3.6-15: Pole figures showing the CPO of quartz sample sample DR40-2a (9°46.495’S, 151°34.478’E); shear plane is horizontal, stretching lineation E-W; lower hemisphere, equal area projection.

The results also show that the omnipresent stretching lineation on the fine-grained Moresby Seamount mylonites is represented by calcite, as the calcite pole figures correspond to the kinematic framework of foliation and lineation while the quartz pole figures are rotated with respect to the latter. Further microstructural and chronological analysis and interpretation of the data is currently in progress.

h. *Characterization of diopside-kaersutite intergrowth in Balmuccia Dunites (S.C. Tarantino, A. Zanetti and M. Zema/Pavia, M. Mazzucchelli/Modena, F. Heidelbach and N. Miyajiima)*

Balmuccia is one of the subcontinental mantle peridotite bodies occurring in the Southern Domain of the Western Italian Alps. It consists of a 4-5 km long, 0-8 km wide lens crossing the Val Sesia just east of the Insubric line. The occurrence of dunites in the spinel-facies mantle massif of Balmuccia represents a precious opportunity to investigate the mineralogical and petrochemical processes governing the dunite formation at relatively high-P conditions (*i.e.*, spinel-facies conditions). Dunite lenses are 15-20 m thick and up to 60 m long and contain pods and dykes rich in amphibole, phlogopite, plagioclase and rutile. The studies dealing with this kind of dunites are currently in progress. The preliminary petrographic investigations highlight that melt escaped from gabbroic pods and/or dykes (cm to dm in thickness) into the surrounding dunite. This determined the development of reaction zones (dm-thick), characterised by segregation of newly-formed minerals, basically amphibole and clinopyroxene. However, up to certain distance (~ 8 cm) from the dunite-gabbroic pod/dyke contact, the early recrystallisation is systematically characterised by the formation of mm-large grains showing a tight intergrowth of clinopyroxene and amphibole lamellae (Fig. 3.6-16). In these sectors, amphibole crystallises in the interstices as relatively late products of the melt-peridotite interaction. Petrographic survey evidences that amphibole sometimes overgrows grains with clinopyroxene-amphibole intergrowths. The latter show the outermost rim cleaned by amphibole lamellae and formed by pure clinopyroxene, likely as a result of chemical re-equilibration (Fig. 3.6-16).

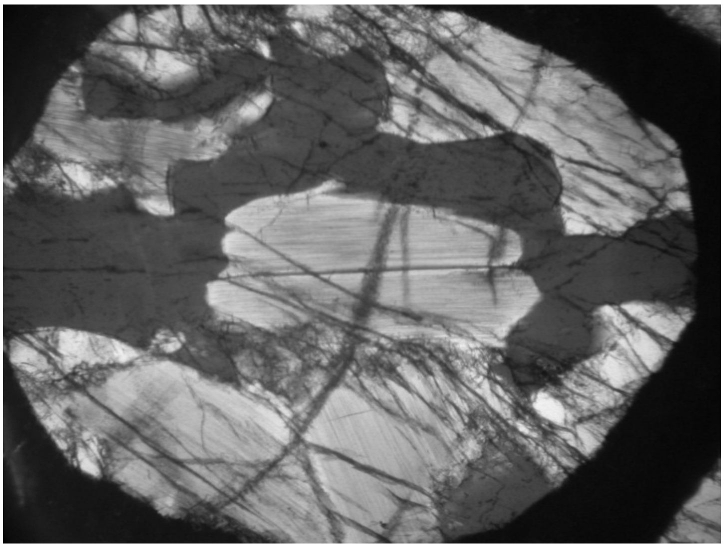

Fig. 3.6-16: Petrographic details of dunites from Balmuccia massif showing pockets related to melt infiltration. These are characterised by early crystallisation of mm-long grains with tight clinopyroxene-amphibole intergrowth. Amphibole and clinopyroxene crystallise as late minerals, and the former locally overgrows the grains with amphibole-clinopyroxene lamellae (long edge 3 mm).

A combined approach which makes use of scanning electron microscopy with electron backscattering diffraction (SEM-EBSD), transmission electron microscopy (TEM) and electron diffraction has been used to characterize the two phases and their relative sizes and orientation and has been associated to petrographic analysis in order to reconstruct their mechanism of formation. Thin sections were prepared from four samples and polished by standard methods (SiC and diamond to 0.5 µm). For the SEM-EBSD analysis, an additional step of combined etching and polishing was performed with a high-pH colloidal silica solution (40 nm particle size) in order to remove the surface layer damaged by previous polishing. The samples were then coated with ca. 4 nm of carbon to reduce charging and possible beam drift during the orientation measurements.

One sample was selected for TEM analysis and prepared from the orientated thin section normal to the **c**-axis. The sample was glued on a Mo-TEM grid and then thinned to electron transparent at 4.5 kV and 0.8 mA by a conventional Ar-milling machine (Gatan Dual milling). The TEM observation of the sample was performed in a transmission electron microscope (*Philips CM20FEG* at Bayerisches Geoinstitut), operating at 200 kV. The micro-textures of amphiboles lamellae were examined using bright field (BF) and weak-beam dark-field images and selected area electron diffraction. High resolution TEM images were recorded under some defocus conditions near the Scherzer defocus (-67 nm). The chemical analysis was also performed using a STEM-EDXS system, combined scanning TEM beam with an energy-dispersive X-ray detector.

Back-Scattered SEM inspection of the amphibole-clinopyroxene intergrowth confirms the occurrence of a tight (µm-scale) alternation of amphibole and clinopyroxene lamellae. In some grains, the thickness of the clinopyroxene lamellae (~ 20 µm) is around ten times that of amphiboles whereas in other cases the thickness of the two phases is comparable (2-5 µm). Semi-quantitative EDS analysis indicate that in most cases the major element composition of amphibole and clinopyroxene lamellae is virtually stoichiometric. EBSD maps allowed to determine, by indexing Kikuchi diffraction patterns, the spatial distribution and the orientation relationships between the two phases. The obtained maps show an extremely ordered phase separation in which the amphibole lamellae as well as the late kaersutite crystals are all parallel to (010) in the pyroxene, in agreement with TEM and consistent with previous studies. The topotaxial orientation of the amphibole lamellae with the matrix of clinopyroxene, as revealed by dark field TEM images, is displayed in Fig. 3.6-17. Diffraction contrast images showed also the presence of finer (less than 100 nm) amphibole lamellae in the diopside. The interface between the two phases contains an array of misfit dislocations due to the differences in the lengths of the **a**-axis. High resolution TEM image of the interface between clinopyroxene and clinoamphibole indicates intercalation of a chain multiplicity fault of single chains (1) parallel to (010) into the lattice characterized by double chains. The chemical analysis across the interface is currently under progress, to discuss the formation mechanisms of the amphibole lamellae. As far as we are aware, this is the first documentation of tight alternation of diopside and kaersutite lamellae in high-T mantle peridotites. On the basis of the preliminary observations, two hypotheses can be tentatively proposed to explain the development of this kind of crystals. The first one involves the crystallisation of a phase having composition intermediate to that of amphibole and clinopyroxene, and subsequent unmixing. The second one would consider the amphibole-clinopyroxene intergrowth as a primary feature, likely due to very special kinetic condition of crystallisation.

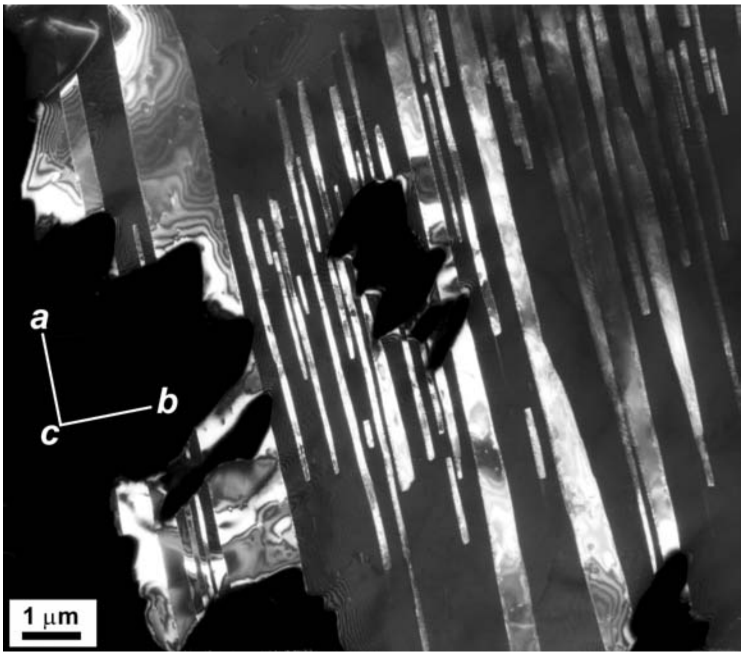

Fig. 3.6-17: A typical texture of amphibole lamellae (white contrast) in the clinopyroxene (black matrix). The both phases share the (010) planes in the same direction. Dark field TEM image with **g** = $5\bar{1}0$ (in the clino-Amphibole diffraction).

3.7 Materials Science

High-pressure material science and technology share with mineral physics and petrology not only common methods of high-pressure, high-temperature experimentation, but also methodologies of *in situ* investigations at extreme conditions. At the Bayerisches Geoinstitut, unique high-pressure equipment and *in situ* technologies are available that make possible sophisticated and challenging research into the physics and chemistry of materials at high pressures. In this annual report, we present results of studies of various classes of solids – elements, oxides, carbides, carbonates and molybdates.

Boron has been for a long time known as a prospective material for numerous applications. α-Boron demonstrates a truly spectacular combination of properties – it is a direct band gap semiconductor, has a very high hardness, is thermally and chemically highly resistive, and is quite light. Such properties may make α-B a material of choice in many industrial semiconductor applications, and, especially, as a working element in solar cells with high efficiency for converting sun light into electrical power. So far research and development on potential applications of α-boron were hindered by concerns about its thermodynamic instability and the absence of a reliable method for synthesizing single crystals. The phase diagram of boron made at Bayerisches Geoinstitut shows that α-B is not only a thermodynamically stable phase over a large pressure-temperature range, but it also can be reproducibly synthesized for large-scale production at conditions readily accessible by modern industry (similar to conditions for producing synthetic diamonds, for example).

An icosahedral, quasimolecular cluster of 12 boron atoms (B_{12}) is the building block of all allotropes of boron as well as of many boron-rich solids. However, the properties of boron polymorphs and boron-rich compounds which make them interesting for materials science and technology (extreme chemical stability associated with high hardness and low compressibility) are highly unusual for molecular solids. An explanation of this phenomenon requires a detailed analysis of chemical bonding between boron atoms that scientists at Bayerisches Geoinstitut have successfully accomplished for the high-pressure boron polymorph γ-B. A topological analysis of the electron density distribution reveals unique one-electron-two-center bonds connecting neighboring B_{12} clusters. A polar-covalent two-electron-three-center bond between a pair of atoms of an icosahedral cluster and one atom of the interstitial B_2 dumbbell explains the observed charge separation in γ-B.

Ammonia borane BH_3NH_3 is promising candidate for hydrogen storage due to its remarkably high gravimetric and volumetric hydrogen content. Investigation of BH_3NH_3 at high pressure is interesting from point of view of understanding its stability, possible changes in chemical bonding, and synthesis of dense polymorphs with even higher volumetric hydrogen contents. Raman spectroscopy studies at BGI have revealed at least three phase transitions at pressures up to 64 GPa. Moreover it has been demonstrated that ammonia borane remains chemically intact on compression at ambient temperature and is able to generate second harmonic of laser light to at least 130 GPa. Thus it is definitely confirmed that, regardless of structural changes, BH_3NH_3 adopts non-centrosymmetric structures in the studied pressure range.

Multiferroic materials are at the focus of intensive scientific research in modern solid state physics and chemistry. Multiferroics demonstrate the coupling of electric and magnetic properties and are important for the development of new electronic devices in which magnetism is controlled by an electric field. Recently a novel class of multiferroics was discovered, in which the symmetry arrangement of ordered magnetic moments breaks inversion symmetry and allows ferroelectricity. The $RbFe(MoO_4)_2$ compound represents a unique example of such materials, exhibiting multiferroic phenomena in combination with geometrically frustrated magnetism on a triangular lattice. A high-pressure study of $RbFe(MoO_4)_2$ at BGI has revealed a complex behaviour of this material and points towards the possibility of synthesising new polymorphs at elevated pressures.

a. *Experimental PT phase diagram of boron (G. Parakhonskiy, N. Dubrovinskaia, E. Bykova, and L. Dubrovinsky; R. Wirth/Potsdam)*

Despite centuries of application and decades of intensive studies of boron compounds, elemental boron still remains in the focus of wide scientific interest due to its enigmatic properties (largely unknown phase diagram, pressure-induced metallization and superconductivity, formation of unusual chemical bonds and potential technological applications), exceptional chemical stability combined with very high hardness and interesting semiconducting and optical properties.

Among elemental boron polymorphs, only α-rhombohedral (α-B), β-rhombohedral (β-B), and γ-orthorhombic boron (γ-B) have been currently established as pure phases. They can be synthesised as single crystals at high pressures and temperatures and are preserved on quenching to ambient conditions. The relative stabilities of α-B and β-B at ambient conditions remain a puzzle. On heating at ambient pressure to temperatures above ~ 1500 K, α-B slowly transforms to β-B which could mean that the stable high-temperature form of boron is the β-phase. The fact that β-B can not be transformed to α-B at ambient pressure may indicate that the α-form is metastable. Using density-functional and first-principle quasi-harmonic phonon calculations, some theoreticians have reached the conclusion that at zero temperature α-B is more stable than β-B. Other theoretical investigations indicate that it is possible to find an arrangement of partially occupied states in β-boron that increases its stability with respect to the α-phase. It was found that boron could be a frustrated system and a series of β-boron structures, nearly degenerate in energy, may be stabilized by a macroscopic concentration of intrinsic defects, which are responsible not only for entropic effects but also for a reduction in internal energy making β-B more stable than α-B at zero temperature.

In the present work we have undertaken a systematic experimental exploration of the pressure-temperature (PT) phase diagram of boron at pressures up to 14 GPa and temperatures up to 2400 K aimed at establishing phase boundaries and resolving the long-standing problem regarding relative stability of the α- and β-B phases. In a series of experiments conducted using the multianvil apparatus (1000-ton Hymag and 1200-ton Sumitiomo presses) single crystals of alpha, beta and gamma boron were obtained. Pure β-B was loaded into a Pt capsule. Either 18/11 or 25/15 high-pressure assemblies with $LaCrO_3$ or graphite furnaces were used. Phase identification was confirmed by Raman spectroscopy and X-ray diffraction. In our experiments at appropriate pressure-temperature conditions α-B crystals grew at the expense of β-B and in some runs all starting β-boron transformed into the α-phase. We also observed the direct transformation of β-B into α-B. These observations prove that α-B is a thermodynamically stable phase. Based on the experimental data, the PT phase diagram (Fig. 3.7-1) was constructed. It allows the PT stability fields of the α-B, β-B, and γ-B phases to be

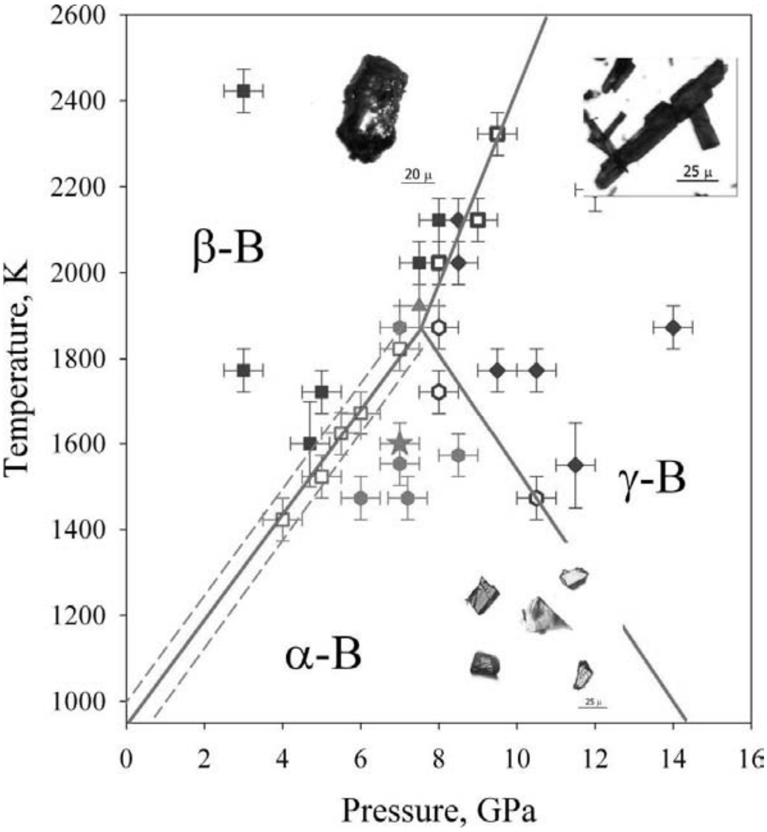

Fig. 3.7-1: Pressure-temperature phase diagram of boron. The PT conditions at which various boron phases crystallize are indicated by different symbols: squares - β-boron; diamonds – γ-boron; hexagons - α-boron; open squares: α-boron + β-boron; thick open squares: β-boron + γ-boron; open hexagons: α-boron + γ-boron; triangle - α-boron + β-boron + γ-boron; the star marks the conditions of a multianvil experiment which resulted in the solid-solid phase transformation of β-B to α-B; solid lines show inferred phase boundaries. The inserts present images of synthesized crystals of α-boron, β-boron, and γ-boron.

defined. The phase boundary separating the β-B and γ-B phase stability fields agrees well with the phase relations found in our previous work. The other two phase boundaries (α-B/β-B, and α-B/γ-B) have not been reported previously based on experimental data. Linear extrapolation of the α-B/β-B boundary, established in the pressure interval of 4 to 8 GPa, to ambient pressure (Fig. 3.7-1) suggests that α-boron is the thermodynamically stable low-temperature boron phase below ~ 970 K. The linear extrapolation is totally justified by considering a potential phase diagram of the unary boron system. Indeed, knowing one point on the coexistence line in the fundamental property diagram one can determine the direction of the line by applying the Gibbs–Duhem relation to both phases using the fact that dT, dP and $d\mu A$ must be the same in both phases when they coexist:

$$d\mu A = -S_\alpha dT + V_\alpha\, dP$$
$$d\mu A = -S_\beta dT + V_\beta\, dP,$$

where μA is the chemical potential of boron, S_α and S_β are molar entropies and V_α and V_β are the molar volumes of α- B and β-B, respectively. This system of equations defines the slope of the α + β coexistence line in the fundamental property diagram. The direction of the projected line in the *T, P* phase diagram, *i.e.*, the α + β phase field, is obtained by eliminating $d\mu A$ from the Gibbs–Duhem relation:

$$dP = \frac{S_\alpha - S_\beta}{V_\alpha - V_\beta}\, dT.$$

Except at very low temperatures the equilibrium boundary is almost straight because differences in *S* and *V* remain almost constant for solid phases.

The phase diagram of boron (Fig. 3.7-1) shows that α-B is not only a thermodynamically stable phase over a large pressure-temperature range, but it also can be reproducibly synthesized at conditions readily accessible by modern industry for large-scale production (similar to the conditions required for producing synthetic diamonds, for example).

b. *Impact of lattice vibrations on the equation of state of gamma-boron (N. Dubrovinskaia, E. Zarechnaya and L. Dubrovinsky, E. Isaev and Yu. Vekilov/Moscow, M. Merlini/Milano, M. Hanfland/Grenoble, S. Simak, A. Mikhaylushkin and I. Abrikosov/Linköping)*

The structure of the high-pressure boron γ-B polymorph is based on B_{12} icosahedra and a B_2 dumbbell linked together, so that its unit cell has an orthorhombic symmetry and contains 28 atoms. Properties of γ-B are remarkable. It is a wide band gap semiconductor characterised by very high hardness (measured Vickers microhardness Hv= 58(5) GPa) and very low compressibility. There are certain concerns regarding both theoretical and experimental results on the equation of state (EOS) of γ-B reported in the literature. In particular, theoretical volumes obtained by different groups agree very well with each other, but they *underestimate* the experimental values by about 2 %, despite the use in the calculations of the Generalized Gradient Approximation (GGA), which usually *overestimates* cell volumes. Also theoretical values of the bulk modulus (K’) for γ-B_{28} considerably overestimate the experimental results, which are quite low for the orthorhombic phase of B.

We report the results of a combined theoretical and experimental study of the equation of state of γ-B. The unique feature of our diamond anvil cell (DAC) experiments is that they were carried out not only on polycrystalline samples, but also on the single crystals of γ-B compressed to about 40 GPa in a helium (He) pressure transmitting medium. Single crystals and polycrystalline aggregates of γ-B were grown at high pressures and temperatures in multianvil presses at BGI. Single crystals of ~ 7 µm x 7 µm x 30 µm in size were selected for X-ray diffraction measurements in DACs (Fig. 3.7-2) at the ID09a beamline of the European Synchrotron Radiation Facility (ESRF). In two different runs the samples were clamped between diamond anvils with culets of 300 µm or 250 µm diameter. Steel gaskets were indented to the thickness of about 50 µm and holes with a diameter of 100 µm or 80 µm were drilled in the center. Helium pressure medium was loaded at 1.4 kbar. Diffraction data were collected at 293 K (0.4143 Å wavelength) using the MAR555 detector. 120 frames in the omega range of ± 30 degrees (with the scanning step size of 0.5° and the exposure time of 1 sec) were taken. At least 60 independent reflections were collected for each pressure point. The data were processed with the Crystalis software. The experimental compressibility curve is shown in Fig. 3.7-3.

In the theoretical calculations, we took into consideration the lattice vibrations, which are commonly neglected in first-principles simulations. We showed that the phonon contribution has a profound effect on the EOS of γ-B, giving rise to anomalously low values of the pressure derivative of bulk modulus and greatly improving agreement between theory and experiment.

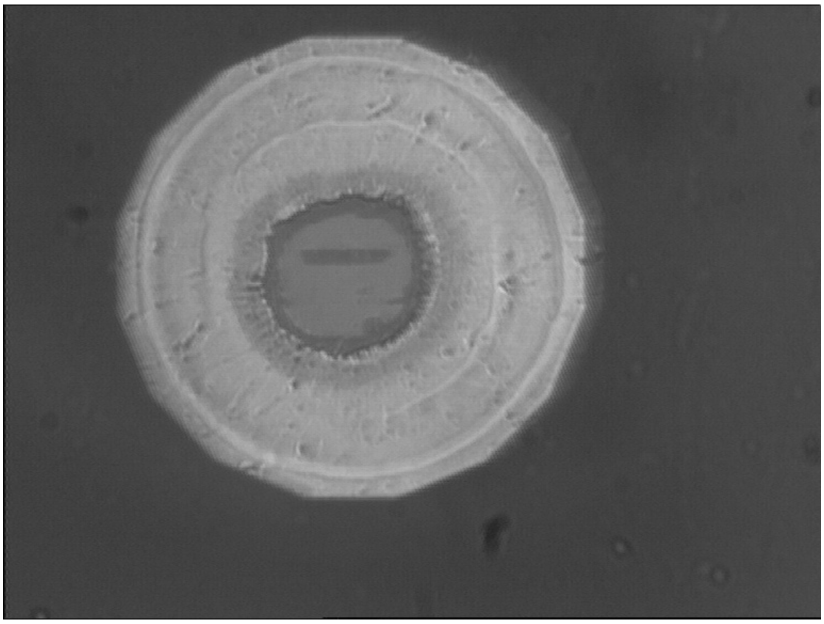

Fig. 3.7-2: A single crystal of B_{28} loaded into the DAC in a He pressure medium.

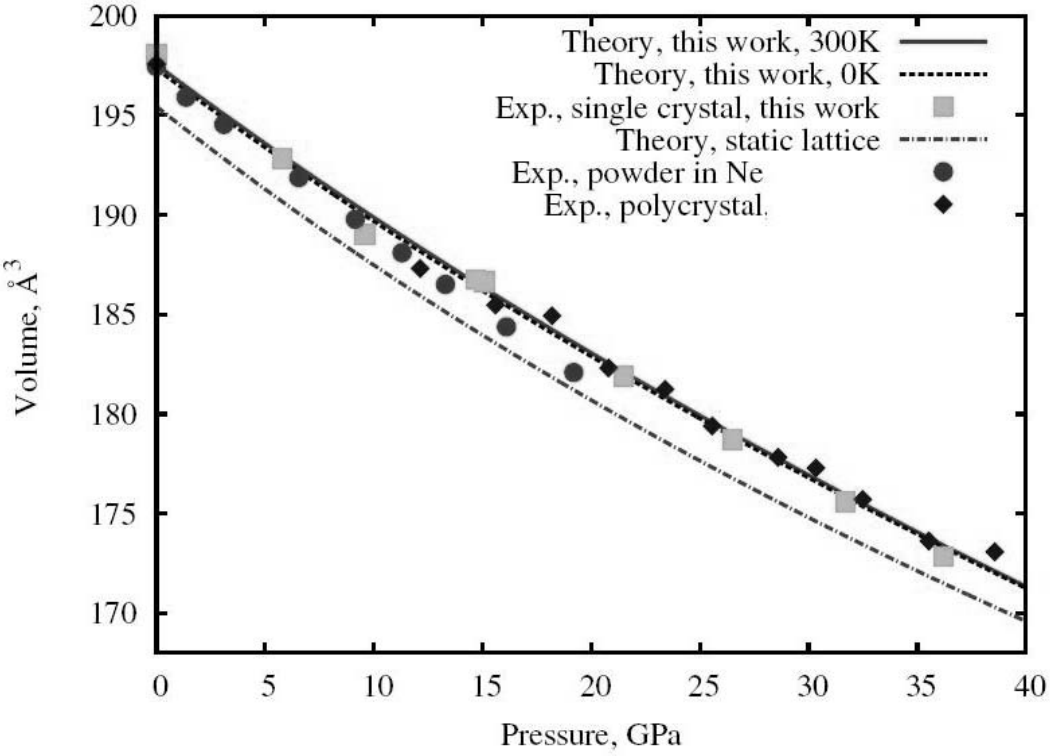

Fig. 3.7-3: Equation of state of B_{28} at pressures up to 40 GPa. Theoretical results are obtained from free energies at 300 K (solid line) and at 0 K including the effect of lattice vibrations (dashed line). Experimental results (squares) were obtained on single crystals. Also shown are theoretical results from static total energy calculations (dashed-dotted line), experimental data for B_{28} powder in Ne pressure medium from our previous work (circles), as well as experimental data on polycrystalline samples from the literature.

c. *Bonding in gamma-boron resolved from single crystal diffraction data (S. Mondal, S. van Smaalen, A. Schönleber, N. Dubrovinskaia, E. Zarechnaya and L. Dubrovinsky; Y. Filinchuk and D. Chernyshov/Grenoble; S. Simak, A. Mikhaylushkin and I. Abrikosov/Linköping)*

An icosahedral, quasimolecular cluster of 12 boron atoms (B_{12}) is the building block of all allotropes of boron as well as many boron-rich solids. However, the properties of boron polymorphs and boron-rich compounds which make them interesting for material science and technology (extreme chemical stability associated with high hardness and low compressibility) are highly unusual for molecular solids. Explanation of this phenomenon requires a detailed analysis of chemical bonding between the boron atoms – as performed in the present study for the high-pressure boron polymorph γ-B. A topological analysis of the electron density distribution reveals one-electron-two-center bonds connecting neighbouring B_{12} clusters. A unique polar-covalent two-electron-three-center bond between a pair of atoms of an icosahedral cluster and one atom of the interstitial B_2 dumbbell explains the observed charge separation in γ-B.

Modern X-ray diffraction methods enable information about the location of electrons in a material to be obtained. For this purpose a single crystal of the compound is required which is preferably investigated using X-ray synchrotron radiation. Experimental data obtained by X-ray diffraction are analyzed by creating electron-density maps which reflect the probability of an electron being present at a specific location, but achieving the required accuracy is a demanding task. For the light element boron this has not been possible previously, mainly because of high-quality single crystals were not available. Recently a reliable method of high-pressure synthesis of boron single crystals has been developed at the Bayerisches Geoinstitut and single crystals of the high-pressure γ-B phase have been obtained.

High-resolution, single-crystal X-ray diffraction data of γ-B_{28} have been collected at a temperature of 85 K at the Swiss-Norwegian beam line BM01A of the European Synchrotron Radiation Facility (ESRF). Electron-density results obtained from high-quality, low-temperature X-ray diffraction data provide important information about chemical bonding in crystalline solids, including the identification of bonding interactions, ionicity vs covalency of bonds, and an estimate about the strength of interactions. A topological analysis of the static electron density has been performed at the Laboratory of Crystallography of the University of Bayreuth according to Baders' quantum theory of atoms in molecules. The quantum theory of atoms in molecules defines a bond critical point (BCP) as the point of minimum density along the bond path between two atoms (saddle point of the electron density). Similarly, ring critical points (RCPs) characterize closed paths of bonded atoms. Bonding interactions require the presence of a BCP and/or RCP, and values of the density and its Laplacian at BCPs and RCPs correlate with properties of chemical bonds. The present experimental static electron density data reveal BCPs for all bonds as well as RCPs for three-center (3c) and polycenter bonds (Figs. 3.7-4, 3.7-5). The arrangement of BCPs and RCPs (Figs. 3.7-4, 3.7-5) is in agreement with the following interpretation of bonding in γ-B: Covalent polycenter bonds exist on the B_{12} clusters. Neighbouring clusters are bonded to each other by two-electron two-center (2e2c) and electron-deficient, one electron two center (1e2c) bonds. Strong 2e2c bonds exist within the B_2 dumbbells and between the dumbbell and icosahedral groups. Finally, a unique polar-covalent two-electron three-center (2e3c) bond has been identified between a pair of atoms of one B_{12} group and one atom of the dumbbell. It is proposed that the charge transfer originates in this peculiar 2e3c bond, to which the three boron atoms contribute unequal amounts of electrons.

The present results explain why boron and boron-rich compounds containing quasimolecular icosahedral B_{12} clusters acquire physical properties unusual for molecular solids. While these clusters geometrically mimic molecules, intericosahedral chemical bonds are of equal or even higher strength than intraicosahedral bonds, and the structures of boron and boron-rich compounds are controlled by individual two- and three-center bonds between boron atoms.

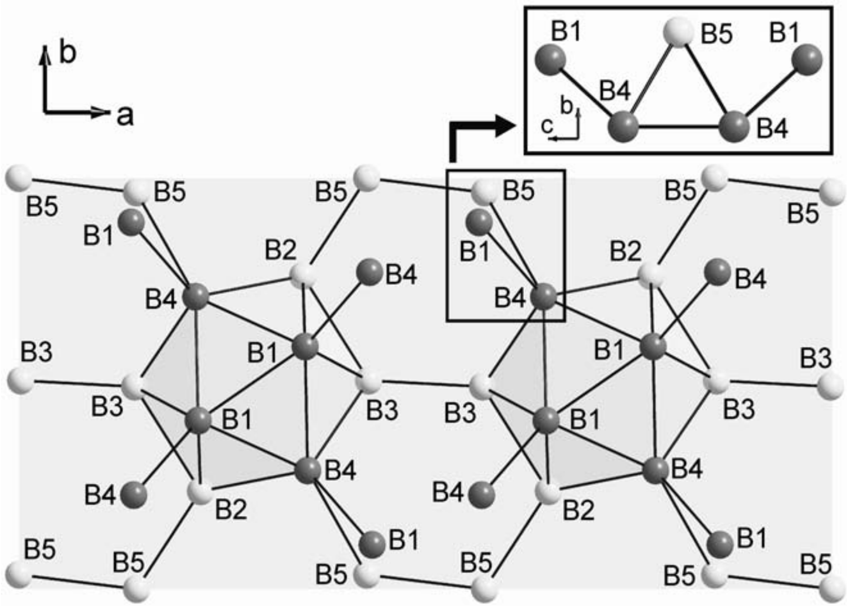

Fig. 3.7-4: Perspective view of the structure of γ-B_{28}. Atoms B2, B3, and B5 are on the crystallographic mirror plane. Atoms B1–B4 form the B_{12} group; atom B5 forms the dumbbell. The box shows the B1-B4-B5-B4-B1 region, perpendicular to the mirror plane.

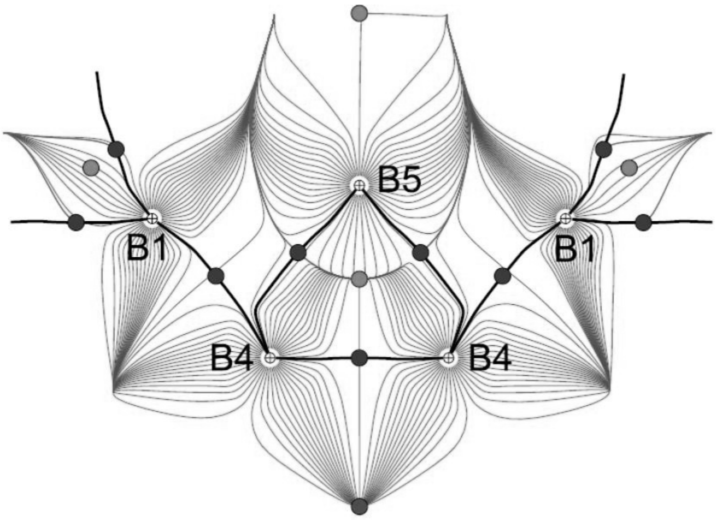

Fig. 3.7-5: Gradient trajectories of the electron density in the high-pressure γ-B phase of boron with different critical points indicated.

d. *The crystal structure of β-rhombohedral boron doped by aluminium (E. Bykova, G. Parakhonskiy, N. Dubrovinskaia and L. Dubrovinsky; D. Chernyshov/Grenoble)*

Boron compounds are widely used as engineering materials (dielectrics, B-doped semiconductors), superhard materials (cBN, boron carbide), reinforcing chemical additives (*e.g.*, for obtaining special glasses and corrosion- or heat-resistant alloys), and superconducting materials (*e.g.*, MgB_2). Two crystalline modifications of pure boron are stable at ambient pressure, namely α-boron and β-boron, and numerous boron-rich compounds are based on these structures. The structure of rhombohedral β-B contains numerous voids of various sizes that can accept different dopants, for example, main group elements (Li, Mg, Al, Si, Ge) and transition metals (Cr, Cu, Fe, Mn, Ni, Sc, V, Zn, Zr). Doping of β-B by transition metals and some other elements, such as Al, Si and Ge, has been shown to increase the micro-hardness of β-B and change its electrical properties.

Here we present results of single crystal X-ray diffraction study of β-B doped by Al. The synthesis experiment was carried out at 3 GPa and 2100 K in a piston-cylinder apparatus. Upon heating, the Pt capsule melted and boron reacted with a corundum thermal insulating sleeve to form aluminium boride. Single-crystal X-ray diffraction data were collected at 80 K using a six-circle Kuma diffractometer (λ = 0.6953Å) equipped with a Titan CCD detector at the Swiss-Norwegian beam line BM01A at ESRF.

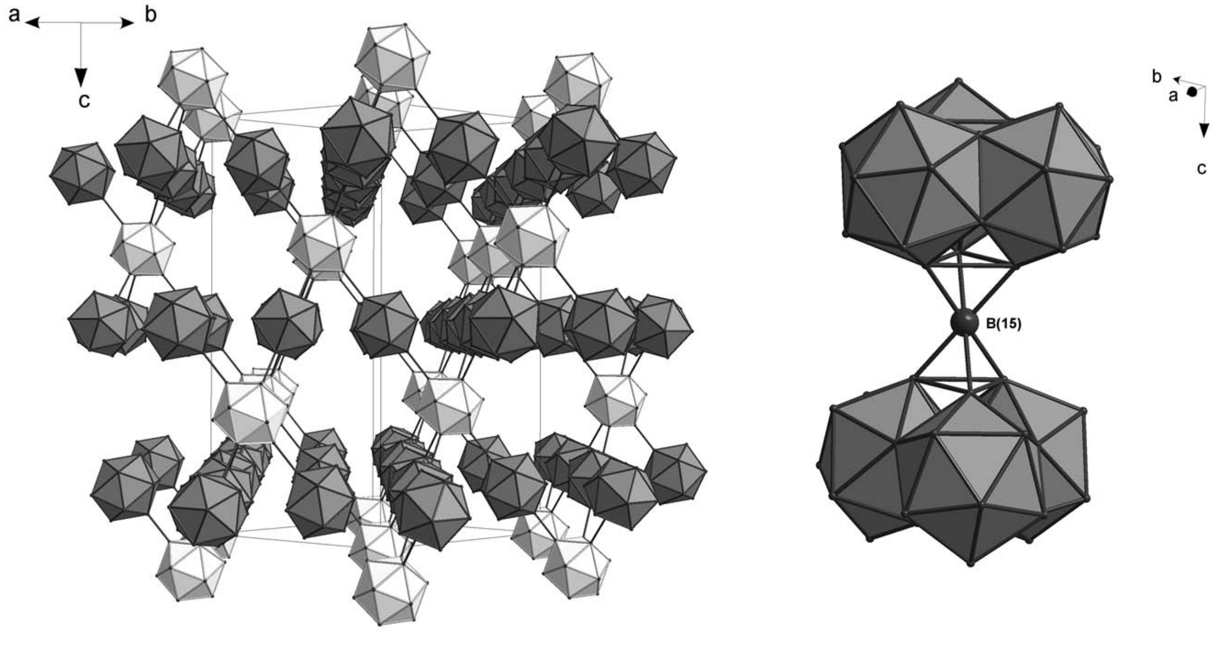

Fig. 3.7-6: "Porous" three-dimensional framework consisting of B_{12} icosahedra is a part of the aluminium boride crystal structure. The framework contains different types of voids and includes interstitial B and Al atoms (not shown) as well as bulky B_{57} units. Each B_{57} unit includes two B_{28} units connected via boron linker marked as B(15). Each B_{28} unit consists of three B_{12} icosahedra that are connected by sharing triangular faces.

The compound crystallized in the *R*3(-)*m* space group with the following unit cell parameters (hexagonal symmetry): *a* = 10.9014(3) Å, *c* = 23.7225(7) Å. The crystal structure consists of B_{12} icosahedra linked together in a "porous" three-dimensional framework shown in Fig. 3.7-6 (left). The framework contains bulky B_{57} units and includes in its voids interstitial B and Al atoms. Figure 3.7-6 (right) shows that each B_{57} unit consists of two B_{28} units connected via a boron linker (marked in the figure as B(15)). Aluminium atoms occupy two different positions in the structure. One Al atom is located inside a tetrahedron formed by four B_{12} icosahedra that are part of the three-dimensional framework. Six aluminium atoms of the second type as well as 12 interstitial boron atoms surround the B(15) atom in a B_{28}–B–B_{28} unit as shown in Fig. 3.7-7. Occupancies of aluminium atoms in the two sites are estimated to be 82.7(6) % and 11.3(4) % respectively. The final composition based on the crystal structure refinement is $AlB_{45.8(5)}$ which is in good agreement with the chemical analysis data obtained from microprobe analysis. Compared with results previously reported for AlB_{31}, we have documented a different distribution of aluminium and boron atoms near B(15). A comparable atomic arrangement has been reported previously for the crystal structure of $SiB_{30.17}C_{0.35}$.

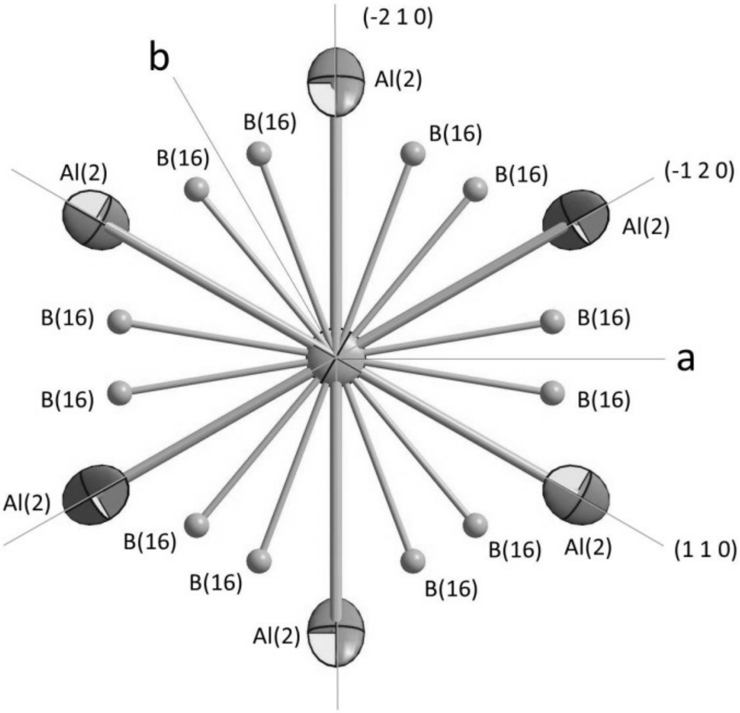

Fig. 3.7-7: Atomic distribution near the B(15) (non-labelled atom in the center of the figure) unit shown along the *c* axis. Anisotropic displacement ellipses for Al(2) and B(15) are shown with 50 % probability level. Unfortunately, attempts to refine B(16) in anisotropic approximation failed, most likely due to the low occupancy of the position (10.6(7) %). The mirror plane with Miller indices (1 1 0) and related to it (-1 2 0) and (-2 1 0) generated by the 3-fold rotation-inversion axis parallel to the *c* axis splits the position of B(16) over two sites.

e. *Melting curve of gold up to 50 GPa (L. Dubrovinsky and N. Dubrovinskaia)*

Laser heating in diamond anvil cells is a common technique to achieve simultaneous high-pressure and high-temperature (HP-HT) conditions on a sample. This powerful method enables extreme conditions to be produced that are comparable to those of the Earth's deep interior, *i.e.*, pressures above 300 GPa and temperatures exceeding 3500 K. The possibility to increase temperature up to melting point of a sample under static high-pressure conditions is of interdisciplinary interest and may provide crucial information for geosciences, solid state physics and chemistry communities. However, melting curves reported by different groups for the same materials are often extremely controversial.

The melting in DAC experiments can be detected through optical observations, or by collecting diffraction patterns or X-ray absorption or Raman spectra. All these methods are associated with specific problems, which can lead to ambiguities in detecting a modification in the state of the material under investigation. For instance, optical observations are based on subjective interpretations of the observer and in many cases only optically visible changes at the sample surface (for example re-crystallization) can be recognized. The identification of melting using X-ray diffraction is in general possible at high-brilliance synchrotron facilities that are suitably equipped. Melting is detected from diffraction data either by the disappearance of Bragg intensities and/or by the appearance of diffuse scattering due to the short-range order in the liquid. In both cases the melt has to be stable for a specific time period and complications can potentially arise due to chemical reactions with the pressure medium or the diamond anvils. Melting detection by X-ray absorption also requires synchrotron radiation facilities and involves the same potential problems as mentioned for X-ray diffraction experiments. Here we present a method for the immediate detection of a melting event through visual observation in laser-heated diamond anvil cells and demonstrate its experimental application through the melting of gold.

Laser heating in our experiments was realized using the portable laser-heating system for diamond anvil cells designed and constructed at BGI. The main parts of the system are the SPI 100 fiber laser (100 W, 1064 nm, pulsed or continuous (CW) mode) and the latest version of the universal laser-heating head (UniHead). For the temperature measurement we employed multi-wavelength spectroradiometry. Thermal emission spectra were collected during laser heating with exposures of 0.008 to 1 second and a repetition rate of 0.1 to 100 Hz in different experiments. The typical uncertainty in the fitting procedure is within 10 K. In order to calibrate the system we melted 10, 15 and 20 µm thick Pt foils at ambient pressure. The foils were heated from one side by a gradual increase of the laser power, while radiation spectra were collected from the opposite side until the metal melted and a hole formed. The melting temperature measured this way was not dependent on the thickness of the foil. However, if temperature was measured from the side on which the foil was heated, the temperature of hole formation (melting) depends on the thickness of the metal and is overestimated by 150 K (for 10 µm thick foil) to 300 K (for 25 µm thick foil). Consequently, in all melting experiments described below we report temperatures measured from the side opposite to that heated by the laser.

One of the most difficult problems in melting experiments in the DAC lies in detecting exactly the beginning of a melting event. We noticed that in absence of phase transitions and chemical reaction the shape of the solid sample upon heating does not change significantly. However, upon melting either the whole sample (when small), or at least some part of it, undergoes a drastic change that involves the rounding of surfaces and the formation of one or more spherical drops (Fig. 3.7-8). The formation of drops during melting in the laser-heated DAC has been reported previously, but there has been no systematic use of this phenomenon for determining melting temperatures at high pressure. We found that for gold a stepwise increase of the laser power at fixed "cold pressure" (*i.e.*, that measured at ambient temperature) allows the temperature at which drops form (*i.e.*, melting) rather precisely (~ 50 K uncertainty resulting from stepwise changes in laser power).

Figure 3.7-9 shows our experimental results for gold compared to melting curves reported by Errandonea (2010) based on experiments in large-volume apparatus at pressures up to about 6 GPa. We found that Simon equation proposed for gold by Errandonea (2010) described our data as well.

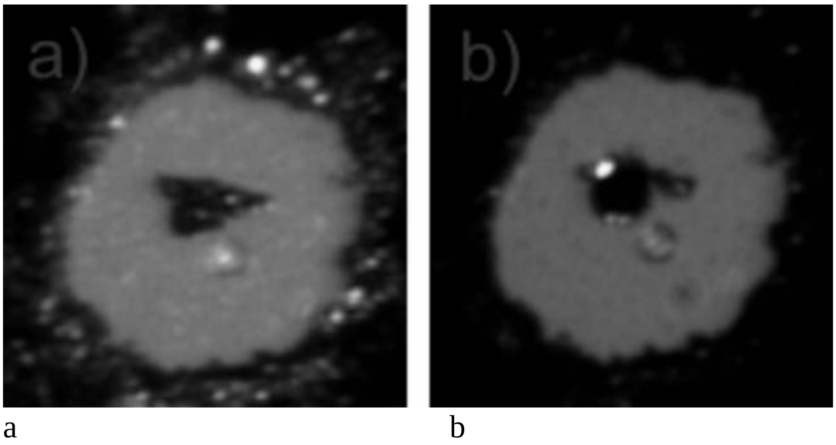

Fig. 3.7-8: A sample of gold after heating at 33(1) GPa and 2510 (25) K (a) and after melting at 34(1) GPa and 2590(25) K (b).

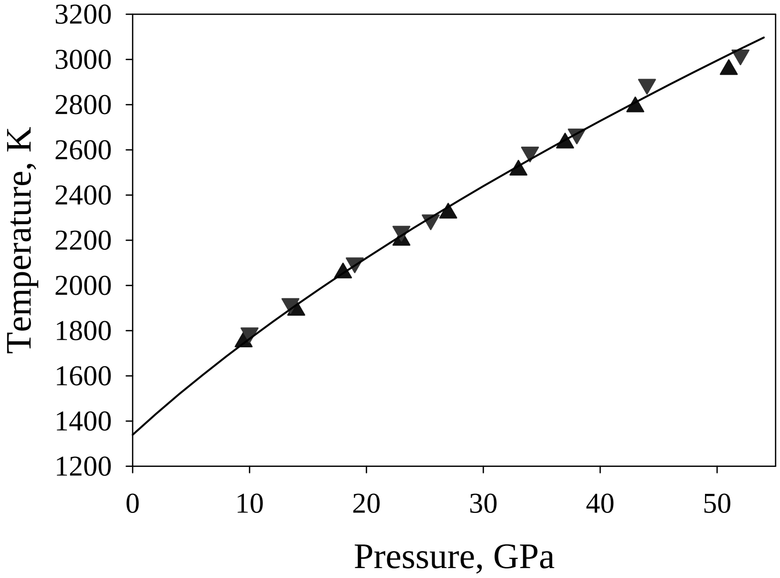

Fig. 3.7-9: Melting curves of gold: our present data (triangles = solid gold, inverse triangles = liquid gold). Melting temperatures were based on the formation of spherical drops.

f. *Synthesis and theoretical investigation of Re_2C (H. Gou, N. Dubrovinskaia, L. Dubrovinsky and S. Ovsyannikov)*

The study of transition metal carbides is of great interest due to their fascinating physical properties, *e.g.*, high melting temperatures and exceptional mechanical properties, high wear and chemical resistance.

The limited solubility of carbon in rhenium makes it difficult to obtain rhenium carbide with a high carbon concentration at ambient pressure. Synthesis of rhenium carbide, ReC, with γ'-MoC-type and NaCl-type structures at high pressure and high temperature has been reported in literature. However, first-principles calculations suggest that these two phases might be unstable. A hexagonal rhenium carbide phase, Re_2C, was observed in other high-pressure experiments, but the synthesis conditions and the location of carbon in this hexagonal structure are in dispute.

We have performed synthesis experiments using the 6-8-type multianvil Sumitomo 1200 t press at 20 GPa and 1973 K. High-purity rhenium and graphite mixed in 1:1 molar ratio were used as staring materials and were loaded into a rhenium capsule. $LaCrO_3$ heaters were used. In three different experiments, the target temperature was maintained for 10, 35, and 100 minutes. X-ray powder diffraction data were obtained for each sample using a high-brilliance Rigaku diffractometer (Mo Kα radiation) equipped with Osmic focusing X-ray optics and a Bruker Apex CCD detector. The structural searches for rhenium carbides were performed employing the code CALYPSO, and the structural optimization, as well as calculation of elastic and electronic properties for Re_2C phases, was based on the density functional theory (DFT). The exchange and correlation function was treated by the Perdew-Burke-Ernzerhof parametrization of Generalized Gradient Approximation (GGA-PBE).

We successfully synthesized rhenium carbide, Re_2C in all high-pressure experiments. The X-ray diffraction (XRD) pattern of Re_2C (Fig. 3.7-10a) confirms its previously proposed hexagonal structure, but determining the location of carbon atoms from powder diffraction data is difficult. Using the structure searching technique, we predicted a low-energy structure of the anti-ReB_2-type for Re_2C and found that its calculated XRD patt-ern is in good agreement with the experimental one (Fig. 3.7-10a). The bulk modulus of Re_2C with the anti-ReB_2-type structure is predicted to be 400 GPa which agrees well with previously reported experimental data (405 GPa). Calculations of linear compressibility (Fig. 3.7-10b) show that along the *c* axis the hexagonal Re_2C is even less compressible than diamond. Calculated values of the heat of formation indicate that hexagonal Re_2C is more stable than ReC and Re_2C+C both at ambient conditions and at pressures up to 50 GPa. This agrees with our experimental observations on at 20 GPa and 1973 K.

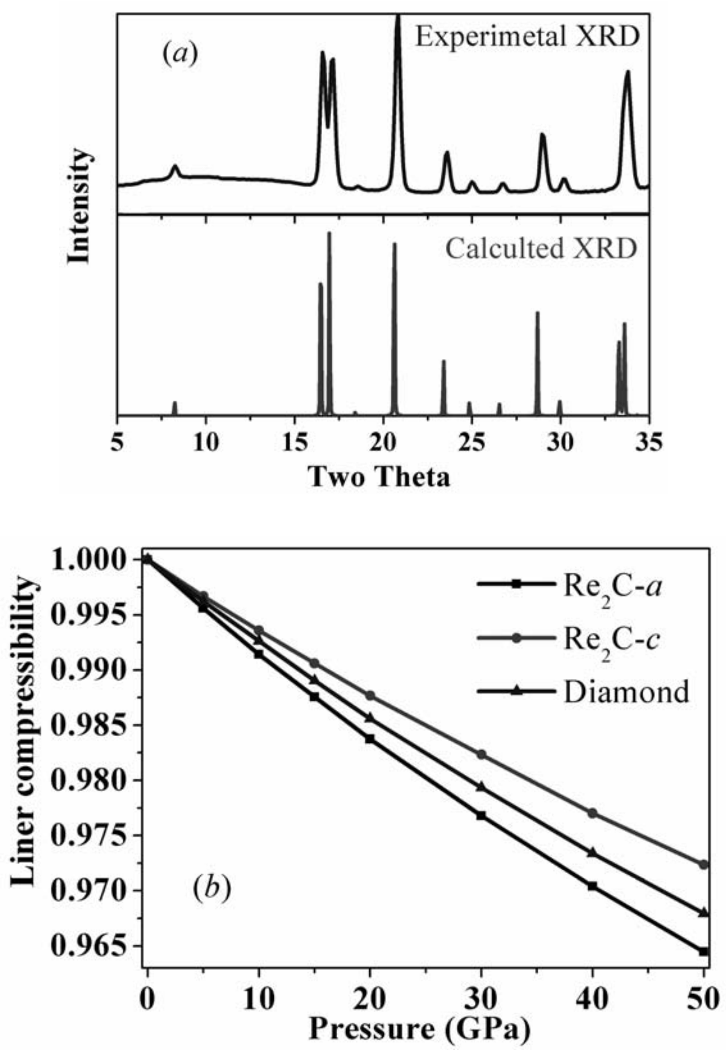

Fig. 3.7-10: The X-ray diffraction pattern of Re_2C compared with the calculated one (a), and the calculated linear compressibility of the hexagonal Re_2C at pressures up to 50 GPa (b) (*c* and *a* designate the crystallographic directions along which the linear compressibility was calculated).

g. *HP-HT synthesis of single crystals with the corundum lattice: Cases of Cr_2O_3 and Ga_2O_3 (S.V. Ovsyannikov and L. Dubrovinsky)*

Sesquioxides M_2O_3 (M = Al, Fe, Ti, Cr, Ga, etc.) are of considerable interest in mineral and condensed matter physics, solid state chemistry, and industry. At ambient conditions many of tese oxides adopt a corundum lattice ($R\bar{3}c$ space group, #167). In this work, by means of HP-HT synthesis we obtained corundum-structured single-crystals of Cr_2O_3 and Ga_2O_3 and have investigated their properties. At ambient conditions, Cr_2O_3 adopts the corundum structure while stable β-Ga_2O_3 has a monoclinic structure (space group *C2*/*m*). Under pressure a very sluggish and irreversible transition in Ga_2O_3 to the corundum structure has been reported to start above 6 GPa and to reach completion at 35-40 GPa.

HP-HT synthesis was conducted in a 1200-tonne multianvil press at BGI. For the synthesis we used commercial Cr_2O_3 (99.999 % purity) powder from Johnson Matthey Alfa Products and Ga_2O_3 (99.99 % purity) from Alfa Produkte. The conditions of the syntheses were as follows: Cr_2O_3 - 21 ± 1 GPa and 1950 ± 50 °C for 3 hours and Ga_2O_3 - 21 ± 1 GPa and 1600 ± 50 °C for 3.5 hours. The synthesized samples were aggregates of single-crystal of 20 to 200 μm in diameter (Fig. 3.7-11). The chemical compositions of the products were verified by Scanning Electron Microscopy (SEM) and electron microprobe analysis. In addition, the samples were examined by Raman and X-ray diffraction (XRD).

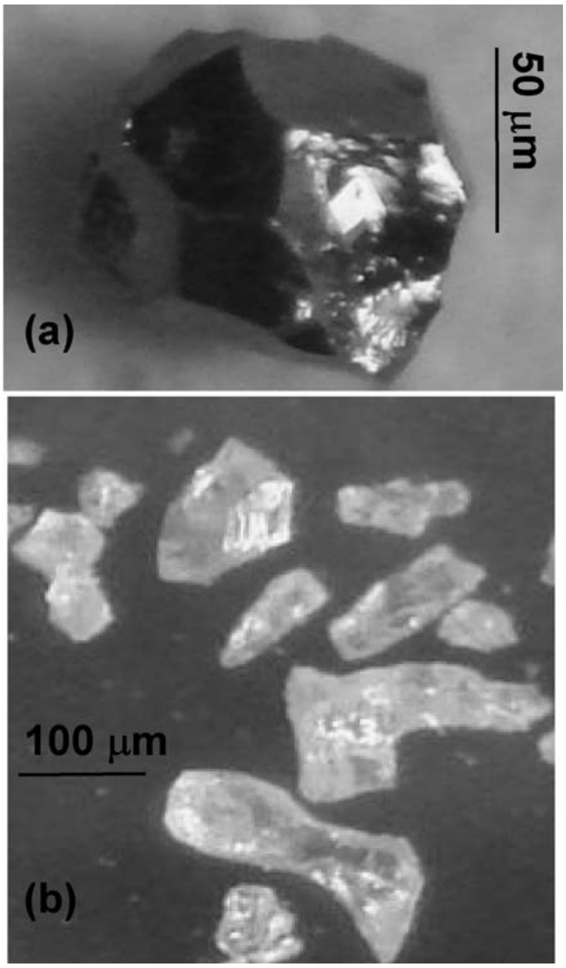

Fig. 3.7-11: Photographs of single-crystal corundum-structured Cr_2O_3 (above) and Ga_2O_3 (below).

Cr_2O_3. After the HP-HT synthesis, green Cr_2O_3 powder was converted into black single crystals (Fig. 3.7-11). XRD and Raman spectroscopy studies of the synthesized material show that it has the same corundum structure and Raman spectrum as the starting material. We performed a single-crystal X-ray diffraction study and determined unit cell parameters and atomic coordinates as follows: a = 4.9530 Å and c = 13.5884 Å (c/a = 2.7434), Cr (12 c): 0, 0, 0.3475, O (18 c): 0.3058, 0, 0.25, *i.e.*, almost identical to those in the literature. Therefore, we rule out the hypothesis of the existence of a stable ‘distorted’ $R\bar{3}c$ –Cr_2O_3 phase above 13-15 GPa that was based only on changes in Raman spectra.

Ga_2O_3. The gallium oxide powder that we used as the starting material has monoclinic symmetry (β-Ga_2O_3) with unit cell parameters as follows: a = 12.2164 Å, b = 3.0379 Å, c = 5.8098 Å, β = 103.64°, V = 209.54 Å^3, Z = 4. A Raman spectrum of β-Ga_2O_3 agreed well with previous reports. After the HP-HT treatment, Ga_2O_3 became transparent and completely transformed into a phase with the corundum structure (α-Ga_2O_3) with lattice parameters as follows: a = 4.9514 Å, c = 13.3903 Å (c/a = 2.7043), V = 284.30 Å^3. The volume decrease at the phase transition is ~ 9.5 %.

h. *In situ* Raman spectroscopic study of pressure-induced structural changes in the ammonia borane complex (I. Kupenko, L. Dubrovinsky and N. Dubrovinskaia)

The ammonia borane complex, BH_3NH_3 (**AB**), is a promising candidate for hydrogen storage due to its remarkably high gravimetric (19.6 wt.% H) and volumetric (145 g liter^{-1}) hydrogen content. At ambient conditions **AB** is a soft white powder. It crystallizes with a tetragonal structure (space group *I4mm*) with disordered hydrogen. Numerous investigations were made to examine the high-pressure behaviour of **AB**, but the results are still controversial. Our study aimed to improve the understanding of high-pressure phase transitions of **AB** that could be useful in the design of hydrogen storage based on this complex. The investigation was performed by *in situ* Raman spectroscopy in a diamond anvil cell and also by studying nonlinear optical properties of **AB**, such as second harmonic generation (SHG) of laser light.

Commercially available crystalline **AB** powder was purchased from Sigma Aldrich. High-pressure measurements were carried out using cells with diamonds having 250 µm culets. A Re gasket 200 µm thick was pre-indented to 30 µm thickness and 125 µm hole was drilled in the centre. Samples were loaded at room temperature and 1.2 kbar with Ne or He as the pressure medium. A few ruby crystals were used as a pressure calibrant and were placed inside the pressure chamber. Raman spectroscopy was performed by exciting Raman modes using a 514.5 nm Ar^+ ion laser (Coherent Innova 300). Generation of second harmonica (λ=535.44 nm) was achieved using the Nd^{3+}:YAG (λ= 1071nm) SPI laser light with a power from 5 to 30W.

Raman vibrational spectra of **AB** were measured as a function of pressure from 0.8 to 64 GPa (Fig. 3.7-12). Modes at 0.8 GPa could be assigned using factor group analysis and are in good agreement with previous studies. We did not focus on the well establish transformation at about 1 GPa (Tr. I). Based on the analyses of the behaviour of Raman modes found in our measurements we report two phase transitions above 2 GPa in **AB** - at around 12 GPa (Tr. II) and 27 GPa (Tr. III). The clear manifestation of Tr. II is splitting at 11.8 GPa of LM1 and ^{11}B-N stretching mode into two modes. Despite the splitting of the low frequency asymmetric B-H bending and asymmetric N-H stretching modes are clearly seen only at 16.5 GPa, the broadening and asymmetry of the corresponding peaks is already visible at 11.8 GPa. The asymmetric N-H bending mode, on the contrary, merges from a doublet to a singlet at 11.8 GPa. The high frequency B-H and N-H rocking deformation mode merges from a triplet to a doublet also at 11.8 GPa.

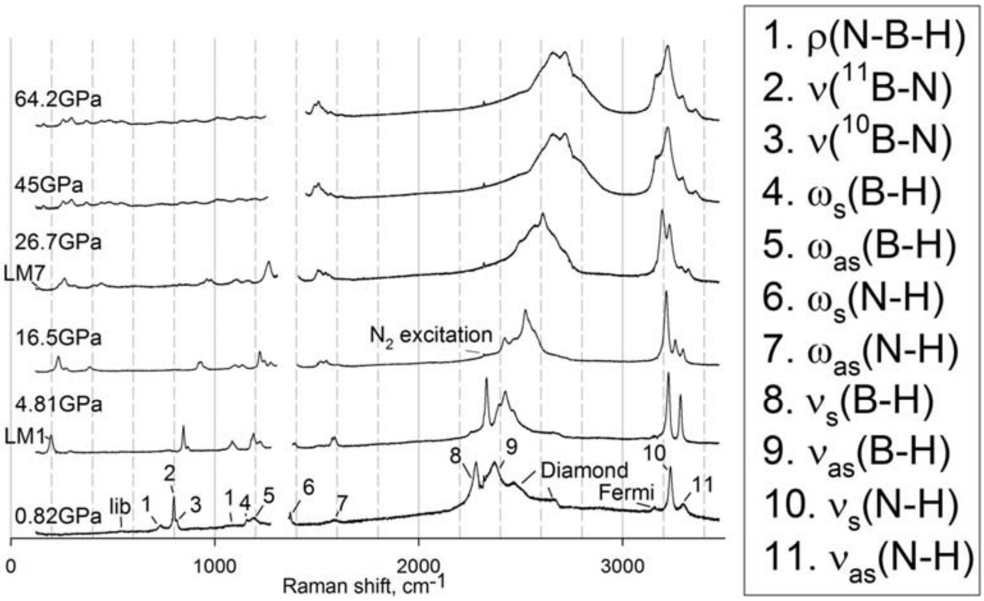

Fig. 3.7-12: Raman spectra of BH_3NH_3 compressed in Ne pressure transmitting medium.

Significant changes are seen in Raman spectra at approximately 27 GPa. First, further splitting of LM1 is obvious, and the splitting of the low frequency B-H and N-H rocking deformation modes appears. The new lattice mode LM7 appears at 27 GPa. The splitting of the high frequency asymmetric N-H stretching mode is also observed.

Upon further compression all **AB** Raman modes are blue shifting except symmetric and low frequency asymmetric N-H stretching modes that are red shifting in all pressure intervals studied. Such behaviour of the modes indicates further strengthening of the B-H···H-N dihydrogen bonding at higher pressures.

There are difficulties of X-ray studies of crystal structure of **AB** at high pressure due to the low scattering power of elements forming ammonia borane. Consequently, structural data on **AB** at pressures above 27 GPa are lacking. Any additional/complimentary information about symmetry of high-pressure phase(s) is thus valuable. It is well-known that SHG may be acquired only in anisotropic media without inversion symmetry. We have demonstrated that **AB** shows a SHG effect up to 130 GPa. Thus we are able to definitely conclude that, regardless of pressure ranges and structural changes, **AB** persists as a non centre symmetry structure at least to 130 GPa.

i. *High-pressure ^{13}C-diamond-forming reaction during the decomposition of $Na_2{}^{13}CO_3$ melt at 20-60 GPa (N.A. Solopova, A.V. Spivak and Yu.A. Litvin/Chernogolovka, I. Kupenko and L. Dubrovinsky)*

Understanding the behaviour of carbonates at high pressures and temperatures is important for both Earth and material sciences. Micro- and nano-inclusions of carbonates (nyerereite

$Na_2Ca(CO_3)_2$ and nahcolite $NaHCO_3$, in particular) were found in inclusions in super-deep diamonds from the Juina area (Brazil), and constraints on the phase stability of sodium carbonate can therefore provide information on the conditions of diamond formation. Diamond growth from carbonates and the application of carbonates for synthesizing diamond-based hard composites are the focus of attention in the material sciences. So far, information on the stability of Na_2CO_3 at high pressures is very limited.

We have studied the high-pressure, high-temperature behaviour of sodium carbonate, Na_2CO_3, using laser-heated diamond anvil cells. The starting material was pure $Na_2{}^{13}CO_3$ mixed with platinum powder in the volume ratio ~ 20:1. The mixture was loaded into the high-pressure chamber between two layers of pure $Na_2{}^{13}CO_3$. Platinum powder acts as an absorber of the NIR laser light. Re gaskets of 200 µm thickness were pre-indented to about 30 µm, then holes of about 130 µm in diameter were drilled in the gasket centres. The samples were compressed between diamond anvils with 250-µm culets at room temperature to pressures between 20 and 60 GPa. Ruby chips placed inside the pressure chamber were used as pressure calibrants. After quenching, the samples were studied by Raman spectroscopy using a Dilor XY Raman spectrometer and an Ar^+ ion laser (514.5 nm, Coherent Innova 300). Using ${}^{13}C$-carbonate we can unambiguously distinguish carbon phases produced in the course of the experiments as the result of decomposition of carbonate and thus avoid possible artefacts due to contribution of ${}^{12}C$ from the diamond anvils.

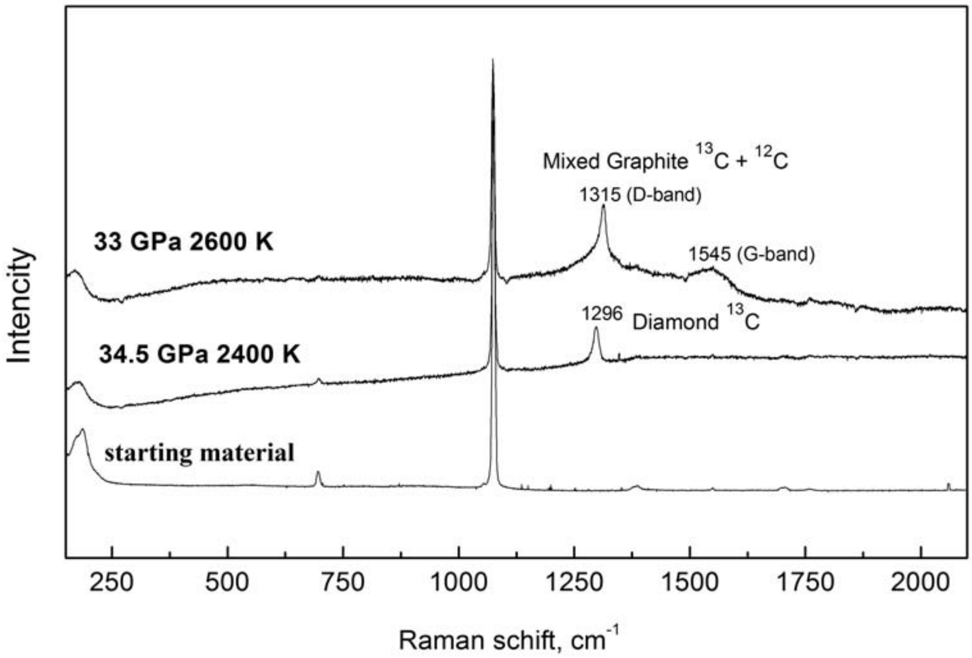

Fig. 3.7-13: Selected Raman spectra of $Na_2{}^{13}CO_3$ as the starting material and after compression and heating.

Raman spectra collected after treatment of the sodium carbonate $Na_2{}^{13}CO_3$ at different pressures and temperatures are presented in Fig. 3.7-13. Formation of ${}^{13}C$-diamond is obvious after heating the sodium carbonate at ~ 35 GPa and 2400 K (Fig. 3.7-13). In the sample heated at 33 GPa and 2600 K we found a broad G-band at 1545 cm^{-1} (graphite) and a sharp band at 1315 cm^{-1} (diamond). These bands correspond to a mixture of graphite and diamond with an isotopic ^{13}C:^{12}C ratio of ~ 1:1. In some of our experiments we observed formation of cavities on the anvil surfaces after laser heating (Fig. 3.7-14). Such observations suggest that sodium carbonate melt can readily dissolve diamond. Further studies are needed in order to establish the melting curve of sodium carbonate and it decomposition boundary.

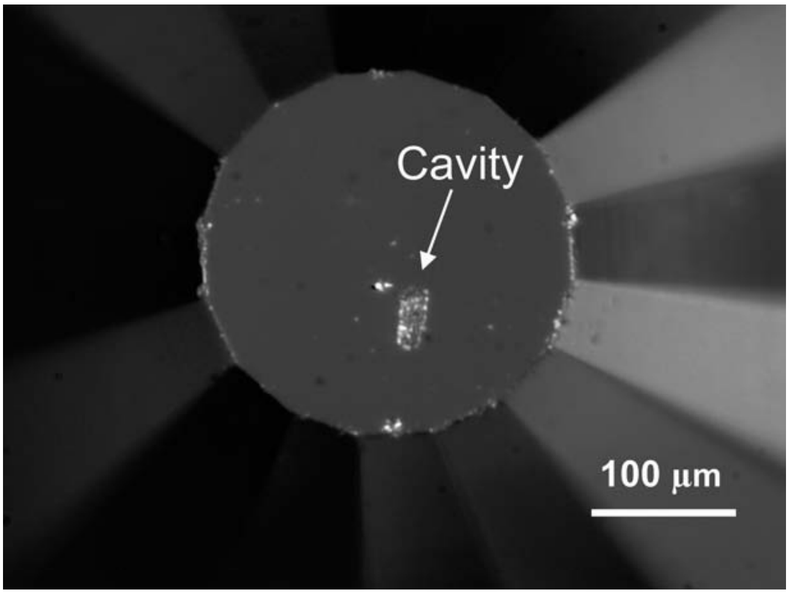

Fig. 3.7-14: Formation of a cavity on the diamond anvil surface after laser heating.

j. *Structural phase transition in RbFe(MoO$_4$)$_2$ at high pressure (D.P. Kozlenko and N.T. Dang/Dubna, A.I. Smirnov/Moscow, L.S. Dubrovinsky)*

Multiferroic materials exhibit the coupling of electric and magnetic properties which provides possibilities for controlling magnetic properties by an electric field and visa versa. Such possibilities are important for the development of new electronic devices and multiferroics are therefore at the focus of scientific research in condensed matter physics. Recently a novel class of multiferroics, in which the symmetry arrangement of ordered magnetic moments breaks the inversion symmetry and allows ferroelectricity, was discovered. The $MFe(MoO_4)_2$ (M = Rb, K) compounds represent unique examples of such materials, exhibiting multiferroic phenomena in combination with geometrically frustrated magnetism on a triangular lattice.

At ambient conditions, $RbFe(MoO_4)_2$ exhibits the trigonal structure of the P3(-)m1 symmetry. Recently amorphization of this material at a pressure of ~ 5 GPa was reported. However, for $KFe(MoO_4)_2$ amorphization at high pressure has not been observed. In order to clarify the nature of the structural response of $RbFe(MoO_4)_2$ at high pressure, X-ray diffraction (XRD) measurements have been performed up to 10 GPa.

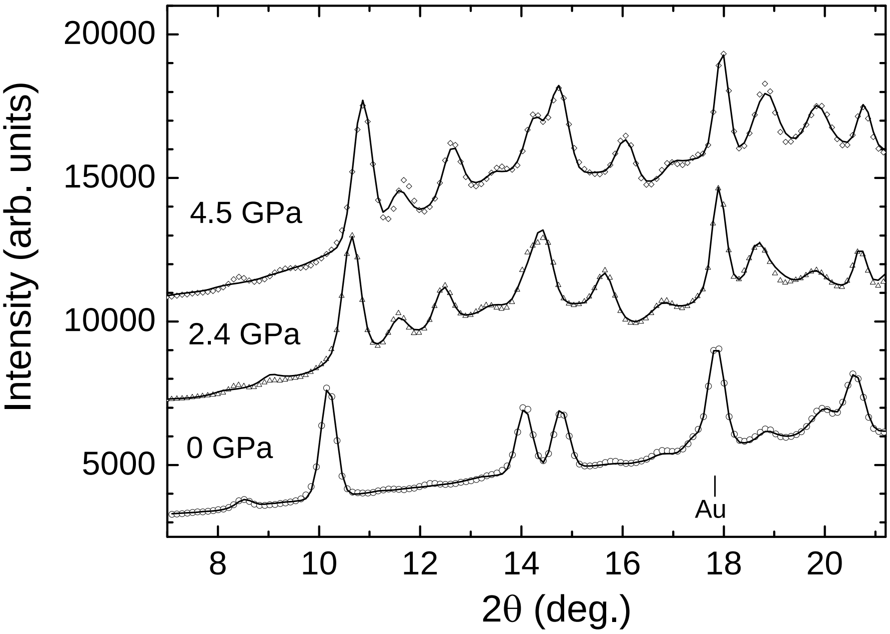

Fig. 3.7-15: X-ray diffraction patterns of $RbFe(MoO_4)_2$ measured at selected pressures and room temperature and processed by the Fullprof program in profile matching mode. The experimental points and calculated profiles are shown. The diffraction peak from Au, which was added for pressure calibration, is indicated.

At pressures above 1 GPa, the appearance of new diffraction peaks in XRD patterns was observed (Fig. 3.7-15), indicating a structural phase transition. The high-pressure diffraction data can be indexed in the monoclinic supercell with lattice parameters $a \approx 2a_{tr}$, b $\approx 2a_{tr}$, $c \approx c_{tr}$ with respect to those of the initial trigonal unit cell. The unit cell parameters values obtained at 4.5 GPa are a = 10.51(4) Å, b = 10.44(4) Å, c = 7.367(7) Å, β = 122.5(2)°. The volume compressibility data of the different phases were fitted by the third-order Birch–Murnaghan equation of state. The bulk modulus values B_0 = 15(1) GPa for the ambient pressure trigonal phase and B_0 = 38(5) GPa for the high-pressure monoclinic phase were obtained. No amorphization of $RbFe(MoO_4)_2$ was observed in the pressure range up to 10 GPa.

k. *Study of pressure-induced structural transformations in bis(glycinium)oxalate (A. Ivanova, S. Aksenov and I. Makarova/Moscow, E. Bykova, N. Dubrovinskaia and L. Dubrovinsky)*

Bis(glycinium)oxalate ($C_2H_6NO_2{\cdot}0.5C_2O_4$) is interesting from the point of view of structural chemistry, as it has a very strong O-H•••O hydrogen bond in addition to other medium-strength N-H•••O and weaker C-H•••O hydrogen bonds. High-pressure structural investigation of these crystals can offer a significant insight into the nature of weak intermolecular interactions that hold these crystals together.

The crystal structure of glycinium oxalate was refined at ambient conditions (a=4.917(1), b=9.957(1), c=10.873(1), β=97.57(0)°, $P2_1/n$, R=0.04) (Fig. 3.7-16). The asymmetric unit consists of one glycine molecule in the cationic form with a positively charged amino group and uncharged acid group. In the crystal structure, oxalic acid exists as a doubly charged oxalate ion at the inversion center of the structure. Each oxalate ion interacts with two glycinium ions.

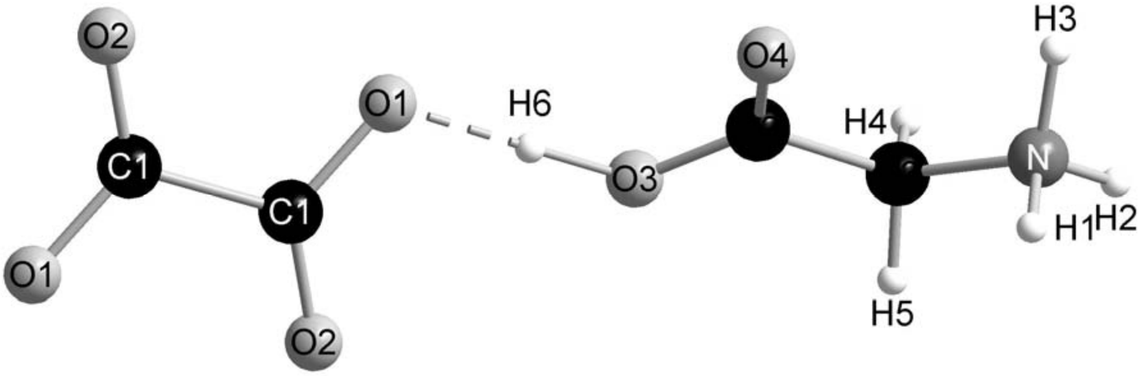

Fig. 3.7-16: Asymmetric unit of bis(glycinium)oxalate.

For high-pressure Raman spectroscopy investigations, we used a BGI-type diamond anvil cell (DAC) that incorporates 16-sided type Ia Raman low-fluorescence diamonds with culet diameters of 250 µm. A single crystal of bis(glycinium) oxalate was loaded into a of 130 µm hole drilled in a Re-gasket preindented to a thickness of 40 µm. Paraffin was used as a pressure transmitting medium. The pressure was determined by ruby fluorescence. Raman spectra (Fig. 3.7-17) were collected using the LabRam spectrometer in a back-scattering geometry with a 632.8 nm/100 mW He–Ne laser as the excitation light source.

Analysis of Raman spectra shows that the hydrogen bonding network of glycine in the environment of the oxalates is easily distorted even at pressure as low as 0.6 GPa. Several spectral features at 2-2.5 GPa, such as changes in a lattice mode, new peaks adjacent to the C-C stretching mode, splitting of the C-C torsion, appearance of the CO_2 symmetric mode, a new mode adjacent to CH_2 stretching modes, indicate transformation to a new high-pressure phase with a possible non-centrosymmetric space group. Above 4.6 GPa the appearance of a new mode in the C-N, NH3-regions and changes in the frequency of other observed Raman modes indicate another structural transformation, possibly to a disordered low symmetry phase. Above 7 GPa C=O, C-H, N-H peaks merge. At 19 GPa the appearance of a new lattice mode and new spectral features in C-C, C-N, N-H and C-H regions suggest further transformation to a disordered phase. Observed broadening of Raman modes may be due to non-hydrostatic stress at such high pressures.

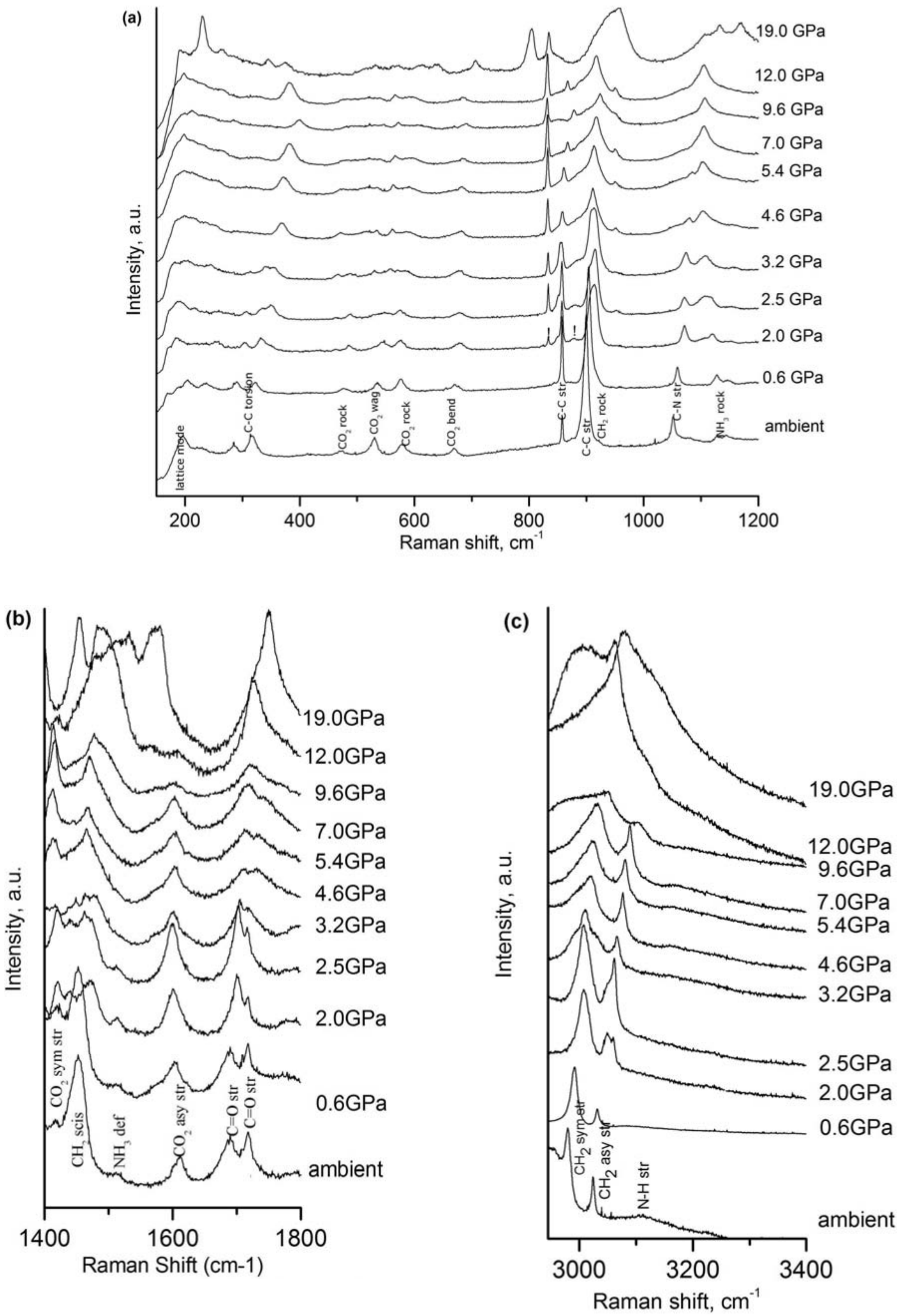

Fig. 3.7-17: Raman spectra of bis(glycinium)oxalate in the spectral region (a) 150-1200 cm^{-1}, (b) 1400-1800 cm^{-1}, (c) 2900-3400 cm^{-1}.

3.8 Methodological Developments

New developments in experimental, analytical and numerical techniques form the backbone of any scientific research. Hence their importance cannot be overemphasized. The Bayerisches Geoinstitut has a long tradition of participating at the highest level in this discipline, with many of its innovations having been adapted by labs worldwide. The design, fabrication and testing of new experimental, analytical and numerical methods is a time-consuming challenge that requires strong technical support, which is provided at the Bayerisches Geoinstitut.

In 2011, a variety of developments have been made for the experiments using multianvil apparatuses and diamond anvil cells and also for the numerical simulation. Bayerisches Geoinstitut built a 6-ram multianvil apparatus in 2009. Its installation was completed in the last year, and now the apparatus is available for scientific research, especially deformation experiment. This kind of multianvil apparatus will be also installed in FRM-II in 2012 for high-pressure neutron experiment. The year 2011 was spent to design the neutron guide for optimizing the neutron beam condition for the diffraction and imaging experiment. Another technical development was made in the high-pressure sound velocity measurement of mantle minerals.

In diamond anvil cell experiments, continuous efforts were made for establishing the *in-house* Brillouin scattering system. The heating system of the diamond anvils cell was also developed for optical spectroscopy at BGI. At ESRF, the heating system and software were developed for the synchrotron Mössbauer experiment.

The main development in geodynamic modeling is to speed up calculations by time-domain parallelization. Another development in this field is accurate simulation of advection based on the wave equation model. Continuous efforts were made to enhance calculation of convection by means of the Schur complement method.

a. *A new multianvil press employing six independently acting hydraulic rams: Concept, design and preliminary experimental applications (M.A.G.M. Manthilake, N. Walte and D.J. Frost)*

Multianvil devices are widely and routinely used to generate high-pressure and -temperature conditions up to 28 GPa and 3000 K. A number of different configurations of multianvil devices have been developed, of which the 6-8 type multianvil system and the DIA-type apparatus, are currently the most commonly used devices. As a result of the short comings noted for the 6-8 and DIA-type systems, a new six-ram multianvil system was developed by the Institute for Study of the Earth's Interior, Misasa, Japan. Here we describe a somewhat simpler system installed at the Bayerisches Geoinstitut that employs six independently acting hydraulic rams with independent oil pressurization systems. The system was principally developed as a prototype for a system that will be installed on a dedicated time-of-flight neutron diffraction beam line at FRM II.

The concept was to create a device capable of compressing an inner high-pressure chamber with 6 square faceted anvils, each of which can be advanced independently. By precisely measuring the position of each anvil, the high-pressure chamber can be adjusted under high loads to preserve or deform its inner cubic geometry. In this way, deformation experiments on cubic sample assemblies can be performed in addition to experiments employing 8 inner cube anvils for octahedral sample assemblies, which require a high level of symmetry in the distribution of force in order to prevent tensile stresses from damaging the anvils. In addition, the press was envisaged as a prototype for a device at a neutron beam line. Due to the absence of conventional guide-blocks, a large amount of angular access exists along the edges of the high-pressure cubic assemblage. In time-of-flight neutron diffraction configuration, with detectors placed at 90° to the incident beam, entering along one edge of the cubic high-pressure assembly, a large section of the arc of diffracted neutrons would be accessible.

The device comprises six 8 MN hydraulic rams approaching at right angles inside a composite steel plate frame. Six servo-controlled spindle-pumping systems maintain the pressure in each ram, and it allows the position of each anvil to be controlled individually in order to maintain the desired anvil geometry during compression and decompression, or to perform complex deformation paths. The position of each anvil is measured relative to the frame of the press using a Heidenhain linear displacement encoder positioned on the rear surface of the frame behind each hydraulic ram. The linear encoders are connected to the rear surface of each anvil by a rod, which passes through the center of each hydraulic ram. The encoders measure the position of each ram with an accuracy of 0.1 μm.

For 6-8 type experiments where an inner packet of second stage anvils is compressed, the lower ram (R1) follows an oil-pressure ramping profile, while the remaining 5 rams are controlled to maintain the position of R1, determined from the linear displacement encoders. The deviation of their relative position is less than 1 micron, and in general close to ±0.5 microns, during the entire cycle of the experiment. Due to anisotropy in the construction of the press frame, the frame expands slightly more in the horizontal compared to the vertical direction during loading. Anisotroipic frame expansion is, however, a function of the applied load, *i.e.*, R1 oil pressure, and can be corrected by calibrating the geometry of the high-pressure chamber as a function of load. After the implementation of this correction in the control software, it shows that differences in opposing anvil distances are in general less than 20 microns up to loads of 1000 tonnes.

A new heating system has been developed with the press. The exchangeable 2:1 and 10:1 step-down transformers are capable of generating a maximum of 3 KW power and are used for semiconductor and metallic furnace settings respectively. Furnace temperature can be ramped up using either power or temperature control modes through an Eurotherm temperature controller. The transformer can be connected to any ram pair, as all rams are electrically isolated from each other. We have performed heating experiments using both the

6-8 multianvil configuration and deformation configuration up to 2000 °C and 1600 °C respectively. Different furnace materials have been tested including $LaCrO_3$, graphite, Re and Pt at different pressures.

During deformation experiments, the survival rate of tungsten carbide anvils at higher press-load was not satisfactory, with anvil often damaged during instantaneous release of pressure (blow-outs), which also resulted in sever deformation of the anvil guide frame. Adopting a similar concept to the current anvil design of the D-DIA apparatus at Bayerisches Geoinstitut, we have designed new composite anvils for the multianvil 6-6 (MA6-6) configuration, which involve tungsten carbide cores embedded in hardened-steel outer casts (Fig. 3.8-1). The hardened-steel layer provides an additional strength, as well as protection for the anvil guide in the event of blow-outs thereby significantly reducing the chance of anvil-breakage.

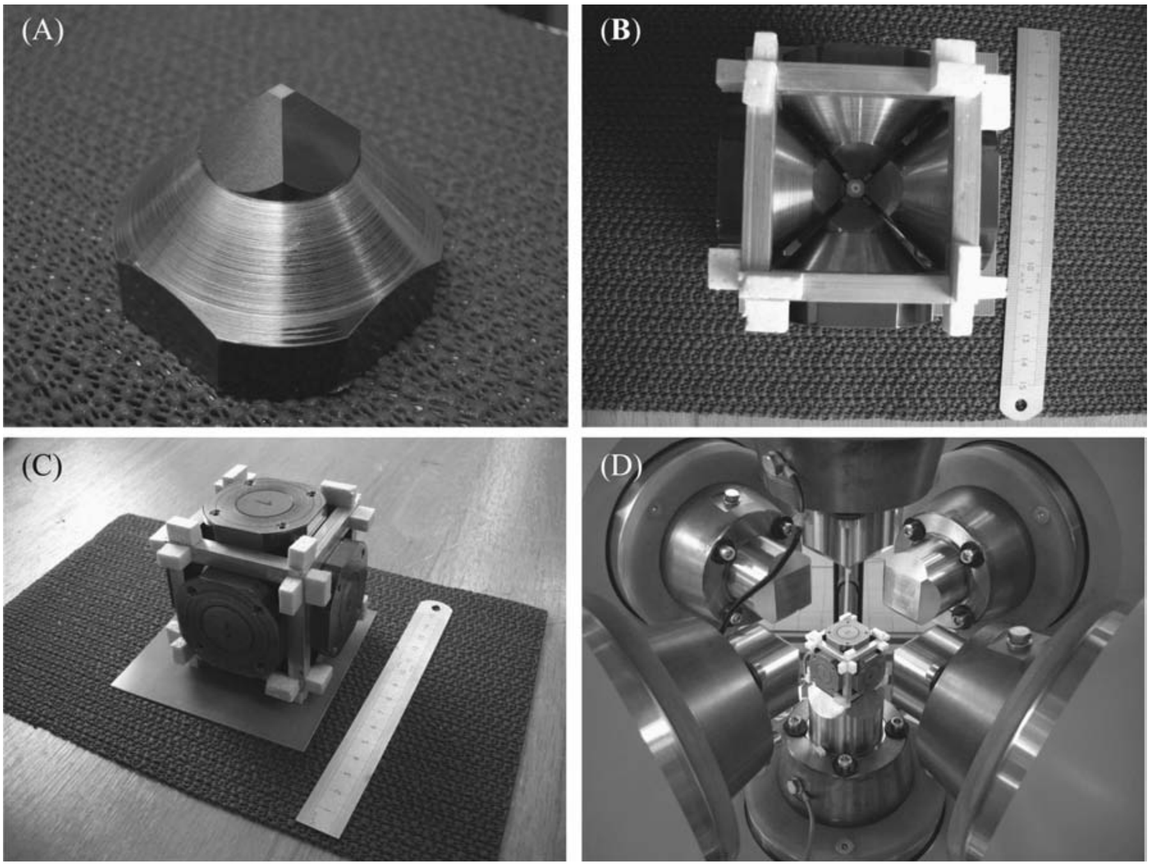

Fig. 3.8-1: New design for the multianvil 6-6 (MA6-6) configuration: (A) A new composite anvil, which involves a tungsten carbide core, embedded in a hardened-steel outer cast. (B) Anvils attached to the aluminium cage with cubic pressure media in the middle. (C) The completed cubic assemblage of 6 inner anvils inside the frame surrounding the cubic pressure medium. (D) The cubic assemblage inside the press.

Room temperature pressure calibrations have been performed for the 6-8 type multianvil configuration using 18/11 and 10/4 assemblies (octahedral edge length/anvil truncation length in mm) using the fixed-point transitions in Bi, ZnTe, ZnS, GaAs and GaP (Fig. 3.8-2). Similar pressure calibrations has been performed for the 6/2 assembly configuration using highly sintered WC cubes with 14 mm edge length (Fig. 3.8-3). The aim was to expand the currently attainable pressure range with WC cubes without loosing significant sample volume and also to gain insight of the optimal assembly configuration, which is to be used with sintered diamond cubes. Pressure generation employing the 6-6 DIA type configuration using a cubic pressure media has been investigated using 8/6, 6/4 6/3 and 5/3 (cube edge length/inner anvil square truncation edge length) configurations (Fig. 3.8-4). Considering that a combined load of only 0.8-1.5 MN (out of a pressure reserve of up to 24 MN) was sufficient to reach ~ 15.6 GPa in 6-mm assemblies, pressure generation and/or sample sizes will be significantly enhanced in the future.

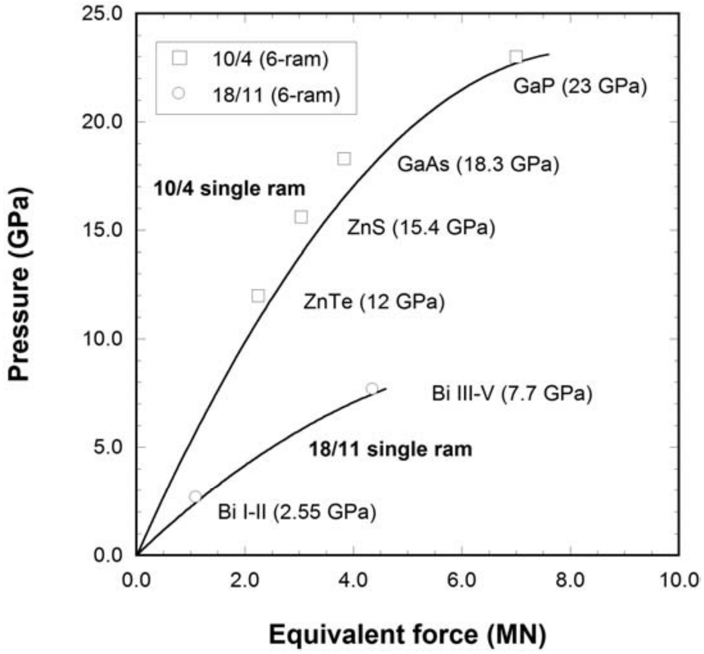

Fig. 3.8-2: Room temperature fixed-point pressure calibrations in the 6-ram press compared to those made in a conventional single-ram 6/8 multianvil. A conversion factor of $3/\sqrt{3}$ is applied to the 6-ram load to allow the different systems to be compared.

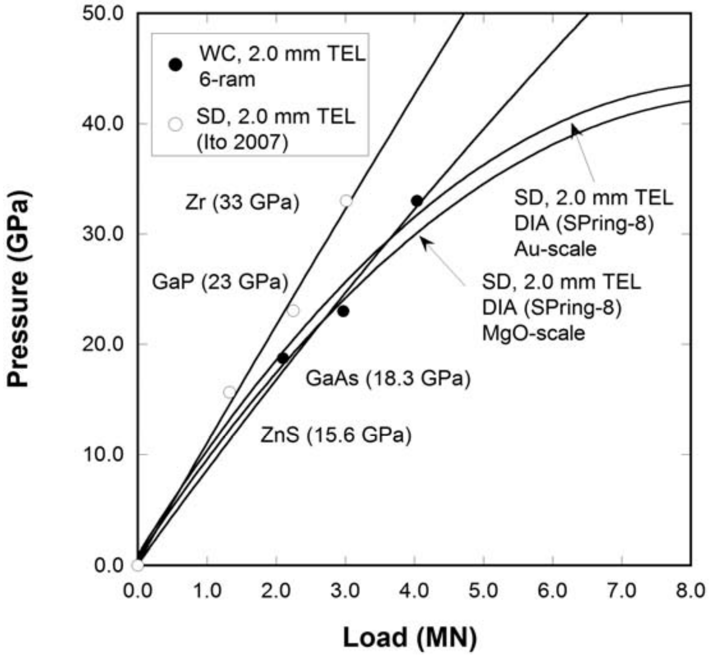

Fig. 3.8-3: Room temperature fixed-point pressure calibrations using the 6/2 assembly configuration using highly sintered WC cubes with 14 mm in the 6-ram press. Pressure calibration made in a DIA and oil reservoir type press using sintered diamond anvils are included for comparison.

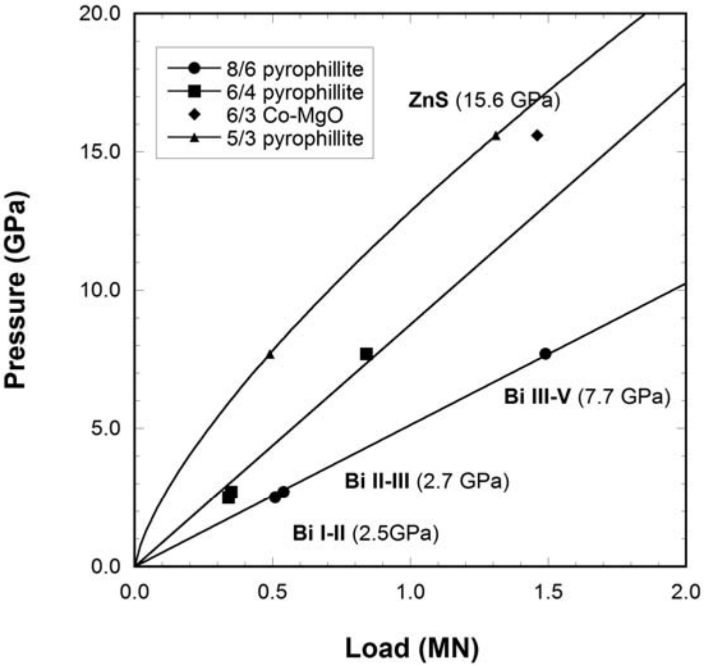

Fig. 3.8-4: Room temperature fixed-point pressure calibrations for the cubic assembly configuration.

Deformation experiments were carried out using a multianvil 6-6 (MA6-6) configuration. Preliminary deformation experiments have been performed in both simple shear and pure shear configurations using the 8/6 assembly configuration. Simple shear experiments have been performed using a pre-synthesized olivine pyroxene mixture at 3 GPa and 1200 °C at a strain rate of ~ 5.10^{-4} s^{-1} to bulk strains up to $\gamma = 1$ (Fig. 3.8-5). In both configurations, samples have been deformed manually by advancing one of the horizontal set of rams to the sample, while keeping the other set of rams at the initial pressure (Fig 3.8-6). This results in a flattening strain (axial compression) of the assembly, which is essentially identical to the strain that is imposed in a conventional D-DIA device.

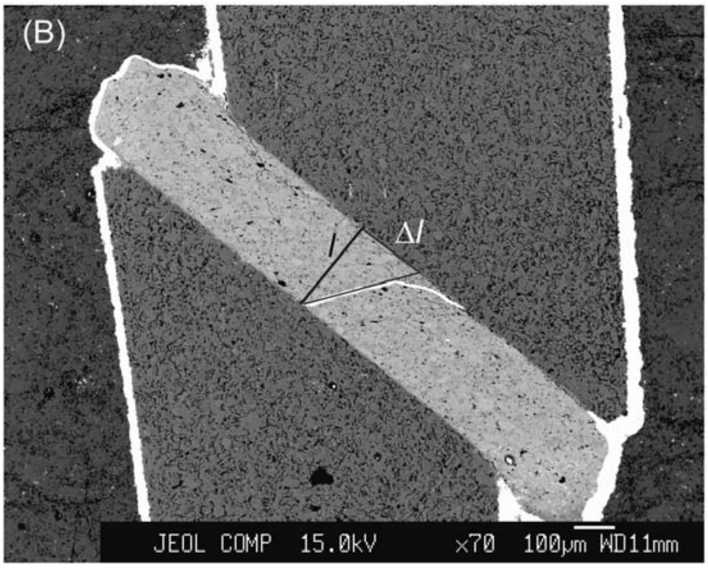

Fig. 3.8-5: Cross-section image of a recovered cell assembly for simple shear deformation experiments at high pressure and high temperature.

Piezoelectric stress measurements using $GaPO_4$ single crystals have been performed using 8/6 MA6-6 configuration at 2 GPa. The highly resistive electrical insulation of 6-ram press renders it possible to obtain high quality data, with minimal signal noise compared to similar measurements attempted with the conventional D-DIA apparatus where charge leakage occurs through the deformation anvils. Crystals of $GaPO_4$ were compressed at room temperature. The charge developed as a result of stress within the assembly was measured across the anvils using an operational amplifier. Differential anvil displacements of the order of 0.5 microns were found to produce a detectable charge on the crystal surfaces at high pressure.

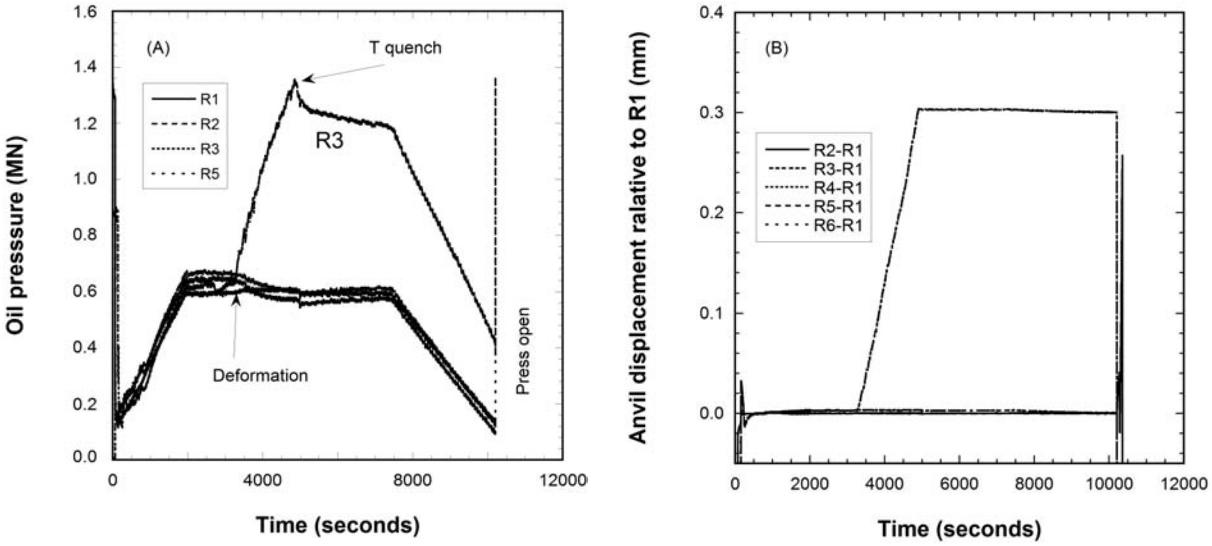

Fig. 3.8-6: (A) The difference in pressure between two horizontal rams (R3 and R6) and the vertical ram (R2) relative to the main lower ram (R1) for sample deformed at 15 bars using 8/6 configuration. In (B) the displacement of differential rams is compared to the static horizontal ram and the vertical ram. The total displacement of the differential rams was set to 300 µm.

b. *Simulating the neutron guide for the 6-ram press at the FRM II neutron source with VITESS 2.10 (N. Walte, H. Keppler, A. Houben/RWTH Aachen and W. Schweika/Jülich)*

An important aspect of the ongoing BMBF project to set up a 6-ram press at the FRM II neutron source is to make sure that the neutron flux that leaves the reactor reaches the samples with minimal loss of intensity. This is achieved with the help of neutron guides, evacuated totally reflecting tubes. In order to reflect the highly penetrating neutrons, the walls are traditionally coated with ^{58}Ni, the material with a high angle of total reflection of neutron beams (*ca.* 0.1° at a wave-length of 1 Å). However, recently developed "supermirror" coatings can reach higher reflecting angles. They consist of alternate Ni and Ti layers that act as a one-dimensional crystal at which neutrons experience Bragg reflection. The Ni/Ti layers have a varying thickness with depth so that neutrons within a whole wavelength range can be reflected. The result is an angle of reflection that is higher by a factor m than the angle of total reflection on Ni, for example an $m = 4$ supermirror would have a maximum angle of reflection of *ca.* 0.4° for $\lambda = 1$ Å neutrons. In combination with parabolic or elliptic shapes, these neutron guides result in a neutron intensity that can be significantly higher than those with a straight shape and Ni coating.

The BGI 6-ram multianvil press shares the neutron beamline with the instrument POWTEX (built in cooperation by RWTH Aachen and Forschungszentrum Jülich), and will be located *ca.* 11 m behind that instrument. The neutrons that reach POWTEX are already focused by a double elliptic neutron guide and need to be guided for the remaining 11 m distance. The requirements for the neutrons at the press are special due to the relatively small size of the samples and the varying use for time-of-flight (TOF) diffraction and radiography. Namely, TOF neutron diffraction requires a high intensity of neutrons with a moderate divergence of the beam, whereas high resolution neutron radiography requires a beam with a very low divergence, which can only come at the cost of intensity. In order to meet both requirements, three different geometries have been investigated: (i) a constant guide with a focusing parabolic end-piece, (ii) a single elliptic neutron guide, and (iii) two ellipses that form an additional focal point in the middle of the path. There are several computer programs available that allow a stochastic simulation of neutron guides. Numerical packets of neutrons are sent out and their interaction with different neutron guide shapes and coatings is simulated. For our purpose, we have applied the "backtracing" technique by A. Houben using the monte-carlo simulation software VITESS 2.10. Here, the program tracks all interactions of the neutrons with the guide. By knowing the reflection angle of the desired neutron wave length at the guide wall as a function of the position along the guide, the coating can be tweaked in each section to ensure optimal transport (Fig. 3.8-7). For example, the simulations for elliptical guides show that the *m*-values need to be highest at both ends of the guide (Fig. 3.8-7).

Guide shape alternative (i) was shown to yield inferior results as compared to both elliptical models. Double elliptic guides (iii) resulted in a lower intensity than (ii) without significant gains in divergence due to the smaller entrance and exit windows and the higher number of reflections on its way. Here we concentrate on the results of the single ellipse simulations (iii). In general ellipses or ellipsoids in 3-D have the advantage of having two focal points with only one reflection in 2-D, which minimizes intensity loss. For our simulation, the first focal point is laid on the sample position of POWTEX, the second focal point is our sample position. Neutron input parameters are taken from previous simulations for POWTEX. Fig. 3.8-8 A and B shows the results of simulations with ellipses with a varying length to width ratio (a/b). The intensity and neutron flux is higher at a lower a/b ratio since more neutrons can be captured by the guide, however, the divergence plot for $a/b = 400$ shows an irregular divergence distribution (Fig. 3.8-8 A), which is undesirable for later TOF analysis. The simulations showed that an ellipse with an a/b ratio of 600 appears to be the best compromise between regularity and high neutron flux (Fig. 3.8-8 B) producing a small spot size, which is desirable for TOF diffraction of small samples. However, for high resolution neutron radiography, this beam has a too high divergence. The divergence is a function of the reflection distance from the sample; neutrons reflected at the end of the guide have the highest divergence. Hence, the final segments of the guide can be exchanged with an absorbing piece. The result is a beam of reduced intensity and low divergence that can be used in the radiography mode (Fig. 3.8-8 C).

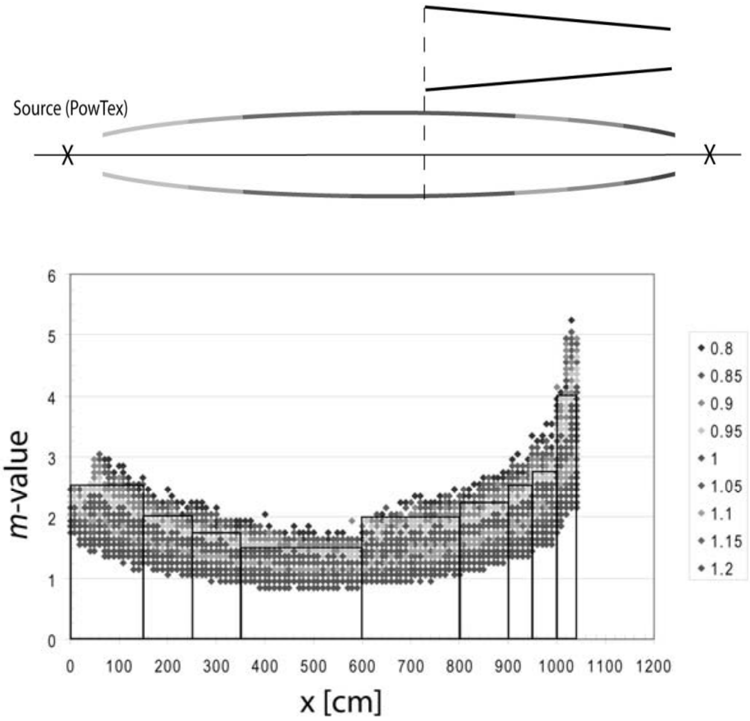

Fig. 3.8-7: Simulation of a single elliptic guide with VITESS. Plot of the guide length (x-axis) versus the necessary m-value (y-axis) for neutron reflection. The boxes denote the *m*-value coating chosen for the guide section to reflect neutrons with a wavelength of 1 µm or larger. The top shows the schematic guide with a high *m*-value at the beginning and end and the exchangeable absorbing piece.

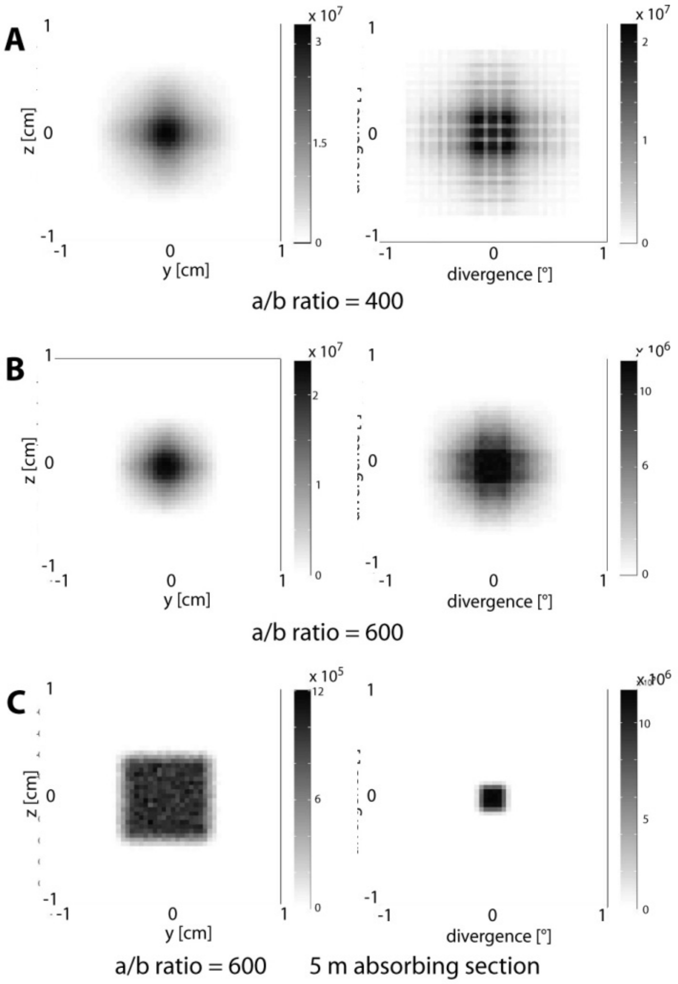

Fig. 3.8-8: Neutron beam simulation of a single elliptic guide. Left: neutron intensity as a function of position. Right: neutron intensity as a function of divergence (the departure from the guide axis). Different a/b ratios of the ellipse are tested in A and B. C shows a simulation with the absorbing piece.

The currently favored neutron guide will have an elliptical shape with a square cross-section and a length of *ca.* 10.4 m. The entrance and exit widths will be *ca.* 7 mm and the greatest width will only be 19 mm. The final 3-5 m of the guide will be interchangeable between the fully reflecting section with an *m*-value up to 4 for high intensity TOF neutron diffraction and an absorbing piece for neutron radiography.

c. *Preliminary measurements of sound wave velocities at high pressure in conjunction with X-ray techniques at the ESRF (J. Chantel, W.A. Crichton/Grenoble and D.J. Frost)*

The measurement of mineral sound wave velocities at high pressure and temperature is a principal concern in mineral physics. Such measurements not only allow velocities in the mantle to be compared with those of proposed mineral assemblages in order to assess the temperature and chemistry of the mantle but also provide direct measurements of mineral physical properties such as the adiabatic bulk, K_S, and shear modulus, G. Coupling MHz ultrasonic measurements with X-ray diffraction and radiographic imaging is a powerful approach in the determination of polycrystalline mineral sound velocities. Recently a new multianvil press has been installed at the ID06 beamline of the ESRF. The press has been constructed with a view to performing angle dispersive X-ray diffraction experiments and, in conjunction with ultrasonic measurements. Hence very precise mineral velocity measurements should be possible.

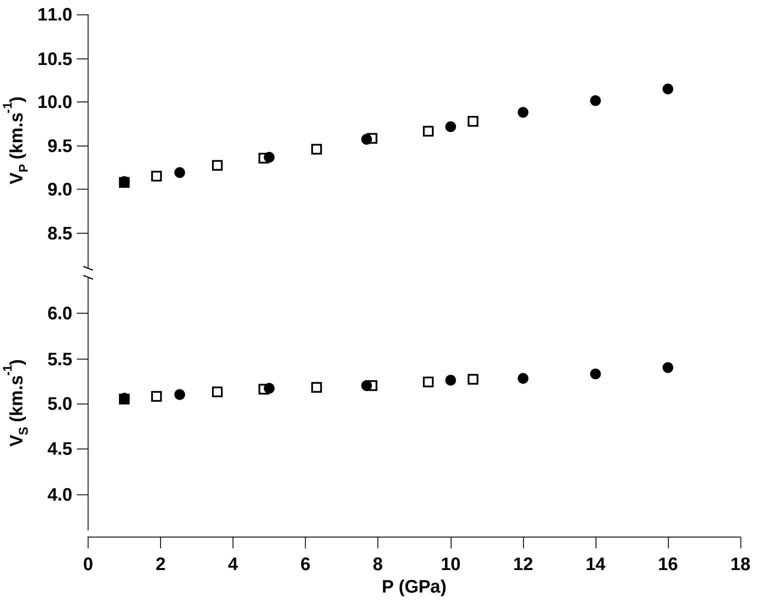

Fig. 3.8-9: Compressional and shear wave velocities for $Py_{50}Mj_{50}$, measured at the BGI (black filled circles) and at the ESRF (open squares).

Figure 3.8-9 shows the results of ultrasonic measurements performed on a sample of pyrope-majorite garnet ($Py_{50}Mj_{50}$) up to 10 GPa at ESRF. The previously hot-pressed garnet sample was placed inside a 10/4 multianvil assembly (10mm: the length of the edge of the MgO octahedra and 4mm: the length of the truncation of the WC anvils) with an Al_2O_3 buffer rod acoustically coupling the sample to the truncation of the tungsten carbide cube. An ultrasonic transducer was used to send a pulse of ultrasound through the carbide cube, buffer rod and sample before being reflected at the back of the sample and returned to the transducer for detection. Gold foil was placed on the surfaces of the sample in order to make them visible in X-ray radiographic images such as in Fig. 3.8-10. Radiographic images obtained *in situ* in the multianvil apparatus are required to make an independent assessment of the change in length of the sample as pressure is raised. Images at each pressure were captured using a Frelon CCD camera.

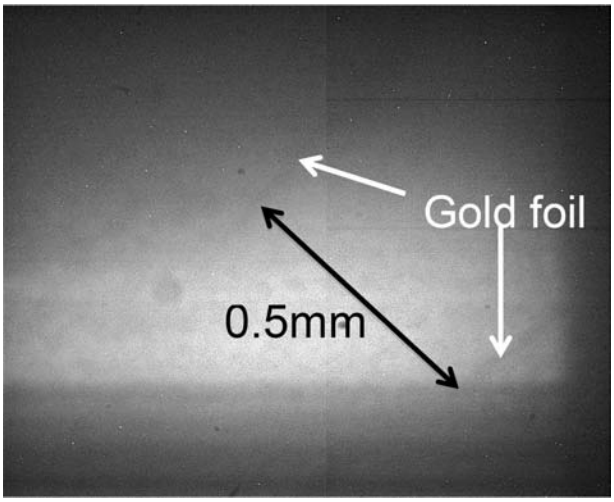

Fig. 3.8-10: *In situ* radiographic image of the $Py_{50}Mj_{50}$ sample at high pressure. Faint lines caused by gold foil placed at either ends of the sample are used to determine the sample length.

Monochromatic angle dispersive X-ray diffraction patterns of the sample were collected at each pressure, while the ultrasonic measurements were conducted, using an image plate detector MAR 345 (Fig. 3.8-11). X-ray diffraction patterns were also collected for a powdered MgO pressure marker placed in the centre of the assembly, next to the sample. Using these MgO X-ray data and the well-establish equation of state of MgO, an accurate determination of the pressure for each ultrasonic measurement could be obtained.

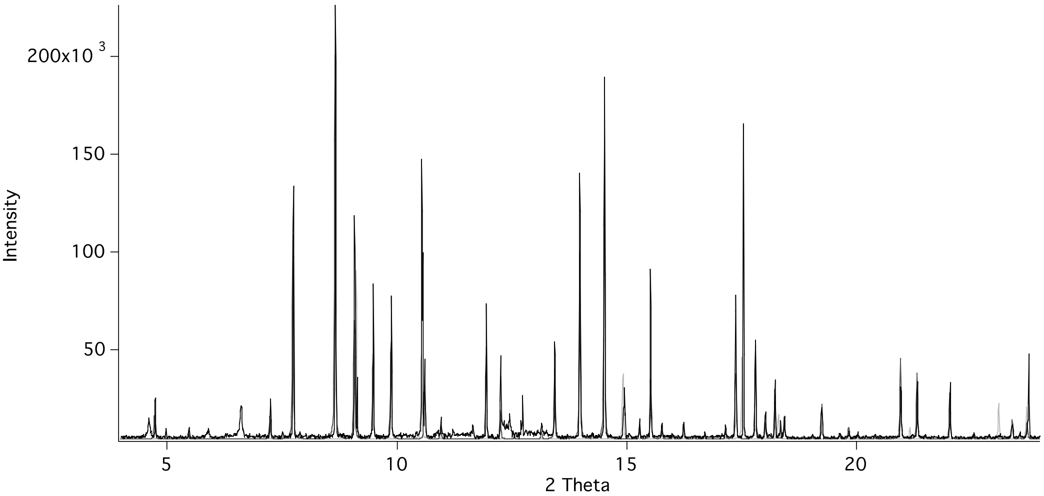

Fig. 3.8-11: Angle dispersive X-ray diffraction pattern of the $Py_{50}Mj_{50}$ sample in the multianvil press at 9.4 GPa and room temperature.

The measured compressional and shear velocities for the ($Py_{50}Mj_{50}$) sample are consistent with velocities previously obtained at the BGI on a similar garnet sample of the same composition (Fig. 3.8-9). In this previous BGI experiment where X-ray techniques were not available, the sample length could not be determined independently but was instead derived through an internally consistent treatment that assumes the sample length changes as a function of the derived elastic properties, in the so called "Cooks Method". Pressure was determined using transformations in Bi metal and Zn detected through *in situ* monitoring of the electrical resistance. Although the agreement between the BGI measurements and those made at the ESRF is very good, X-ray determination of sample length and pressure are essential for high-temperature measurements.

d. *The development of a routine for the extraction of elastic constants from experimental Brillouin scattering data (D.M. Trots, A. Kurnosov and D.J. Frost)*

As a result of recent developments in high-pressure X-ray diffraction and Brillouin spectroscopy it is possible to measure densities and acoustic velocities of single crystal samples in diamond anvil cells at megabar pressures. Such experiments, however, require software for the extraction of elastic (C_{ij}) or piezo-elastic constants for crystals of different orientations and symmetries. In this contribution, we describe the first attempt at the development of such software, *i.e.*, MathCad encoded routines for C_{ij} extraction from velocity ($\boldsymbol{v}$) vs. orientation (or phonon direction, $\boldsymbol{q}$) dependencies for single crystals of arbitrary crystallographic orientation. These routines have been successfully employed for simultaneous measurements of sound velocities and densities of Earth minerals at extreme conditions.

The routines are based on the well-known general closed-form expressions for acoustic waves in elastically anisotropic solids (A.G. Every, *Phys. Rev. B* 22, 1746, 1980). The polarization and frequencies of the three acoustic modes for a particular phonon direction are determinated by elastic constants via the equation of motion. Applying a plane monochromatic wave solution of this equation leads to the characteristic equation $\left|\Gamma_{rs} - \rho v^2 \delta_{rs}\right| = 0$, where $v = \omega / k$ is the phase velocity and $\Gamma_{rs} = C_{rlsm} q_l q_m$ is the Christoffel matrix. The characteristic equation relates the velocity, the direction of the wave and elastic constants of the medium, and is cubic in $\boldsymbol{v}^2$, *i.e.*, its solutions result in three acoustic velocities. In addition, we note the following issues.

(i) All three velocities (longitudinal or quasi-longitudinal velocity v_L for arbitrary crystallographic orientation and fast and slow transverse or quasi-transverse velocities v_{S1} and v_{S2}) are functions of $\boldsymbol{q}$, C_{ij} and density ρ, $v_{L,S1,S2} = f(\rho, C_{ij}, \boldsymbol{q})$. Both crystal orientation and elastic constants can be determined by fitting solutions of the equation of motion to measured sound velocities.

(ii) Crystallographic orientation and density are experimentally obtained in the same setup from diffraction very precisely. This provides particularly useful constraints for elastic constant extraction.

(iii) The form of the solution depends strictly on crystal symmetry. It can be simplified by choosing a crystal orientation in a high symmetry direction; in general nine different forms of solutions are possible for the 32 crystal Laue groups.

The crystallographic direction (or phonon direction) is described by q_x, q_y, q_z components of $\boldsymbol{q}$, which are direction cosines between the diffractometer and crystal axes, and are extracted from the routinely obtained crystal orientation *UB* matrix. During collection of orientation dispersion curves, the crystal orientation is changed by movement of the χ-circle of Eulerian cradle, while the components of the initial orientation/phonon direction q_{x0}, q_{y0}, q_{z0} are related to the orientation at any χ via a general Cartesian rotation matrix. Elastic constants could be then extracted from dispersion curves via inversion of the acoustic velocities $v_{L,S1,S2} = f(\rho^{CONSTRAINED}, C_{ij}, \boldsymbol{q}^{CONSTRAINED})$. This requires a multi-dimensional minimization, *i.e.*, a fit of three solutions of the characteristic equation with shared C_{ij} to multiple $\boldsymbol{v}$ *vs.* $\boldsymbol{q}$ data. The multi-dimensionality can be reduced, however, to a regular minimization weighted by uncertainties in sound velocities through the creation of a function consisting of the sum of all solution residuals squared. This is then minimized over shared elastic constants. The same approach can be used for extraction of C_{ij} from $\boldsymbol{v}$ measured for several differently oriented crystals, which is crucial for crystals with symmetry lower than cubic. According to recent results (Kurnosov *et al.* 2011, BGI Yearbook), strong correlations between several elastic constants were observed for arbitrarily oriented orthorhombic $MgSiO_3$ perovskite and the measurement of a second crystal is necessary to reduce these correlations and improve the accuracy of the results.

The routines include several diagnostic tools, such as the calculation of dispersion curves for crystals of known orientation with a priori known elastic constants and analysis of correlations between fitting parameters, which serve to optimize the data collection strategy. A future development of the diagnostic tool allowing prediction of maxima in phonon intensity in Brillouin spectra for particular polarization direction of the scattered and incident laser light will significantly save measurement time in scattering experiments and would be, in principal, possible with a priori knowledge of both elastic and elasto-optic constants of the material under investigation. We have tested these routines for isotropic solids such as Sm-doped $Y_3Al_5O_{12}$ garnet (see Trots *et al.*, BGI Yearbook 2011), in addition to all cubic and orthorhombic point groups and rhombohedral point groups *32*, *3m*, $\bar{3}$m (see dispersion relations of α-quartz in Fig. 3.8-12).

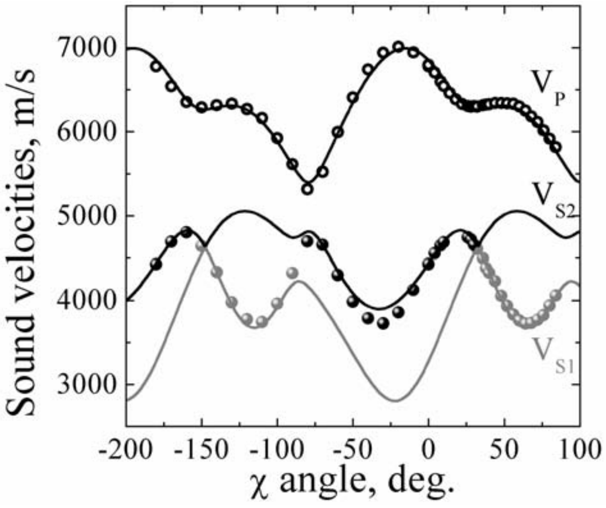

Fig. 3.8-12: Symbols represent measured orientation dependency of sound velocities of α-quartz (reciprocal lattice vector [-1 1.9 0] of crystal is parallel to the DAC load axis) while lines through the symbols are results of fits of $\boldsymbol{v}_{L,S1,S2} = f(\rho^{CONSTRAINED}, C_{ij}, \boldsymbol{q}^{CONSTRAINED})$ to experimental sound velocities with C_{11}=89(4), C_{12}=19(4), C_{13}=7(3), C_{33}=104.0(7), C_{44}=56.8(4), C_{14}=-18.7(4) GPa. Note that correlations over 90 % were observed between C_{11} and C_{12} (C_{13}) elastic constants for a crystal polished perpendicular to [-1 1.9 0]. This requires an experiment on a second crystal (envisaged in nearest future) and simultaneous processing of data collected from both crystals for improvement of accuracy in determination of C_{11}, C_{12}, C_{13}.

e. *A calibration of Sm-doped $Y_3Al_5O_{12}$ as a primary pressure standard (D.M. Trots, A. Kurnosov, T. Boffa Ballaran and D.J. Frost, in collaboration with S. Tkachev, K. Zhuravlev and V.B. Prakapenka/Chicago)*

The absence of absolute pressure/temperature calibrants brings large uncertainties in pressure measurements, which lead to discrepancies in elasticity and high-temperature high-pressure phase boundaries of the mantle minerals. The commonly used optical pressure sensors (ruby and Sm-doped $Y_3Al_5O_{12}$ (Sm:YAG)) are secondary standards calibrated from the equations of state (EoS) of metals derived from shock-wave data (primary standard) and therefore are biased by the uncertainties of such EoS. A more precise and accurate approach is to calibrate the fluorescence shift of such materials versus an absolute pressure obtained by measuring simultaneously their density and their full elastic constant tensor. To this end, we have undertaken a X-ray single-crystal diffraction and Brillouin and Raman spectroscopic studies of Sm:YAG at high pressure and room temperature. We are planning to extend such calibration also at high temperature.

The sample of Sm:YAG was initially characterized by single crystal diffraction indicating excellent crystallinity even after double sided polishing of the sample to a thickness less than 20 µm. The composition and homogeneity of the sample were checked by laser-ablation ICP-MS, revealing a composition of 46 wt.% Al_2O_3 + 47 wt.% Y_2O_3 + 7 wt.% Sm_2O_3 and a small amount of ZrO_2. We note that the pressure response in Sm:YAG is insensitive to its doping amount.

The absolute pressure was derived from simultaneous Brillouin and X-ray diffraction measurements on this double-side polished Sm:YAG loaded in a diamond anvil cell (DAC). Fluorescence shifts were measured on the same sample by Raman spectrometer. Such a combination of techniques performed on the same sample eliminates any influence of the temperature and pressure gradients in DACs and allows the implementation of this pressure marker for both X-ray and optical pressure determinations in DAC. The measurements were commenced at the Advanced Photon Source in Chicago (13-BM-D-GSECARS) up to 21 GPa. Further extensive measurements are being undertaken at the BGI, aiming to reach pressure above 60 GPa.

The results obtained so far (Fig. 3.8-13) indicate that at 21 GPa there is a 5 % deviation from the universally employed ruby pressure scale, in agreement with the suggestion of recent studies reporting simultaneous ultrasonic and X-ray diffraction measurements on MgO. These results have major implications in the field of high-pressure research and particular in the determination of the depth in the Earth's interior at which processes observed in high-pressure experiments may take place.

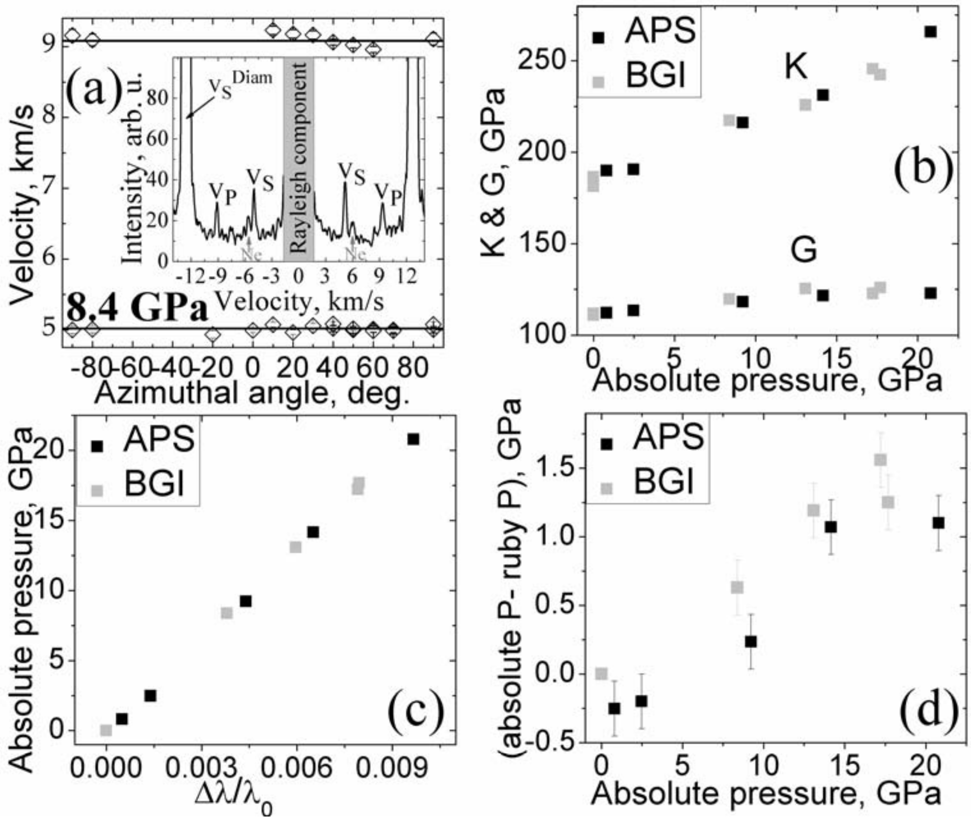

Fig. 3.8-13: (a) typical high-pressure dispersion curve, which reveals elastic isotropy, and Brillouin spectra of Sm:YAG in DAC. (b) pressure dependency of bulk and shear moduli of Sm:YAG. (c) absolute pressure vs. $\Delta\lambda/\lambda_0$ dependency; (d) – deviation from universally employed ruby scale.

f. *Test measurements of double-sided laser heating of (Mg,Fe)O in the diamond anvil cell using a synchrotron Mössbauer source (C. McCammon, L. Dubrovinsky, K. Glazyrin, C. Prescher and I. Kupenko; V. Potapkin, A.I. Chumakov, R. Rüffer, A. Kantor and I. Kantor/Grenoble; G.V. Smirnov and S.L. Popov/Moscow)*

^{57}Fe Mössbauer spectroscopy measured in the energy domain remains one of the best methods to determine iron valence and the nature of spin transitions in lower mantle phases, but up until now measurements at high *P-T* using a diamond anvil cell could only be made using external heating and hence were limited to a maximum of around 800 K. Higher temperatures are possible through laser heating; however conventional radioactive sources have limited intensity and essentially no possibilities for focusing in a laboratory setting. To overcome these limitations we have developed an energy domain synchrotron Mössbauer source on beamline ID18 at the European Synchrotron Radiation Facility, enabling rapid collection of high quality energy domain Mössbauer spectra (see BGI Annual Reports 2009 and 2010). To reach conditions at combined high pressures and temperatures, we used a portable laser heating system installed on the beam line (see BGI Annual Report 2009). Preliminary measurements using a single-sided laser heating system gave puzzling results (apparent mixture of phases), so we carried out test measurements using a well-studied material in order to understand effects during single-sided and double-sided laser heating. The centre shift enables an independent measurement of temperature through the second-order Doppler shift; hence the temperature of individual iron atoms that give rise to the Mössbauer signal can be directly determined.

We selected $Fe_{0.2}Mg_{0.8}O$ since its Mössbauer spectra at high pressure and temperature are already known from our previous work using an externally heated diamond anvil cell. All measurements were carried out at ID18 using the synchrotron Mössbauer source, and each spectrum took roughly 10 minutes to collect. The Mössbauer spectrum of the high-spin phase ($P < 50$ GPa) consists of a single quadrupole doublet arising from octahedral Fe^{2+} (Fig. 3.8-14a). Upon heating from only one side with a laser (or during double-sided heating when the X-ray beam and laser spot are not well aligned), the spectrum becomes asymmetric (Fig. 3.8-14b). Since we know from previous experiments on $Fe_{0.2}Mg_{0.8}O$ that temperature causes a decrease in quadrupole splitting, we interpret the spectrum in Fig. 3.8-14b to indicate a temperature gradient in the sample from relatively cool material (grey doublet) to a hotter region (black singlet), corresponding to temperatures of 450 K and 1000 K, respectively. During double-sided heating with good alignment of X-ray beam and laser spot, the Mössbauer spectrum becomes more symmetric (Fig. 3.8-14c) and indicates a temperature of 1300 K. We found that temperature gradients also arise from double-sided laser heating of thick samples (25-30 µm), where the interior of the sample remains cooler than the surface. Further, we observed that temperature measured by spectrophotometry inevitably overestimated the actual sample temperature. Not only do these results provide important constraints for the interpretation of more complex laser-heated Mössbauer spectra (such as silicate perovskite), but they also challenge some of the conventional assumptions made for laser-heated diamond anvil cell experiments and the measurement of temperature.

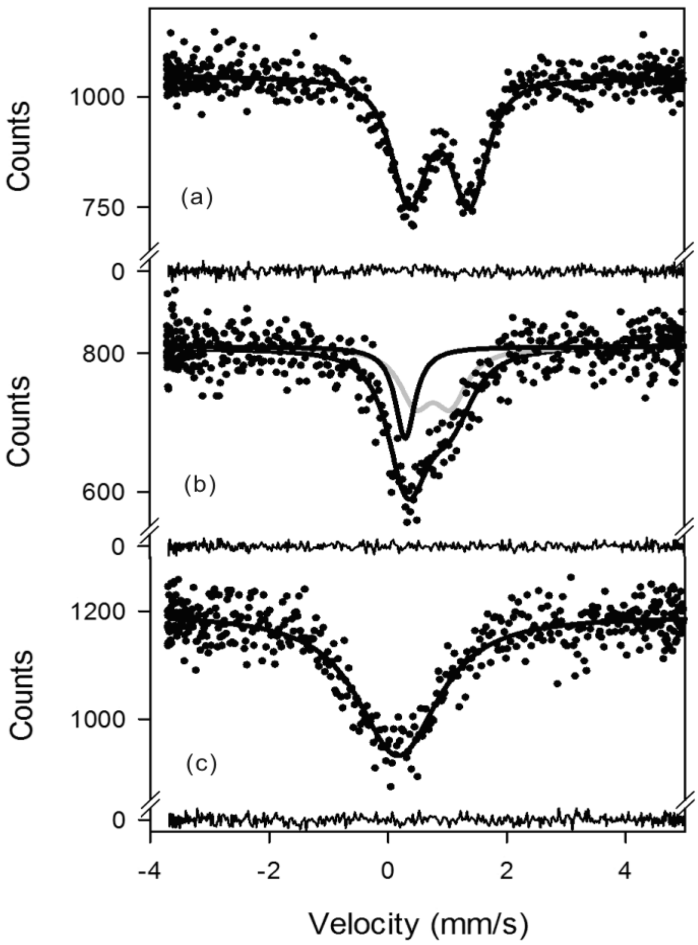

Fig. 3.8-14: Synchrotron Mössbauer source spectra of $Fe_{0.2}Mg_{0.8}O$ at 29 GPa: (a) room temperature; (b) laser heating with misaligned beam; (c) double-sided laser heating with good alignment. The temperatures determined from the centre shift are (b) 450 K (grey doublet) and 1000 K (black singlet) and (c) 1300 K (singlet). The fit residuals are shown below each spectrum.

g. *MossA – a program for analyzing energy-domain Mössbauer spectra from conventional and synchrotron source (C. Prescher, C. McCammon and L. Dubrovinsky)*

Mössbauer spectroscopy is a unique tool for sampling spin states, oxidation states, and coordination of specific elements. Particularly in the Earth sciences it is frequently used due to the ease of obtaining structural information and the oxidation state of iron in rocks and minerals. The Mössbauer milliprobe technique has enabled an evaluation of the spin and oxidation states of iron in materials relevant to the Earth's interior up to pressures of the Earth's core. However, detailed analysis of compounds with different iron environments or a mixture of different phases containing iron is challenging due to the ambiguity of possible fitting models. The outcome of the fitting procedure can depend strongly on the input of the initial parameters of the distribution of sites. Therefore complex spectra need to be evaluated visually before fitting in order to define the initial parameters, and the progress of the fit should ideally be tracked while fitting in order to allow intervention if the solution becomes physically improbable.

We developed a Matlab-based Mössbauer fitting program "MossA" which overcomes these usual difficulties in the analysis of complicated spectra. Through its clear graphical user interface (GUI) and straightforward procedures for handling data and exporting parameters and fitted spectra, it is easy to analyze complex Mössbauer spectra even for users that are unfamiliar with Mössbauer spectroscopy (Fig. 3.8-15).

The program MossA provides a straightforward approach to the fitting of ^{57}Fe conventional and synchrotron energy-domain Mössbauer spectra. Sites can be defined simply by mouse clicks and hyperfine parameters can be constrained to constant values, within specific ranges, and be coupled linearly among different subspectra. The program includes a full transmission integral fit with Lorentzian line shape (conventional source) or Lorentzian-squared line shape (synchrotron source). The fitting process is graphically displayed in real time while fitting and can be interrupted at any time. Gaussian-shaped quadrupole splitting distributions for analyzing non-magnetic amorphous materials is included. MossA is designed especially for the rapid and comprehensive analysis of complex Mössbauer spectra due to its native graphical user input.

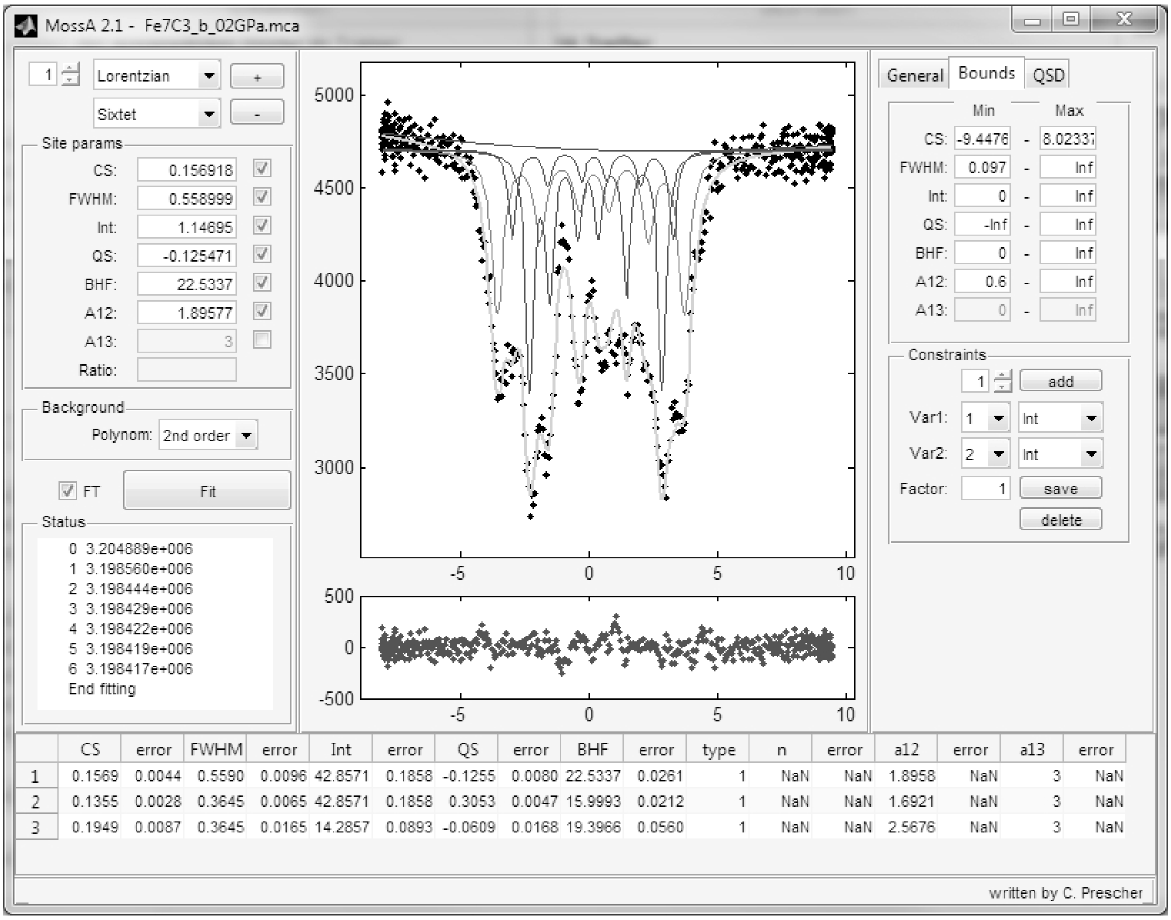
MossA 2.1 - Fe7C3_b_02GPa.mca

1 Lorentzian

Sixtet

Site params

CS: 0.156918 ☑

FWHM: 0.558999 ☑

Int: 1.14695 ☑

QS: -0.125471 ☑

BHF: 22.5337 ☑

A12: 1.89577 ☑

A13: 3 ☐

Ratio:

Background

Polynom: 2nd order

☑ FT

Status

```
0  3.204889e+006
1  3.198560e+006
2  3.198444e+006
3  3.198429e+006
4  3.198422e+006
5  3.198419e+006
6  3.198417e+006
End fitting
```

Bounds

	Min		Max
CS:	-9.4476	-	8.02337
FWHM:	0.097	-	Inf
Int:	0	-	Inf
QS:	-Inf	-	Inf
BHF:	0	-	Inf
A12:	0.6	-	Inf
A13:	0	-	Inf

Constraints

1

Var1: 1 Int

Var2: 2 Int

Factor: 1

	CS	error	FWHM	error	Int	error	QS	error	BHF	error	type	n	error	a12	error	a13	error
1	0.1569	0.0044	0.5590	0.0096	42.8571	0.1858	-0.1255	0.0080	22.5337	0.0261	1	NaN	NaN	1.8958	NaN	3	NaN
2	0.1355	0.0028	0.3645	0.0065	42.8571	0.1858	0.3053	0.0047	15.9993	0.0212	1	NaN	NaN	1.6921	NaN	3	NaN
3	0.1949	0.0087	0.3645	0.0165	14.2857	0.0893	-0.0609	0.0168	19.3966	0.0560	1	NaN	NaN	2.5676	NaN	3	NaN

written by C. Prescher

Fig. 3.8-15: User interface during the fitting process. The example spectrum shown is for a full transmission integral fit to Fe_7C_3 with three sextets, each with the component area ratio A_{13} fixed to 3 and the intensities of the first and second sextets constrained to be equal as required by crystallographic constraints.

h. *Development of electrically heated diamond anvil cell for optical spectroscopy measurements (A. Cernok and L. Dubrovinsky)*

Heating in diamond anvil cell (DAC) can be conducted either using laser light or an electrical heater. Laser heating technique is employed to shortly expose sample to temperatures higher than 1300 K. Using external electrical heaters one can cover wide range of temperatures – from 300 to over 1000 K, holding to constant temperatures for many hours or even days at rather high pressures. However, long-time high-temperature treatment of the DACs results in heating of surrounding equipment, and should eventually affect its performance and even lead to damage it.

We are currently developing a thermal insulation box for experiments carried out using electrically heated diamond anvil cells at temperatures up to 600 °C and at variable pressures (up to 100 GPa) (Fig. 3.8-16). The purpose of constructing such a device is to protect stage and objectives of a Raman-spectrometer used during the heating experiment, to provide homogenous temperature distribution around the DAC placed inside the box, and to maintain temperatures at a constant value for a longer period of time.

Two kinds of external electrical heaters were applied separately and simultaneously for the purposes of heating-resistive Pt-wire heater placed in the cavity around diamond anvils and the whole-cell heater (Fig. 3.8-16 A and B). The smaller heater placed around the anvils is made of Pt wire (300 or 500 µm Ø) folded around a 3 mm thick ring made of zirconia-based ceramics. The whole-cell heater has an external diameter of 50 mm, which is made of fired pyrophyllite and contains Pt wire 500 µm in diameter folded over the inner surface. We used a piston-cylinder type DACs developed at BGI in collaboration with I. Kantor, which is made of high-temperature resistant alloy. Loading screws as well as the contact surface between the two parts of the cell were covered by Molykote 1000 lubricant to avoid welding or locking of different parts. Diamonds and Re gasket were glued with high-temperature resistant graphite bond produced by AREMCO Products Inc. Temperature is measured with an external S type thermocouple, placed very close to the contact of the anvils and the Re gasket (Fig. 3.8-16 A). As previously reported by Dubrovinskaia and Dubrovinsky (Rev. Sci. Instr. 74, 3433, 2003), the temperature gradient in the center of the high-pressure assemblage is practically absent on heating to 1000 °C. In the area of about 5 mm in diameter around the diamonds, the temperature differences are not more than 2-3 °C.

The thermal insulator is made of a square-shaped double-layered stainless steel box (Fig. 3.8-16 B and C). Stainless steel of type 1.4571 is temperature-resistant and shows no oxidation effect to at least 600 °C. Each layer is 1 mm thick, contains a 3 mm wide slit on the side to allow thermocouple and heaters contacts to be outside of the box, and has openings on the bottom and the top to provide optical access to the cell. Opening on the top is 35 mm in diameter and it provides easy access to all four screws of the cell aiming at easy pressure adjustment during the heating experiment. The inner box has dimensions 67×66×38 mm and the outer 90×80×48 mm. They are spaced by 5-10 mm thick fiber-based insulation material used in high-temperature furnace. DAC and the whole-cell heater are fixed on a stainless steel holder (Fig. 3.8-16 B).

The outer heater was controlled by Laboratory Power Supply EA-PS 9065-20 and the inner by EA-PS 9028-100. Maximal output power in the case where only outer heater was used to 600 °C was 270 W (output current 9 A). In the case where the heaters were used simultaneously, we heated with the inner heater to 300 °C (80 W, 10 A) and then joined the outer heater. At 600 °C maximal output power for the inner heater was 144 W (12 A) and for the outer 84 W (6 A). Our first experiments showed that using an insulation box minimizes the power required to heat the cell and successfully protects stage of the Raman microscope from the heat.

The new heating assemblage is easily coupled with already existing DAC experimental setup and can be used with Raman spectrometers and, in future, at Mössbauer, IR and synchrotron radiation facilities.

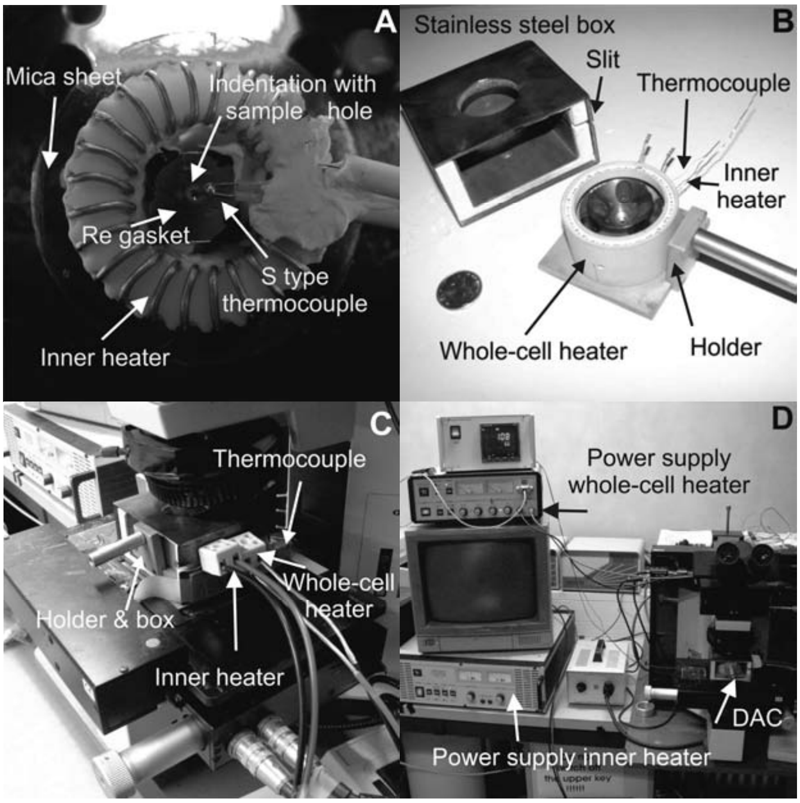

Fig. 3.8-16: A. Bottom part of diamond anvil cell with indented Re gasket, a sample hole, S type thermocouple and surrounding inner heater. B. DAC with an inner heater and whole cell heater placed on a holder and double-layered insulation box of stainless steel. C. Closed insulation box under the Raman microscope. D. Power suppliers for a DAC with two heaters.

i. *Time-domain parallelization for geodynamic modeling (H. Samuel)*

Modern computational geodynamics heavily relies on parallel algorithms to speed up calculations. Such a tendency is continuously growing over time as the available parallel resources increase. One of the most widely used approaches in parallel geodynamic codes is spatial decomposition, where the physical computational domain is subdivided into smaller domains that are attributed to one processor or to a set of processors. Each sub-domain carries out its own calculation in parallel and exchanges information periodically with other sub-domains. Such an approach is efficient as long as the size of the sub-domains is large enough so that computational time remains larger than the communication time. However, when the size of the sub-domains becomes too small, the speed-up stagnates, which puts bounds on the maximum performances of the algorithm.

An alternative approach named *parareal* (Fig. 3.8-17) is presented here, based on time-domain decomposition. The method has not been applied in geodynamic studies where motions relevant to the Earth and other planetary mantles are that of an infinite *Prandtl* number convective fluid. In that case, the time-dependence of the mass and momentum equations is only implicit, due to thermal and/or viscous couplings with the explicitly time-dependent energy equation. This requires a number of modifications to the original algorithm.

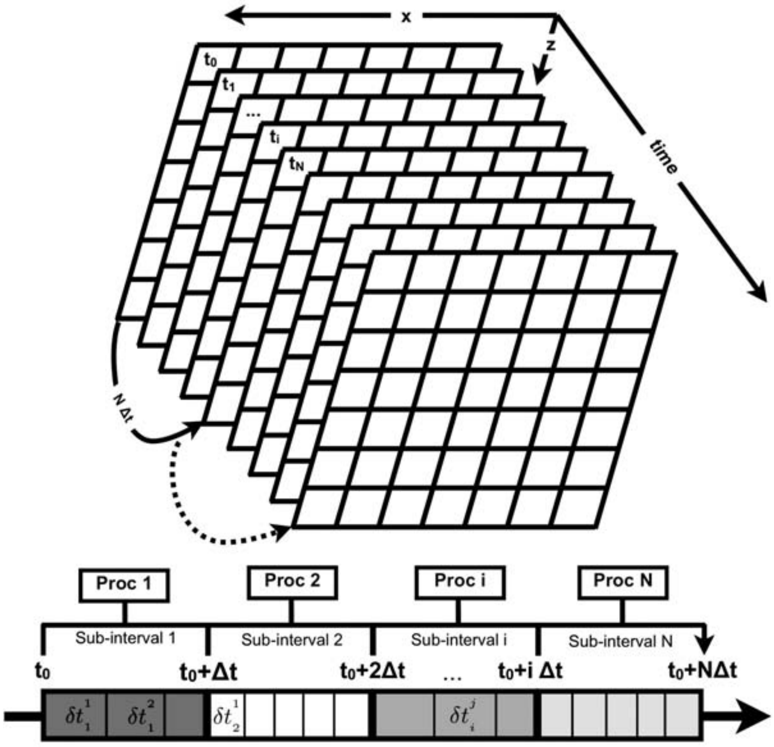

Fig. 3.8-17: Schematic representation of the *parareal* algorithm. Top: representation of the discrete grid in a 3D space-time domain (x,z,t). Bottom: Representation of the discrete domain along the time axis (*i.e.,* cross section in time of the 3D domain above) for one *parareal* time interval N~Δt, distributed among N slave processors.

The *parareal* approach is based on the use of coarse, $C_{\Delta t}$, and fine, $F_{\delta t}$, operators to predict and to iteratively correct the solution λ over a given time interval. The coarse operator, applied serially, propagates the solution in time using a time step larger than a CFL time step, while the fine operator propagates the solution using a CFL time step and can be applied in parallel, over *N* time sub-intervals, distributed among *N* slave processors. The algorithm consists of two steps, monitored by an iteration index *k:*

1. The initialization ($k = 0$), where a first guess is obtained over $\Delta t_{parareal}$ by propagating the solution with the coarse operator:

$$\lambda_0^0 = C_{\Delta t}(\lambda_0^0) \ .$$

As the knowledge of the solution at the previous time step is required, this step needs to be performed in serial.

2. The iterative (*k*-indexed) improvement of the solution according to:

$$\lambda_i^k = C_{\Delta t}(\lambda_{i-1}^k) + [F_{\delta t}(\lambda_{i-1}^{k-1}) - C_{\Delta t}(\lambda_{i-1}^{k-1})] \ .$$

The first term on the left hand side of the above equation can be seen as a predictor step, while the second represents a correction, which is simply the jump between the fine and coarse solutions at a given time step *i* and at the previous *parareal* iteration *k-1*. Since the coarse predictor term requires the knowledge of the coarse solution from the previous time step *i-1* at the present *parareal* iteration *k*, it must be computed serially. However, this is not the case of the jump, which can be computed in parallel over each of the *N* time sub-intervals. This iterative procedure continues until the solution has reached the desirable level of accuracy, which in all cases is bounded by the truncation error of the fine operator.

I have verified experimentally that the method converges within the minimum of *k=1* iteration, even for cases with large values of *N* (~ 10-100). Using a simple performance model I have shown that under optimum conditions, the parallel execution time scales linearly with the number of CPUs used. These theoretical predictions are in good agreement with numerical experiments (Fig. 3.8-18) for which speedup close to 10 were measured, using at most 40 CPUs.

This *parareal* approach can be applied in addition to spatial domain decomposition or to any other parallel algorithm, therefore allowing easily an additional increase in speed-up by a factor of 5-10, even beyond the saturation point of spatial decomposition.

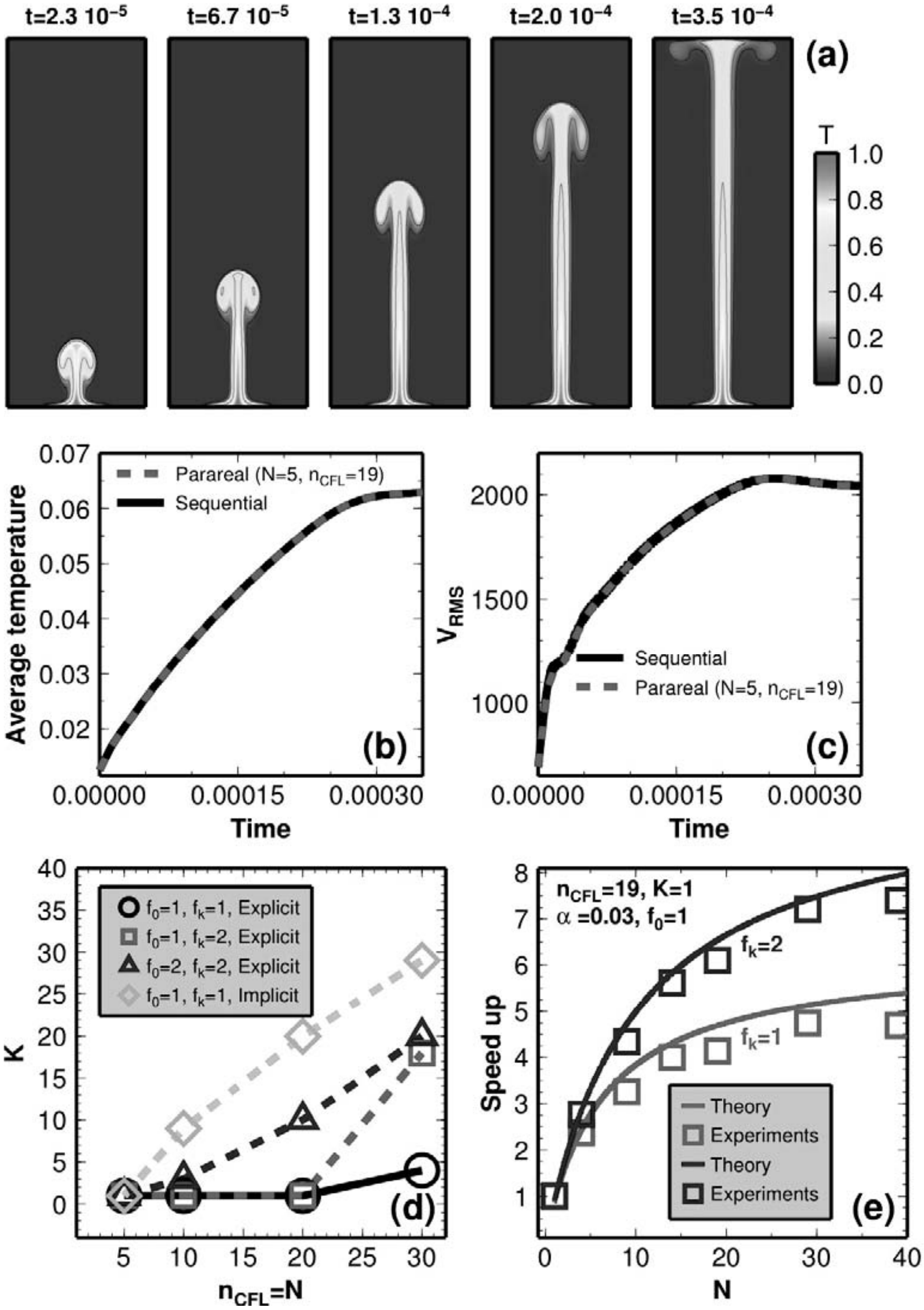

Fig. 3.8-18: Result of an axisymmetric plume test. (a) Snapshots in time showing the plume dimensionless temperature field. Comparison between the sequential (black) and *parareal* (gray) solutions displayed with the dimensionless average temperature (b) and RMS velocities (c). (d) Total number of *parareal* iterations K required to reach convergence as a function of the number of slave processors N, for the optimum setup ($N=n_{\mathrm{CFL}}$), for different values of spatial coarsening (f_0 and f_k), and using either explicit or implicit schemes for the coarse propagation. (e) Comparison of the speedup predicted with a theoretical model, (solid curves) and the one measured experimentally (squares) for two configurations: f_k=1 in gray (*i.e.*, no spatial coarsening) and f_k=2 in black (*i.e.*, using spatial grid coarsening during the coarse propagation).

j. *A wave equation model for highly accurate advection (H. Samuel)*

Accurate modeling of advection is a fundamental requirement of computational geodynamics. Such a process may be described by the following hyperbolic equation:

$$\frac{\partial C}{\partial t} + U \bullet \nabla C = 0$$

where *C* is a scalar variable having more than two values (*i.e.*, the concentration of a chemical component), *U* is the velocity field and *t* is the time.

If diffusion is also present, the advected field is continuous, but can locally vary sharply. While discontinuities in advected quantities are reasonably well handled by flux limiters or high-order WENO schemes, Eulerian approaches tend to be inaccurate when the advected quantity remains continuous but varies sharply. These usually result in an artificial sharpening or in excessive numerical diffusion, both affecting the accuracy of the solution significantly. An alternative to these approaches is the use of a Wave Equation Model (WEM): differencing the advection equation above with respect to time, and rearranging yields a classical wave equation:

$$\frac{\partial^2 C}{\partial t^2} = UU :: \nabla\nabla C + \left[-\frac{\partial U}{\partial t} + (U \bullet \nabla) U \right] \bullet \nabla C$$

By construction, the solution of the above equation also satisfies the advection equation. In fact, the above two-way wave Equation corresponds to twice the use of the advection (or one-way wave) operator in opposite directions. This symmetry is a particularly desirable property because the numerical diffusion in both directions tends to cancel each other, and the resulting solution has a much higher accuracy than the simple use of the (one-way) advection equation, even when discretizing the special derivatives with high-order schemes.

To illustrate the advantage of the WEM approach, I have performed one-dimensional advection tests of continuous quantities with sharp variations (Fig. 3.8-18). The wave equation is solved using finite differences. Spatial derivatives are discretized with a numerical scheme of arbitrary high order, using automatic finite difference stencil formulas. The temporal derivative is approximated by an explicit second-order centered scheme. While monotone schemes yield artificial sharpening or diffusion of the solution, the WEM solution closely matches the analytical solution. Surprisingly, even though the WEM scheme is neither monotone nor conservative, the solution of the two-way wave equation results in no numerical diffusion or dispersion, for an overall comparable computational cost.

Future tests should extend these investigations to two- and three-dimensional advection-diffusion problems relevant to geodynamic scenarios. Currently the WEM does not handle discontinuities, which may result in dispersion errors in absence of diffusion. However, the addition of flux corrections would allow the use of the WEM for advecting quasi-discontinuous fields. Another possibility would be to develop a hybrid scheme based on the use of a WENO reconstruction in discontinuous regions, and the use of a WEM for continuous (but not necessarily smooth) regions.

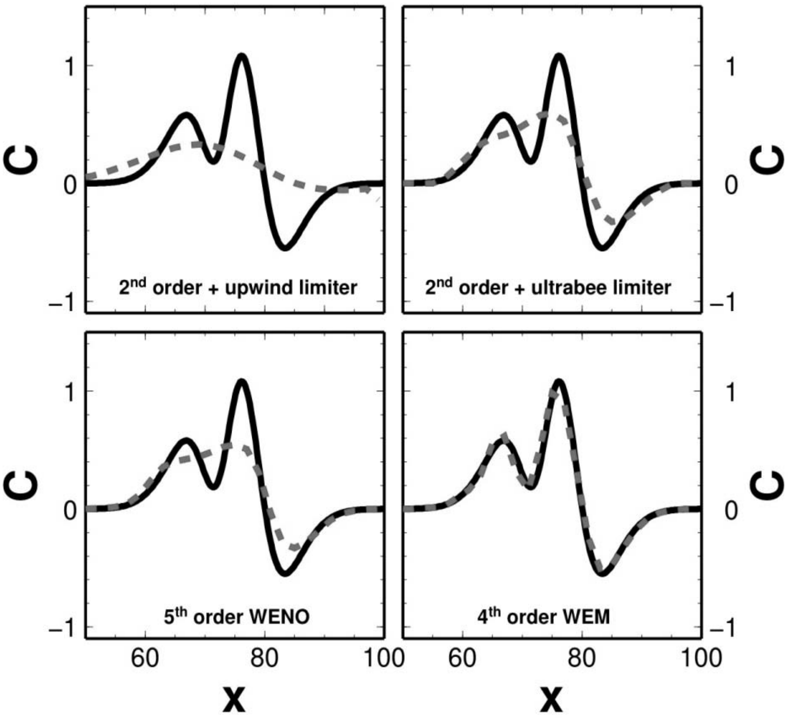

Fig. 3.8-17: One-dimensional rightwards advection of Gaussian pulses using different Eulerian numerical schemes (dashed curves). The Wave Equation Model is the closest to the analytical solution (plain curves) and clearly shows its superiority, even when compared with the best, higher order schemes such as fifth-order WENO.

k. *Solution of convection problems by the Schur complement method (V. Aleksandrov and H. Samuel)*

The report describes the new capabilities introduced to the Schur solver, presented in *BGI Annual Report 2010.* The program is parallelized by assigning the Schur complement computation of each domain to a separate group of processes – this has major impact for the performance. The domain partition strategy is the most influential factor for reaching high efficiency because it determines the total amount of operations required to solve the system. The optimal division geometry has a minimal interface size for a given count of subdomains. In most cases, using four or eight subdomains gives the best results, but domains with very large extent in one direction may be dissectioned even in more parts. The more subdomains are used, the larger the interface becomes. If the Schur complement system is sufficiently large, then an iterative method (CG, BiCG) could solve it faster. The single obstacle, when iterative solver is used on the Schur complement system, is that the convergence severely deteriorates for PDE with variable coefficients. This issue is surmounted using a preconditioner, which stabilizes the iteration count. The preconditioner is constituted only from the largest elements above given threshold in each row of the Schur matrix.

Another feature of the program is its ability to solve general sparse linear systems. The method is generalized by graph formulation. For the purpose, it is supported by routine, which finds *graph separator* using an existing *edge separator*. The edge separator in turn is constructed by the CHACO graph partitioner (*Hendrickson, Leland*). The steps of the solver are shown on Fig. 3.8-18.

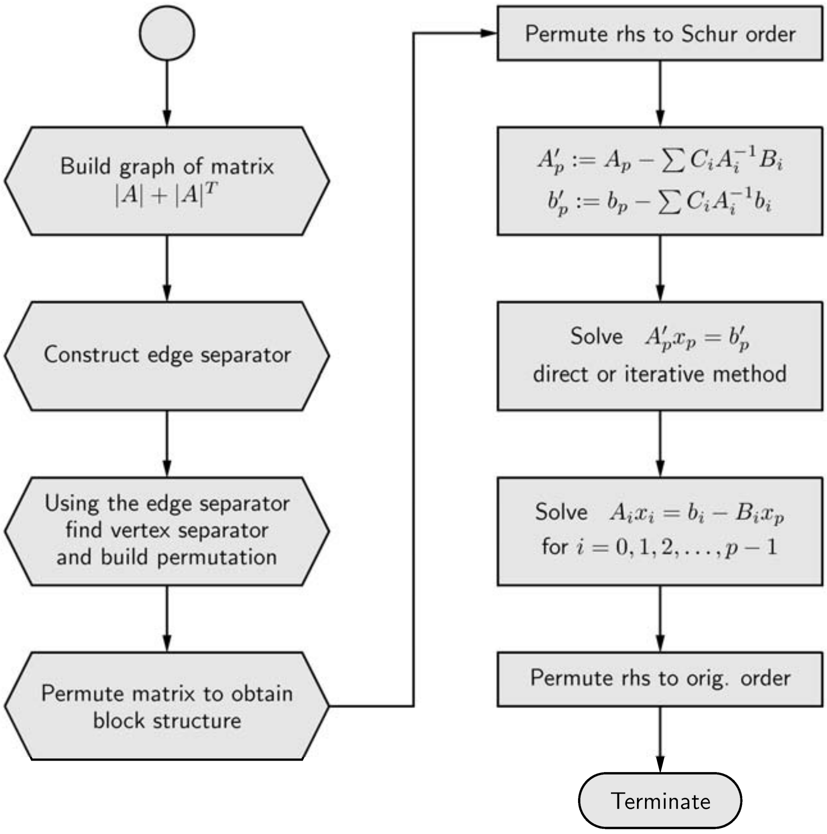

Fig. 3.8-18: Program sequence.

The program is tested on the *Tricomi* equation, the *Poisson* equation and the biharmonic equation in two and three dimensions, the steady-state diffusion equation in two dimensions with piecewise constant conductivity in rectangular domains. The dependence of the total solution time as function of the aspect ratio for various partition geometries is studied. The results show that the method can solve a problem in rectangular box on average twice faster than MUMPS (see Fig. 3.8-18a). Domains with large extent can be solved more than six times faster (Fig. 3.8-18b).

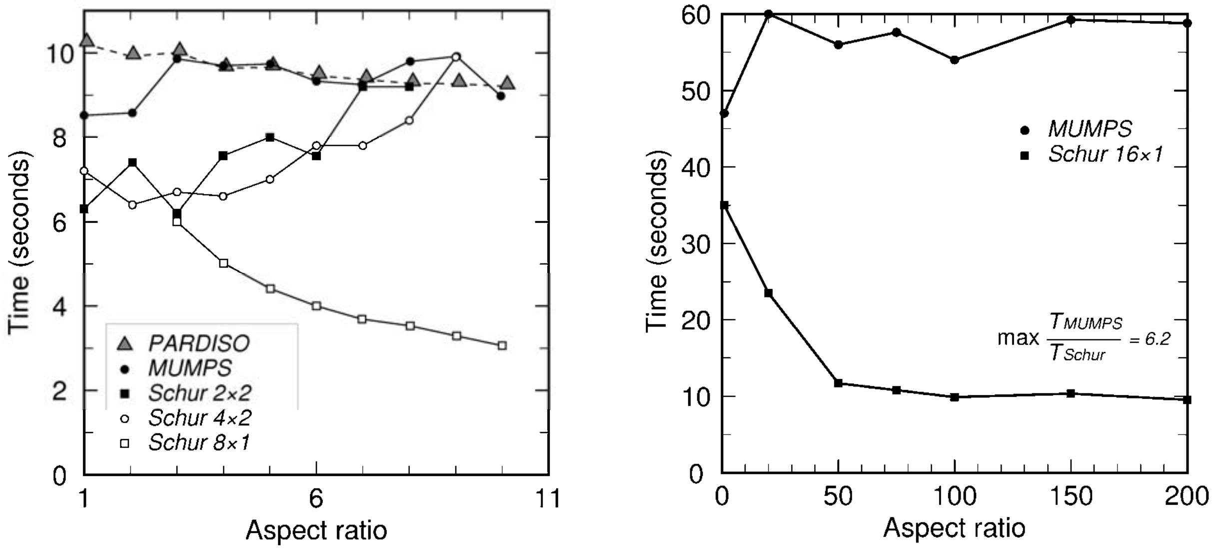

Fig. 3.8-18: (a) Elapsed time to solve the *2D Poisson* equation with 8 processors on uniform grid in rectangular box as function of the aspect ratio *nx/ny*. Number of unknowns is 1,000,000. (b) *2D Poisson* equation with 16 processors for large aspect ratios and 4,000,000 unknowns. ScaLAPACK is used on the Schur complement system.

A three-dimensional *Boussinesq* thermal convection problem at infinite Prandtl number is solved with the Schur method. The flow velocity ***u*** is solenoidal, which allows a presentation of the form

$$\boldsymbol{u} = \nabla \times \boldsymbol{\Psi}$$

where $\boldsymbol{\Psi}$ is called *vector potential of the velocity flow*.
The momentum equation is

$$\Delta^2 \boldsymbol{\Psi} = \frac{1}{\mu} \nabla \times (\rho \boldsymbol{f})$$

with boundary conditions: $\boldsymbol{\Psi} = \mathbf{0}$, $\boldsymbol{\omega} = \mathbf{0}$ on the surface of the unit cube.
When the component ω_z is zero, the vector system is splitted into four *Poisson* equations:

$$\Delta\omega_x + R\frac{\partial T}{\partial y} = 0$$

$$\Delta\Psi_x + \omega_x = 0$$

$$\Delta\omega_y - R\frac{\partial T}{\partial x} = 0$$

$$\Delta\Psi_y + \omega_y = 0$$

R is the Rayleigh number and the potential field is $\boldsymbol{f} = (0,\ 0,\ -g)$ (where $g > 0$). The temperature at the initial instant is one in the cube:
$1/3 < x < 2/3$, $1/3 < y < 2/3$, $1/3 < z < 2/3$ and zero outside. Fig. 3.8-19 depicts the velocity field.

The future work will generalize the approach in order to solve convection problems of fluid in presence of plate.

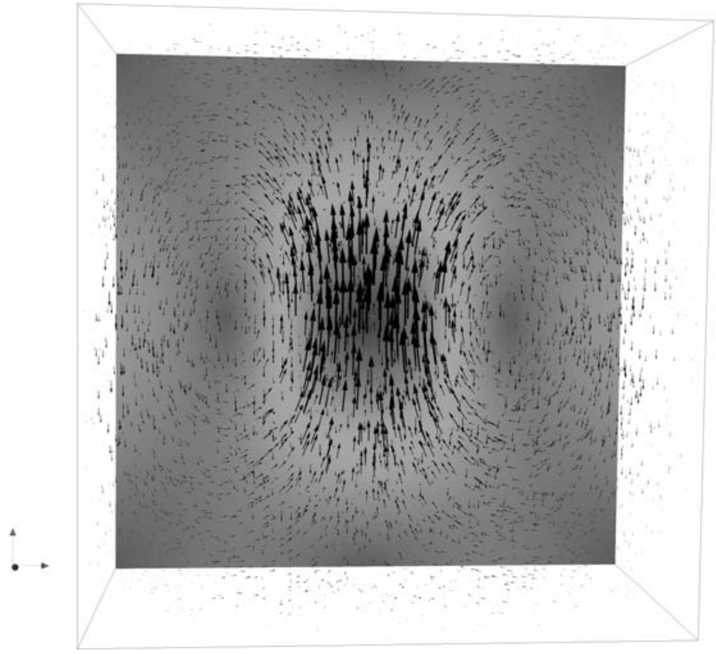

Fig. 3.8-19: The velocity vector field of a three-dimensional *Boussinesq* thermal convection at infinite Prandtl number in a unit cube. The approach follows the **(Ψ, ω)** formalism.

4. International Graduate School – Elitenetzwerk Bayern/Elite Network of Bavaria "Structure, Reactivity and Properties of Oxide Materials" (OXIDES)

The interdisciplinary Graduate School is funded by the State of Bavaria and it encompasses three cooperating institutes: Bayerisches Geoinstitut (BGI), Institute of Inorganic Chemistry I (AC I), both in Bayreuth, and the Fraunhofer Institute for Silicate Research (ISC) in Würzburg. These institutes provide their experimental and analytical facilities, complementary expertise in basic and applied research, and commitment to capitalize on synergies as well as international contacts to other leading research institutes all over the world.

The Graduate School is chaired by Prof. Dr. Hans Keppler/BGI and it includes eleven other faculty members and one coordinator. Enrollment in 2011 was eleven doctoral students on a full-time basis at all three institutes (BGI, AC I, ISC) and, in addition, eighteen doctoral students have associate status in the school which provides them with full access to all educational activities. Research projects include physical and chemical properties of oxides and mineral assemblages and mineral/melt interactions at P-T conditions of the deep Earth, synthesis and investigation of new layer silicates, polymer coatings, transition metal oxides (ceramics) and polyoxometalates as well as the development of new methods in NMR crystallography.

During 2011, five students have graduated:

Vincenzo Stagno (M.Sc. Geology 2006, Palermo) on 30.05.2011	*The carbon speciation in the Earth's interior as function of pressure, temperature and oxygen fugacity.* Supervisor: Prof. D. Rubie Dr. Stagno took a post-doctoral position at the Carnegie Institution/Geophysical Laboratory, Washington D.C.
Diego Bernini (M.Sc. Mineralogy 2006, Pavia) on 26.07.2011	*Halogens and trace elements in subduction zones.* Supervisor: Prof. H. Keppler Dr. Bernini took a post-doctoral position at the POLARIS Research Centre, Dipartimento di Scienze dell'Ambiente e del Territorio, Milano.
Willem van Mierlo (M.Sc. Structural Geology 2007, Utrecht) on 26.07.2011	*Major element diffusion and exsolution of majoritic garnet from aluminous enstatite at conditions of the Earth's upper mantle.* Supervisor: Prof. F. Langenhorst Dr. van Mierlo took a position at "Materialwissenschaftliche Elektronenmikroskopie" at the University of Ulm.

Michael Schütz (associate) (Dipl.-Chem. 2008, Bayreuth) on 10.05.2011	*Novel layered compounds for nanocomposites with enhanced flame retardant properties*. Supervisor: Prof. J. Breu Dr. Schütz took a position with OSRAM at Regensburg
Konstantin Glazyrin (M.Sc. Metal Physics 2004, Moscow) on 28.11.2011	*Iron in oxides, silicates and alloys under extreme pressure-temperature conditions.* Supervisor: Prof. L. Dubrovinsky Dr. Glazyrin took a position at Yale University.

Two students have submitted their thesis in summer 2011 and and will graduate early in 2012:

Sushant Shekhar (M.Sc. in Exploration Geophysics, 2008, Indian Institute of Technology, Kharagpur)	*Rheological properties of olivine-pyroxene-garnet assemblage at P-T conditions applicable to subduction zones* Supervisor: Prof. F. Langenhorst, Dr. D. Frost
Dunja Hirsemann (Dipl. in Chemistry, 2008, University of Bayreuth, Germany)	*Development of innovative Janus-particles based on the layered silicate kaolinite*. Supervisor: Prof. J. Senker Meanwhile Ms Hirsemann has taken a position with BASF at Trostberg.

Two new students were accepted to the doctoral program:

Ana Cernok (M.Sc. Geosciences 2011, Wien) since 11.07.2011	*Silica behaviour in planetary interiors*. Supervisor: Prof. L. Dubrovinsky
Stephan Blaha (M.Sc. Geosciences 2011, Wien) since 01.10.2011	*Temperature dependence of dislocation recovery rate of mantle minerals.* Supervisor: Prof. T. Katsura

Five new associate students were accepted to the doctoral program at BGI:

Ilya Kupenko (M.Sc. 2009, Moscow) since 13.01.2011	*Development of test sites for the characterization of nanostructures, molecular switches, microbiological samples and matter under extreme conditions with nuclear resonant scattering techniques.* Supervisor: Prof. L. Dubrovinsky

Elena Bykowa (M.Sc. 2010, Novosibirsk) since 01.03.2011	*High-pressure crystallography in laser-heated diamond anvil cells.* Supervisors: Prof. L. Dubrovinsky, Prof. N. Dubrovinskaia
Antje-Kathrin Vogel (Dipl.-Min. 2010, Köln) since 01.03.2011	*Element partitioning during the formation of the Earth's core.* Supervisors: Dr. D. Frost, Prof. D. Rubie
Christopher Beyer (M.Sc. 2011, Münster) since 01.10.2011	*Elastic properties and phase relations of minerals of the Earth's mantle.* Supervisors: Dr. D. Frost, Prof. D. Rubie
Vojtech Vlcek (M.Sc. 2011, Bayreuth) since 01.10.2011	*Band structure and radiative thermal conductivity for silicates and oxides through density functional theory computations.* Supervisors: Dr. G. Steinle-Neumann, Prof. S. Kümmel

Descriptions of some of the student research projects are listed in Chapter 3 of this yearbook. Students also gave presentations at major international meetings in 2011. The list of presentations and publications may be found in Chapter 5.

As part of program requirements, all students undergo an intensive training program, in addition to their research project, that encompasses lectures, short courses, research colloquium, doctoral seminar, seminars by invited leading experts and weekend seminars on soft skills such as scientific writing, ethics and team work. Invited speakers from overseas and Europe gave 10 lectures during the last year and presented novel experimental techniques and current research results.

The following courses and seminars were offered by ENB in 2011:

- Doctoral seminar, Goldkronach; Graduate School "*Oxides*", 29.-30.01.2011 (Univ. Bayreuth, ISC Würzburg)
- Short course on "*High-pressure experimental techniques and applications to the Earth's interior*", 14.-18.02.2011, Bayerisches Geoinstitut
- Short course on "*Laser ablation-ICPMS*", 18.-20.03.2011, Bayerisches Geoinstitut
- Geological field trip to Fichtelgebirge and Oberpfalz, 26.-28.05.2011, Bayerisches Geoinstitut
- Soft skills short course on "*Career planning for PhD students*", 10.-11.10.2011, Bayerisches Geoinstitut, Golin Wissenschaftsmanagement GmbH, Hamburg

- During 2011 six invited international scientists contributed to the ENB series of lectures with 10 seminars on recent research results.

Furthermore, students of the graduate school participated in several external short courses/seminars during 2011.

Two doctoral students (*D. Hirsemann, M. Schütz*, associated), the speaker and the coordinator of the graduate school, *Prof. H. Keppler* and *Dr. F. Heidelbach* and *Prof. J. Breu* (Institute of Organic Chemistry, Bayreuth) participated in the Graduation Ceremony of the Elite Network of Bavaria with the State Minister Dr. W. Heubisch in Bayreuth on October 28, 2011.

Students and members of the graduate program received international awards for their research; these awards are listed in section 7.2.

Detailed information on the Graduate School "Structure, Reactivity and Properties of Oxide Materials" can be found at http://www.uni-bayreuth.de/elitenetzwerk/oxides.

5. Publications, Conference Presentations, Seminars

5.1 Publications (published)

Supplement to **2010** (papers published at the end of 2010):

GU, T.; WU, X.; QIN, S.; DUBROVINSKY, L. (2010): In situ high-pressure study of FeP: Implications for planetary cores. Physics of the Earth and Planetary Interiors 184, 154-159

2011

a) Refereed international journals

ADJAOUD, O.; STEINLE-NEUMANN, G.; JAHN, S. (2011): Transport properties of Mg_2SiO_4 liquid at high pressure: Physical state of a magma ocean. Earth and Planetary Science Letters 312, 463-470

AUDÉTAT, A.; DOLEJS, D.; LOWENSTERN, J.B. (2011): Molybdenite saturation in silicic magmas: occurrence and petrological implications. Journal of Petrology 52, 891-904

BALI, E.; AUDÉTAT, A.; KEPPLER, H. (2011): The mobility of U and Th in subduction zone fluids: an indicator of oxygen fugacity and fluid salinity. Contributions to Mineralogy and Petrology 161, 597-613

BASYUK, T.; BEREZOVETS, V.; TROTS, D.; HOFFMANN, S.; NIEWA, R.; VASYLECHKO, L. (2011): Phase diagram of the $PrAlO_3$-$GdAlO_3$ system. Zeitschrift für Kristallographie Proc. 1, 319-324

BINDER, B.; KEPPLER, H. (2011): The oxidation state of sulfur in magmatic fluids. Earth and Planetary Science Letters 301, 190-198

CHELAZZI, L.; BOFFA BALLARAN, T.; NESTOLA, F.; BINDI, L.; BONAZZI, P. (2011): High-pressure behavior of the synthetic $Ca_2Sb_2O_7$ weberite-type compound. Solid State Sciences 13, 1092-1095

DEMOUCHY, S.; MAINPRICE, D.; TOMMASI, A.; COUVY, H.; BAROU, F.; FROST, D.J.; CORDIER, P. (2011): Forsterite to wadsleyite phase transformation under shear stress and consequences for the Earth's mantle transition zone. Physics of Earth and Planetary Interiors 184 (1-2), 91-104

EREMINA, R.M.; FAZLIZHANOV, I.I.; YATSYK, I.V.; SHARIPOV, K.R.; PYATAEV, A.V.; KRUG, H.-A.; NIDDA, H.-A.; PASCHER, N.; LOIDL, A.; GLAZYRIN, K.V.; MUKOVSKII, Ya.M. (2011): Phase separation in paramagnetic $Eu_{0.6}La_{0.4-x}Sr_xMnO_3$. Physical Review B 84, 064410

ESCUDERO, A.; DELEVOYE, L.; LANGENHORST, F. (2011): Aluminum incorporation in TiO_2 rutile at high pressure: An XRD and high-resolution ^{27}Al NMR study. Journal of Physical Chemistry C 115, 12196-12201

FERNÁNDEZ-CARRIÓN, A.J.; ALBA, M.D.; ESCUDERO, A.; BECERRO, A.I. (2011): Solid solubility of $Yb_2Si_2O_7$ in β-, γ- and δ-$Y_2Si_2O_7$. Journal of Solid State Chemistry 184, 1882-1889

FABIAN, K.; MIYAJIMA, N.; ROBINSON, P.; MCENROE, S.A.; BOFFA BALLARAN, T.; BURTON, B.P. (2011): Chemical and magnetic properties of rapidly cooled metastable ferri-ilmenite solid solutions: implications for magnetic self-reversal and exchange bias-I. Fe-Ti order transition in quenched synthetic ilmenite 61. Geophysical Journal Intenational, 186, 997-1014

FUJI-TA, K.; KATSURA, T.; ICHIKI, M.; MATSUZAKI, T.; KOBAYASHI, T. (2011): Variations in electrical conductivity of rocks above metamorphic conditions. Tectonophysics 504, 116-121

GANNOUN, A.; BOYET, M.; EL GORESY, A.; DEVOUARD, B. (2011): REE and actinide microdistribution in Sahara 97072 and ALHA77295 EH3 chondrites. Geochimica et Cosmochimica Acta 75, No. 11, 3269-3289

GANNOUN, A.; BOYET, M.; RIZOT, H.; EL GORESY, A. (2011): ^{146}Sm-^{142}Nd systematics of enstatite chondrites reveals a heterogeneous distribution of ^{142}Nd in the solar nebula. Proceedings of the National Academy of Sciences, 1017332108

GLAZYRIN, K.; DUBROVINSKY, L.; KLOTZ, S.; UHLARZ, M.; WOSNITZA, J.; HANSEN, Th.; DUBROVINSKAIA, N. (2001): Effect of composition and pressure on phase transitions in Fe$_x$O at low temperature. Journal of Applied Physics 110, 026109

GREENBERG, E.; DUBROVINSKY, L.; MCCAMMON, C.; ROUQUETTE, J.; KANTOR, I.; PRAKAPENKA, V.; ROZENBERG, G.; PASTERNAK, M. (2011): Pressure-induced structural phase transition of the iron end-member of ringwoodite (γ-Fe$_2$SiO$_4$) investigated by X-ray diffraction and Mossbauer spectroscopy. American Mineralogist 96, 833-840

GYORGY, F.; TOMMASI, A.; SOUSTELLE, V. (2011): The effect of dynamic recrystallization on olivine crystal preferred orientations in mantle xenoliths deformed under varied stress conditions. Journal of Structural Geology 33 (11), 1528-1540

HAMMOUDA, T.; ANDRAULT, D.; KOGA, K.; KATSURA, T.; MARTIN, A.M. (2011): Ordering in double carbonates and implications for processes at subduction zones. Contributions to Mineralogy and Petrology 161, 439-450

HARRIES, D.; POLLOK, K.; LANGENHORST, F. (2011): Translation interface modulation in NC-pyrrhotites: Direct imaging by TEM and a model toward understanding partially disordered structural states. American Mineralogist 96, 716-731

HUSHUR, A.; MANGHNANI, M.H.; SMYTH, J.R.; WILLIAMS, Q.; HELLEBRAND, E.; LONAPPAN, D.; YE, Y.; DERA, P.; FROST, D.J. (2011): Hydrogen bond symmetrization and equation of state of phase D. Journal of Geophysical Research 116, B06203, doi: 10.1029/2010JB008087

ISAEV, E.I.; SIMAK, S.; MIKHAYLUSHKIN, A.; VEKILOV, Yu.; ZARECHNAYA, E.; DUBROVINSKY, L.; DUBROVINSKAIA, N.; MERLINI, M.; HANFLAND, M.; ABRIKOSOV, I.: Impact of lattice vibrations on equation of state of the hardest boron phase. Physical Review B 83**,** 132106

KEEFNER, J.W.; MACKWELL, S.J.; KOHLSTEDT, D.; HEIDELBACH, F. (2011): Dependence of the creep of dunite on oxygen fugacity: Implications for viscosity variations in Earth’s mantle. Journal of Geophysical Research, 116, B05201, doi: 10.1029/2010JB007748

KICHANOV, S.E.; KOZLENKO, D.P.; WASICKI, J.; BELUSHKIN, A.V.; NAWROCIK, W.; CZARNECKI, P.; DUBROVINSKY, L.S.; LATHE, C.; SAVENKO, B.N. (2011): Study of the P-T phase diagram of pyridinium perchlorate by X-ray diffraction and Raman spectroscopy. Journal of Surface Investigations. X-ray, Synchrotron and Neutron Techniques 5, No 4, 611-618

KOZLENKO, D.P.; CHAN, T.A.; KICHANOV, S.E.; JIRAK, Z.; DUBROVINSKY, L.S.; SAVENKO, B.N. (2011): Structural and magnetic phase transitions in $Pr_{0.7}Ca_{0.3}MnO_3$ at high pressures, JETP Letters 92, No. 9, 590-594

KOZLENKO, D.P.; CHAN, T.A.; TRUKHANOV, A.V.; KICHANOV, S.E.; TRUKHANOV, S.V.; DUBROVINSKY, L.S.; SAVENKO, B.N. (2011): Effect of high pressure on the crystal and magnetic structure and on the Raman spectra of $Pr_{0.7}Ba_{0.3}MnO_3$ manganite. JETP Letters 94, No. 7, 579-584

LITASOV, K.D.; SHATSKIY, A.; OHTANI, E.; KATSURA, T. (2011): Systematic study of hydrogen incorporation into Fe-free wadsleyite. Physics and Chemistry of Minerals 38, 75-84

LONGO, M.; MCCAMMON, C.; JACOBSEN, S. (2011): Microanalysis of the iron oxidation state in (Mg,Fe)O and application to the study of microscale processes. Contributions to Mineralogy and Petrology 162, 1249-1257

MANAKOV, A.Yu.; LIKHACHEVA, A.Yu.; POTEMKIN, V.A.; OGIENKO, A.G.; KURNOSOV, A.V.; ANCHAROV, A.I. (2011): Compressibility of gas hydrates. ChemPhysChem 12, 2476-2484

MANTHILAKE, M.A.G.M.; DE KOKER, N.; FROST, D.J.; MCCAMMON, C.A. (2011): Lattice thermal conductivity of lower mantle minerals and heat flux from Earth's core. Proceedings of the National Academy of Sciences 108 (44), 17901-17904

MANTHILAKE, M.A.G.M.; DE KOKER, N.; FROST, D.J. (2011): Thermal conductivity of $CaGeO_3$ perovskite at high pressure. Geophysical Research Letters 38, L08301, doi: 10.1029/2011GL046882

MANTOVANI, M.; ESCUDERO, A.; BECERRO, A.I. (2011): Influence of OH^- concentration on the illitization of kaolinite at high pressure. Applied Clay Science 51, 220-225

MAO, Z.; JACOBSEN, S.D.; FROST, D.J.; MCCAMMON, C.A.; HAURI, E.H.; DUFFY, T.S. (2011): Effect of hydration on the single-crystal elasticity of Fe-bearing wadsleyite. American Mineralogist 96, 1606-1612

MAO, Z.; LIN, J.F.; SCOTT, H.P.; WATSON, H.C.; PRAKAPENKA, V.B.; XIAO, Y.; CHOW, P.; MCCAMMON, C. (2011): Iron-rich perovskite in the Earth's lower mantle. Earth and Planetary Science Letters 309, 179-184

MATIZAMHUKA, W.; SIGALAS, I.; HERRMANN, M.; DUBRONVINSKY, L.; DUBROVINSKAIA, N.; MIYAJIMA, N.; MERA, G.; RIEDEL, R. (2011): High pressure-high temperature phase transition of a cubic BC_2N phase from a polymer derived t-BC_2N ceramic. Materials 4, 2061-2072

MCCORMACK, R.; DOBSON, D.P.; WALTE, N.P.; MIYAJIMA, N.; TANIGUCHI, T.; WOOD, I.G. (2011): The development of shape- and crystallographic-preferred orientation in $CaPtO_3$ post-perovskite deformed in pure shear. American Mineralogist 96, 1630-1635

MIKHAILOVA, D.; BRAMNIK, N.N.; BRAMNIK, K.G.; REICHEL, P.; OSWALD, S.; SENYSHYN, A.; TROTS, D.M.; EHRENBERG, H. (2011): Layered Li_xMoO_2 phases with different composition for electrochemical application: structural considerations. Chemistry of Materials 23, 3429-3441

MITTAL, R.; MISHRA, S.K.; CHAPLOT, S.L.; OVSYANNIKOV, S.V.; GREENBERG, E.; TROTS, D.M.; DUBROVINSKY, L.; SU, Y.; BRUECKEL, Th.; MATSUISHI, S.; HOSONO, H.; GARBARINO, G. (2011): Ambient- and low-temperature synchrotron X-ray diffraction study of $BaFe_2As_2$ and $CaFe_2As_2$ at high pressures up to 56 GPa. Physical Review B 83, 054503

MITTAL, R.; MISHRA, S.K.; CHAPLOT, S.L.; OVSYANNIKOV, S.V.; GREENBERG, E.; TROTS, D.M.; DUBROVINSKY, L.; SU, Y.; BRUECKEL, Th.; MATSUISHI, S.; HOSONO, H.; GARBARINO, G. (2011): High-pressure structural phase transitions in FeAs based compounds at ambient and low temperatures. AIP Conference Proceedings 1349, 103-104

MIYAHARA, M.; OHTANI, E.; OZAWA, S.; KIMURA, M.; EL GORESY, E.; SAKAI, T.; NAGASE, T.; HIRAGA, K.; HIRAO, N.; OHISHI, Y. (2011): Natural dissociation of olivine to perovskite and magensiowüstite in a Martian meteorite. Proceedings of the National Academy of Sciences 1016921108, 105

MONDAL, S.; VAN SMAALEN, S.; SCHOENLEBER, A.; FILINCHUK, Y.; CHERNYSHOV, D.; SIMAK, S.; MIKHAYLUSHKIN, A.; ABRIKOSOV, I.; ZARECHNAYA, E.; DUBROVINSKY, L.; DUBROVINSKAIA, N. (2011): Electron-deficient and polycenter bonds in the high-pressure gamma-B-28 phase of boron. Physical Review Letters 106, 215502

MOOKHERJEE, M. (2011): Elasticity and anisotropy of Fe_3C: implications for the Earths inner core. American Mineralogist 96, 1530-1536

MOOKHERJEE, M. (2011): Mid-mantle anisotropy: Elasticity of aluminous phases in subducted MORB. Geophysical Research Letters 38, L14302

MOOKHERJEE, M.; CAPITANI, G.C. (2011): Trench parallel anisotropy and large delay times: Elasticity and anisotropy of antigorite at high pressures. Geophysical Research Letters 38, L09315, doi: 10.1029/2011GL047160

MOOKHERJEE, M.; NAKAJIMA, Y.; STEINLE-NEUMANN, G.; GLAZYRIN, K.; WU, X.; DUBROVINSKY, L.; MCCAMMON, C.; CHUMAKOV, C.A. (2011): High-pressure behavior of iron carbide (Fe_7C_3) at inner core conditions. Journal of Geophysical Research 116, B04201, doi: 10.1029/2010JB007819

NAKAJMA, Y. (2011): Possible role of carbon and hydrogen in the Earth's core. The Review of High Pressure Science and Technology 21, 98-108

NAKAJMA, Y.; TAKAHASHI, E.; SATA, N.; NISHIHARA, Y.; HIROSE, K.; FUNAKOSHI, K.; OHISHI (2011): Thermoelastic property and high-pressure stability of Fe_7C_3: Implication for iron-carbide in the Earth's core. American Mineralogist 96, 1158-1165

NARYGINA, O.; DUBROVINSKY, L.S.; SAMUEL, H.; MCCAMMON, C.; KANTOR, I.; GLAZYRIN, K.; PASCARELLI, S.; AQUILANTI, G.; PRAKAPENKA, V. (2011): Chemically homogeneous spin transition zone in Earth's lower mantle. Physics of the Earth and Planetary Interiors 185, 107-111

NARYGINA, O.; DUBROVINSKY, L.; MCCAMMON, C.; KURNOSOV, A.; KANTOR, I.; PRAKAPENKA, V.; DUBROVINSKAIA, N. (2011): X-ray diffraction and Mossbauer spectroscopy study of fcc iron hydride FeH at high pressures and implications for the composition of the Earth's core. Earth and Planetary Science Letters 307, 409-414

NARYGINA, O.; DUBROVINSKY, L.; MIYAJIMA, N.; MCCAMMON, C.A.; KANTOR, I.Y.; MEZOUAR, M.; PRAKAPENKA, V.B.; DUBROVINSKAIA, N.; DMITRIEV, V. (2011): Phase relations in the Fe-Ni-C system at high pressures and temperatures: Implications for the Earth's Core. Physics and Chemistry of Minerals 38, 203-214

NESTOLA, F.; PASQUAL, D.; SMYTH, J.R.; NOVELLA, D.; SECCO, L.; MANGHNANI, M.H.; DAL NEGRO, A. (2011): New accurate elastic parameters for the forsterite-fayalite solid solution. American Mineralogist 96, No. 11-12, 1742-1747

NI, H.; KEPPLER, H.; MANTHILAKE, M.A.G.M.; KATSURA, T. (2011): Electrical conductivity of dry and hydrous $NaAlSi_3O_8$ glasses and liquids at high pressures. Contributions to Mineralogy and Petrology 162, 501-513

NI, H.; KEPPLER, H.; BEHRENS, H. (2011): Electrical conductivity of hydrous basaltic melts: implications for partial melting in the upper mantle. Contributions to Mineralogy and Petrology 162, 637-650

NI, H.; DE KOKER, N. (2011): Thermodynamics, diffusion and structure of $NaAlSi_2O_6$ liquid at mantle conditions: a first-principles molecular dynamics investigation. Journal of Geophysical Research 116, B09202, doi: 10.1029/2010JB008072

OVSYANNIKOV, S.V.; DUBROVINSKY, L.S. (2011): High-pressure high-temperature synthesis of Cr_2O_3 and Ga_2O_3. High Pressure Research 31, 23-29

PANDOLFO, F.; BOFFA BALLARAN, T.; NESTOLA, F.; KOCH MÜLLER, M.; MROSKO, M.; BRUNO, E. (2011): High-pressure $I2/c$-$P2_1/c$ phase transformation in $SrAl_2Si_2O_8$ feldspar. American Mineralogist 96, 1182-1185

PARAKHONSKIY, G.; DUBROVINSKAIA, N.; BYKOVA, E.; WIRTH, R.; DUBROVINSKY, L. (2011): Experimental pressure-temperature phase diagram of boron: resolving the long-standing enigma. Nature Scientific Reports 1, 96, doi: 10.1038/srep00096

PARAKHONSKIY, G.; DUBROVINSKAIA, N.; DUBROVINSKY, L.; MONDAL, S.; VAN SMAALEN, S. (2011): High pressure synthesis of single crystals of alpha-boron. Journal of Crystal Growth 321, 162-166

PETTKE, T.; OBERLI, F.; AUDÉTAT, A.; WIECHERT, U.; HEINRICH, C.A. (2011): Quantification of transient signals in multiple collector inductively coupled plasma mass spectrometry: Accurate lead isotope ratio determination by laser ablation of individual fluid inclusions. Journal of Analytical Atomic Spectrometry 26, 465-636

POKROVSKI, G.S.; DUBROVINSKY, L.S. (2011): The S_3^- ion is stable in geological fluids at elevated temperatures and pressures. Science 331, 1052-1054

POLLOK, K.; PUTNIS, C.V.; PUTNIS, A. (2011): Mineral replacement reactions in solid solution-aqueous solution systems: Volume changes, reactions paths and end-points using the example of model salt systems. American Journal of Science 311, 211-236

PRESCHER, C.; LANGENHORST, F.; HORNEMANN, U.; DEUTSCH, A. (2011): Shock experiments on anhydrite and new constraints on the impact induced SO_x release at the K-Pg boundary. Meteoritics & Planetary Science 46(11), 1619-1629

RUBIE, D.C.; FROST, D.J.; MANN, U.; ASAHARA, Y.; NIMMO, F.; TSUNO, K.; KEGLER, P.; HOLZHEID, A.; PALME, H. (2011): Heterogeneous accretion, composition and core-mantle differentiation of the Earth. Earth and Planetary Science Letters 301 (1-2), 31-42, doi: 10.1016/j.epsl.2010.11.030

QUI, N.V.; SCHOLZ, P.; KRECH, T.; KELLER, T.; POLLOK, K.; ONDRUSCHKA, B. (2011): Multiwalled carbon nanotubes oxidized by UV/H_2O_2 as catalyst for oxidative dehydrogenation of ethylbenzene. Catalysis Communications 12, 464-469

SAMUEL, H.; ALEKSANDROV, V.; DEO, B. (2011): The effect of continents on mantle convective stirring efficiency. Geophysical Research Letters 38, L04307, doi: 10.1029/2010GL046046, 2011

SCHILLING, J.; WU, F.-Y.; MCCAMMON, C.; WENZEL, T.; MARKS, M.A.W.; PFAFF, K.; JACOB, D.E.; MARKL, G. (2011): The compositional variability of eudialyte-group minerals. Mineralogical Magazine 75, 87-115

SCHOLLENBRUCH, K.; WOODLAND, A.B.; FROST, D.J.; WANG, Y.; SANEHIRA, T.; LANGENHORST, F. (2011): In situ determination of the spinel post-spinel transition in Fe_3O_4 at high pressure and temperature by synchrotron X-ray diffraction. American Mineralogist 96 (5-6), 820-827

SCHOUWINK, P.; DUBROVINSKY, L.; GLAZYRIN, K.; MERLINI, M.; HANFLAND, M.; PIPPINGER, T.; MILETICH, R. (2011): High-pressure structural behavior of α-Fe_2O_3 studied by single-crystal X-ray diffraction and synchrotron radiation up to 25 GPa. American Mineralogist 96, 1781-1786

SHATSKIY, A.; BORZDOV, Y.M.; LITASOV, K.D.; OHTANI, E.; KHOKHRYAKOV, A.F.; PAL'YANOV, Y.N.; KATSURA, T. (2001): Pressless split-sphere apparatus equipped with scaled-up Kawai-cell for mineralogical studies at 10-20 GPa. American Mineralogist 96, 541-548

SINMYO, R.; HIROSE, K.; MUTO, S.; OHISHI, Y.; YASUHARA, A. (2011): The valence state and partitioning of iron in the Earth’s lowermost mantle. Journal of Geophysical Research 116, B07205, doi: 10.1029/2010JB008179

SMITH, E.M.; KOPYLOVA, M.G.; DUBROVINSKY, L.; NAVON, O.; RYDER, J.; TOMLINSON, E.L. (2011): Transmission X-ray diffraction as a new tool for diamond fluid inclusion studies. Mineralogical Magazine 75, 2657-2675

SOUGAWA, M.; SUMIYA, T.; TAKARABE, K.; MORI, Y.; OKADA, T.; GOTOU, H.; YAGI, T.; YAMAZAKI, D.; TOMIOKA, N.; KATSURA, T.; KARIYAZAKI, H.; SUEOKA, K.; KUNITSUGU, S. (2001): Crystal structure of new carbon-nitride-related material $C_2N_2(CH_2)$. Japanese Journal of Applied Physics 50, 095503

SPIVAK, A.V.; DUBROVINSKY, L.S.; LITVIN, Yu.A. (2011): Congruent melting of calcium carbonate in a static experiment at 3500 K and 10-22 GPa: Its role in the genesis of ultradeep diamonds. Doklady Earth Sciences 439, 1171-1174

STAGNO, V.; TANGE, Y.; MIYAJIMA, N.; MCCAMMON, C.A.; IRIFUNE, T.; FROST, D.J. (2011): The stability of magnesite in the transition zone and the lower mantle as a function of oxygen fugacity. Geophysical Research Letters 38, L19309, doi: 10.1029/2011GL049560

STENETEG, P.; CHIRITA, V.; DUBROVINSKAIA, N.; DUBROVINSKY, L.; ABRIKOSOV, I. (2011): Missing-atom structure of diamond Sigma 5 (001) twist grain boundary. Physical Review B 83, 144112

SUN, N.; STIXRUDE, L.; DE KOKER, N.; KARKI, B.B. (2011): First principles molecular dynamics simulations of diopside ($CaMgSi_2O_6$) liquid to high pressure. Geochimica et Cosmochimica Acta 75, 3792-3802

SUSHIL, S.; SCHOLZ, P.; POLLOK, K.; ONDRUSCHKA, B.; BATRA, V.S. (2011): Application of industrial waste based catalysts for total oxidation of propane. Chemical Engineering Journal 166, 568-578

TOMLINSON, E.L.; HOWELL, D.; JONES, A.P.; FROST, D.J. (2011): Characteristics of HPHT diamond grown at sub-lithosphere conditions (10-20 GPa). Diamond and Related Materials 20 (1), 11-17

TROTS, D.M.; KURNOSOV, A.; VASYLECHKO, L.; BERKOWSKI, M.; BOFFA BALLARAN, T.; FROST, D.J. (2011): Elasticity and equation of state of $Li_2B_4O_7$. Physics and Chemistry of Minerals 38 (7), 561-567

TSUNO, K.; FROST, D.J.; RUBIE, D.C. (2011): The effects of nickel and sulphur on the core-mantle partitioning of oxygen in Earth and Mars. Physics of Earth and Planetary Interiors 185 (1-2), 1-12

URAKAWA, S.; MATSUBARA, R.; KATSURA, T.; WATANABE, T.; KIKEGAWA, T. (2011): Stability and bulk modulus of Ni_3S, a new nickel sulfur compound, and the melting relations of the system Ni-NiS up to 10 GPa. American Mineralogist 96, 558-565

WALTE, N.P.; RUBIE, D.C.; BONS, P.D.; FROST, D.J. (2011): Deformation of a crystalline aggregate with a small percentage of high-dihedral-angle liquid: Implications for core-mantle differentiation during planetary formation. Earth and Planetary Science Letters 305 (1-2), 124-134, doi: 10.1016/j.epsl.2011.02.049

WEI, Q.; DUBROVINSKAIA, N.; DUBROVINSKY, L. (2011): Ruby and Sm:YAG fluorescence pressure gauges up to 120 GPa and 700 K. Journal of Applied Physics 110, 043513

WU, X.; MOOKHERJEE, M.; GU, T.; QIN, S. (2011): Elasticity and anisotropy of iron-nickel phosphides at high pressures. Geophysical Research Letters 38, L20301

YAMAZAKI, D.; ITO, E.; KATSURA, T.; YOSHINO, T.; ZHAI, S.M.; FUKUI, H.; SHATSKIY, A.; GUO, X.Z.; SHAN, S.M.; OKUCHI, T.; TANGE, Y.; HIGO, Y.; FUNAKOSHI, K: (2011): Phase boundary between perovskite and post-perovskite structures in $MnGe_3$ determined by in situ X-ray diffraction measurements using sintered diamond anvils. American Mineralogist 96, 89-92

YANG, X. (2011): Origin of high electrical conductivity in the lower continental crust: a review. Surveys in Geophysics 32 (6), 875-903, doi: 10.1007/s10712-011-9145-z

YANG, X.; HEIDELBACH, F. (2011): Grain size effect on the electrical conductivity of clinopyroxene. Contributions to Mineralogy and Petrology (published online) doi: 10.1007/s00410-011-0707-3

YANG, X.; KEPPLER, H. (2011): In-situ infrared spectra of OH in olivine to 1100 °C. American Mineralogist 96, 451-454

YANG, X.; KEPPLER, H.; MCCAMMON, C.; NI, H. (2011): Electrical conductivity of orthopyroxene and plagioclase in the lower crust. Contributions to Mineralogy and Petrology 163, 33-48, doi: 10.1007/s00410-011-0657-9

YANG, X.; KEPPLER, H.; MCCAMMON, C.; NI, H.; XIA, Q.; FAN, Q. (2011): Effect of water on the electrical conductivity of lower crustal clinopyroxene. Journal of Geophysical Research 116, B04208, doi: 10.1029/2010JB008010

YOSHINO, T.; ITO, E.; KATSURA, T.; YAMAZAKI, D.; SHAN, S.M.; GUO, X.Z.; NISHI, M.; HIGO, Y.; FUNAKOSHI, K. (2011): Effect of iron content on electrical conductivity of ferropericlase with implications for the spin transition pressure. Journal of Geophysical Research – Solid Earth 116, B04202

XIONG, X.; KEPPLER, H.; AUDÉTAT, A.; NI, H.; SUN, W.; LI, Y. (2011): Partitioning of Nb and Ta between rutile and felsic melt and the fractionation of Nb/Ta during partial melting of hydrous metabasalt. Geochimica et Cosmochimica Acta 75, 1673-1692

ZHANG, L.; AUDÉTAT, A. (2011): Solubility of molybdenite (MoS_2) in aqueous fluids at 600-800 °C, 200 MPa: a synthetic fluid inclusion study. Geochimica et Cosmochimica Acta 77, 175-185

b) Popular scientific magazines

DE KOKER, N. (2011): Less of a Surprise – earthquake early warning in Japan. Civil Engineering, April 2011, 4-6

5.2 Publications (submitted, in press)

ADJAOUD, O.; STEINLE-NEUMANN, G.; JAHN, S.: Transport properties of Mg_2SiO_4 liquid at high pressure: Physical state of a magma ocean. Earth and Planetary Science Letters (in press)

AUDÉTAT, A.; LOWENSTERN, J.B.: Melt inclusions. – In: TUREKIAN, K.K.; HOLLAND, H.D. (Eds.): Treatise on Geochemistry 12 (submitted)

AUDÉTAT, A.; SIMON, A.: Magmatic controls on porphyry Cu genesis. – In: HEDENQUIST, J.; HARRIS, M.; CAMUS, F. (Eds.): Geology and genesis of major copper deposits and districts of the world: a tribute to Richard Sillitoe (submitted)

BERNINI, D.; AUDÉTAT, A.; DOLEJS, D.; KEPPLER, H.: Zircon solubility in aqueous fluid at high temperatures and pressures. Geochimica et Cosmochimica Acta (submitted)

BOFFA BALLARAN, T.; KURNOSOV, A.; GLAZYRIN, K.; FROST, D.J.; MERLINI, M.; HANFLAND, M.; CARACAS, R.: Effect of chemistry on the compressibility of silicate perovskite in the lower mantle. Earth an Planetary Science Letters (submitted)

BOLFAN-CASANOVA, N.; MUÑOZ, M.; MCCAMMON, C.; DELOULE, E.; FÉROT, A.; DEMOUCHY, S.; FRANCE, L.; ANDRAULT, D.; PASCARELLI, S.: Ferric iron and water incorporation in wadsleyite under hydrous and oxidizing conditions: a XANES and SIMS study. American Mineralogist (submitted)

BULL, J.N.; TENNANT, W.C.; BOFFA BALLARAN, T.; MCCAMMON, C.A.; NESTOLA, F.: Anisotropic mean-squared-displacement tensor in cubic almandine garnet: a combined ^{57}Fe Mössbauer and X-ray single crystal study. Physics and Chemistry of Minerals (submitted)

COCHAIN, B.; NEUVILLE, D.R.; HENDERSON, G.S.; MCCAMMON, C.; PINET, O.; RICHET, P.: Iron content, redox state and structure of sodium borosilicate glasses: A Raman, Mössbauer and boron K-edge XANES spectroscopy study. Journal of the American Ceramic Society (in press)

DE KOKER, N.: Melting of cubic boron nitride at extreme pressures from first-principles. Physical Review B (submitted)

DE KOKER, N.; STEINLE-NEUMANN, G.; VLČEK, V.: Electrical resistivity and thermal conductivity of liquid Fe alloys at high *P* and *T*, and heat flux in Earth's core. Proceedings of the National Academy of Sciences (in press)

DE KOKER, N.; KARKI, B.B.; STIXRUDE, L.: Multi-component melting of Earth's lowermost mantle from first-principles. Nature (submitted)

ESCUDERO, A.; MIYAJIMA, M.; LANGENHORST, F.: Microstructure, composition and P-T conditions of rutile from diamondiferous gneiss of the Saxonian Erzgebirge, Germany. Chemie der Erde – Geochemistry (in press) doi: 10.1016/j.chemer.2011.11.001

ESCUDERO, A.; LANGENHORST, F.: Incorporation of Si into TiO_2 phases at high pressure. American Mineralogist (in press)

ESCUDERO, A.; LANGENHORST, F.; MÜLLER, W.F.: Aluminum solubility in rutile at high pressure and experimental evidence for a $CaCl_2$ structured polymorph. American Mineralogist (submitted)

ESCUDERO, A.; LANGENHORST, F.: Aluminum incorporation in $\alpha - PbO_2$ type TiO_2 at pressures up to 20 GPa. Physics of the Earth and Planetary Interiors (submitted)

ESCUDERO, A.; LANGENHORST, F.: Chromium incorporation in rutile (TiO_2) at high pressure. Journal of Solid State Chemistry (submitted)

EVONUK, M.; SAMUEL, H.: Simulating rotating fluid bodies: When is vorticity generation via density-stratification important? Earth and Planetary Science Letters (accepted)

GLAZYRIN, K.; MCCAMMON, C.; DUBROVINSKY, L.; MERLINI, M.; SCHOLLENBRUCH, K.; WOODLAND, A.; HANFLAND, M.: Effect of high pressure on the crystal structure and electronic properties of magnetite below 25 GPa. American Minerologist (in press)

GU, T.; WU, X.; QIN, S.; MCCAMMON, C.; DUBROVINSKY, L.: Mössbauer spectroscopic study of pressure-induced phase transition of Fe_2P. Journal of Physics: Condensed Matter (submitted)

HELLIGE, K.; POLLOK, K.; LARESE-CASANOVA, P.; BEHRENDS, T.; PEIFFER, S.: Pathways of ferrous iron mineral formation upon sulfidation of lepidocrocite surfaces. Geochimica et Cosmochimica Acta (accepted)

HUANG, R.; AUDÉTAT, A.: A critical look at the titanium-in-quartz (TitaniQ) thermobarometer. Geochimica et Cosmochimica Acta (in press)

KEPPLER, H.: Volatiles under high pressure. Physics and Chemistry of the Deep Earth (Monograph, Wiley-Blackwell) (submitted)

LERCHBAUMER, L.; AUDÉTAT, A.: The 'quartz capsule' – a new method to avoid alloying problems with noble metal capsules in hydrothermal experiments. European Journal of Mineralogy (in press)

LERCHBAUMER, L.; AUDÉTAT, A.: Vapor or brine: which fluids formed porphyry copper deposits? Geochimica et Cosmochimica Acta (submitted)

LI, Y.; AUDÉTAT, A.: Partitioning of V, Mn, Co, Ni, Cu, Zn, As, Mo, Ag, Sn, Sb, W, Au, Pb, and Bi between sulfide phases and hydrous basanite melt at upper mantle conditions. Earth and Planetary Science Letters (submitted)

LIN, J.-F.; ALP, E.E.; MAO, Z.; INOUE, T.; MCCAMMON, C.; XIAO, Y.; CHOW, P.; ZHAO, J.: Electronic spin states of ferric and ferrous iron in the lower-mantle silicate perovskite. American Mineralogist (in press)

MANN, U.; FROST, D.J.; RUBIE, D.C.; BECKER, H.; AUDÉTAT, A.: Partitioning of Ru, Rh, Pd, Re, Ir and Pt between liquid metal and silicate at high pressures and high temperatures – Implications for the origin of highly siderophile element concentrations in the Earth’s mantle. Geochimica et Cosmochimica Acta (submitted)

MANTHILAKE, M.A.G.M.; MIYAJIMA, N.; HEIDELBACH, F.; FROST, D.J.: The effect of aluminum and water on the development of orthopyroxene fabrics. Tectonophysics (submitted)

MANTHILAKE, M.A.G.M.; FROST, D.J.; WALTE, N.: A new multi-anvil press employing six independently acting 800 tonne hydraulic rams. Physics of the Earth and Planetary Interiors (submitted)

MISHRA, S.K.; MITTAL, R.; CHAPLOT, S.L.; OVSYANNIKOV, S.V.; TROTS, D.M.; DUBROVINSKY, L.; SU, Y.; BRUECKEL, Th.; MATSUISHI, S.; HOSONO, H.; GARBARINO, G.: Pressure dependence of the low- temperature crystal structure and phase transition behaviour of CaFeAsF and SrFeAsF: A synchrotron x-ray diffraction study. Physical Review B (submitted)

MISHRA, S.K.; MITTAL, R.; CHAPLOT, S.L.; OVSYANNIKOV, S.V.; TROTS, D.M.; DUBROVINSKY, L.; SU, Y.; BRUECKEL, Th.; MATSUISHI, S.; HOSONO, H.; GARBARINO, G. (2011): Pressure-driven phase transition in CaFeAsF at 40 and 300 K. Journal of Physics: Conference Series (submitted)

MÜLLNER, M.; LUNKENBEIN, T.; SCHIEDER, M.; MIYAJIMA, N.; FÖRTSCH, M.; BREU, J.; CARUSO, F.; MÜLLER, A.H.E.: Template-directed mild synthesis of anatase nanotubes within cylindrical core-shell-corona polymer brushes. ACS Nano (submitted)

MÜLLNER, M.; LUNKENBEIN, T.; MIYAJIMA, N.; BREU, J.; MÜLLER, A.H.E.: A facile polymer templating route toward high aspect ratio crystalline titania nanostructures. Angewandte Chemie (submitted)

NALIBOFF, J.; LITHGOW-BERTELLONI, C.; RUFF, L.; DE KOKER, N.: The effects of lithospheric thickness and density structure on Earth's stress field. Geophysical Journal International (in press)

NI, H.: Compositional dependence of alkali diffusivity in silicate melts: mixed alkali effect and pseudo alkali effect. American Mineralogist (in press) doi: 10.2138/am.2012.3739

NI, H.; KEPPLER H.: In situ Raman spectroscopic study on sulfur speciation in oxidized magmatic hydrothermal fluids. American Mineralogist (submitted)

NIWA, K.; MIYAJIMA, N.; OHGUSHI, K.; GOTOU, H.; YAGI, T. (2010): In-situ observation of shear stress-induced perovskite to post-perovskite phase transition in $CaIrO_3$ and the development of its deformation texture in a diamond-anvil cell up to 30 GPa. Physics and Chemistry of Minerals (in press)

NISHIHARA, Y.; NAKAJIMA, Y.; AKASHI, A.; TSUJINO, N.; TAKAHASHI, E.; FUNAKOSHI, K.; HIGO, Y.: Isothermal compression of face-centered cubic iron. American Mineralogist (submitted)

NOVELLA, D.; KESHAV, S.; GUDFINNSSON, G.H.; GOSH, S.: Melting of simplified carbonated peridotite in the system CaO-MgO-Al_2O_3-SiO_2-CO_2 at 2-3 GPa: reconsideration of the carbonated peridotite solidus and calciocarbonatitic-silicate melt unmixing. Journal of Petrology (submitted)

OVSYANNIKOV, S.V.; WU, X.; KARKIN, A.E.; SHCHENNIKOV, V.V.; MANTHILAKE, M.A.G.M.; UHLARZ, M.; WOSNITZA, J.; DUBROVINSKAIA, N.; DUBROVINSKY, L.: Insight into a 'Golden Oxide': pressure-driven phase transitions, a P-T phase diagram and properties of Ti_2O_3 in the Th_2S_3-type phase. Physical Review B (submitted)

OTSUKA, K.; LONGO, M.; MCCAMMON, C.A.; KARATO, S.-I.: Ferric iron content of ferropericlase as a function of composition, oxygen fugacity, temperature and pressure: Implications for redox conditions during diamond formation in the lower mantle. Earth and Planetary Science Letters (submitted)

PALME, H.; KEGLER, P.; HOLZHEID, A.; FROST, D.J.; RUBIE, D.C.: Comment on "Prediction of metal-silicate partition coefficients for siderophile elements: An update and assessment of PT conditions for metal–silicate equilibrium during accretion of the Earth" by K. RIGHTER, Earth and Planetary Science Letters 304, 158-167, 2011. Earth and Planetary Science Letters (in press)

ROBINSON, P.; HARRISON, R.J.; MIYAJIMA, N.; MCENROE, S.A.; FABIAN, K. (2011): Chemical and magnetic properties of rapidly cooled metastable ferri-ilmenite solid solutions: implications for magnetic self-reversal and exchange bias, II. Chemical changes during quench and annealing. Geophysical Journal International (in press)

SAMUEL, H.: A re-evaluation of metal diapir breakup and equilibration in terrestrial magma oceans. Earth and Planetary Science Letters (in press)

SHCHEKA, S.; KEPPLER, H.: The origin of the terrestrial noble gas signature. Nature (submitted)

SITTE, J.; POLLOK, K.; LANGENHORST, F.; KÜSEL, K.: Nanocrystalline nickel and cobalt sulfides formed by a heavy metal-tolerant, sulfate-reducing enrichment culture. Geomicrobiology Journal (accepted)

SMYTH, J.R.; MIYAJIMA, N.; HUSS, G.R.; HELLEBRAND, E.; RUBIE, D.C.; FROST, D.J. (2011): Olivine-wadsleyite-pyroxene epitaxy: Evidence for coherent nucleation and diffusion-controlled growth at the 410-km discontinuity. Physics of Earth and Planetary Interiors (submitted)

SHCHENNIKOV, V.V.; MOROZOVA, N.V.; OVSYANNIKOV, S.V.: Similar behavior of thermoelectric properties of lanthanides under strong compression up to 20 GPa. Journal of Applied Physics (in press)

SHCHENNIKOV, V.V.; MOROZOVA, N.V.; TYAGUR, I.; TYAGUR, Y.; OVSYANNIKOV, S.V.: Colossal tuning of an energy gap in $Sn_2P_2S_6$ under pressure. Applied Physics Letters (in press)

SOUSTELLE, V.; TOMMASI, A.; DEMOUCHY, S.; FRANZ, L.: Effect of fluid-rock interactions on deformation and seismic properties of the oceanic sub-arc mantle: Microstructural study of mantle xenoliths from seamounts near Lihir Island, Papua-New-Guinea. Tectonophysics (submitted)

TAN, J.; WEI, J.; AUDÉTAT, A.: Source of metals in the Guocheng gold deposit, North China Craton: evidence for a link to mafic magmatism. Ore Geology Reviews (submitted)

TANG, Z.; STEINLE-NEUMANN, G.: Magnetic structure of Fe_2SiO_4 spinel from electronic structure and lattice dynamics calculations. Physical Review B (submitted)

TROTS, D.M.; KURNOSOV, A.; BOFFA BALLARAN, T.; FROST, D.J.: High-temperature structural behaviors of anhydrous wadsleyite and forsterite. American Mineralogist (submitted)

WU, X.; QIN, S.; GU, T-T.; MANTHILAKE, G.: Structural and elastic properties of $CaGeO_3$ perovskite at high pressure. Physics of the Earth and Planetary Interiors (in press)

XU, J.; YAMAZAKI, D.; KATSURA, T.; WU, X.; REMMERT, P.; CHAKRABORTY, S.; YURIMOTO, H.: Silicon and magnesium diffusion in single crystal of $MgSiO_3$ perovskite. Journal of Geophysical Research – Solid Earth (in press)

YANG, X.: Orientation-related electrical conductivity of hydrous olivine, clinopyroxene and plagioclase and implications for the structure of the lower continental crust and uppermost mantle. Earth and Planetary Science Letters (in press) doi: 10.1016/j.epsl.2011.11.011

YANG, X.; MCCAMMON, C.: Fe^{3+}-rich augite and high electrical conductivity in the deep lithosphere. Geology (in press) doi: 10.1130/G32725.1

YANG, X.; DUBROVINSKY, L.; MANTHILAKE, M.A.G.M.; WEI, Q.: High pressure and high temperature Raman spectroscopic study of hydrous wadsleyite (β-Mg_2SiO4). Physics and Chemistry of Minerals (in press) doi: 10.1007/s00269-011-0459-7

YANG, X.; KEPPLER, H.; MCCAMMON, C.; NI, H.: Electrical conductivity of orthopyroxene and plagioclase in the lower crust. Contributions to Mineralogy and Petrology (in press)

YANG, X.; MCCAMMON, C.: Fe^{3+}-rich augite and high electrical conductivity in the deep lithosphere. Geology (in press)

YOSHINO, T.; MCISAAC, E.; LAUMONIER, M.; KATSURA, T.: Electrical conductivity of partial molten carbonate peridotite. Physics of the Earth and Planetary Interiors (submitted)

ZANG, X.; DUBROVINSKY, L.; MANTHILAKE, M.A.G.M.; WEI, Q.: High pressure, high temperature Raman spectra of hydrous wadsleyite (β-Mg_2SiO_4). Physics and Chemistry of Minerals (in press)

ZHANG, L.; AUDÉTAT, A.: Solubility of molybdenite (MoS_2) in aqueous fluids at 600-800 °C, 200 MPa: a synthetic fluid inclusion study. Geochimica et Cosmochimica Acta (in press)

ZUCCHINI, A.; COMODI, P.; KATERINOPOULOU, A.; BALIC-ZUNIC, T.; MCCAMMON, C.; FRONDINI, F.: Order-disorder-reorder process in thermally treated dolomite samples: a combined powder and single crystal X-ray diffraction study. Physics and Chemistry of Minerals (submitted)

5.3 Presentations at scientific institutions and at congresses

ALÉON, J.; MARIN-CARBONNE, J.; MCKEEGAN, K.D.; EL GORESY, A.: 08.-12.08.2011, 74th Annual Meeting of the Meteoritical Society, London, U.K.: "Magnesium isotopes in the ultrarefractory CAI Efremovks 101,1: Evidence of open system behavior"

ALEKSANDROV, V.; SAMUEL, H.: 20.-25.08.2011, 12th International Workshop on Modeling of Mantle Convection and Lithospheric Dynamics, Groß Dölln, Germany: "A parallel direct-iterative solver using domain decomposition approach for geodynamic modeling"

AUDÉTAT, A.: 07.-08.09.2011, Fermor Meeting 2011, London, U.K. *(invited)*: "The role of magmatic sulfides and low-density fluids in the formation of porphyry-type ore deposits"

BERNINI, D.; DOLEJŠ, D.; DE KOKER, N.; AUDÉTAT, A.; KEPPLER, H.; WIEDENBECK, M.: 14.-19.08.2011, Goldschmidt Conference 2011, Prague, Czech Republic: "Solubility of fluorine and chlorine in nominally anhydrous mantle minerals: Implication for mantle metasomatism and arc magmas", Mineralogical Magazine, Vol. 75 (3), 521

BOFFA BALLARAN, T.; KURNOSOV, A.; GLAZYRIN, K.; FROST, D.J.; MERLINI, M.; HANFLAND, M.: 14.-19.08.2011, Goldschmidt Conference 2011, Prague, Czech Republic: "Structural distortion of $MgSiO_3$ perovskite and the influence of Fe and Al at pressures of the Earth's lower mantle", Mineralogical Magazine, Vol. 75 (3), 542

BOFFA BALLARAN, T.; KURNOSOV, A.; GLAZYRIN, K.; FROST, D.J.; MERLINI, M.; HANFLAND, M.; CARACAS, R.: 10.-13.10.2011, CECAM Workshop on Dynamical Properties of Earth and Planetary Materials, Lausanne, Switzerland: "Effect of Fe and Al substitution on the elastic properties of perovskite: a single-crystal diffraction study up to 75 GPa "

BOFFA BALLARAN, T.; KURNOSOV, A.; GLAZYRIN, K.; FROST, D.J.; MERLINI, M.; HANFLAND, M.; CARACAS, R.: 14.11.2011, European Seminar Series in Earth Sciences, Ecole Normale Superieure de Lyon, France: "The effect of cation substitution on the structural distortion of $MgSiO_3$ perovskite at pressures of the Earth's lower mantle"

BOFFA BALLARAN, T.: 15.11.2011, Ecole Normale Superieure de Lyon, France, "High-pressure crystallography" (lecture + practical)

BOLFAN-CASANOVA, N.; MUNOZ, M.; MCCAMMON, C.; DELOULE, E.; FEROT, A.; DEMOUCHY, S.; FRANCE, L.; ANDRAULT, D.; PASCARELLI, S.: 14.-19.08.2011, Goldschmidt Conference 2011, Prague, Czech Republic: "Ferric iron and water incorporation in wadsleyite under hydrous and oxidizing conditions", Mineralogical Magazine, Vol. 75 (3), 547

BOYET, M.; EL GORESY, A.; MIYAHARA, M.; GANNOUN, A.: 08.-12.08.2011, 74th Annual Meeting of the Meteoritical Society, London, U.K.: "A new meteorite type: Forsterite chondrite with EH-3 affinity – Sahara 97158"

BYKOVA, E.; GREENBERG, E.; GLAZYRIN, K.; BOFFA BALLARAN, T.; DUBROVINSKAIA, N.; DUBROVINSKY, L.: 20.-24.09.2011, Joint Meeting DGK, DMG and OMG 'Crystals, Minerals and Materials', Salzburg, Germany: "High pressure behavior of α-FeOOH studied on powder and single crystal samples"

CAILLET KOMOROWSKI, C.; BOUDOUMA, O.; REYNARD, B.; VAN DE MOORTÈLE, B.; EL GORESY, A.: 08.-12.08.2011, 74th Annual Meeting of the Meteoritical Society, London, U.K.: "Insights on the thermal history of the Paris CM chondrite based on the phase relations of its opaque assemblages"

CLAY, P.L.; BUSEMANN, H.; EL GORESY, A.: 08.-12.08.2011, 74th Annual Meeting of the Meteoritical Society, London, U.K.: "Petrography and chemistry of djerfisherite in enstatite chondrites"

CLAY, P.; BUSEMANN, H.; EL GORESY, A.; WIELER, R.: 07.-09.11.2011, Workshop on 'Formation of the First Solids in the Solar System', Koloa, Hawaii, USA: "Petrography, chemistry and noble gas cosmochemistry of nebula condensate djerfisherite in enstatite chondrites"

DE KOKER, N.; STEINLE-NEUMANN, G.; VLČEK, V.: 20.01.2011, SPP 1488 Annual Meeting, Tutzing, Germany: "Electrical and thermal conductivity of liquid iron in Earth's core"

DE KOKER, N.; MANTHILAKE, G.; FROST, D.: 28.02.-02.03.2011, 4th Berichtskolloquium of the SPP 1236 'Structures and characteristics of crystals at extremely high pressures and temperatures', Hünfeld, Germany: "Combining experimental and computational approaches to determine high P and T thermal conductivity of $CaGeO_3$ and $MgSiO_3$ perovskite"

DE KOKER, N.; STEINLE-NEUMANN, G.; VLČEK, V.: 03.-08.04.2011, European Geosciences Union General Assembly 2011, Vienna, Austria: "Thermal conductivity of Earth's liquid outer core from first-principles calculations"

DE KOKER, N.; MANTHILAKE, G.; FROST, D.: 03.-08.04.2011, European Geosciences Union General Assembly 2011, Vienna, Austria: "Thermal conductivity of the lowermost mantle"

DE KOKER, N.: 11.05.2011, Charles University, Geology Department, Prague, Czech Republic: "First-principles computations of thermal conductivity in the deep Earth"

DE KOKER, N.; STIXRUDE, L.; KARKI, B.: 12.05.2011, Charles University, Geology Department, Prague, Czech Republic: "Melting the deep mantle: Magma oceans and ultra-low velocity zones"

DE KOKER, N.; STIXRUDE, L.; KARKI, B.: 19.05.2011, Universität Münster, Institut für Mineralogie, Münster, Germany: "Incongruent melting of Earth's lowermost mantle"

DE KOKER, N.; STEINLE-NEUMANN, G.; VLČEK, V.: 12.07.2011, International Research Frontier Seminar, Ehime University, Geodynamics Research Center, Matsuyama, Japan: "Electrical and thermal conductivity of Fe, Fe-Si and Fe-O liquid alloys at extreme pressure and temperature conditions"

DE KOKER, N., STIXRUDE, L.; KARKI, B.: 14.-19.08.2011, Goldschmidt Conference 2011, Prague, Czech Republic *(keynote lecture)*: "Melting at extreme conditions: Insights from first-principles molecular dynamics", Mineralogical Magazine, Vol. 75 (3), 736

DE KOKER, N.: 29.09.2011, University of the Witwatersrand, Department of Physics, Johannesburg, South Africa: "Melting at extreme pressures in phases of technological and planetary importance computed from first principles"

DUBROVINSKY, L.S.: 28.02.-02.03.2011, 4th Berichtskolloquium of the SPP 1236 'Structures and characteristics of crystals at extremely high pressures and temperatures', Hünfeld, Germany: "Elasticity of iron and iron-based alloys at conditions of the Earth's and planetary cores"

DUBROVINSKY, L.S.: 14.-18.03.2011, ICDD Spring Meetings, ICDD Headquarters, Newtown Square, USA *(plenary lecture)*: "Look at the Earth's interior with X-rays through a diamond window"

DUBROVINSKY, L.; MCCAMMON, C.; GLAZYRIN, K.; POTAPKIN, V.; NARYGINA, O.; MERLINI, M.; KANTOR, I.; HANFLAND, M.; CHUMAKOV, A.: 13.-17.06.2011, 7th Seeheim Workshop on Mössbauer Spectroscopy, Frankfurt/M., Germany: "Nuclear resonance and Mössbauer spectroscopy in laser-heated DACs: Electronic behaviour of iron in Earth's lower mantle minerals"

DUBROVINSKY, L.S.; GLAZYRIN, K.; MCCAMMON, C.A.; KANTOR, A.; DUBROVINSKAIA, N.A.; PRAKAPENKA, V.; MERLINI, M.; HANFLAND, M.; CUMAKOV, A.; PASCARELLI, S.: 14.-19.08.2011, Goldschmidt Conference 2011, Prague, Czech Republic *(keynote lecture)*: "High pressure geochemistry in laser-heated diamond anvil cells with synchrotron light", Mineralogical Magazine, Vol. 75 (3), 787

EL GORESY, A.: 21.06.2011, Chinese Academy of Sciences, Institute of Geology and Geophysics, Beijing, China: "Forty years research on shocked igneous Martian rocks: Discrepant equilibrium shock-pressure estimates and the resulting controversial radiometric ages"

EL GORESY, A.: 30.06.2011, Chinese Academy of Sciences, Institute of Geology and Geophysics, Beijing, China: "Mineralogy, Petrology, Chosmochemistry, REE Abundances in Enstatite Chondrites and in Almahata Sitta EL-3 Chondrite Fragment"

EL GORESY, A.; BOYET, M.; MIYAHARA, M.: 08.-12.08.2011, 74th Annual Meeting of the Meteoritical Society, London, U.K.: "Almahata Sitta MS-17 EL-3 chondrite: Contrasting oldhamite assemblages in chondrules and matrix and significant oldhamite REE-patterns"

EL GORESY, A.; BOYET, M.; DUBROVINSKY, L.; LIN, Y.; FENG, L.; MOSTEFAOUI, S.; MIYAHARA, M.: 17.-19.10.2011, 2nd Annual Meeting of the SPP 1385 'The First 10 Million Years of the Solar System – a Planetary Materials Approach', Mainz, Germany: "Mineralogical and chemical study of the earliest solar condensates in unequilibrated enstatite chondrites"

EVONUK, M.: 20.-25.08.2011, 12th International Workshop on Modeling of Mantle Convection and Lithospheric Dynamics, Groß Dölln, Germany: "Scaling of vorticity generation due to density stratification: Implications for the Earth"

FEI, H.; KATSURA, T.; CHAKRABORTY, S.; DOHMEN, R.; HEGODA, C.; YAMAZAKI, D.; WIEDENBECK, M.; YURIMOTO, H.; SHCHEKA, S.; POLLOK, K.; AUDÉTAT, A.: 14.-19.08.2011, Goldschmidt Conference 2011, Prague, Czech Republic: "Silicon self-diffusion in forsterite, revisited", Mineralogical Magazine, Vol. 75 (3), 834

FROST, D.J.: 22.02.2011, Carnegie Institution of Washington, Geophysical Laboratory, Washington, DC, USA: "The cycling of volatiles through the Earth's mantle"

FROST, D.J.; STAGNO, V.; MCCAMMON, C.M.: 21-26.02.2011, Short course 'Diamonds, the mantle petrologist's best friends', Brixen, Italy: "Mantle oxygen fugacity and the speciation of carbon"

FROST, D.J.: 14-15.07.2011, Workshop 'Blowing the Earth's trumpet: New insights into deep volatiles and volatile-rich magmas', University of Bristol, Department of Earth Sciences, Bristol, U.K.: "Upper mantle oxygen fugacity and its effect on the speciation of volatile elements"

FROST, D.J.: 29.11.2011, Technische Universität Bergakademie Freiberg, Freiberger Hochdruckforschungszentrum, Freiberg, Germany: "Investigating the Earth's interior through high pressure and temperature laboratory studies"

FUJI-TA, K.; SEKI, M.; KATSURA, T.; ICHIKI, M.: 28.06.-07.07.2011, The XXV IUGG General Assembly, 'Earth on the Edge: Science for a Sustainable Planet', Melbourne, Australia: "An electrical conductivity network model within the hydrous rock and mineral"

GIANNINI, M.; BOFFA BALLARAN, T.; LANGENHORST, F.; BISCHOFF, A.: 08.-12.08.2011, 74th Annual Meeting of the Meteoritical Society, London, U.K.: "TEM-EELS study of titanium oxidation state in meteoritic hibonites", Meteoritics & Planetary Science 46, A77

GIANNINI, M.; BOFFA BALLARAN, T.; LANGENHORST, F.: 17.-19.10.2011, 2nd Annual Meeting of the SPP 1385 'The First 10 Million Years of the Solar System – a Planetary Materials Approach', Mainz, Germany: "Crystal chemistry of hibonite as indicator for oxygen fugacities during solar nebula condensation"

GIANNINI, M.; BOFFA BALLARAN, T.; LANGENHORST, F.; BISCHOFF, A.: 07.-09.11.2011, Workshop on 'Formation of the First Solids in the Solar System', Koloa, Hawaii, USA: "TEM-EELS measurements of titanium oxidation state in hibonites"

GLAZYRIN, K.; DUBROVINSKY, L.; MCCAMMON, C.; KLOTZ, S.; HANSEN, Th.; MERLINI, M.; HANFLAND, M.; SCHOLLENBRUCH, K.; WOODLAND, A.: 25.07.2011, European Synchrotron Radiation Facility, Grenoble, France: "Fe-O system under extreme conditions: magnetite and wüstite"

HARRIES, D.; BERG, T.; PALME, H.; LANGENHORST, F.: 07.-09.11.2011, Workshop on 'Formation of the First Solids in the Solar System', Koloa, Hawaii, USA: "The fate of metals in the solar nebula: From condensation to oxidation, sulfidation, and nitridation" , Abstract 9071

HARRIES, D.; POLLOK, K.; LANGENHORST, F.: 20.-24.09.2011, Joint Meeting DGK, DMG and OMG 'Crystals, Minerals and Materials', Salzburg, Germany: "Pyrrhotite oxidative dissolution: Crystallographic and microstructural controls observed by FIB-TEM and 3D topometry"

HARRIES, D.; POLLOK, K.; LANGENHORST, F.: 14.-19.08.2011, Goldschmidt Conference 2011, Prague, Czech Republic: "Pyrrhotite oxidative dissolution: A microstructural perspective by FIB-TEM and surface topometry", Mineralogical Magazine, Vol. 75 (3), 980

HARRIES, D.; LANGENHORST, F.: 08.-12.08.2011, 74th Annual Meeting of the Meteoritical Society, London, U.K.: "Nanocrystalline P-bearing pentlandite and chromium nitrides from CM2 chondrites Y-791198 and Y-793321, Abstract 5165

HARRIES, D.; LANGENHORST, F.: 08.-12.08.2011, 74th Annual Meeting of the Meteoritical Society, London, U.K.: "Sulfides in CM and CM/CI-like chondrites and their record of thermal metamorphism: A FIB-TEM study", Abstract 5166

HARRIES, D.; FABIAN, K.; POLLOK, K.; MCENROE, S.A.: 03.-08.04.2011, European Geosciences Union General Assembly 2011, Vienna, Austria: "Correlation of microstructures and exsolution lamellae in natural pyrrhotites and magnetic properties", Abstract 12987

HARRIES, D.; BERG, T.; PALME, H.; LANGENHORST, F.: 07.-11.03.2011, 42nd Lunar and Planetary Science Conference, The Woodlands, USA: "The structure of refractory metal alloys, condensates from the early solar nebula", Abstract 1837

HEIDELBACH, F.: 10.03.2011, University of Pavia, Italy: "Electron backscatter diffraction (EBSD) of minerals and rocks"

HOPF, J.; POLLOK, K.; HOCHELLA, M.F.; LANGENHORST, F.: 14.-19.08.2011, Goldschmidt Conference 2011, Prague, Czech Republic: "Bacterial oxidation of pyrrhotite and troilite under acidic conditions", Mineralogical Magazine, Vol. 75 (3), 1042

HUANG, R.; AUDÉTAT, A.: 14.-19.08.2011, Goldschmidt Conference 2011, Prague, Czech Republic: "A critical look at the titanium-in-quartz (TitaniQ) thermobarometer", Mineralogical Magazine, Vol. 75 (3), 1065

KATSURA, T.: 01.04.2011, ETH Zurich, Institut für Geophysik, Zurich, Switzerland: "Electrical conductivity of the upper mantle minerals, and implication for the mantle dynamics"

KATSURA, T.: 16.05.2011, Universität Göttingen, Institut für Geophysik, Germany: "Electrical conductivity of the upper mantle minerals, and implication for the mantle dynamics"

KATSURA, T.; YOSHINO, T.: 28.06.-07.07.2011, The XXV IUGG General Assembly, 'Earth on the Edge: Science for a Sustainable Planet', Melbourne, Australia: "Effects of volatile components on electrical conductivity of the deep mantle"

KEPPLER, H.: 14.-19.08.2011, Goldschmidt Conference 2011, Prague, Czech Republic: "Water in the mantle, melting, and the evolution of Earth's atmosphere", Mineralogical Magazine, Vol. 75 (3), 1172

KEPPLER, H.: 21.10.2011, Bavarian Academy of Sciences, Munich: "Vorhersage von Vulkaneruptionen"

KURNOSOV, A.; TROTS, D.; BOFFA BALLARAN, T.; HARRIES, D.; FROST, D.: 14.-19.08.2011, Goldschmidt Conference 2011, Prague, Czech Republic: "High-pressure single-crystal elasticity of $MgSiO_3$ and $(Mg,Fe)SiO_3$ perovskites at pressures of the Earth's lower mantle", Mineralogical Magazine, Vol. 75 (3), 1256

LERCHBAUMER, L.; AUDÉTAT, A.: 03.-08.04.2011, European Geosciences Union General Assembly 2011, Vienna, Austria: "Preferential partitioning of copper into the vapor phase: fact or a natural artifact?", Geophysical Research Abstracts 13, EGU2011-11906, 2011

LERCHBAUMER, L.; AUDÉTAT, A.: 14.-19.08.2011, Goldschmidt Conference 2011, Prague, Czech Republic *(invited)*: "Preferential partitioning of copper into the vapor phase: An artifact?", Mineralogical Magazine, Vol. 75 (3), 1302

LI, Y.; KEPPLER, H.; AUDÉTAT, A.: 14.-19.08.2011, Goldschmidt Conference 2011, Prague, Czech Republic: "Nitrogen speciation in the mantle fluids", Mineralogical Magazine, Vol. 75 (3), 1322

LIN, Y.; EL GORESY, A.; BOYET, M.; FENG, L.; ZHANG, J.; HAO, J.: 07.-09.11.2011, Workshop on 'Formation of the First Solids in the Solar System', Koloa, Hawaii, USA: "Earliest solid condensates consisting of the assemblage oldhamite, sinoite, graphite and excess 36S in lawrencite from Almahata Sitta MS-17 EL-3 chondrite fragment"

MANTHILAKE, M.A.G.M.; DE KOKER, N.; FROST, D.J.: 28.02.-02.03.2011, 4th Berichtskolloquium of the SPP 1236 'Structures and characteristics of crystals at extremely high pressures and temperatures', Hünfeld, Germany: "Lattice thermal conductivity of the lower mantle"

MARIN-CARBONNE, J.; ALÉON, J.; MCKEEGAN, K.D.; EL GORESY, A.: 08.-12.08.2011, 74th Annual Meeting of the Meteoritical Society, London, U.K.: "Si isotopes composition of Efremovka 101,1 CAI"

MCCAMMON, C.: 28.02.-02.03.2011, 4th Berichtskolloquium of the SPP 1236 'Structures and characteristics of crystals at extremely high pressures and temperatures', Hünfeld, Germany: "Mössbauer spectroscopy in a laser heated diamond anvil cell"

MCCAMMON, C.A.; DUBROVINSKY, L.S.; GLAZYRIN, K.; PRESCHER, C.; POTAPKIN, V.; CHUMAKOV, A.; RÜFFER, R.; KANTOR, A.; KANTOR, I.; SMIRNOV, G.; POPOV, S.L.: 13.-17.06.2011, 7th Seeheim Workshop on Mössbauer Spectroscopy, Frankfurt/M., Germany: "Mössbauer spectroscopy of lower mantle phases at high pressures and high temperatures"

MCCAMMON, C.A.: 25.10.2011, European Photon & Neutron Science Campus, Grenoble, France: "Deep secrets revealed"

MCCAMMON, C.A.: 10.11.2011, Westfälische Wilhelms-Universität Münster, Institut für Mineralogie, Münster, Germany: "Microscopic to macroscopic: The influence of iron on the Earth's interior"

MCCAMMON, C.A.; DUBROVINSKY, L.S.; POTAPKIN, V.; GLAZYRIN, K.; PRESCHER, C.; KUPENKO, I.; CHUMAKOV, A.; RÜFFER, R.; KANTOR, A.; KANTOR, I.; SMIRNOV, G.V.; POPOV, S.: 05.-09.12.2011, Fall Meeting of the American Geophysical Union, San Francisco, USA: "Laser-heated DAC Mössbauer study of lower mantle phases: Spin transitions and implications for mantle heterogeneity", Abstract MR34A-07, 2011

MCENROE, S.; ROBINSON, P.; FABIAN, K.; HARRISON, R.J.; MIYAJIMA, N.; LANGENHORST, F.: 14.-19.08.2011, Goldschmidt Conference 2011, Prague, Czech Republic: "Interfaces and exchange coupling", Mineralogical Magazine, Vol. 75 (3), 1438

MISHRA, S.K.; MITTAL, R.; CHAPLOT, S.L.; OVSYANNIKOV, S.V.; GREENBERG, E.; TROTS, D.; DUBROVINSKY, L.; SU, Y.; BRUECKEL, Th.; MATSUISHI, S.; HOSONO, H.; GARBARINO, G.: 25-30.09.2011, XXIII AIRAPT International Conference on High Pressure Science and Technology, Mumbai, India: "Pressure driven phase transition in CaFeAsF at 40 K and 300 K", p. 191

MITTAL, R.; MISHRA, S.K.; CHAPLOT, S.L.; OVSYANNIKOV, S.V.; GREENBERG, E.; TROTS, D.; DUBROVINSKY, L.; SU, Y.; BRUECKEL, Th.; MATSUISHI, S.; HOSONO, H.; GARBARINO, G.: 25-30.09.2011, XXIII AIRAPT International Conference on High Pressure Science and Technology, Mumbai, India: "Structure and Dynamics of FeAs compounds at high pressure", p. 131

MIYAJIMA, N.; SUN, W.: 20.-24.09.2011, Joint Meeting DGK, DMG and OMG 'Crystals, Minerals and Materials', Salzburg, Germany: "Electron channelling spectroscopy of Cr-spinels"

MIYAJIMA, N.: 10-14.10.2011, MinTEM 2011, Joint Graduate and PhD Course, Villeneuve-d'Ascq, France: two lectures on "Defects" and "EELS"

MOOKHERJEE, M.: 05.01.2011, Indian Institute of Science, Bangalore, India: "Fluids, melts and volatiles in the deep Earth"

MOOKHERJEE, M.: 07.04.2011, Rice University, Houston, TX, USA: "Crust to core: Physics and chemistry of volatile bearing Earth materials"

MOOKHERJEE, M.: 15.04.2011, University of Maryland, College Park, USA: "Crust to core: Geophysical implications of volatile bearing Earth materials"

MOOKHERJEE, M.: 08.06.2011, Cornell University, Ithaca, USA: "Fluids and melts in the Earth's interior"

MOOKHERJEE, M.: 03.-05.11.2011, Thermodynamix-III Workshop, Dublin, Ireland (*invited*): "Elasticity of hydrous silicates at high pressure: geophysical implications"

MOOKHERJEE, M.; CAPITANI, G.: 05.-09.12.2011, Fall Meeting of the American Geophysical Union, San Francisco, USA: "Elasticity of antigorite at high pressures: implications for subduction zone anisotropy", Abstract DI31A-2171, 2011

MROSKO, M.; LENZ, S.; MCCAMMON, C.; WIRTH, R.; KOCH-MÜLLER, M.: 04.-07.09.2011, 7th European Conference on Mineralogy and Spectroscopy, Potsdam, Germany: "Incorporation of Fe^{3+} in ringwoodite studied via EELS, FTIR-, and Mössbauer spectroscopy"

MROSKO, M.; LENZ, S.; MCCAMMON, C.A.; TARAN, M.; WIRTH, R.; KOCH-MÜLLER, M.: 05.-09.12.2011, Fall Meeting of the American Geophysical Union, San Francisco, USA: "Hydrogen incorporation and the oxidation state of iron in ringwoodite – a spectroscopic study", Abstract DI21A-2067, 2011

NI, H.; DE KOKER, N.: 14.-19.08.2011, Goldschmidt Conference 2011, Prague, Czech Republic: "First-principles simulations of alkali aluminosilicate liquids", Mineralogical Magazine, Vol. 75 (3), 1428

NOVELLA, D.; FROST, D.J.: 14.-19.08.2011, Goldschmidt Conference 2011, Prague, Czech Republic: "Water contents of incipient partial melts in equilibrium with peridotite at upper mantle conditions", Mineralogical Magazine, Vol. 75 (3), 1551

NOVELLA, D.; FROST, D.J.: 05.-09.12.2011, Fall Meeting of the American Geophysical Union, San Francisco, USA: "Water partitioning between low degree melts and mineral phases in the upper mantle", Abstract DI21A-2065, 2011

OVSYANNIKOV, S.V.; WU, X.; SHCHENNIKOV, V.V; KARKIN, A.E.; DUBROVINSKY, L.S.: 28.08.-02.09.2011, 49th European High Pressure Research Group Conference (EHPRG), Budapest, Hungary: "Advances in HP-HT studies of sesquioxides M_2O_3 (M is a Metal)", p. 299

OVSYANNIKOV, S.V.; WU, X.; SHCHENNIKOV, V.V.; KARKIN, A.E.; DUBROVINSKY, L.S.: 25-30.09.2011, XXIII AIRAPT International Conference on High Pressure Science and Technology, Mumbai, India: "New trends in HP-HT studies of sesquioxides M_2O_3 (M is a metal)", p. 181

PALKE, A.; STEBBINS, J.F.; FROST, D.J.; MCCAMMON, C.A.: 14.-19.08.2011, Goldschmidt Conference 2011, Prague, Czech Republic: "Al and Fe substitution in $MgSiO_3$ perovskite: An ^{27}Al and ^{29}Si NMR study", Mineralogical Magazine, Vol. 75 (3), 1590

PALKE, A.; STEBBINS, J.F.; FROST, D.J.; MCCAMMON, C.A.: 05.-09.12.2011, Fall Meeting of the American Geophysical Union, San Francisco, USA: "^{27}Al and ^{29}Si NMR spectroscopy of $MgSiO_3$ perovskite: mechanisms of Al and Fe incorporation", Abstract MR31A-2194, 2011

PAMATO, M.G.; BOFFA BALLARAN, T.; FROST, D.J.; KURNOSOV, A.; TROTS, D.M.; HEIDELBACH, F.; MIYAJIMA N.: 23.-26.05.2011, Workshop 'Methods of in situ-high-pressure single-crystal diffraction', Obergurgl, Austria: "Hydrous minerals in the Earth's deep mantle"

PAMATO, M.G.; BOFFA BALLARAN, T.; FROST, D.J.; KURNOSOV, A.; TROTS D.M.: 14.-19.08.2011, Goldschmidt Conference 2011, Prague, Czech Republic: "The elasticity of hydrous minerals in the lower mantle", Mineralogical Magazine 75 (3), 1591

PARAKHONSKIY, G.: 28.02.-02.03.2011, 4th Berichtskolloquium of the SPP 1236 'Structures and characteristics of crystals at extremely high pressures and temperatures', Hünfeld, Germany: "Phase relations in boron up to 11 GPa and 2000 °C"

POKROVSKI, G.S.; DUBROVINSKY, L.S.; DUBESSY, J.: 14.-19.08.2011, Goldschmidt Conference 2011, Prague, Czech Republic: "A new view on sulfur speciation in geological fluids at elevated temperatures and pressures", Mineralogical Magazine 75 (3), 1654

POLLOK, K.; HARRIES, D.; HOPF, J.; ETZEL, K.; SCHEITER, D.; CHUST, T.; PUTNIS, C.V.; PUTNIS, A.; LANGENHORST, F.: 08.-09.06.2011, 3. Statusseminar 'Mineral Surfaces – From atomic processes to industrial applications', Karlsruhe, Germany: "Microstructural controls on monosulphide weathering and heavy metal release"

POLLOK, K.; PUTNIS, C.V.; PUTNIS, A.: 14.-19.08.2011, Goldschmidt Conference 2011, Prague, Czech Republic: "Reaction paths and volume changes of solid solutions in coupled dissolution-precipitation reactions: The role of endmember solubility", Mineralogical Magazine, Vol. 75 (3), 1656

POLLOK, K. : 20.-24.09.2011, Joint Meeting DGK, DMG and OMG 'Crystals, Minerals and Materials', Salzburg, Germany: "Secondary phases and surface topography: How can reliable mineral weathering rates be obtained?"

POLLOK, K.: 10.-14.10.2011, Workshop 'MinTEM 2011', Lille, France: "Imaging and contrast in transmission transmission electron microscopy"

POLLOK, K.: 10.-14.10.2011, Workshop 'MinTEM 2011', Lille, France: "High-resolution transmission electron microscopy"

POTAPKIN, V.; CHUMAKOV, A.; RÜFFER, R.; SMIRNOV, G.; POPOV, S.L.; DUBROVINSKY, L.; MCCAMMON, C.: 13.-17.06.2011, 7th Seeheim Workshop on Mössbauer Spectroscopy, Frankfurt/M., Germany: "First results with synchrotron Mössbauer source at the ESRF"

POTAPKIN, V.; CHUMAKOV, A.; RÜFFER, R.; SMIRNOV, G.V.; POPOV, S.; DUBROVINSKY, L.S.; MCCAMMON, C.A.: 25.-30.09.2011, International Conference on the Applications of the Mössbauer Effect, Kobe, Japan: "Synchrotron Mössbauer source at the ESRF"

POTAPKIN, V.; DUBROVINSKY, L.S.; MCCAMMON, C.A.; KANTOR, A.; KUPENKO, I.; GLAZYRIN, K.; CHUMAKOV, A.; KANTOR, I.; RÜFFER, R.; PRESCHER, C.; SMIRNOV, G.V.; POPOV, S.: 05.-09.12.2011, Fall Meeting of the American Geophysical Union, San Francisco, USA: "Novel Mössbauer measurements of spin transitions in lower mantle silicate perovskite", Abstract MR23C-07, 2011

RUBIE, D.C.; O'BRIEN D.P.; NIMMO, F.; MORBIDELLI, A.; FROST, D.J.; PALME, H.: 07.-11.03.2011, 42nd Lunar and Planetary Science Conference, The Woodlands, USA: "Heterogeneous accretion of the terrestrial planets", Abstract 1061

RUBIE, D.C.; FROST, D.J.; O'BRIEN D.P.; NIMMO, F.; MORBIDELLI, A.; PALME, H.; 14.-19.08.2011, Goldschmidt Conference 2011, Prague, Czech Republic: "Core formation in the Earth and the terrestrial planets", Mineralogical Magazine, Vol. 75 (3), 1763

RUBIE, D.C.; O'BRIEN D.P.; NIMMO, F.; MORBIDELLI, A.; FROST, D.J.; PALME, H.: 17.-22.07.2011, Gordon Research Conference on Origins of Solar Systems, Mount Holyoke College, South Hadley, USA: "Heterogeneous accretion of the terrestrial planets"

RUBIE, D.C.; VOGEL, A.; O'BRIEN D.P.; NIMMO, F.; MORBIDELLI, A.; FROST, D.J.; PALME, H.: 17.-19.10.2011, 2nd Annual Meeting of the SPP 1385 'The First 10 Million Years of the Solar System – a Planetary Materials Approach', Mainz, Germany: "Accretion and early differentiation of the terrestrial planets"

RUBIE, D.C.; FROST, D.J.; PALME, H.: 07.-09.11.2011, Workshop on 'Formation of the First Solids in the Solar System', Koloa, Hawaii, USA: "Meteorites, composition of the Earth and early accreting material in the inner solar system", Abstract 9015

SAMUEL, H.: 14.-19.08.2011, Goldschmidt Conference 2011, Prague, Czech Republic: "The breakup and chemical equilibration of metal diapirs in terrestrial magma oceans", Mineralogical Magazine, Vol. 75 (3), 1787

SAMUEL, H.: 20.-25.08.2011, 12th International Workshop on Modeling of Mantle Convection and Lithospheric Dynamics, Groß Dölln, Germany: "Time domain parallelization for geodynamic modeling"

SAMUEL, H.: 20.-25.08.2011, 12th International Workshop on Modeling of Mantle Convection and Lithospheric Dynamics, Groß Dölln, Germany: "Erosion, breakup and chemical equilibration of iron diapirs in terrestrial magma oceans"

SAMUEL, H.; TOSI, N.: 20.-25.08.2011, 12th International Workshop on Modeling of Mantle Convection and Lithospheric Dynamics, Groß Dölln, Germany: "The influence of post-peroskite rheology on mantle convective stirring efficiency"

SAMUEL, H.; TOSI, N.: 05.-09.12.2011, Fall Meeting of the American Geophysical Union, San Francisco, USA: "The influence of post-peroskite rheology on mantle convective stirring efficiency", Abstract DI11A-2135, 2011

SCHIAVI, F.; HUBER, J.; GOLLNER, G.; KEPPLER, H.: 19.-23.09.2011, Geoitalia 2011, The 8th Edition of the Italian Forum of Earth Sciences, Torino, Italy: "Adsorption of HCl gas onto volcanic ash", Abstract Volume 4, 328

SHARP, T.G.; GILLET, P.; OHTANI, E.; MIYAHARA, M.; OZAWA, S.; BECK, P.; FERROIR, T.; KIMURA, M.; DECARLI, P.; XIE, Z.; EL GORESY, A.: 08.-12.08.2011, 74th Annual Meeting of the Meteoritical Society, London, U.K.: "A fundamental rebut contra shock-pressure estimates using Stöffler-Fritz "*parameters*": And consequences to the alleged short igneous crystallization ages"

SHCHEKA, S.; KEPPLER, H.: 28.02.-02.03.2011, 4th Berichtskolloquium of the SPP 1236 'Structures and characteristics of crystals at extremely high pressures and temperatures', Hünfeld, Germany: "$MgSiO_3$-perovskite and the terrestrial noble gas signature"

SINMYO, R; HIROSE, K.; OHISHI, Y.: 20-25.05.2011, Japan Geoscience Union Meeting 2011, Chiba, Japan: "Density profile of pyrolitic lower mantle"

SOUSTELLE, V.; MANTHILAKE, G.; MIYAJIMA, N.; WALTE, N.; FROST, D.; HEIDELBACH, F.: 05.-09.12.2011, Fall Meeting of the American Geophysical Union, San Francisco, USA: "Interaction between deformation and reactive melt percolation in the upper mantle: Deformation-DIA experiments at high pressure and temperature", Abstract T52B-02, 2011

SOUSTELLE; V.; TOMMASI; A.; DEMOUCHY; S.: 05.-09.12.2011, Fall Meeting of the American Geophysical Union, San Francisco, USA *(invited)*: "Water contents and deformation in spinel peridotite xenoliths from the supra-subduction mantle", Abstract T24B-04, 2011

STAGNO, V.; MCCAMMON, C.M.; FROST, D.J.: 14.-19.08.2011, Goldschmidt Conference 2011, Prague, Czech Republic: "High-pressure calibration of the oxygen fugacity recorded by garnet bearing peridotites", Mineralogical Magazine, Vol. 75 (3), 1928

STAGNO, V.; FROST, D.J.; MCCAMMON, C.: 05.-09.12.2011, Fall Meeting of the American Geophysical Union, San Francisco, USA *(invited)*: "The oxygen fugacity within carbonated eclogites", Abstract DI21A-2060, 2011

STAGNO, V.; OJWANG, D.; MCCAMMON, C.A.; FROST, D.J.: 05.-09.12.2011, Fall Meeting of the American Geophysical Union, San Francisco, USA *(invited)*: "The oxidation state of garnet peridotites and the speciation of carbon in the mantle", Abstract DI13B-01, 2011

STEINLE-NEUMANN, G.; VLCEK, V.; HOLBIG, E.; WU, X.: 14.-19.08.2011, Goldschmidt Conference 2011, Prague, Czech Republic: "Failure of density functional theory for ground state calculations on TiO_2", Mineralogical Magazine, Vol. 75 (3), 1936

TRIELOFF, M.; EL GORESY, A.; ALTHERR, R.; LUDWIG, T., MOSTEFAOUI, S.: 17.-19.10.2011, 2nd Annual Meeting of the SPP 1385 'The First 10 Million Years of the Solar System – a Planetary Materials Approach', Mainz, Germany: "Short-lived nuclide systems in sulfides from enstatite chondrites"

VAN MIERLO, W.; LANGENHORST, F.; MIYAJIMA, N.; FROST, D.; RUBIE, D.: 27.03.-02.04.2011, Study of Matter at Extreme Conditions (SMEC) 2011, Miami, USA: "Diffusion of the majorite component in garnet"

VOGEL, A.K.; RUBIE, D.C.; FROST, D.J.; PALME, H.: 14.-19.08.2011, Goldschmidt Conference 2011, Prague, Czech Republic: "The partitioning of volatile and other siderophile elements between metal and silicate at high pressures and temperatures", Mineralogical Magazine, Vol. 75 (3), 2097

VOGEL, A.K.; RUBIE, D.C.; FROST, D.J.; PALME, H.: 17.-19.10.2011, 2nd Annual Meeting of the SPP 1385 'The First 10 Million Years of the Solar System – a Planetary Materials Approach', Mainz, Germany: "The partitioning of volatile and other siderophile elements between metal and silicate at high pressures and temperatures"

WU, X.; MOOKHERJEE, M.; GU, T.; QIN, S.; STEINLE-NEUMANN, G.: 25-30.09.2011, XXIII AIRAPT International Conference on High Pressure Science and Technology, Mumbai, India: "Structural and elastic properties of (Fe,Ni)4P at high pressures from ab-initio calculation", p. 127

YOSHINO, T.; ITO, E.; KATSURA, T.; YAMAZAKI, D.; SHAN, S.: 28.06.-07.07.2011, The XXV IUGG General Assembly, 'Earth on the Edge: Science for a Sustainable Planet', Melbourne, Australia: "Effect of iron content in ferropericlase on spin transition pressure deduced from electrical conductivity measurement"

YOSHINO, T.; SHIMOJUKU, A.; KATSURA, T.: 14.-19.08.2011, Goldschmidt Conference 2011, Prague, Czech Republic: "Laboratory-based conductivity structure in the mantle transition zone", Mineralogical Magazine, Vol. 75 (3), 2227

ZUCCHINI, A.; COMODI, P.; PRENCIPE, M.; FRONDINI, F.; MCCAMMON, C.; KATERINOPOULOU, A.; BALIC-ZUNIC, T.: 19.-23.09.2011, Geoitalia 2011, The 8th Edition of the Italian Forum of Earth Sciences, Torino, Italy: "About cation distribution in dolomite structure by theory and experiments"

ZUCCHINI, A.; COMODI, P.; PRENCIPE, M.; FRONDINI, F.; MCCAMMON, C.; BALIC-ZUNIC, T.: 03.-08.04.2011, European Geosciences Union General Assembly 2011, Vienna, Austria: "Cation disordering in dolomite: theoretical and experimental approach"

5.4 Lectures and seminars at Bayerisches Geoinstitut

ALEXEEV, A., Nikolaev Institute of Inorganic Chemistry, Novosibirsk, Russia: "Debye-Scherrer method: Everything old is new again", 06.10.2011

AUDÉTAT, A., Bayerisches Geoinstitut, Bayreuth, Germany: "Introduction to laser-ablation ICP-MS: principles, applications and limitations", Short Course 18.-20.04.2011

BHATTACHARYA, S., SN Bose National Center for Basic Sciences, Kolkata, India: "First principle study of silicate minerals", 30.11.2011

BÖNI, P., Technische Universität München, Experimentalphysik II, Garching, Germany: "Neutron imaging and scattering under extreme conditions", 05.05.2011

BOETIUS, A., Alfred-Wegener-Institut, Bremerhaven, Germany: "Life under pressure - extreme environments of the deep", 21.11.2011

BOETIUS, A., Alfred-Wegener-Institut, Bremerhaven, Germany: "Pressure and temperature effects on methane-munging microorganisms", 22.11.2011

CARPENTER, M., University of Cambridge, Department of Earth Sciences, Cambridge, U.K.: "Strain, order parameters and phase transitions in minerals and functional oxides", 12.09.2011

CARPENTER, M., University of Cambridge, Department of Earth Sciences, Cambridge, U.K.: "Elastic anomalies and anelasticity due to phase transitions in minerals and functional oxides", 13.09.2011

CORONA, J.C., State University of New York at Binghamton, USA: "Stability relationships in the Na_2O-MgO-FeO-Al_2O_3-SiO_2-H_2O system, implications for the P-T limits of blueschist facies metamorphism", 01.03.2011

DASGUPTA, R., Rice University, Department of Earth Science, Houston, USA: "From crustal recycling to magma ocean – Earth's deep carbon cycle through time", 24.10.2011

DASGUPTA, R., Rice University, Department of Earth Science, Houston, USA: "Mantle hybridization through melt-rock reaction – composition and temperature of ocean island basalt source regions", 25.10.2011

DE KOKER, N., Bayerisches Geoinstitut, Bayreuth, Germany: "Incongruent melting of Earth's lowermost mantle", 10.03.2011

DE KOKER, N., Bayerisches Geoinstitut, Bayreuth, Germany: "Diffusion in silicate melts", Ringvorlesung 06.06.2011

EVONUK, M., Bayerisches Geoinstitut, Bayreuth, Germany: "Transitioning to rotationally dominated fluid flow", 09.06.2011

GILDER, S., LMU München, Department für Geo- und Umweltwissenschaften, München, Germany: "High pressure magnetism with implications for planetary magnetic fields", 27.01.2011

GLAZYRIN, K., Bayerisches Geoinstitut, Bayreuth, Germany: "Single crystal study of Fe-Al bearing magnesium silicate perovskite at high pressure - high temperature conditions", 03.11.2011

KATSURA, T., Bayerisches Geoinstitut, Bayreuth, Germany: "Effect of volatile components on electrical conductivity of the upper mantle and implication to the structure of the oceanic asthenosphere", 14.07.2011

KENNETT, B.L.N., The Australian National University, Research School of Earth Sciences, Canberra, Australia: "The interface between seismology and mineral physics", 13.10.2011

KURNOSOV, A., Bayerisches Geoinstitut, Bayreuth, Germany: "Development of HP-HT Brillouin spectroscopy in combination with single crystal x-ray diffraction", 21.04.2011

MAIEROVA, P., Charles University Prague, Geophysical Department, Prague, Czech Republic: "The effect of a realistic thermal diffusivity on numerical model of a subducting slab", 01.12.2011

MIYAHARA, M., Tohoku University, Institute of Mineralogy, Petrology and Economic Geology, Sendai, Japan: "Dissociation of olivine to silicate-perovskite and magesiowüstite in a shocked Martian meteorite", 18.08.2011

MIYAJIMA, N., Bayerisches Geoinstitut, Bayreuth, Germany: "Dislocation microstructures of rock-forming minerals in the Earth's mantle: Revisiting a weak-beam TEM technique", 16.06.2011

MOOKHERJEE, M., Bayerisches Geoinstitut, Bayreuth, Germany: "Crust to Core – Geophysical implications of volatile bearing Earth materials", 17.03.2011

MOOKHERJEE, M., Bayerisches Geoinstitut, Bayreuth, Germany: "Elasticity of hydrous phases: Geophysical implications", 15.12.2011

MORBIDELLI, A., Observatoire de la Côte d'Azur, France: " The grand tack scenario: A new model of terrestrial planets formation", 10.01.2011

MYHILL, R., University of Cambridge, Department of Earth Sciences, Cambridge, U.K.: "Insights into deep earthquake mechanics from their spatial distributions, fault plane orientations and local conditions", 03.11.2011

NI, H., Bayerisches Geoinstitut, Bayreuth, Germany: "Diffusion in silicate melts", 06.10.2011

O'BRIEN, P., Universität Potsdam, Institut für Erd- und Umweltwissenschaften, Potsdam, Germany: "Deep subduction of continental crust: direct evidence in diamond- and/or coesite-bearing rocks and geodynamic and geochemical consequences", 21.07.2011

OVSYANNIKOV, S., Bayerisches Geoinstitut, Bayreuth, Germany: "Advances in HP-HT studies of sesquioxides", 20.01.2011

POLLOK, K., Bayerisches Geoinstitut, Bayreuth, Germany: "Reaction paths and volume changes of coupled dissolution-precipitation reactions in solid solution-aqueous solution systems", 07.07.2011

PRAKAPENKA, V., CARS, University of Chicago, Argonne National Lab, Chicago, USA: "Advanced synchrotron x-ray and on-line optical techniques in high pressure research", 10.11.2011

PRAKAPENKA, V., CARS, University of Chicago, Argonne National Lab, Chicago, USA: "High pressure melting: Experiments vs theory", 11.11.2011

ROSS, N., Virginia Polytechnic Institute and State University, Department of Geosciences, Blacksburgh, USA: "Sulfides: Analogues for oxides under extreme high-pressure conditions?", 19.07.2011

SATSUKAWA, T., Shizuoka University, Graduate School of Science & Technology, Educational Division of Environment & Energy Systems, Shizouka, Japan: "Seismic anisotropy of the uppermost mantle beneath the Rio Grande rift: Evidence from Kilbourne Hole peridotite xenoliths, New Mexico", 12.05.2011

SHEKHAR, S., Bayerisches Geoinstitut, Bayreuth, Germany: "Effect of stress and water on the slip systems in olivine", 19.05.2011

STAGNO, V., Bayerisches Geoinstitut, Bayreuth, Germany: "Carbon and carbonate in the Earth's interior", 24.03.2011

SUN, W., Bayerisches Geoinstitut, Bayreuth, Germany: "Determination of $Fe^{3+}/\Sigma Fe$ in chromite by TEM with implications for the mantle oxidation state", 03.03.2011

TROTS, D., Bayerisches Geoinstitut, Bayreuth, Germany: "A calibration of Sm:YAG as a primary pressure standard", 22.09.2011

VAN MIERLO, W., Bayerisches Geoinstitut, Bayreuth, Germany: "Garnet and pyroxene in Earth's upper mantle", 28.04.2011

VLCEK, V., Bayerisches Geoinstitut, Bayreuth, Germany: "Electrical and thermal conductivity of liquid Al at elevated pressures and temperatures from first-principles calculations", 28.07.2011

WEI, Q., Bayerisches Geoinstitut, Bayreuth, Germany: "Raman spectroscopy of diamond at high pressure and temperature", 24.02.2011

ZAJAC, Z., ETH Zürich, Institut für Geochemie und Petrologie, Zürich, Switzerland: "The role of mafic to intermediate magmas in the genesis of magmatic-hydrothermal ore deposits: an experimental approach", 15.09.2011

ZHANG, L., Bayerisches Geoinstitut, Bayreuth, Germany: "Partitioning of vanadium between hydrous rhyloite melt and Fe-Ti oxides", 24.08.2011

5.5 Conference organization

14.-19.08.2011, Goldschmidt Conference, Prague, Czech Republic: Theme 20: Frontiers in Mineralogy and Mineral Physics (F. LANGENHORST; C. MCCAMMON)

28.07.-07.07.2011, International Union of Geodesy and Geophysics Conference, Melbourne, Australia: Symposium JS04/JV03: Physics and Chemistry of Earth Materials with Implications for Earth Structure and Processes (G. YAXLEY; H. O'NEILL; I. JACKSON; T. IRIFUNE; T. YOSHINO; C. MCCAMMON)

05.-09.12.2011, AGU Fall Meeting, San Francisco, USA: Session MR04: Earth Materials under Compression: Advances in Experimental and Numerical Methods (S. MERKEL; G. STEINLE-NEUMANN; M. MOOKHERJEE; Y. WANG)

6. Visiting scientists

6.1 Visiting scientists funded by the Bayerisches Geoinstitut

ALEXEEV, A., Nikolaev Institute of Inorganic Chemistry, Novosibirsk, Russia: 04.-08.10.2011

AMIN, B., Hazara University, Department of Physics, Mansehra, Pakistan: 24.-30.10.2011

BALI, E., Universität Göttingen, Experimentelle und Angewandte Mineralogie, Göttingen, Germany: 06.-18.03.2011, 25.-27.08.2011

BHATTACHARYA, S., SN Bose National Center for Basic Sciences, Kolkata, India: 29.11.-01.12.2011

BLAHA, S., Universität Wien, Center for Geosciences, Wien, Austria: 17.01.-30.03.2011

BÖNI, P., Technische Universität München, Experimentalphysik II, Garching, Germany: 05.05.2011

CERNOK, A., Universität Wien, Center for Geosciences, Wien, Austria: 17.01.-30.03.2011

CORONA, J.C., State University of New York at Binghamton, USA: 28.02.-06.03.2011

DEON, L., Università di Bologna, Italy: 30.11.-02.12.2011

DOLEJŠ, D., Charles University, Institute of Petrology and Structural Geology, Prague, Czech Republic: 14.-18.02.2011

FOUSTOUKOS, D., Carnegie Institution of Washington, Geophysical Laboratory, Washington DC, USA: 16.-20.11.2011

HIRAGA, T., University of Tokyo, Earthquake Research Institute, Tokyo, Japan: 16.-20.11.2011

LONGO, M., Università degli Studi di Padova, Dipartimento di Geoscienze, Padova, Italy: 30.01.-11.02.2011

MAIEROVA, P., Charles University Prague, Geophysical Department, Prague, Czech Republic: 30.11.-03.12.2011

MCCANTA, M., Tufts University, Department of Geology, Medford, USA: 01.10.-30.11.2011

MIYAHARA, M., Tohoku University, Institute of Mineralogy, Petrology and Economic Geology, Sendai, Japan: 14.-20.08.2011

MYHILL, R., University of Cambridge, Department of Earth Sciences, Cambridge, U.K.: 30.10.-03.11.2011

O'BRIEN, P., Universität Potsdam, Institut für Erd- und Umweltwissenschaften, Potsdam, Germany: 21.-22.07.2011

REICHE, S., Universität Tübingen, Fachbereich Geowissenschaften, Tübingen, Germany: 14.02.-18.04.2011

RIGO, F., Università degli Studi di Padova, Dipartimento di Geoscienze, Padova, Italy: 13.-18.02.2011

SATSUKAWA, T., Shizuoka University, Graduate School of Science & Technology, Educational Division of Environment & Energy Systems, Shizouka, Japan: 10.-15.05.2011

SECLAMAN, A., University of Bucharest, Faculty of Geology and Geophysics, Bucharest, Romania: 16.-20.02.2011

TSUNO, K., Rice University, Department of Earth Science, Houston, USA: 10.-14.08.2011

VAN WESTRENEN, W., VU University Amsterdam, Faculty of Earth and Life Sciences, Amsterdam, The Netherlands: 16.-18.11.2011

ZAJAC, Z., ETH Zürich, Institut für Geochemie und Petrologie, Zürich, Switzerland: 15.-16.09.2011

6.2 Visiting scientists supported by other externally funded BGI projects

ADEBAMBO, P., University of Agriculture, Department of Physics, Abeokuta, Nigeria: 11.-17.01.2011 (ENB [*B])

BEYER, C., Universität Münster, Institut für Mineralogie, Münster, Germany: 27.-28.07.2011 (ERC [*D])

BOETIUS, A., Alfred-Wegener-Institut, Bremerhaven, Germany: 21.-22.11.2011 (ENB [*B])

CARPENTER, M., University of Cambridge, Department of Earth Sciences, Cambridge, U.K.: 09.-14.09.2011 (ENB [*B])

DASGUPTA, R., Rice University, Department of Earth Science, Houston, USA: 23.-28.10.2011 (ENB [*B])

GILDER, S., LMU München, Department für Geo- und Umweltwissenschaften, München, Germany: 27.01.2011 (DFG [*C])

GREENBERG, E., Tel Aviv University, Israel: 01.-31.07.2011 (IND [*E])

KENNETT, B.L.N., The Australian National University, Research School of Earth Sciences, Canberra, Australia: 12.-14.10.2011 (ERC [*D])

LIEBSKE, C., ETH Zürich, Institut für Geochemie und Petrologie, Zürich, Switzerland: 14.-17.09.2011 (ERC [*D])

MORBIDELLI, A., Observatoire de la Côte d'Azur, Nice, France: 09.-11.01.2011 (ENB [*B])

PRAKAPENKA, V., CARS, University of Chicago, Argonne National Lab, Chicago, USA: 09.-12.11.2011 (ENB [*B])

ROSS, N., Virginia Polytechnic Institute and State University, Department of Geosciences, Blacksburgh, USA: 18.-24.07.2011 (ENB [*B])

SOLOPOVA, N., Institute of Experimental Mineralogy, Chernogolovka, Moscow region, Russia: 29.05.-29.06.2011 (IND [*E])

SPEZIALE, S., Helmholtz-Zentrum Potsdam, Deutsches GeoForschungsZentrum GFZ, Potsdam, Germany: 06.-09.06.2011 (ERC [*D])

SPIVAK, A., Institute of Experimental Mineralogy, Chernogolovka, Moscow region, Russia: 01.07.-30.09.2011 (IND [*E])

[*A)] c2c: EU Marie Curie Research Training Network - the fate of subducted material

[*B)] ENB: International Graduate School under the Elitenetzwerk Bayern

[*C)] DFG: Deutsche Forschungsgemeinschaft

[*D)] ERC: European Research Council

[*E)] IND: Industrial Grant

6.3 Visitors (externally funded)

ANDO, J.-i., Hiroshima University, Department of Earth and Planetary Systems Science, Hiroshima, Japan: 19.-29.05.2011

ANGEL, R., Virginia Polytechnic Institute and State University, Geosciences, Blacksburgh, USA: 03.-04.03.2011

BABUSHKIN, A., Ural State University, Ekaterinburg, Russia: 08.-21.11.2011

BEKHEET, M., Technische Universität Darmstadt, Fachbereich Materialwissenschaft, Darmstadt, Germany: 01.02.2011

BENSE, F., Universität Göttingen, Fakultät für Geowissenschaften und Geographie, Göttingen, Germany: 29.-30.09.2011

BOBROV, A., Moscow State University, Petrological Department, Moscow, Russia: 22.08.-21.09.2011

BUREAU, H., Institut de Minéralogie et de Physique des Milieux Condensés, Paris, France: 14.-17.02.2011

CAILLET, C., Museum National d'Histoire Naturelle, Paris, France: 03.-14.10.2011

CARACAS, R., Laboratoire de Sciences de la Terre, CNRS UMR5570, Ecole Normale Supérieure de Lyon, France: 14.-18.02.2011, 09.-13.05.2011

CHANTEL, J., European Synchrotron Radiation Facility, Grenoble, France: 02.-08.10.2011

CHELAZZI, L., Università degli Studi di Firenze, Dipartimento di Scienze della Terra, Firenze, Italy: 05.-22.12.2011

CORDIER, P., Université des Sciences et Technologies de Lille, Laboratoire de Structure et Propriétés de l'Etat Solide, Villeneuve d'Ascq, France: 20.-30.07.2011

FABIAN, K., Geological Survey of Norway, Trondheim, Norway: 03.02.2011

GALUSKIN, E., University of Silesia, Department of Geochemistry, Mineralogy and Petrography, Sosnowiec, Poland: 13.-15.01.2011, 01.-06.03.2011

GALUSKINA, I., University of Silesia, Department of Geochemistry, Mineralogy and Petrography, Sosnowiec, Poland: 13.-15.01.2011, 01.-06.03.2011

KOMABAYASHI, T., Tokyo Institute of Technology, Department of Earth and Planetary Sciences, Tokyo, Japan: 21.-23.08.2011

LEPORE, G., Università degli Studi di Firenze, Facoltà di Scienze Matematiche, Fisiche e Naturali, Firenze, Italy: 13.02.-21.04.2011

MA, Q., École Polytechnique Fédérale de Lausanne, Switzerland: 16.-27.05.2011, 18.-29.07.2011

MCCORMACK, R., University College London, Department of Earth Sciences, London, U.K.: 14.-18.03.2011

MARQUARDT, H., Helmholtz-Zentrum Potsdam, Deutsches GeoForschungsZentrum GFZ, Potsdam, Germany: 26.-27.05.2011

NOMURA, R., Tokyo Institute of Technology, Department of Earth and Planetary Sciences, Tokyo, Japan: 21.-23.08.2011

NORRBY, N., Linköping University, Department of Physics, Chemistry, and Biology (IFM), Linköping, Sweden: 16.-27.05.2011, 21.-25.11.2011

OTSUKA, K., Yale University, Department of Geology and Geophysics, New Haven, USA: 27.01.-11.02.2011

SMYTH, J.R., University of Colorado at Boulder, Department of Geological Sciences, Boulder, USA: 22.08.-02.09.2011

SOLOPOVA, N., Institute of Experimental Mineralogy, Chernogolovka, Moscow region, Russia: 01.10.-31.12.2011

SPECKBACHER, R., Leibniz-Institut für Meereswissenschaften, IFM-GEOMAR, Kiel, Germany: 17.-21.10.2011

SUGIMURA, E., Tokyo Institute of Technology, Department of Earth and Planetary Sciences, Tokyo, Japan: 21.-23.08.2011

TARANTINO, S., Università di Pavia, Dipartimento di Scienze della Terra, Pavia, Italy: 15.05.-12.06.2011

TRØNNES, R., University of Oslo, Natural History Museum, Oslo, Norway: 05.-22.09.2011, 07.11.-16.12.2011

VOLKOVA, Y., Ural State University, Ekaterinburg, Russia: 08.-21.11.2011

ZAKHARCHENKO, E., Institute of Experimental Mineralogy, Chernogolovka, Moscow region, Russia: 01.07.-15.08.2011

7. Additional scientific activities

7.1 Theses

Ph.D. theses

BERNINI, Diego: Halogens and trace elements in subduction zone
GLAZYRIN, Konstantin: Iron in oxides, silicates and alloys under extreme pressure-temperature conditions
STAGNO, Vincenzo: The carbon speciation in the Earth's interior as a function of pressure, temperature and oxygen fugacity
VAN MIERLO, Willem: Major element diffusion in garnet and the exsolution of majoritic garnet from aluminous enstatite in Earth's upper mantle

M.Sc. theses

SUN, Wei: Electron energy-loss near-edge structure of Cr-spinel: Implications for mantle oxidation state
VLCEK, Vojtech: Electrical and thermal conductivity of liquid Al at high pressures and temperatures from ab-initio computations
WEI, Qingguo: Raman spectroscopy of diamond at high pressure and temperature
ZHANG, Li: Partitioning of vanadium between hydrous rhyolite melt and magnetite

7.2 Honours and awards

FROST, Daniel	received the Arnold Sommerfeld Prize 2011 of the Bavarian Academy of Science
HARRIES, Dennis	received the Gordon A. McKay Prize 2011 of the Meteoritical Society received the Paul Ramdohr Price 2011 of the German Mineralogical Society
RUBIE, David	was elected Fellow of the Geochemical Society
SOUSTELLE, Vincent	received the Van Straelen Prize 2011 of the French Geological Society (SGF)

7.3 Editorship of scientific journals

HEIDELBACH, Florian	Associate Editor "American Mineralogist"
KATSURA, Tomoo	Associate Editor "Reviews of Geophysics"

KEPPLER, Hans	Editorial Advisory Board "Elements" Editorial Board "Contributions to Mineralogy and Petrology"
MCCAMMON, Catherine	Chief Editor "Physics and Chemistry of Minerals" Advisory Editor "Springer Briefs in Earth Sciences"
RUBIE, David	Editorial Board "Physics of the Earth and Planetary Interiors"

7.4 Membership of scientific advisory bodies

BOFFA BALLARAN, Tiziana	Member of the Peer Review Panel of Engineering and Environment for beamlines I12, I15 and I16 of Diamond Light Source
DUBROVINSKY, Leonid	Chair of SIG "Crystallography at extreme conditions" of the European Crystallography Union Member, Editorial Board of the Journal of High Pressure Research Member, Review Panel of Canadian Light Source Member, Review Panel of SPRING8 Chair, Subcomission on Spectroscopy, Diffraction, and new Instrumentations in Mineral Physics of the International Mineralogical Association Scientific expert for the Research Council of Lithuania Member, Deep Carbon Observatory Scientific Steering Committee
FROST, Dan	Member of the council of the European Association of Geochemistry (EAG)
KEPPLER, Hans	Member, Research Council of the German Mineralogical Society (Forschungskollegium Mineralogie der DMG) Member, Abraham Gottlob Werner Medal Committee, German Mineralogical Society (DMG) Member, Roebling Medal Committee, Mineralogical Society of America Chair, Goldschmidt Medal Committee, European Association of Geochemistry Member, American Geophysical Union Fellow Committee (VGP section) Member, Commission for Research of Bayreuth University (Präsidialkommission für Forschung und wissenschaftlichen Nachwuchs) Member, German National Academy of Sciences (Leopoldina)

	Member, Bavarian Academy of Sciences Member, Deep Carbon Observatory Scientific Steering Committee Member, Alexander von Humboldt Foundation Selection Panel for Humboldt Awardees
MCCAMMON, Catherine	President Elect, Volcanology, Geochemistry & Petrology Section of the American Geophysical Union Member, Council of the American Geophysical Union Member, Science Innovation Award Committee 2011 of the European Association of Geochemistry Member, Lecture Program Committee of the Mineralogical Society of America Member, Advisory Board of the Mössbauer Information Exchange Chairman, Sub-committee "Earth's Deep Interior" of the Commission of the Physics of Minerals, International Mineralogical Association Member, International Advisory Board and Program Committee for the 7th Seeheim Workshop on Mössbauer Spectroscopy

8. Scientific and Technical Personnel

Name		**Position**	**Duration in 2011**	**Funding source**
ALEKSANDROV, Vladislav	M.Sc.	Wiss. Mitarbeiter		DFG
AUDÉTAT, Andreas	Dr.	Akad. Rat z.A.		BGI
BEYER, Christopher	M.Sc.	Wiss. Mitarbeiter	from 01.10.	EU
BLAHA, Stephan	M.Sc.	Wiss. Mitarbeiter	from 01.10.	BGI/IGS
BÖHM, Ulrich		Mechaniker		BGI
BOFFA BALLARAN, Tiziana	Dr.	Akad. Rätin		BGI
BROCKMANN, Nicolas	Dipl.-Chem.	Wiss. Mitarbeiter		BGI/IGS[1]
BUCHERT, Petra		Fremdsprachen-sekretärin		BGI
CERANTOLA, Valerio	B.Sc.	stud. Hilfskraft		DFG/BGI
CERNOK, Ana	M.Sc.	Wiss. Mitarbeiterin	from 11.07.	BGI/IGS
CHANTEL, Julien	M.Sc.	Wiss. Mitarbeiter	to 28.02.	EU
CHUST, Thomas	Dipl. Geophys.	Wiss. Mitarbeiter		DFG
DE KOKER, Nico	Dr.	Gastwissenschaftler	to 31.01.	EU
		Wiss. Mitarbeiter	from 01.02.	DFG
DITTMANN, Uwe		Präparator	to 30.06.	BGI
DUBROVINSKY, Leonid	Apl. Prof. Dr.	Akad. Direktor		BGI
EL GORESY, Ahmed	Prof. Dr.			BGI/VP[2]
EVONUK, Martha	Dr.	Wiss. Mitarbeiterin		DFG
FEI, Hongzhan	B.Sc.	Wiss. Mitarbeiter		BGI/VP
FISCHER, Heinz		Mechaniker		BGI
FISCHER, Nicole	ROI	Verwalt. Beamtin		BGI
FRIGO, Corinne	B.Sc.	stud. Hilfskraft	from 01.10.	DFG
FROST, Daniel	Dr.	Akad. Direktor		BGI
GIANNINI, Mattia	M.Sc.	Wiss. Mitarbeiter		DFG
GLAZYRIN, Konstantin	Ing. Phys.	Wiss. Mitarbeiter	to 30.09.	BGI/IGS
			from 01.10.	EU
GOLLNER, Gertrud		Chem.-Techn. Assistentin		BGI
HARRIES, Dennis	Dipl. Geowiss.	Wiss. Mitarbeiter	to 30.09.	BMBF
HASSANI SHABESTARI, Asiye Sadat	B.Sc.	stud. Hilfskraft	to 14.08.	DFG
			15.08.-30.09.	BMBF
			from 01.10.	DFG
HEIDELBACH, Florian	Dr.	Wiss. Mitarbeiter		BGI/IGS
HIRSEMANN, Dunja	Dipl.-Chem.	Wiss. Mitarbeiterin	to 30.09.	BGI/IGS[4]
HOPF, Juliane	Dr. rer. nat.	Wiss. Mitarbeiterin	01.07.-30.09.	BMBF

HUANG, Ruifang	B.Sc.	stud. Hilfskraft	to 31.03.	DFG[3]
			from 01.04.	DFG
HUBER, Julia		Chem.-Techn. Assistentin	to 30.09.	BGI
KANTOR, Anastasia	Dr.	Wiss. Mitarbeiterin		BMBF
KATSURA, Tomoo	Prof. Dr.	Stellvertr. Leiter		BGI
KEPPLER, Hans	Prof. Dr.	Leiter		BGI
KEYSSNER, Stefan	Dr.	Akad. Oberrat		BGI
KING, Scott	Prof. Dr.	Forschungspreisträger	04.07.-31.07.	AvH
KISON-HERZING, Lydia		Sekretärin		BGI
KLASINSKI, Kurt	Dipl.-Ing. (FH)	Techn. Angestellter		BGI
KRAUßE, Detlef	Dipl.-Inform. (FH)	Techn. Angestellter		BGI
KRIEGL, Holger		Haustechniker		BGI
KULARATNE, Kanchana	B.Sc.	Stud. Hilfskraft	from 05.10.	DFG
KUNZ, Daniel	Dipl.-Chem.	Wiss. Mitarbeiter	from 11.11.	BGI/IGS[4]
KUPENKO, Ilya	Dipl.-Phys.	Wiss. Mitarbeiter	from 13.01.	BMBF
KURNOSOV, Alexander	Dr.	Wiss. Mitarbeiter		EU
LANGENHORST, Falko	Prof. Dr.		to 31.03.	BGI
LERCHBAUMER, Linda	Mag. rer. nat.	Wiss. Mitarbeiterin	to 30.03.	DFG
			31.03.-03.06.	UBT[7]
			from 01.07.	DFG
LI, Yuan	M.Sc.	Wiss. Mitarbeiter		BGI/IGS
LINHARDT, Sven		Elektrotechniker		BGI
LUNKENBEIN, Thomas	Dipl.-Chem.	Wiss. Mitarbeiter		BGI/IGS[4]
MAIEROVA, Petra	M.Sc.	Gastwissenschaftlerin	to 31.01.	EU
MANNING, Craig	Prof. Dr.	Forschungspreisträger	01.08.-23.08.	AvH
MANTHILAKE, Geeth	Dr.	Wiss. Mitarbeiter		BGI/VP
MCCAMMON, Catherine	Dr.	Akad. Oberrätin		BGI
MIYAJIMA, Nobuyoshi	Dr.	Akad. Rat		BGI
MOOKHERJEE, Mainak	Dr.	Wiss. Mitarbeiter	to 13.10.	BGI/VP
			from 14.10.	BGI
NAKAJIMA, Yoichi	Dr.	Wiss. Mitarbeiter		BGI/VP
NI, Huaiwei	Dr.	Wiss. Mitarbeiter	to 06.07.	BGI/VP
			from 07.07.	DFG
NJUL, Raphael		Präparator	from 01.12.	BGI
NOVELLA, Davide	M.Sc.	Wiss. Mitarbeiter		BGI/IGS
OERTEL, Tina	Dipl.-Ing.	Wiss. Mitarbeiterin		BGI/IGS[1]
OJWANG, Dickson	B.Sc.	Stud. Hilfskraft	from 01.06.	DFG
OUSSADOU, Mezhoura	M.Sc.	Gastwissenschaftlerin	to 31.01.	EU
			from 01.02.	DFG
OVSYANNIKOV, Sergey	Dr.	Forschungsstipendiat	to 31.03.	AvH
			15.04.-14.07.	BGI/VP
			from 15.07.	DFG

PAMATO, Martha	M.Sc.	nebenberufliche wiss. Hilfskraft		DFG u. UB e.V.
PARAKHONSKIY, Gleb	M.Sc.	Wiss. Mitarbeiter	to 31.01. 01.02.-31.05.	DFG IND
PESCE, Giacomo	B.Sc.	stud. Hilfskraft	to 14.12. from 15.12.	DFG BGI/HiWi
POLLOK, Kilian	Dr.	Akad. Rat a.Z.	to 15.07.	BGI
POTZEL, Anke		Chem.-Techn. Assistentin		BGI
PRESCHER, Clemens	Dipl.-Min.	wiss. Mitarbeiter		BGI/IGS
RAMMING, Gerd		Elektroniker		BGI
RAUSCH, Oliver		Mechaniker		BGI
RUBIE, David C.	Prof. Dr.			EU
SAMUEL, Henri	Prof. Dr.	Juniorprofessor		Stiftung[5]
SAVCHUK, Oles	B.Sc.	stud. Hilfskraft	from 01.10.	DFG
SCHEITER, Daniel		Wiss. Mitarbeiter	to 30.06.	BMBF
SCHMITT, Veronika	Dipl.-Min.	Wiss. Mitarbeiterin		BGI/IGS[1]
SCHULZE, Hubert		Präparator		BGI
SHCHEKA, Svyatoslav	Dr.	Wiss. Mitarbeiter		DFG
SHEKHAR, Sushant	M.Sc.	Wiss. Mitarbeiter	to 31.05.	BGI/IGS
SINMYO, Ryosuke	Dr.	Wiss. Mitarbeiter	from 01.07.	BGI/VP
STAGNO, Vincenzo	Dipl.-Geol.	Wiss. Mitarbeiter	to 31.03. 01.06.-27.08.	DFG EU
STEINLE-NEUMANN, Gerd	Dr.	Akad. Rat		BGI
SUN, Wei	B.Sc.	stud. Hilfskraft	to 31.03.	DFG
TRENZ, Ulrike		Biol.-Techn. Assistentin	from 01.12.	BGI
TROTS, Dmytro	Dr.	Wiss. Mitarbeiter		EU
ÜBELHACK, Stefan		Mechaniker		BGI
VAN MIERLO, Willem	M.Sc.	Gastwissenschaftler	to 03.01. 04.01.-31.03.	EU BGI/VP
VLCEK, Vojtech	B.Sc.	stud. Hilfskraft	to 31.07. 01.08.-30.09.	EU BMBF
		Wiss. Mitarbeiter	from 01.10.	DFG
VOGEL, Antje	Dipl.-Min.	Wiss. Mitarbeiterin	from 01.03.	DFG
WACK, Julia	Dipl.-Chem.	Wiss. Mitarbeiterin		BGI/IGS[4]
WALTE, Nicolas	Dr.	Wiss. Mitarbeiter		BMBF
WEI, Qingguo	B.Sc.	stud. Hilfskraft	to 31.05.	DFG
YANG, Xiaozhi	Dr.	Forschungsstipendiat	to 31.08. 01.09.-14.12. from 15.12.	AvH BGI/VP BGI

Abbreviations/explanations:

AvH	Alexander von Humboldt Foundation
BGI	Staff Position of Bayerisches Geoinstitut
BGI/HiWi	Hilfskraftmittel BGI
BGI/VP	Visiting Scientists' Program of Bayerisches Geoinstitut
BMBF	Federal Ministry of Education and Research
DFG	German Science Foundation
EXZ	Exzellenzinitiative der Universität Bayreuth
EU	European Union
IGS	International Graduate School under the Elitenetzwerk Bayern "Structure, Reactivity and Properties of Oxide Materials"
IND	Industry
MPG	Max-Planck-Gesellschaft
UB e.V.	Universität Bayern e.V.
UBT	Universität Bayreuth

---

[1] Fraunhofer ISC Würzburg

[2] partially funded by the Visiting Scientists' Program of Bayerisches Geoinstitut

[3] Leibniz award Prof. Langenhorst

[4] Chair of Inorganic Chemistry I, Prof. Breu

[5] Juniorprofessorship for Geodynamic Modeling funded by Stifterverband für die Deutsche Wissenschaft

[7] Übergangsmittel für Doktoranden ("Feuerwehrfonds")

Index